

ResearchOnline@JCU

This file is part of the following reference:

Leong, Kenneth Tak Ming (2000) *Precise measurements of surface resistance of high temperature superconducting thin films using a novel method of Q-factor computations for sapphire dielectric resonators in the transmission mode.* PhD thesis, James Cook University.

Access to this file is available from:

<http://researchonline.jcu.edu.au/41458/>

If you believe that this work constitutes a copyright infringement, please contact ResearchOnline@jcu.edu.au and quote <http://researchonline.jcu.edu.au/41458/>

**Precise Measurements of Surface Resistance of
High Temperature Superconducting Thin
Films using a Novel Method of Q-Factor
Computations for Sapphire Dielectric
Resonators in the Transmission Mode**

Thesis submitted by
Kenneth Tak Ming LEONG BE (Hons)
in March 2000

for the degree of Doctor of Philosophy
in Electrical and Computer Engineering
School of Engineering
James Cook University

Access to Thesis

I, the undersigned, the author of this thesis, understand that James Cook University will make it available for use within the University Library and, by microfilm or other photographic means, allow access to users in other approved libraries. All users consulting this thesis will have to sign the following statement:

"In consulting this thesis I agree not to copy or closely paraphrase it in whole or in part without the written consent of the author; and to make proper written acknowledgement for any assistance which I have obtained from it."

Beyond this, I do not wish to place any restriction on access to this thesis.

(signature)

.....6/3/2000

(date)

Declaration

I declare that this thesis is my own work and has not been submitted in any form for another degree or diploma at any university or other institution of tertiary education. Information derived from the published work of others has been acknowledged in the text and a list of references is given.

(signature)

.....6/3/2000

(date)

Acknowledgements

I wish to convey warmest thanks to my family; Jackson, Roslyn, Helen and Selina, who have given me endless support throughout my studies.

I express sincere thanks to my supervisor A/Prof Janina Mazierska who has provided me tremendous support and guidance.

I also thank Jerzy Krupka of the Institute of Microelectronics and Optoelectronics, Warsaw University of Technology for his expert help and recommendations, as well as A/Prof Greg Allen, A/Prof Keith Kikkert, Dr. Graham Woods of the Department of Electronic and Computer Engineering at James Cook University, Dr. Graeme Sneddon of the Department of Mathematics and Physics at James Cook University, and Patrick Xie of the Texas Center for Superconductivity at the University of Houston.

I wish to thank Dr. Darko Kajfez of the Department of Electrical Engineering at the University of Mississippi for his expert help and encouragement in the early stages of my work on this thesis.

I also thank all staff of the School of Engineering at James Cook University for their kind help.

Finally, I thank my wonderful friends who were always there for me in support inside and outside the academic environment.

Dedication

This work is dedicated to my parents; Jackson and Roslyn, and my sisters; Helen and Selina.

Abstract

The work presented in this thesis belongs to the area of microwave characterisation of High Temperature Superconductor (HTS) materials and is devoted to precise measurements of the surface resistance R_s of HTS thin films using the sapphire dielectric resonator structure. Accurate measurements of surface resistance of HTS films are essential for advancement of knowledge and technological progress in the field especially for commercial applications of HTS materials in wireless communications.

In typical measurements of R_s , the superconductor film sample is made an integral part of a microwave resonator, which is a structure that can store microwave energy. The unloaded quality factor Q_0 of the structure measured typically in the transmission mode and is used for calculations of the surface resistance. While there is a need for accurate procedures to measure the surface resistance, no standard procedure has yet been developed for such purpose as no detailed comparative studies were done on the accuracy of existing techniques as well as a lack of superior techniques to determine the unloaded Q_0 -factor of microwave resonators working in the transmission mode.

In this thesis, a novel method to accurately and conveniently determine the unloaded Q_0 -factor of the transmission mode sapphire resonator for measurements of R_s of high temperature superconducting thin films is presented. The developed Transmission Mode Q_0 -Factor Technique is based on measurements of S-parameters and it accounts for practical effects introduced by a real measurement system which are not always accounted for in simple Q_0 -factor techniques. The developed method is applicable not only to the testing of HTS materials using sapphire resonators, but can be successfully employed in any measurements involving transmission mode dielectric resonators.

Contents

1	Introduction	1
1.1	Major Issues in Measurements of The Surface Resistance of HTS Thin Films	4
2	Review of Superconducting Materials, Phenomena of Superconductivity and Applications of Superconducting Materials	11
2.1	Superconductor Materials	11
2.2	Physical Phenomena Associated With Superconductivity and Material Parameters of Superconductors	15
2.2.1	Vanishing Resistance	15
2.2.2	The Meissner Effect	16
2.2.3	Zero Dispersion in Superconductor Materials	17
2.3	Relationship Between Transition Temperature, Critical Field, Critical Current and Critical Frequency	18
2.4	Concept of Resistance and Surface Impedance in Metals and Superconductors	22
2.5	Progress in The Understanding of Superconductivity	27
2.5.1	London Theory of Electrodynamics in Conventional Superconductors	28
2.5.2	Ginzburg-Landau Theory	30
2.5.3	Two Fluid Model	30
2.5.4	BCS Theory of Superconductivity	33
2.5.5	Progress in the Understanding of High Temperature Superconductivity	33
2.6	Applications of Superconducting Materials	34
2.7	Applications of High Temperature Superconductors	35
2.7.1	Filters and Other Systems for Wireless Communications	37
2.7.2	Delay Lines for Analog Signal Processing	40

2.7.3	HTS Wires and Tapes for Electrical Power Applications, Magnetic Levitational Transport, and High Energy Physics Research	42
2.7.4	Josephson Devices for DSP Applications, Detection of Weak Magnetic Fields, Mixers for Wireless Communications, Medical Diagnostics, Digital Electronics and Other Applications	43
2.7.5	Device Packaging for High Speed Digital Electronics	45
3	Review of Experimental Techniques Used for Measurements of The Surface Resistance of HTS Thin Films	49
3.1	Quality Factor Definition and Energy Transactions in Resonators	49
3.2	Equations for Calculations of The Surface Resistance of Superconductor Films Using Loss Equations and Accuracy of Calculations	51
3.3	Review of Q-Factor Relationships in Microwave Resonators	54
3.4	Resonators Used for The Microwave Characterisation of Superconducting Films	57
3.5	Geometrical Factors and EM Field Distribution in Dielectric Resonators	63
3.6	Determination of the Surface Resistance of HTS Films Using The Sapphire Dielectric Resonator of the Hakki Coleman Type	66
3.7	Analysis of Errors in Calculations of R_s of HTS Films Using Hakki Coleman Resonators Due to Uncertainties in Measurement Parameters	70
3.8	Unloaded Q_o -factor Measurement Techniques	72
3.8.1	Time Domain Techniques for Measurements of Unloaded Q_o -Factor	74
3.8.2	Frequency Domain Techniques for Measurements of Unloaded Q_o -Factor	77
3.9	Circle Fitting Procedures Used to Obtain The Unloaded Q_o -Factors of Microwave Resonators From Measurements of S-Parameters	85
3.9.1	S_{21} Phase Technique of Loaded Q_L -Factor Measurements	85

3.9.2	The S_{11} Technique of Loaded Q_L -Factor and Coupling Coefficient Measurements	89
4	Development of a Novel Method for The Accurate Determination of Unloaded Q-Factors of Transmission Mode Dielectric Resonators Based on Measurements of Scattering Parameters and Circle-Fitting	99
4.1	General Issues to be Considered in the Development of A Model of a Hakki Coleman Dielectric Resonator Test System	99
4.2	Practical Effects Introduced by the HTS Microwave Characterisation System	103
4.2.1	Assessment of Practical Effects Introduced by a Real Measurement System to The Transmission and Reflection Responses of the Dielectric Resonator	112
4.3	Development of A Transmission Mode Method for The Accurate Determination of The Unloaded Q_0 -Factor of Microwave Resonators Based on Measurements of S-Parameters.	116
4.4	Equations for The Fractional Linear Curve Fitting Procedure to The Transmission Mode Resonator Responses	128
5	Assessment of The Accuracy of The Novel Transmission Mode Q_0-Factor Technique Using Computer Simulations	131
5.1	Influence of Noise on The Error in The Unloaded Q_0 -Factor Obtained From The Transmission Mode Q_0 -Factor Technique	134
5.2	Influence of Frequency Dependence of Delay Due to Transmission Lines on Errors in Q_0 and a Method to Remove This Effect From Reflection (S_{11} or S_{22}) Q-Circles	140
5.3	Influence of The Frequency Dependence of The Coupling Reactance X_s on Errors in Q_0 in The Absence of Transmission Line Delay	147
5.4	Influence of Variation in Coupling Losses (Modelled Using R_s) on Errors in Q_0 in The Presence of Cable Delay	151

5.5	Influence of Variation in The Coupling Reactance X_s on Errors in Q_0 in The Presence of Cable Delay	155
6	Measurements of Surface Resistance of $YBa_2Cu_3O_7$ Thin Films Using The Sapphire Resonator and The Transmission Mode Q_0-Factor Technique Based on S-Parameters	161
6.1	Measurement Systems for R_s Testing of HTS Films	161
6.2	Measurements of Good Quality $YBa_2Cu_3O_7$ Thin Films Using a 10 GigaHertz Hakki Coleman Sapphire Resonator	167
6.2.1	Measurements of The Unloaded Q_0 -Factor Using the Transmission Mode Q_0 -Factor Technique Without Phase Correction of S_{11} and S_{22} Traces	174
6.2.2	Measurements of The Unloaded Q_0 -Factor Under Very Weak Coupling	175
6.2.3	Calculations of The Surface Resistance of $YBa_2Cu_3O_7$ HTS Films on $LaAlO_3$ Substrate	177
6.2.4	Measurements of Poor Quality $YBa_2Cu_3O_7$ Thin Films Using a 25 GigaHertz Hakki Coleman Sapphire Resonator	178
6.3	Assessment of The Feasible Range of Q_0 -Factor Measurements Using the Transmission Q_0 -Factor Technique	183
7	Conclusions	186
7.1	Future Work and Recommendations	190
7.2	Publications Related to Work Presented in This Thesis	191
A.	Equations for The Fractional Linear Curve Fitting Procedure to The Transmission Mode Resonator Responses	194
B.	Implementation of The Fractional Linear Curve Fitting Technique for Fitting to S_{21}-Parameter Q-Circle Data Sets	203
C.	Enhanced Phase Correction Procedure	207

D. Method to Find The Centre and Radius of The Circle Passing Through Data Points Distributed Around a Circular Path Using Linear Least Squares Curve Fitting Technique	212
E. Fit Results for The 10 GHz Measurements on $\text{YBa}_2\text{Cu}_3\text{O}_7$ HTS Thin Films	214
F. Fit Results for The 25 GHz Measurements on $\text{YBa}_2\text{Cu}_3\text{O}_7$ HTS Thin Films	218

List of Figures

Figure 2.1	YBCO structure.	14
Figure 2.2	Typical temperature dependence of DC resistivity in a superconductor.	16
Figure 2.3	The Meissner effect.	17
Figure 2.4	The effect of a dispersive medium and a non-dispersive medium on a square pulse passing through.	18
Figure 2.5	Superconductor phase diagram.	19
Figure 2.6	Evolution of transition temperature T_c since the discovery of superconductivity.	20
Figure 2.7	Critical field versus temperature for Type I superconductors.	21
Figure 2.8	Critical fields versus temperature for Type II superconductor.	22
Figure 2.9	Normal wire conductor of length L , cross-sectional area A , with a voltage V applied across it's terminals. The wire has a conductivity σ .	23
Figure 2.10	Frequency dependence of surface resistance of copper and $YBa_2Cu_3O_{7-x}$ (YBCO) thin film superconductor around the 800-900 MHz cellular band.	26
Figure 2.11	Penetration of magnetic field in a superconducting sample.	29
Figure 2.12	Equivalent circuit for a superconductor modelled on the Two Fluid model.	32
Figure 2.13	Equivalent circuit for the admittance of a unit cube of superconductor in the Two Fluid model.	32
Figure 2.14	Possible applications of high temperature superconductors.	37
Figure 2.15	Comparison of performance parameters between a high temperature superconducting filter and a conventional normal conducting filter.	38
Figure 2.16	A 19 pole HTS bandpass filter developed by Conductus Inc. for cellular wireless communications and the insertion loss characteristics of the filter.	39

Figure 2.17	Comparison of system noise figure between a conventional MRC-800 cellular receiver system with the same system fitted with a superconducting filter and low noise amplifier on the front end.	39
Figure 2.18	Superconductive electronic applications of HTS in wireless communications and digital electronics.	40
Figure 2.19	A 11 nanosecond delay line made by Dupont. The superconducting line is arranged in a spiral pattern.	41
Figure 2.20	Block diagram of a monolithic YBCO Josephson mixer circuit mounted in a microwave package.	44
Figure 3.1	Time dependence of stored energies in a resonator.	50
Figure 3.2	Microwave losses of a dielectric resonator.	51
Figure 3.3	Power dissipation in a loaded resonant system consisting of a microwave resonator connected to a external circuit.	54
Figure 3.4	Power dissipation in a loaded resonant system consisting of a microwave resonator working in the transmission mode.	56
Figure 3.5	Dielectric resonator fitted with single superconductor film sample.	58
Figure 3.6	Hakki Coleman type dielectric resonator used in this thesis.	58
Figure 3.7	Parallel plate resonator.	59
Figure 3.8	Conventional microstrip resonator.	60
Figure 3.9	Microstrip resonator in the flip-chip configuration.	60
Figure 3.10	Stripline resonator.	61
Figure 3.11	Coplanar wave guide resonator.	61
Figure 3.12	Confocal resonator.	62
Figure 3.13	Endplate replacement cavity.	63
Figure 3.14	Magnetic field distribution (axial Z component) for TE ₀₁₁ mode of sapphire resonator with dimensions : Height of the sapphire = 7.41 mm, cavity diameter = 24 mm, sapphire diameter = 12.32 mm, dielectric constant = 9.28, Resonant frequency = 10 GHz.	65
Figure 3.15	Electric field distribution (azimuthal ϕ component) for the TE ₀₁₁ mode of sapphire resonator with dimensions : Height of the sapphire = 7.41	

-
- mm, cavity diameter = 24 mm, sapphire diameter = 12.32 mm,
dielectric constant = 9.28, Resonant frequency = 10 GHz. 66
- Figure 3.16 Losses in Sapphire DR. 67
- Figure 3.17 The most probable relative error in R_s versus R_s for various values of uncertainty in unloaded Q_o -factor $\Delta Q_o/Q_o$ for a 10 GHz sapphire resonator with assumed uncertainties $\Delta A/A = 0.5\%$, $\Delta Q_d/Q_d$ of 1%, $\Delta \tan \delta / \tan \delta = 5\%$; and assumed values $A_m = 27616$, $A_s = 279$, $R_m = 15$ m Ω , $\tan \delta = 5 \cdot 10^{-8}$, $p_e = 0.971$. 72
- Figure 3.18 Two groups of methods used in determination of the unloaded Q_o -factor of microwave resonators with typical modes and names of measurements indicated. 74
- Figure 3.19 Time domain Q-Factor measurement system. 74
- Figure 3.20 Time domain determination of Q factor. 75
- Figure 3.21 Power curves measured at the output side, needed to obtain the radiated power $P_{rad}(t_1)$ to be used in the calculation of the coupling coefficient on the output side of transmission mode cavity resonator. 76
- Figure 3.22 Reflected power curve measured from the input side, needed to obtain the reflected power $P_{ref}(t_1)$ to be used in the calculation of the coupling coefficient on the output side of transmission mode cavity resonator. 76
- Figure 3.23 Microwave signals entering and leaving ports for 2-Port microwave resonator. 78
- Figure 3.24 Illustration of measurements of S-parameters on a Two Port microwave resonator. 79
- Figure 3.25 Three Frequency Method used to obtain the loaded Q_L -factor from the S_{21} transmission (magnitude) response. 80
- Figure 3.26 A noisy trace introduces uncertainty in the selected resonant frequency and half power frequencies used in the Three Frequency Method to calculated the loaded Q_L -factor. 81

-
- Figure 3.27 The finite resolution of measurement instrument introduces measurement uncertainty, which contributes to uncertainties in the determination of the loaded Q_L -factor using Three Frequency Method. 81
- Figure 3.28 Distortion in S_{21} trace due to crosstalk. 84
- Figure 3.29 A series RLC circuit of a microwave resonator. 85
- Figure 3.30 Ideal S_{21} Q-circle. 87
- Figure 3.31 Q-circle which has undergone a rotation around the origin due to cable phase shift. 88
- Figure 3.32 Q-circle which has undergone a rotation around the origin due to cable phase shift, followed by a translation due to crosstalk effects. 88
- Figure 3.33 S_{21} Q-circle with centre at the origin. The phase-frequency dependence of the S_{21} vector is given by (3.66) to the phase data. 88
- Figure 3.34 Equivalent circuit of the dielectric resonator in the reflection mode. 90
- Figure 3.35 Position of a S_{11} Q-circle for a case of lossless coupling, zero coupling reactance, and no delay due to transmission lines. 91
- Figure 3.36 Equivalent circuit to model lossy coupling. 92
- Figure 4.1 A ideal case measurement system used to measure the unloaded Q_o -factor of microwave resonators. The input ports of the resonator are accessible. 99
- Figure 4.2 A measurement system used to measure the unloaded Q_o -factor of microwave resonators under low temperature/vacuum conditions. The input ports of the resonator cannot be accessed due to practical constraints. 100
- Figure 4.3 A circuit diagram of a perfect one-port measurement system to measure the unloaded Q_o -factor of microwave resonators. 100
- Figure 4.4 A circuit diagram showing the input port of a practical resonant system to measure the unloaded Q_o -factor of microwave resonators. 100
- Figure 4.5 Component effects of a network connected between the measurement point and the microwave resonator modelled as a cascade of sections. 102

Figure 4.6	The R_s measurement system.	103
Figure 4.7	Distortion of reflection (S_{11} in this case) Q-circle caused by frequency dependence of transmission line delay.	105
Figure 4.8	The frequency dependence of delay due to transmission line causes the insertion phase to change linearly with frequency.	106
Figure 4.9	The transmission S_{21} Q-circle is much less effected by the frequency dependence of delay in transmission lines than for reflection (S_{11} or S_{22}) circles.	106
Figure 4.10	Mismatch effect observed in the off-resonance part of the reflection S_{22} trace.	107
Figure 4.11	Mismatch effect observed in the S_{22} magnitude trace.	108
Figure 4.12	Mismatch effects can cause non-linearities in the phase of the reflection response (S_{11} or S_{22}).	109
Figure 4.13	The S_{21} magnitude trace measured under a relatively weak coupling condition and averaged over 16 sweeps is reasonably well defined.	110
Figure 4.14	The magnitude-of- S_{11} reflection trace is clearly much more noisy than the S_{21} trace of Fig. 4.13 under the same coupling conditions even after averaging over 16 sweeps.	110
Figure 4.15	A circuit model of ideal transmission mode resonator system modelled by parallel RLC elements with lossless transmission line connecting to the microwave source and load.	112
Figure 4.16	Illustrative summary of influences of practical effects on S_{21} Q-circles and S_{21} magnitude trace.	113
Figure 4.17	Reflection Q-circles for various cases of coupling loss and coupling reactance.	114
Figure 4.18	Circuit model of a practical transmission resonator measurement system.	117
Figure 4.19	Equivalent circuit to model coupling losses.	123
Figure 4.20	S_{11} circle and coupling loss circle in the Smith Chart for the case when observations are made at the input of the resonator.	125

Figure 5.1	Circuit model of the transmission mode dielectric resonator used in the development of the Transmission Mode Q_o -factor Technique.	131
Figure 5.2	S_{21} , NR=0.001 equal couplings.	137
Figure 5.3	S_{11} , NR=0.001 equal couplings.	137
Figure 5.4	S_{21} , NR=0.002 equal couplings.	137
Figure 5.5	S_{11} , NR=0.002 equal couplings.	137
Figure 5.6	S_{21} , NR=0.001 unequal couplings.	139
Figure 5.7	S_{11} , NR=0.001 unequal couplings.	139
Figure 5.8	S_{22} , NR=0.001 unequal couplings.	140
Figure 5.9	Error in Q_o using Q_L of S_{21} and S_{11} fits for Q_o of 1000.	143
Figure 5.10	Error in Q_L obtained from S_{21} and S_{11} fits for Q_o of 1000.	143
Figure 5.11	Error in Q_o using Q_L of S_{21} and S_{11} fits for Q_o of 10000.	143
Figure 5.12	Error in Q_L obtained from S_{21} and S_{11} fits for Q_o of 10000.	143
Figure 5.13	Error in Q_o using Q_L of S_{21} and S_{11} fits for Q_o of 100000.	144
Figure 5.14	Error in Q_L obtained from S_{21} and S_{11} fits for Q_o of 100000.	144
Figure 5.15	S_{21} Q-circle for line length = 30λ , span = 6.96 MHz.	145
Figure 5.16	S_{11} Q-circle for line length = 30λ , span = 6.96 MHz.	145
Figure 5.17	A 101 point S_{21} Q-circle subset of the 401 point S_{21} Q-circle of Fig. 5.15.	146
Figure 5.18	S_{21} circle fitted over 401 points of simulated data, with parameters $R_{s1}=R_{s2}=5\Omega$, $X_{s1}=X_{s2}=20\Omega$, $Q_o = 1000$, $L/\lambda=0.55$, $f_o = 10$ GHz.	146
Figure 5.19	S_{11} circle fitted over 401 points of simulated data, with parameters $R_{s1}=R_{s2}=5\Omega$, $X_{s1}=X_{s2}=20\Omega$, $Q_o = 1000$, $L/\lambda=0.55$, $f_o = 10$ GHz.	146
Figure 5.20	Error in Q_o using Q_L of S_{21} and S_{11} fits for Q_o of 1000 over various values of X_s with dependence on frequency.	149
Figure 5.21	Error in Q_L obtained from S_{21} and S_{11} fits for Q_o of 1000 over various values of X_s with dependence on frequency.	149
Figure 5.22	Error in fitted coupling coefficient obtained for Q_o of 1000 over various values of X_s with dependence on frequency. Equal couplings are used.	149

Figure 5.23 Error in Q_o using Q_L of S_{21} and S_{11} fits for Q_o of 10000 over various values of X_s with dependence on frequency.	150
Figure 5.24 Error in Q_o using Q_L of S_{21} and S_{11} fits for Q_o of 10000 over various values of X_s with dependence on frequency.	150
Figure 5.25 Error in fitted coupling coefficient for a case of $Q_o = 10000$ over various values of X_s with dependence on frequency.	150
Figure 5.26 Error in Q_o using Q_L of S_{21} and S_{11} fits for various R_s and nominal Q_o of 1000. $L=0.2\lambda$.	153
Figure 5.27 Error in Q_L obtained from Q_L of S_{21} and S_{11} fits for various R_s and nominal Q_o of 1000. $L=0.2\lambda$.	153
Figure 5.28 Error in coupling coefficient for various R_s and nominal Q_o of 1000. $L=0.2\lambda$.	153
Figure 5.29 Error in Q_o using Q_L of S_{21} and S_{11} fits for various R_s and nominal Q_o of 10000. $L=0.2\lambda$.	154
Figure 5.30 Error in Q_L obtained from S_{21} and S_{11} fits for various R_s and nominal Q_o of 10000. $L=0.2\lambda$.	154
Figure 5.31 Error in coupling coefficient for various R_s and nominal Q_o of 10000. $L=0.2\lambda$.	154
Figure 5.32 Error in Q_o using Q_L of S_{21} and S_{11} fits for various X_s , nominal Q_o of 1000 and $L=0.2\lambda$.	157
Figure 5.33 Error in Q_L obtained from S_{21} and S_{11} fits for various X_s , nominal Q_o of 1000 and $L=0.2\lambda$.	157
Figure 5.34 Error in coupling coefficient for various X_s , nominal Q_o of 1000 and $L=0.2\lambda$.	157
Figure 5.35 Error in Q_o using Q_L of S_{21} and S_{11} fits for various X_s , nominal Q_o of 10000 and $L=0.2\lambda$.	158
Figure 5.36 Error in Q_L obtained from S_{21} and S_{11} fits for various X_s , nominal Q_o of 10000. $L=0.2\lambda$.	158
Figure 5.37 Error in coupling coefficient for various X_s , nominal Q_o of 10000 and $L=0.2\lambda$.	158

-
- Figure 6.1 R_s measurement system using the liquid nitrogen bath for refrigeration of the resonator containing the superconductor samples. 162
- Figure 6.2 R_s measurement system using the closed cycle cryocooler for refrigeration of the resonator containing the superconductor samples. 163
- Figure 6.3 The 10 GHz Hakki Coleman resonator used in this thesis for measurements of the surface resistance of one inch round wafers of $\text{YBa}_2\text{Cu}_3\text{O}_{7-x}$ HTS thin films. 164
- Figure 6.4 10 GHz Hakki Coleman sapphire resonator with one of the endplates removed, showing the sapphire dielectric puck sitting on top of a superconductor film. The coupling loops are inside the cavity for display purposes only. 164
- Figure 6.5 Sapphire resonator inside the vacuum dewar can be seen through the round perspex plate. The cold head which is not visible is below the brass platform. 166
- Figure 6.6 Photo of the main measurement system used in this thesis, showing the HP8722C network analyser, temperature controller, vacuum dewar with the cold head, IBM-PC computer, and rotary vacuum pump. The compressor of the cryocooler system is not visible in the photo. 167
- Figure 6.7 Measured S_{21} Q-circle with 1601 points spanning 100 kHz and the fitted circle. The fitted Q_L -factor is 403130, and the fitted resonant frequency f_0 is 9.997 GHz. 168
- Figure 6.8 Measured S_{11} Q-circle with some of the off-resonance trace visible. The span is 2 MHz. 169
- Figure 6.9 Measured S_{22} Q-circle with some of the off-resonance trace visible. The span is 2 MHz. 169
- Figure 6.10 Measured S_{11} wide-span off-resonance trace (red) shown with the fitted circle (blue). The central coordinates of the circle are (0.026963, 0.038702). 170

-
- Figure 6.11 Measured S_{22} wide-span off-resonance trace (red) shown with the fitted circle (blue). The central coordinates of the circle are (0.020116, 0.050223). 170
- Figure 6.12 Phase of S_{11} plotted with respect to the centre of the off-resonance circle (of Fig. 6.10) versus frequency. A linear fit gives of rate of change in phase of about $-3.668 \cdot 10^{-8}$ rad/Hz. 171
- Figure 6.13 Phase of S_{22} plotted with respect to the centre of the off-resonance circle (of Fig. 6.11) versus frequency. A linear fit gives a rate of change in phase of about $-4.224 \cdot 10^{-8}$ rad/Hz. 171
- Figure 6.14 Corrected S_{11} Q-circle after phase correction has been applied to the Q-circle of Fig. 6.8. 172
- Figure 6.15 Corrected S_{22} Q-circle after phase correction has been applied to the Q-circle of Fig. 6.9. 172
- Figure 6.16 Reduced data set of the corrected S_{11} Q-circle of Fig. 6.14, together with the fitted circle. 173
- Figure 6.17 Reduced data set of the corrected S_{22} Q-circle of Fig. 6.15, together with the fitted circle. 173
- Figure 6.18 A 1601 point S_{11} Q-circle spanning 120 kHz shown with the fitted circle. 174
- Figure 6.19 A 1601 point S_{22} Q-circle spanning 120 kHz shown with the fitted circle. 174
- Figure 6.20 A 1601 point S_{21} Q-circle measured under very weak coupling condition, spanning 100 kHz. The insertion loss at the resonance is about 58 dB. The fitted trace is shown and the fitted Q_L -factor is 421426. The data scatter D_s is 0.195. 176
- Figure 6.21 A 628 point subset from the S_{21} Q-circle of Fig. 6.20 and showing the fitted circle. The span is 39.187 kHz and the fitted loaded Q_L -factor is 431634. The data scatter D_s is 0.075. 176

-
- Figure 6.22 Measured 401 point S_{21} Q-circle (red) spanning 5 MHz and fitted circle (blue). The fitted loaded Q_L -factor is 22718 and resonant frequency is 24.75 GHz. 179
- Figure 6.23 Measured S_{11} trace over a wide span of 120 MHz centred about the resonance. The S_{11} Q-circle is lies within the circular off-resonance trace. 180
- Figure 6.24 Measured S_{22} trace over a wide span of 120 MHz centred about the resonance. The S_{22} Q-circle is lies within the circular off-resonance trace.. 180
- Figure 6.25 Corrected S_{11} circle containing 28 points spanning 8.1 MHz with the fitted trace. 181
- Figure 6.26 Corrected S_{22} circle containing 18 points spanning 5.1 MHz with the fitted trace. 181
- Figure B1 The value of S_{21} at the resonant frequency may not be so accurate for the first curve fitting procedure. 205
- Figure C1 Synthesised S_{11} trace spanning 40 times the loaded bandwidth, showing the distorted S_{11} Q-circle and off-resonance curve. The circuit parameters used to generate the trace are : $X_{s1}=X_{s2}=20\Omega$, $R_1=R_2=5\Omega$, $R_o=5\Omega$, $Q_o=9000$, $Q_L=7754$, $f_o=10\text{GHz}$, $L_1=L_2=70\lambda$, $N=401$ points. 208
- Figure C2 Phase of S_{11} versus frequency in off-resonance region. 209
- Figure C3 S_{11} Q-circle after the removal of phase distortion from the S_{11} Q-circle of Fig. C1. 210
- Figure D1 N data points distributed about a circular path with the first point (x_1, y_1) and last point (x_N, y_N) . The circle has centre (h, k) and radius R which need to be determined. 212
- Figure E1 Printout results of the linear fractional curve fitting procedure applied to the S_{21} Q-circle with fitted Q_L of 403130. 215

-
- Figure E2 Printout results of the linear fractional curve fitting procedure applied to the corrected S_{11} Q-circle showing the real and imaginary parts of the fitted coefficients a_1 , a_2 and a_3 . 216
- Figure E3 Printout of the linear fractional curve fitting to the corrected S_{22} Q-circle showing the real and imaginary parts of the fitted coefficients a_1 , a_2 and a_3 . 216
- Figure E4 Comparison of the loaded Q_L -factors, resonant frequencies and Q-circle diameters, and signal-to-noise ratios obtained from S_{21} , S_{11} and S_{22} fits. 217
- Figure E5 Results obtained from the Transmission Mode Q_o -factor Technique showing the computed port coupling coefficients K_1 and K_2 of 0.027 and 0.053 respectively, and the unloaded Q_o -factor of 435393 (calculated from Q_L of S_{21} -fit and the port coupling coefficients). 217
- Figure E6 Unloaded Q_o -factor and port coupling coefficients obtained for the case with no phase correction of reflection Q-circles applied. The computed unloaded Q_o -factor is 434765. 218
- Figure F1 The loaded Q_L -factors, resonant frequencies, and signal to noise ratios obtained from the curve fitting procedure applied to the S_{21} trace, and the corrected S_{11} and S_{22} traces. 218
- Figure F2 Fitted unloaded Q_o -factor and coupling coefficient results obtained from the full unloaded Q_o -factor circle fitting procedure. 219

List of Tables

Table 2.1	Superconducting elements and their transition temperatures.	12
Table 2.2	Conventional superconducting compounds and their transition temperatures.	12
Table 2.3	HTS materials and their transition temperatures.	13
Table 5.1	Errors in unloaded and loaded values of Q-factor, and coupling coefficients under equal couplings in the presence of noise. The computed signal to noise ratio for each noise condition is also given. The noise radius is varied between 0.0005 and 0.02.	136
Table 5.2	Errors in unloaded and loaded values of Q-factor, and coupling coefficients under different couplings in the presence of noise. The computed signal to noise ratio for each noise condition is also given. The noise radius is varied between 0.0005 and 0.004.	139
Table 5.3	Maximum error in Q_0 obtained from Q_L of S_{21} and S_{11} fit, and corresponding values of Q_L and coupling coefficient for $Q_0 = 1000$ for varying transmission line length.	142
Table 5.4	Maximum error in Q_0 obtained from Q_L of S_{21} and S_{11} fit, and corresponding values of Q_L and coupling coefficient for $Q_0 = 10000$ for varying transmission line length.	143
Table 5.5	Error in Q_0 calculated from Q_L of S_{21} -fit for variations in X_s/R_c .	149
Table 5.6	Error in Q_L calculated from Q_L of S_{11} -fit for variations in X_s/R_c .	149
Table 5.7	Errors in the unloaded Q_0 -factor calculated from the Q_L -factors of S_{21} -fit for variations of R_s/R_c .	153
Table 5.8	Errors in the unloaded Q_0 -factor calculated from the Q_L -factors of S_{11} -fit for variations of R_s/R_c .	153
Table 5.9	Errors in the unloaded Q_0 -factors calculated from Q_L of S_{21} -fit for variations in X_s/R_c and $L_1=L_2=0.2\lambda$.	157
Table 5.10	Errors in the unloaded Q_0 -factors calculated from Q_L of S_{11} -fit for variations in X_s/R_c and $L_1=L_2=0.2\lambda$.	157
Table 6.1	Results obtained from the Transmission Mode Q_0 -Factor Technique showing the loaded Q_L -factor of S_{21} fit, coupling coefficients, and the	

	unloaded Q_0 -factor calculated from Q_L of S_{21} -fit and the coupling coefficients.	174
Table 6.2	Surface resistances of $YBa_2Cu_3O_7$ on $LaAlO_3$ substrate at 9.997 GHz and 77 K calculated from the unloaded Q_0 -factors obtained using three different methods.	179
Table 6.3	Results obtained from the Transmission Mode Q_0 -Factor Technique showing the loaded Q_L -factor of S_{21} fit, coupling coefficients and the calculated unloaded Q_0 -factor calculated from Q_L of S_{21} -fit and the coupling coefficients.	182

CHAPTER 1

INTRODUCTION

Aims to enhance our society and lifestyles through electronic inventions create needs to improve the performance of electronic devices in various ways such as increase in the operating speed and efficiency, reduced power consumption, and reduced size. Superconductor materials provide opportunities for such improvements to be made. They bring prospects of new technologies as well as hold enormous foreseen potential for commercial applications in a wide range of major industries including wireless communications, remote sensing, digital signal processing, transportation, and medicine. Since the discovery of high temperature superconductivity in 1986 by Bednorz and Mueller, outstanding progress has been made in developments of superconductive products. While attempts to expand on the limited range of industrial applications for superconductors have been unsuccessful even after a few decades of intensive developmental efforts using low temperature superconductors, the excellent results achieved with high temperature superconductors over the last ten years look very promising.

At present, the most promising applications for superconductors are based on high temperature superconductors in the form of thin films. For applications in high frequency systems, the conventional thin film technology enables realisations of planar HTS devices with superior performances to match conventional state-of-the-art equivalents, with significantly reduced size and weight. Even with incomplete knowledge of physical mechanisms causing high temperature superconductivity, a plethora of HTS thin film devices and components for wireless communications systems have already been developed. For cellular mobile communications and space communications, which represent the largest future market for high temperature superconductors, a wide range of HTS circuits and components have been built. These include resonators, filters, mixers, miniature antennas and delay lines. While such circuits are mostly intended for feasibility studies, unambiguous demonstrations of their performance prove that they can be superior to versions made of normal conductors. For example, field trials of prototype consumer HTS filters used in

cellular mobile base-stations have been performed in rural areas with impressive results. The results include significantly reduced numbers of dropped calls, significant increase in the area of coverage, and significant increase in the number of satisfied customers using that communications service. Such convincing demonstrations of superconductor products have attracted wide publicity and keen interest among prospective customers in the commercial superconductor market of the future, resulting in about 500 HTS filters already installed in cellular base stations in USA.

Having introduced some of the significant potential benefits of high temperature superconductors, it should now be mentioned that the excellent progress achieved so far in the HTS field has not been easy. While intensive research and developmental efforts have managed to overcome various major obstacles that had prevented rapid technological progress in superconductive electronics, there are remaining barriers to overcome before the expected benefits of the technology can be acquired. Apart from difficult issues involving the costs and complexities of refrigeration of HTS components, packaging, integration of HTS systems with normal conducting systems, and the fabrication of HTS films, technological progress in the HTS field has been slowed by the incomplete knowledge and control of the behaviour of HTS films.

To implement high temperature superconductors effectively, circuit designers need to know the material parameters accurately as well as the characteristics of the material under practical conditions. To obtain accurate parameters and characteristics of HTS films, measurements need to be done as properties of HTS films are very sensitive to fabrication processes [1]. Fabrication processes require precise control of various process parameters to produce HTS films of good quality, such as the temperature, pressure, parameters related to the rate of growth of the film, and parameters related to the control of the stoichiometry. Even small changes in the fabrication process can influence the quality of the film significantly. The electrical characteristics of HTS films are also influenced by the thickness and the type of the supporting substrate, as well as the thickness of the film [2,3]. Furthermore, the

influence of imperfections in the microstructure of the superconductor material on the quality of the film are uncertain until measurements are done to assess it. Due to the above issues, the material parameters of HTS films can only be obtained accurately from measurements of specific films.

In the characterisation of HTS films for applications in wireless communications, the surface resistance is one of the most important parameters to be measured. There is particular interest in the surface resistance for the following three reasons. First, the accurate knowledge of R_s is essential in the design of high frequency superconducting circuits. Secondly, it is used to assess the usefulness of HTS films. Finally, knowledge of the behaviour of R_s in terms of its dependencies on temperature, frequency, and power can aid in the understanding of high temperature superconductivity which is not yet fully understood in terms of the physical mechanisms involved. A better understanding of high temperature superconductivity could ensure the optimisation of fabrication processes to improve the characteristics and quality of superconductors, or perhaps even to customise superconductors to achieve desired physical and electrical properties. Hence there are needs to measure the surface resistance of HTS films accurately.

The surface resistance of HTS films is calculated using the unloaded quality factor Q_0 of the microwave resonator structure used for the measurement. However, a standard procedure has not yet been developed to measure the unloaded quality factor of microwave resonators used for microwave characterisation of HTS films. A International Standards Committee, namely the “International Electrotechnical Commission (IEC) Technical Committee Tc(90) : Superconductivity” [4] has been established for two years with aims to propose a standard structure and measurement devices to be used for measurements of R_s . Reasons for the delay in the development of a standard may be understood in the following introductory background which describes various aspects of surface resistance measurements of HTS films.

1.1 MAJOR ISSUES IN MEASUREMENTS OF THE SURFACE RESISTANCE OF HTS THIN FILMS

All measurement systems used to measure the surface resistance R_s of HTS films feature a microwave resonator in which the superconductor sample is mounted, and which serves as a platform for measurements to be made. Measurements are then done to obtain the resonator's unloaded Quality factor which is used in the calculation of R_s via an equation which involves the geometrical constants of the resonator and material constants.

Uncertainty in the calculated value of R_s is primarily dependent on uncertainties in the measured unloaded Q_0 -factor. Therefore it is important to measure the unloaded Q_0 -factor accurately in order to achieve accurate values of surface resistance. The minimisation of errors in R_s also requires :

- 1) Accurate knowledge of material constants such as the dielectric loss tangent associated with dielectric losses in the resonator, as well as the surface resistance of normal conducting components in the resonator which account for normal conductor losses.
- 2) Accurate values of the *geometrical factors* of resonator components to be calculated from the knowledge of the resonator geometry and EM field distribution.

Measurements of dielectric loss tangents and of surface resistance of normal conductors also involve measurements of unloaded Q_0 -factors of microwave resonators. Hence their accurate measurement are difficult issues in themselves. As for the geometrical factors, they are not easy to obtain accurately for just any kind of a resonator structure (used for measurements of surface resistance of HTS films) as it requires the accurate determination of the EM fields in microwave resonator, which can be complicated even for structures with relatively simple geometry. In this thesis, accurate knowledge of the dielectric loss tangent, surface resistance of the normal

conducting parts, and the geometrical factors of the structure are assumed so that the focus of the work is on accurate measurements of the unloaded Q_0 -factor.

While there are various methods used to measure the unloaded Q_0 -factor of microwave resonators, there is no standard procedure. The reason for the lack of a standard procedure is due to the lack of detailed systematic studies of accuracy and reliability of the various existing procedures used, and is also due to a lack of a superior technique to determine the unloaded Q_0 -factor of transmission mode microwave resonators which take into account practical effects introduced by a real measurement system. Such practical effects include noise, coupling reactance, coupling loss, electrical delay due to transmission lines, impedance mismatch and crosstalk. Failure to account for the mentioned practical effects contributes toward the uncertainty in the unloaded Q_0 -factor obtained from characterisation of the resonator. Hence to measure the unloaded Q_0 -factor accurately, it is necessary to account for the practical effects listed above. Unfortunately, this is a very difficult issue particularly when the microwave resonator is confined within a cryogenic or vacuum environment where observations cannot be made at locations as required by idealised Q_0 -factor determination techniques. The inability to perform standard device calibration on a microwave resonator due to practical constraints is a main problem to be solved in accurate measurements of the Q_0 -factor of microwave resonators.

The lack of a standard Q_0 -factor procedure also implies the lack of a standard procedure to measure R_s . Without a standard R_s measurement procedure, it is difficult to compare results obtained from various measurement laboratories due to the uncertainty in measurement conditions and measurement processing methods used. The development of a standard procedure for the measurement of R_s of HTS films requires consideration of the structure to be used, the types of measurements to be made, and the techniques used to process those measurements to obtain the unloaded Q_0 -factor result needed to calculate R_s . The need for a standard technique has already been acknowledged, and steps to develop one is already in progress. A sub-committee, namely Tc-90 of the International Electrotechnical Commission (IEC) has been established for 2 years with aims to propose a standard structure to be used for R_s measurement. So far, a two-resonator system [4] has been proposed

which does not require knowledge of the loss tangent of the resonator that is used in calculations of R_s . However, the committee has not yet addressed procedures to accurately measure the unloaded Q_0 -factor of the resonator.

Resonant structures so far used in measurements of R_s of HTS films include the parallel plate resonator, confocal resonator, dielectric resonator, and transmission line resonators. Most of these structures have the potential for accurate measurements of R_s , but not all of them have the same capacity for convenience, reliability, and accuracy in practical situations. Best structures are ones for which analytical solutions for EM fields can be obtained. Also, resonators need to be robust, easy to maintain, and facilitate easy mounting of film samples. Because Hakki-Coleman dielectric resonator structures provide the above desirable qualities, they have become very popular for measurements of R_s of HTS films and make an excellent candidate for the standard device to be used for measurements of the surface resistance [5].

Techniques used to determine the unloaded Q_0 -factor of microwave resonators can be divided into time domain and frequency domain techniques and both involve measurements of one or more selected response types around the resonance. For time domain techniques, the unloaded Q_0 -factor is obtained by analysing the time-response of the resonator after it has been excited with a pulse of energy from a microwave source. For frequency domain techniques, the unloaded Q_0 -factor is found by processing one of various circuit parameters (impedance, VSWR, microwave power, or S-parameter response) measured around the resonance. Additionally, all Q_0 -factor techniques involve the determination of the loaded quality factor Q_L and the port coupling coefficient(s) which are used to calculate the unloaded Q_0 -factor.

As Q_0 -factor measurement techniques are developed from circuit models of resonator systems, the accuracy of any Q_0 -factor technique depends on its ability to account for practical effects which influence the behaviour of the real resonant system. The best technique available so far which takes practical effects into account is the Kajfez method [6,7] to be discussed in detail in Chapter 3.9. The Kajfez method is developed from a full systematic analysis of the losses in a dielectric resonator in the reflection mode and it takes advantage of the circular form of the S-

parameter locus observed at a input port of a microwave resonator around the resonance. However, the method is applicable only to resonators working in the reflection mode and there has been no method of similar quality developed for resonators working in the transmission mode. So far, there has especially been a need for accurate Q_0 -factor techniques for transmission mode resonators because measurements of R_s of HTS films and parameters of dielectric materials are typically performed in the transmission mode.

Reasons for the popularity of transmission mode resonators for measurements of R_s using dielectric resonators are various. A most obvious one is the relative ease in which the unloaded Q_0 -factor can be obtained from transmission measurements using existing transmission mode techniques such as the Three Frequency Method [8], and the Insertion Loss Method [9], even when measurements are done under conditions of very weak coupling.

A weak coupling condition can occur when coupling structures (such as coupling loops or probes) of dielectric resonators are placed outside the cavity to prevent disturbance of the nominal EM field distribution in the resonator. A disturbed field distribution is undesirable because Q_0 -factor measurements are based on a ideal field distribution. For weakly coupled resonators (but not so weak where transmission and reflection mode measurements cannot be made), observations of the S-parameter responses of microwave resonators around the resonance show that the reflection response (S_{11} or S_{22}) can be significantly influenced by noise while the transmission response (S_{21}) has a much higher signal to noise ratio. For such case described above, it is believed (in my opinion) that the loaded Q_L -factor of the resonator can be obtained more accurately from transmission mode measurements than from reflection mode measurements of a weakly coupled resonators where the signal-to-noise ratio is much higher in transmission mode measurements than in the reflection mode. For a case of weak coupling, the uncertainty in the unloaded Q_0 -factor (calculated from the loaded Q_L -factor and the port coupling coefficients) depends largely on the uncertainty in loaded Q_L -factor.

For dielectric resonator cavities fitted with coupling loops, there are cases where the reflection response is too weak and noisy to provide any reliable measurements of the Q_0 -factor for any position of the coupling structure outside the

cavity while the transmission response can still be measured reliably. Under such circumstances described, it is advantageous to use transmission mode measurements for characterisation of HTS films.

Also, for high power measurements of the surface resistance of HTS films where an amplifier is inserted between the measurement instrument and the resonator, measurements of the reflection response of the resonant system can be impeded by the amplifier. For such a case it is advantageous to use a transmission mode resonator because transmission measurements can still be performed. All of the issues discussed above contribute towards the popularity of transmission resonators for measurements of surface resistance of superconducting materials.

From the knowledge obtained from literature and discussions with scientists and engineers working in the HTS field, the author has identified a need for accurate measurements of the unloaded Q_0 -factor of transmission mode resonators via measurements of S-parameters when taking into consideration practical effects introduced by a real measurement system, such as noise, crosstalk, transmission line delay, coupling losses, coupling reactance, and impedance mismatch. Hence, the aim of this thesis was to develop an accurate transmission mode technique based on the above considerations and issues. The format of the thesis is as follows :

Chapter Two of this thesis is devoted to the phenomenon of superconductivity. The goals of this chapter are to provide a reader with specific knowledge of various aspects of superconductivity, namely material properties, overview of physics of superconductors, and basic applications of superconducting materials.

Chapter Three discusses experimental techniques used for measurements of surface resistance of HTS films. The chapter begins with a general description of basic measurement principles followed by definitions of the Quality factor; a general procedure to calculate the surface resistance of HTS films from a loss equation; relationships between the unloaded Q_0 -factor of an isolated resonator and the loaded Q_L -factor; and a review of microwave resonator structures used in measurements of R_s . Also included in the chapter is a review of Q_0 -factor measurement techniques, with comments on their advantages and deficiencies; and discussion on uncertainties in R_s calculations.

In Chapter Four, a new method for accurate measurements of the unloaded Q_0 -factor of transmission mode dielectric resonators developed in the course of this work is presented. The procedure is based on measurements of all three S-parameter modes (S_{21} , S_{11} and S_{22}) around the resonance and features a accurate curve fitting technique. The method takes into account important practical and parasitic effects introduced by the measurement environment which include noise, cross-talk, effects of connecting cables such as cable loss and delay; coupling losses, and coupling reactance.

Chapter Five presents assessments of the developed transmission mode unloaded Q_0 -factor determination technique using computer simulations. The assessment is based on studies of the accuracy in the unloaded Q_0 -factor obtained from the application of the technique to simulated data in the presence of practical effects such as electrical delay due to cables connected between the measurement device and the test resonator, coupling reactance, and coupling loss. The study proved that the developed technique can provide accurate Q_0 -factor results with less than 1 percent error.

In Chapter Six, measurements of the surface resistance of $\text{YBa}_2\text{Cu}_3\text{O}_7$ HTS thin films using Hakki Coleman sapphire resonators at 10 GHz and 25 GHz and the developed Transmission Mode Q_0 -Factor Technique are presented to verify the accuracy and usefulness of the technique.

The conclusions to the thesis are presented in Chapter Seven, which includes a discussion on the achievements made in the course of this thesis, future work to be done and a list of publications related to the work presented in this thesis.

BIBLIOGRAPHY OF CHAPTER 1

- [1] R. Humphreys, "Growth and processing of HTS thin films", NATO Advanced Study Institute Microwave Superconductivity, 1999.
- [2] J. Ceremuga, J. Krupka, R. Geyer, J. Modelski, "Influence of film thickness and air gaps on surface impedance measurements of high temperature superconductors using the dielectric resonator technique", *IEICE Trans. Electronics*, Vol. E78-C, No. 8, pp. 1106-1110, 1995.
- [3] P. Hartemann, "Effective and intrinsic surface impedances of high- T_c superconducting thin films", *IEEE Trans. Appl. Supercond.*, Vol. 2, No. 4, pp. 228-235, Dec 1992.
- [4] "Superconductivity: Measurement Method of Surface Resistance of Superconductors at Microwave Frequencies", International Electrotechnical Commission (IEC) Technical Committee Tc(90): Working Group 7.
- [5] J. Mazierska, "Dielectric resonators as a possible standard for characterisation of high temperature superconducting films for microwave applications", *Journal of Superconductivity*, Vol. 10, No. 2, pp. 73-85, 1997.
- [6] D. Kajfez, "Q Factor", *Vector Fields*, 1994.
- [7] D. Kajfez: "Linear fractional curve fitting for measurement of high Q factors", *IEEE Trans. Microwave Theory Tech.*, Vol. 42, No. 7, pp. 1149-1153, 1994.
- [8] D. Kajfez, P. Guillon, "Dielectric Resonators", *Vector Fields*, 1990.
- [9] D. Kajfez et al, "Uncertainty analysis of the transmission-type measurement of Q-factor", *IEEE Trans. Appl. Supercond.*, Vol. 47, No. 3, pp. 367-371, Mar 1999.

CHAPTER 2

REVIEW OF SUPERCONDUCTING MATERIALS, PHENOMENA OF SUPERCONDUCTIVITY AND APPLICATIONS OF SUPERCONDUCTING MATERIALS

From earliest observations of superconductors, superconductivity manifested itself in the remarkable disappearance of electrical resistance at reduced temperatures. Materials of such nature were accordingly named superconductors although the proper classification of superconductors involve a number of other exotic behaviours. The ability of a superconductor to carry current without resistance creates numerous possibilities for electronic applications. Electrical power passing through a resistance-free medium is not lost in the form of heat. It means that electrical devices and components made out of resistance-less conductors could be made very efficient, and high efficiency is very beneficial to the performance of electronic systems. Other properties of superconducting materials include zero dispersion and diamagnetism, which also provide vast possibilities for electronic applications. Hence much work is being done to develop superconducting materials of enhanced properties for commercial applications.

2.1 SUPERCONDUCTOR MATERIALS

Superconductor materials have been classified into two categories depending on their transition temperatures, namely the conventional low temperature superconductors (LTS) and the high temperature superconductors (HTS). While the physics of superconductors is discussed later in this chapter, it is useful to mention at this point that the underlying mechanisms responsible for superconductivity in the two classes of materials are not alike.

Conventional superconductors are found to exist in both organic and non-organic forms. Organic superconductors include fullerenes doped with alkali metals such as K_3C_{60} and Rb_3C_{60} , but so far they have no electronic applications. The non-organic group, which include a host of simple elements, alloys and polymers have potential for electronic applications. A list of conventional superconductor elements

and compounds, and their transition temperatures T_c are presented respectively in Table 2.1 and Table 2.2 [1]. The temperature of a superconductor needs to be below its transition temperature in order to exhibit superconducting phenomena, provided that other critical values, namely the operating frequency, current and magnetic field are not exceeded. Mercury, with a T_c of about 4.2K was the first superconductor discovered by Onnes in 1911 [1]. As far as it is known, the element tungsten has the lowest transition temperature with T_c of 0.012 K. A niobium compound (Nb_3Ge) discovered in 1973 has the highest T_c (about 22.3 K) of the conventional superconductors.

Table 2.1 Superconducting elements and their transition temperatures [1].

Element	T_c (K)	Element	T_c (K)
Al	1.196	Pa	1.4
Cd	0.56	Pb	7.19
Ga	1.091	Re	1.698
Hf	0.09	Ru	0.49
α -Hg	4.15	Sn	3.72
β -Hg	3.95	Ta	4.48
In	3.40	Tc	7.77
Ir	0.14	Th	1.368
α -La	4.9	V	5.30
β -La	6.06	W	0.012
Mo	0.92	Zn	0.875
Nb	9.26	Zr	0.65
Os	0.655		

Table 2.2 Conventional superconducting compounds and their transition temperatures [1].

Compound	T_c (K)
Nb_3Sn	18.05
Nb_3Ge	22.3
NbN	16
NbO	1.2
$BaPb_{0.75}Bi_{0.25}O_3$	11
UBe_{13}	0.75
$Pb_{0.7}Bi_{0.3}$	8.45
$(SN)_x$	0.26
$(BEDT)_2Cu(NCS)_2$	10

High temperature superconductors were discovered in 1986 when Bednorz and Mueller detected superconductivity in the cuprate La-Ba-Cu-O (with T_c up to 40K). Their discovery was unexpected because the transition temperature of La-Ba-Cu-O far exceeded those of superconductors known at that time [1,2]. While the physical nature of high temperature superconductivity is still not fully understood, a great deal is now known about the chemistry and physical characteristics of high temperature superconductors. All high temperature superconductors discovered so far are cuprates (copper oxide compounds) with structures based on perovskite cells.

Their transition temperatures are significantly higher than those of conventional superconductors. As they are ceramic materials, high T_c cuprates have hard and brittle textural characteristics. A range of high T_c cuprates are listed in Table 2.3 [3], which includes three most popular HTS materials for electronic applications, namely $\text{YBa}_2\text{Cu}_3\text{O}_7$ (YBCO, $T_c=93\text{K}$ for bulk material), $\text{Bi}_2(\text{Sr}_2\text{Ca})\text{Cu}_2\text{O}_8$ (BSCCO, $T_c=110\text{K}$), and $\text{Tl}_2\text{Ba}_2\text{Ca}_2\text{CuO}_3\text{O}_{10}$ (TBCCO, $T_c=125\text{K}$).

Table 2.3 HTS materials and their transition temperatures [3].

Class	HTS Compounds	T_c (K)	Notation
Cuprates	$(\text{La,Ba})_2\text{CuO}_{4-x}$	38	La-0201
	$(\text{La,Sr,Ca})_3\text{Cu}_2\text{O}_{6\pm x}$	60	La-0212
	$\text{YBa}_2\text{Cu}_3\text{O}_7$	92	Y-123
	$\text{YBa}_2\text{Cu}_4\text{O}_8$	80	Y-124
	$\text{Y}_2\text{Ba}_4\text{Cu}_7\text{O}_{15}$	40	Y-247
	$\text{Bi}_2\text{Sr}_2\text{CaCu}_2\text{O}_8$	90	Bi-2212
	$\text{Bi}_2\text{Sr}_2\text{Ca}_2\text{Cu}_3\text{O}_{10}$	110	Bi-2223
	$\text{CuBa}_2\text{CaCu}_3\text{O}_8$	125	Cu-1234
	$\text{CuBa}_2\text{Ca}_3\text{Cu}_4\text{O}_{10}$	120	Cu-1223
	$(\text{Sr,Ca})_4\text{Cu}_3\text{O}_8$	90	0223
	$(\text{Sr,Ca})_5\text{Cu}_4\text{O}_{10}$	80	0234
	$\text{Tl}_2\text{Ba}_2\text{CaCu}_2\text{O}_8$	110	Tl-2212
	$\text{Tl}_2\text{Ba}_2\text{Ca}_3\text{Cu}_4\text{O}_{12}$	121	Tl-2234
	$\text{TlBa}_2\text{CaCu}_2\text{O}_7$	100	Tl-1212
	$\text{TlBa}_2\text{Ca}_2\text{Cu}_3\text{O}_9$	123	Tl-1223
	$\text{TlBa}_2\text{Ca}_3\text{Cu}_4\text{O}_{11}$	122	Tl-1234
	$\text{TlBa}_2\text{Ca}_2\text{Cu}_3\text{O}_{10}$	127	Tl-1223
	$\text{Tl}_2\text{Ba}_2\text{CuO}_6$	95	Tl-221
	$\text{Tl}_2\text{Ba}_2\text{Ca}_3\text{Cu}_4\text{O}_{12}$	112	Tl-2234
	$\text{Hg Ba}_2\text{Ca}_2\text{Cu}_3\text{O}_8$	134	Hg-1223

	Hg Ba ₂ Ca ₂ Cu ₃ O ₈	164(under pressure)	Hg-1223
	Hg Ba ₂ Cu ₃ O _{4+x}	95	Hg-1201
	Hg Ba ₂ Ca ₂ Cu ₂ O _{6+x}	125	Hg-125
	Hg Ba ₂ Ca ₃ Cu ₄ O ₁₀	130	Hg-1234
	Pb ₂ YSr ₂ Cu ₃ O ₈	70	Pb-2123
	(Pb,Cu)(Sr,La) ₂ CuO ₅	53	PbCu-1212
	PbBaSrYCu ₃ O ₈	50	Pb-2212

Structurally, a high T_c cuprate is typically made up of a layered arrangement of Cu-O planes with oxygen layers or rare earth layers in between as illustrated for the YBCO compound in Fig. 2.1 [1,4]. The CuO planes (a-b plane) are considered to be the active superconducting layers while the other layers serve to chemically stabilize the structure and to dope the CuO planes. Since conduction is generally along the a-b plane, HTS cuprates are grown with the c-axis perpendicular to the substrate layer. Material properties of high T_c cuprates depend strongly on the stoichiometry so that a high T_c material is achieved only for particular levels of doping. Depending on the doping, a material can be either metallic, insulating, superconducting, antiferromagnetic or a spin glass [5,6].

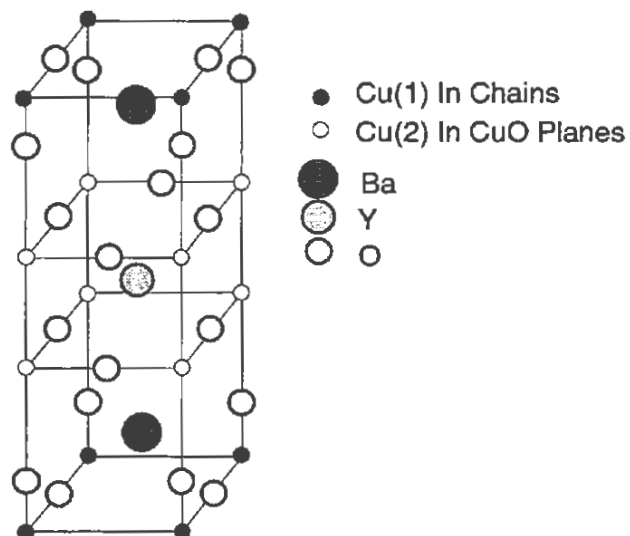


Figure 2.1 YBCO structure [1,4].

2.2 PHYSICAL PHENOMENA ASSOCIATED WITH SUPERCONDUCTIVITY AND MATERIAL PARAMETERS OF SUPERCONDUCTORS

Superconducting materials have three fundamental phenomena associated with them, which include the vanishing resistance phenomenon, diamagnetic behaviour, and zero dispersion property. In this section, aspects of these phenomena are discussed.

2.2.1 VANISHING RESISTANCE

According to the classical theory of superconductivity, the DC resistivity of a superconductor is zero at temperatures below its transition temperature T_c . That is, when a constant, time-independent EM field is applied to a superconducting material at a temperature below the transition temperature, it will exhibit no resistance to current flow and no power will be dissipated in the material. While absolute zero temperature has never been achieved, the DC resistivity of a superconductor has been measured (by measuring over a long period of time the magnetic field associated with a induced current that flowed around a superconducting coil after the source had been removed) with the most sensitive equipment to be less than 10^{-27} Ω -cm for temperatures well below the transition temperature. Such a value is considered insignificant and it strongly supports the theoretical predictions of a zero DC resistance [1].

The DC resistivity of a superconductor has a temperature dependence as shown in Fig 2.2. At temperatures above the transition temperature, the material is in the normal state and therefore exhibits its normal resistivity. As the temperature is reduced gradually, the resistance also decreases gradually with the temperature until T_c is reached, where the resistance drops abruptly to zero.

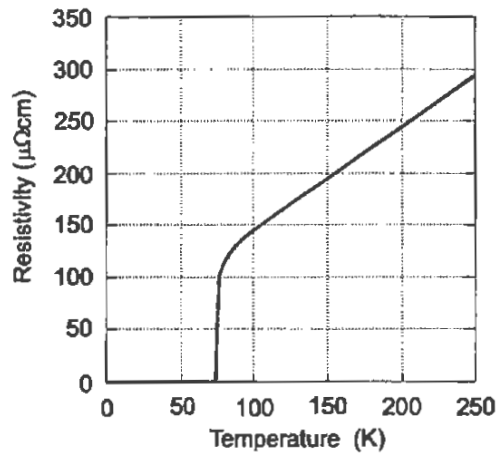


Figure 2.2 Typical temperature dependence of DC resistivity in a superconductor [7].

In the presence of a time varying field, the resistance of a superconductor is non-zero, although the magnitude of its resistance is much lower than in best conventional conductors over a wide range of frequencies. In the microwave frequency range, where some of the most promising applications for superconductors exist, the typical resistance of a superconductor is lower than in the best normal conductors by a few orders of magnitude.

2.2.2 THE MEISSNER EFFECT

The Meissner effect (discovered in 1933 by Meissner and Ochsenfeld) describes the diamagnetic behaviour of superconducting materials and expulsion of magnetic fields [1]. When a constant, time-independent magnetic field is applied to a superconducting material, it causes induced currents to be set up in the surface region of a superconductor. These currents flow in rings and are referred to as screening currents to distinguish them from transport currents. The applied magnetic field is opposed by the magnetic fields associated with the screening currents, which results in the diamagnetic behaviour of superconductors known as the Meissner as illustrated in Fig. 2.3.

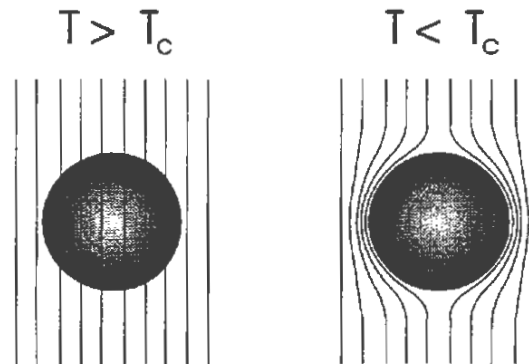


Figure 2.3 The Meissner effect. Magnetic fields penetrate into the superconductor when it is in the normal state, but the field is repelled when the material is in the superconducting state [1].

The magnetic fields are not completely screened out from the superconductor, and they actually penetrate a small distance into the material. The penetration distance is very small because the strength of the field decays exponentially with distance from the surface. The depth at which the field falls to $1/e$ of the field at the surface is called the London penetration depth, or simply the penetration depth [1,2,8]. In relation to the distribution of currents in the material, transport currents flowing in superconducting material are confined mostly to the region bounded by the surface of the superconductor down to the penetration depth. In this respect, the penetration depth is comparable to the skin depth (due to the skin effect) of normal metals, except that the penetration depth has no frequency dependence, but has a temperature dependence.

2.2.3 ZERO DISPERSION IN SUPERCONDUCTOR MATERIALS

Superconductors have a zero dispersion property [9]. It means that frequency components in a composite signal can travel through superconducting materials at the same velocity. For practical purposes, dispersion-free conductors would be very beneficial to pulse type electronic applications, namely digital and analog signal processing. The benefits of dispersion-free media can be understood by considering a square pulse that travels through a transmission line. If the line is dispersive, the

result is a distortion of the pulse in the time domain due to the frequency dependence of the phase velocity of frequency components in the signal [10]. The effect of dispersion is recognised by a rounding of the edges of the pulse as illustrated in Fig. 2.4 [11]. Such distortion is undesirable in signal processing applications where detection of the pulse edges are important. At high clock speeds where pulses are very narrow and closely spaced in time, the effects of dispersion become a limiting factor in the speed of pulse applications [12]. If the transmission line is a non-dispersive one, then the shape of the pulse is preserved (Fig. 2.4). While practical superconducting transmission lines exhibit some dispersion due to the influence of the supporting structures such as dielectric substrates, the level of dispersion is considered to be negligible for the current frequency ranges of interest for electronic applications, such as below 150 GHz [1].

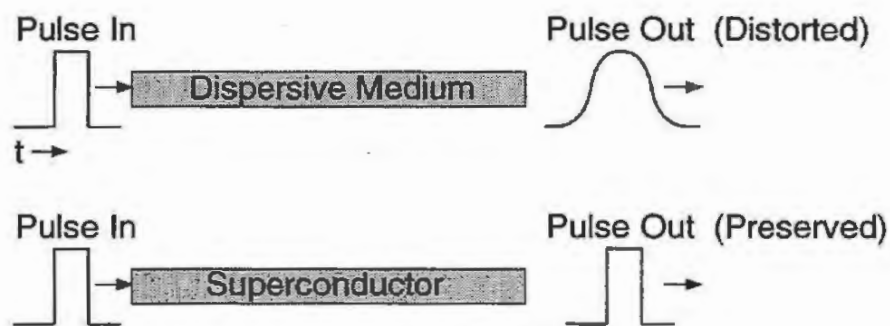


Figure 2.4 The effect of a dispersive medium and a non-dispersive medium on a square pulse passing through [11].

2.3 RELATIONSHIP BETWEEN TRANSITION TEMPERATURE, CRITICAL FIELD, CRITICAL CURRENT AND CRITICAL FREQUENCY

In order to exhibit superconducting phenomena, a superconductor must operate below threshold values of temperature, applied magnetic field, current, and frequency, which are known respectively as the transition (critical) temperature T_c , critical field H_c , critical current J_c and critical frequency.

The critical frequency of a superconductor is in the order of 100 GHz for low temperature superconductors [8], which is in the optical range. At these frequencies, the photons of electromagnetic waves excite superconducting electrons with enough energy to drive them to the normal state. But as electronic applications for superconductor materials are mainly aimed for frequencies well below 100 GHz, the critical frequency is not so important. The interdependence of T_c , H_c and J_c is illustrated in the phase diagram (Fig. 2.5) which shows the transitional boundary between the superconducting phase and the normal phase of a superconductor.

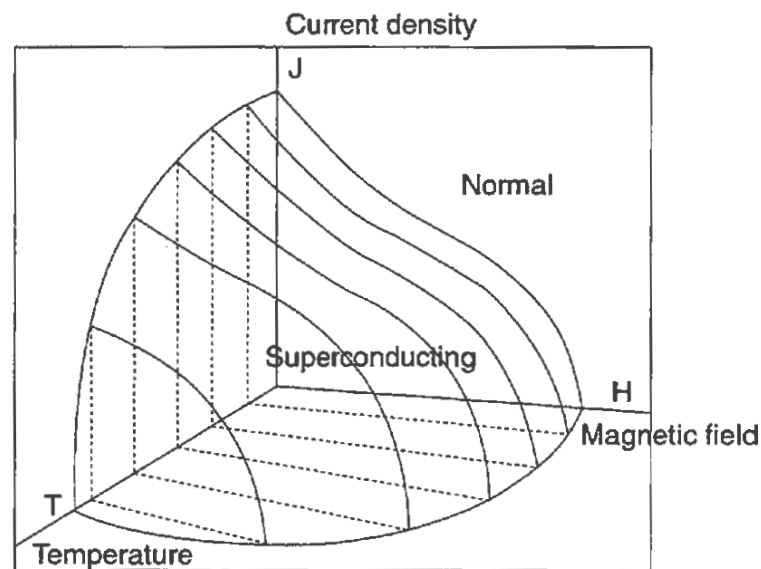


Figure 2.5 Superconductor phase diagram [13].

The transition temperature (also referred to as the critical temperature) is the highest temperature at which a material can exist in the superconducting state. For practical applications of superconductivity, it is desirable to operate at the highest possible temperature to minimise the overheads of cryogenic refrigeration, and also to minimise the stresses on device components during temperature cycling. Superconductors with transition temperatures as high as 162 K have been found [14], and materials with even higher transition temperatures are still being sought. Fig. 2.6 illustrates the evolution of transition temperatures since the discovery of superconductivity.

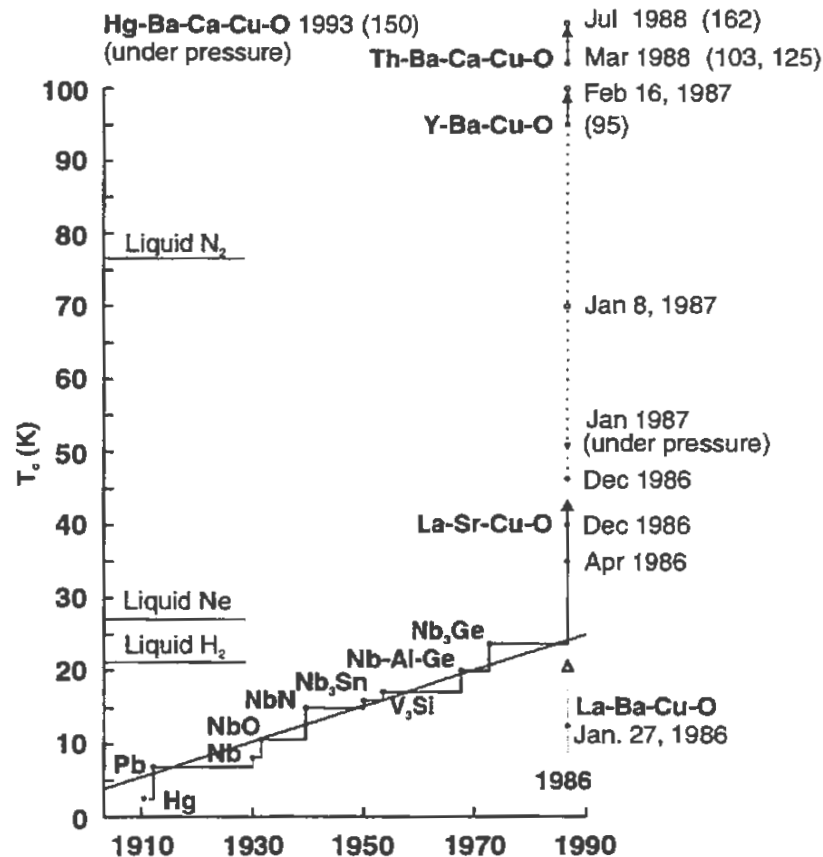


Figure 2.6 Evolution of transition temperature T_c since the discovery of superconductivity [15].

The critical field for a superconductor is defined as the highest value of external magnetic field strength applied to a superconductor without causing superconductivity to be destroyed, although there is a variation to the definition of the critical field for a Type II superconductor [1]. In general, the critical field of a superconductor has a value of zero at T_c and reaches a maximum value at absolute zero temperature [1]. The temperature dependence of the critical field follows one of two general types of characteristics which depends on the type of superconductor being considered. There are three types of superconductors. Type I include superconductors with penetration depth λ less than the coherence length ξ_0 which characterises the spatial correlation between pairs of superconducting electrons [1]. Type I superconductors have a single critical field at any fixed temperature and their critical fields are not very high, ranging from 100 to 1000 Gauss (1 Gauss = 10^{-4}

Tesla) [1]. All superconducting metals except Nb are type I superconductors [1]. The critical field for a type I superconductor has the a temperature dependence shown in Fig. 2.7.

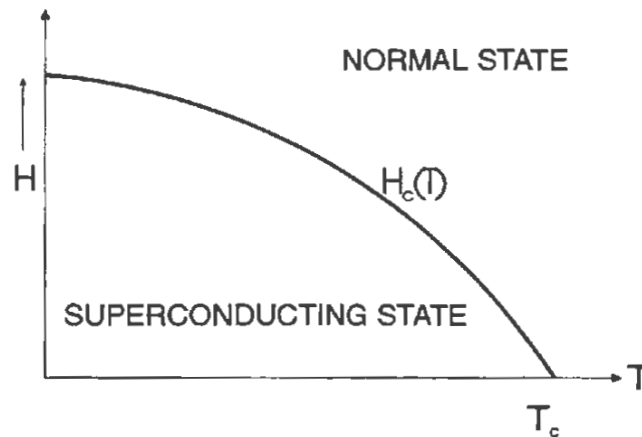


Figure 2.7 Critical field versus temperature for Type I superconductors [1].

Type II superconductors have coherence lengths greater than the penetration depth and are peculiar in the way of having two values of critical magnetic field - a lower and a upper one, H_{c1} and H_{c2} . For external fields below H_{c1} , the superconductor is in a superconducting state with a minor concentration of normal charge carriers. When the field exceeds H_{c1} , the superconductor transforms into a intermediate phase which is a mixture between the superconducting and normal phase. In this 'mixed-state', a remarkable condition exists where the transport currents can still flow through the material without resistance even though significant portions of the superconductor material are in the normal state [8]. Superconductivity is destroyed only when the external field exceeds the upper critical field H_{c2} . The critical fields in Type II superconductors depends on the temperature as shown in the phase diagram of Fig. 2.8.

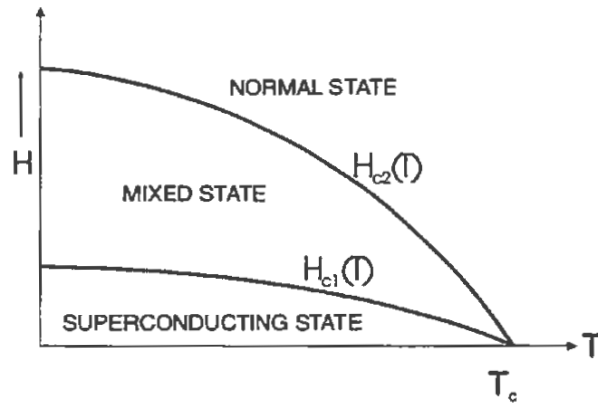


Figure 2.8 Critical fields versus temperature for Type II superconductor [8].

The upper critical field H_{c2} of Type II superconductors are typically much higher than critical fields of type I superconductors. For example, upper critical fields of Type II materials can be higher than 10 Tesla [16] while Type I materials are below about 0.2 Tesla [1]. Hence type II superconductors have been used to create very strong magnetic fields with applications in strong magnets, and particle accelerators. The current carrying capacity of Type II superconductors is sensitive to impurities. It is known that point-like impurities can cause Type II superconductors to have a zero critical current [1]. As the critical current is defined as the maximum amount of electrical current that a superconductor can carry through a given area without causing superconductivity to be destroyed, it means that impurities can cause type II superconductors to have no current carrying ability. However, if large inhomogeneities are introduced into the sample (eg. by plastic deformation), a Type III [1] superconductor can be formed, which can exhibit large critical currents. In case of confusion, the critical current is also known as the critical current *density*, which is a more appropriate label for the definition of critical current.

2.4 CONCEPT OF RESISTANCE AND SURFACE IMPEDANCE IN METALS AND SUPERCONDUCTORS

As this thesis is dedicated to measurements of surface resistance of superconductor films, the definitions of resistance and phenomena related to the

behaviour of charge carriers in conventional and superconducting materials need to be discussed. In general, electrical resistance in any material means resistance to the flow of charge carriers due to the scattering of free conduction electrons caused by any of three possible mechanisms; crystal lattice vibrations (phonons), defects in the crystal lattice, and impurities in the crystal lattice. As electrons are scattered, the kinetic energy is converted to thermal energy which is dissipated in the form of heat. Thus, resistance is a source of power loss. While the meaning of resistance is fundamental, there exist variations in the meaning due to certain transport phenomena which occur in conventional conductors and superconductors. First, consider the simple case of a constant DC potential applied across the two ends of a normal metal wire as in Fig. 2.9.

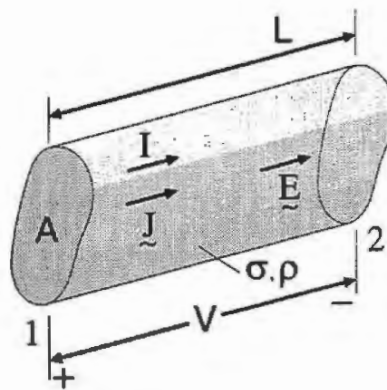


Figure 2.9 Normal wire conductor of length L , cross-sectional area A , with a voltage V applied across its terminals. The wire has a conductivity σ .

The electric potential causes free electrons to flow through the wire in the direction of the developed electric field \mathbf{E} . The scattering of the electrons caused by electron-lattice interactions provides resistance to the flow of electrons. Applying Ohm's Law to the wire, the relationship between the voltage V across its terminals and the current I flowing through it is simply :

$$V = IR \quad (2.1)$$

where R is the resistance of the wire. In terms of the geometry of the wire and its material parameters, the specific DC resistance of the wire of length L and cross sectional area A is given by [10]:

$$R_{DC} = \frac{\rho L}{A} \quad (2.2)$$

where

ρ is the resistivity ($=1/\sigma$) with typical units of ohm-cm (ohm-unit length), and the conductivity σ of the metal is a constant of proportionality that relates the current density to the electric field acting on the electrons as shown in the following physical relationship [2,17,18]:

$$\mathbf{J} = \left(\frac{Nq_e^2 \tau}{m_e} \right) \mathbf{E} = \sigma \mathbf{E} \quad (2.3)$$

where \mathbf{J} is the current density, and the term in brackets is an expression for the conductivity where N is the number of electrons per unit volume, q_e is the charge of an electron, τ is the mean time between scattering of an electron, and m_e is the electron mass.

At frequencies well below RF down to DC, electrical currents flow through the entire cross section of a conductor. At sufficiently high frequency, there is a significant difference in the manner in which the current flows. For high frequencies, such as in the microwave range, the *skin effect* phenomenon occurs where the currents flow near the surface region of the conductor only. The depth of penetration of the current and of the EM field is expressed by the skin depth δ which depends on properties of the material and frequency [10,19]:

$$\delta = \sqrt{\frac{1}{\pi f \sigma \mu}} \quad (2.4)$$

where f is the frequency, and the constants σ and μ are the conductivity and magnetic permeability of the material respectively. The skin depth decreases with frequency, and reduced skin depths at high frequencies mean that there is less cross-sectional area for current flow, which leads to increased resistance to current flow. The resistance seen by

the surface current is called the *surface resistance* to distinguish it from the conventional resistance at frequencies well below RF. It is the surface resistance which is used to characterise the conductor losses at high frequencies.

Similar to the skin effect for normal metals at high frequencies, the electrical current flowing through a *superconducting* material is also confined to the surface regions. Here, the resistance to the flow of these surface currents is also known as the surface resistance, which for any material may be defined as the ratio of the Joule losses and the square of the surface magnetic field [1]. A superconductor at a non-zero frequency has Joule losses, and therefore it has a finite surface resistance which depends on both the temperature and the frequency, and has the following BCS form for temperatures less than half the critical temperature [1]:

$$R_s(T, \omega) = \frac{A\omega^2}{T} e^{-\Delta/k_B T} \quad (2.5)$$

where Δ is the energy gap of the superconductor, and A is a constant that depends on the penetration depth. By comparison, the equation of the surface resistance of a normal metal is given by [1]:

$$R_s = \left(\frac{\mu\omega}{2\sigma} \right)^{1/2} \quad (2.6)$$

where σ is the electrical conductivity, and μ is the magnetic permeability of the conductor. From the above equations (2.5) and (2.6), it can be seen that the surface resistance of a normal metal increases with square root of the frequency while the surface resistance of a superconductor increases with the square of the frequency. Even though the surface resistance of the superconductor has a much greater rate of change with frequency than in the normal metal, the surface resistance of a superconducting material is smaller than of normal conductors for frequencies up to 200 GHz [20]. For example, the surface resistance of the high temperature superconductor $YBa_2Cu_3O_{7-x}$ in thin film form can be a few orders of magnitude smaller than that of copper in the frequency range from 800 to 900 MHz around the cellular band for mobile

communications. In the example shown in Fig. 2.10, the surface resistance of copper at 890 MHz has a typical value of 4.5 mΩ, while the surface resistance for thin film YBa₂Cu₃O_{7-x} high temperature superconductor is about three orders of magnitude smaller.

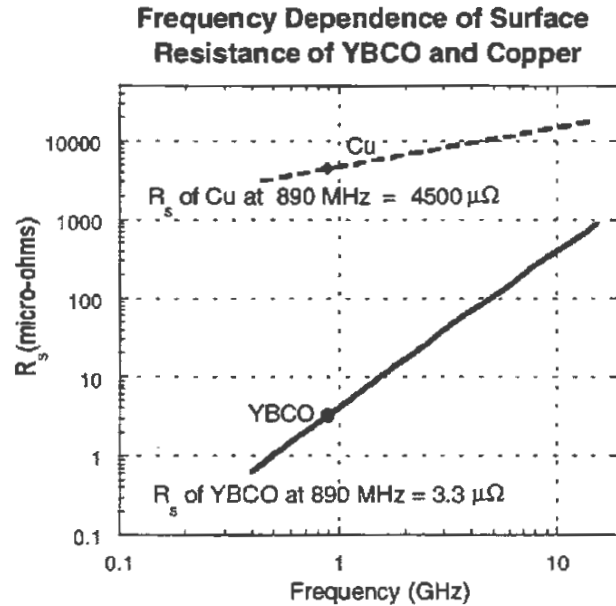


Figure 2.10 Frequency dependence of surface resistance of copper and YBa₂Cu₃O_{7-x} (YBCO) thin film superconductor around the 800-900 MHz cellular band at 77K.

The surface resistance R_s of conductors and superconductors is also defined as the real part of the surface impedance Z_s of the superconductor; and the surface impedance is defined as the ratio of the tangential components of electric field to the magnetic field at the surface of the conductor [10,17,19]. The surface impedance can also be expressed as the square root of the ratio of the complex permeability to the complex permittivity of the medium given by :

$$Z_s = \frac{E_t}{H_t} \Big|_{\text{at the surface}} = R_s + jX_s = \sqrt{\frac{\mu}{\epsilon' - j\frac{\sigma}{\omega}}} = \sqrt{\frac{j\omega\mu}{\sigma}} \quad (2.7)$$

The real part of the surface impedance, the *surface resistance* R_s is related to microwave power loss in the superconductor. The imaginary part of the surface impedance is the surface reactance X_s , which describes the stored magnetic energy [21,22].

For conductors, the conductivity σ is a real quantity while it is complex for superconductors, namely [2,17]:

$$\sigma = \sigma_1 - j\sigma_2 \quad (2.8)$$

or sometimes (depending on the convention used) as [23]:

$$\sigma = \sigma_1 + j\sigma_2 \quad (2.9)$$

where σ_1 and σ_2 are the conductivities relating to the normal (in context of the Two Fluid model) and the supercurrent respectively. The real part of the complex conductivity σ_1 is directly related to the skin depth δ of the superconductor in the normal state; and the imaginary part σ_2 is directly related to the magnetic penetration depth λ , namely [17, 23]:

$$\delta = \sqrt{\frac{2}{\omega\mu\sigma_1}} \quad (2.10)$$

$$\lambda = \sqrt{\frac{1}{\omega\mu\sigma_2}} \quad (2.11)$$

2.5 PROGRESS IN THE UNDERSTANDING OF SUPERCONDUCTIVITY

While the exotic phenomena observed in superconducting materials (which include the ‘disappearance’ of electrical resistance and repulsion of magnetic fields) were once considered mere novelties, attempts to understand superconductivity provided a challenge which kept scientists puzzled for almost half a decade. It was only on the 46th anniversary of the discovery of superconductivity when Bardeen, Cooper, and Schrieffer formulated the microscopic theory of superconductivity to provide a complete picture for the underlying causes of superconductivity in superconductors discovered at that time. The formulation of the theory was a

remarkable achievement as it was conceived from natural intuition and high level of understanding in various areas of science including quantum mechanics, thermodynamics and electromagnetism.

Unfortunately, the classical theory of superconductivity which works so well to explain the nature of conventional low temperature superconductors does not apply well to the high temperature materials. Even now, fourteen years after the HTS discovery, there is no unified theory to explain the nature of high temperature superconductivity (due to much higher complexity of HTS materials). However, extensions of the knowledge of conventional superconductivity may lead to the understanding of high temperature superconductivity. In the section to follow, the theories developed for conventional superconductivity are reviewed.

2.5.1 LONDON THEORY OF ELECTRODYNAMICS IN CONVENTIONAL SUPERCONDUCTORS

Well before the development of the Bardeen-Cooper-Schrieffer theory of superconductivity [1], various theories were proposed to describe and predict electromagnetic and thermal properties of conventional superconductors. These theories were not developed from the fundamental properties of the superconductor, but from existing theories of electromagnetism and are therefore known as phenomenological theories. Such theories include the London Equations (1935) and the Ginzburg-Landau theory (1950) [1,2,8]. The electrodynamics of conventional superconductors in weak fields are described by the famous London Equations [8]:

$$\begin{aligned}\frac{\partial \mathbf{J}_s}{\partial t} &= \frac{\mathbf{E}}{\mu_0 \lambda^2} \\ \text{curl } \mathbf{J}_s &= -\frac{1}{\mu_0 \lambda^2} \mathbf{B}\end{aligned}\tag{2.12}$$

where \mathbf{E} and \mathbf{B} are the electric field intensity and magnetic flux density respectively inside the material, \mathbf{J}_s is the superconducting current density, and the penetration depth λ is given by [8]:

$$\lambda = \sqrt{\frac{m_s}{\mu_0 n_s e^2}} \quad (2.13)$$

where m_s and n_s is the superconducting electron mass and volume density, and e is the electron charge [8]. The first London equation describes the resistanceless property of a superconductor where an applied electric field produces a continuously increasing current. The second London equation describes the Meissner effect and can be used to derive an equation to determine the magnetic field inside a superconducting body subjected to an applied field [8]. When a uniform magnetic field is applied in a direction parallel to a slab of superconductor material, the flux density B can be obtained as a function of distance x into the material, of the following form :

$$B(x) = B_a \exp\left(\frac{-x}{\lambda}\right) \quad (2.14)$$

where B_a is the value of magnetic flux density at the surface of the superconductor, and the constant $\alpha = m/\mu_0 n_s e^2$. The flux density B decays exponentially with distance into the superconductor as illustrated in Fig. 2.11. The exponential rate of decay of the flux density also means that the magnetic fields do not penetrate very far into the surface of a superconductor. The depth at which the field decays to $1/e$ of the value at the surface is the penetration depth λ .

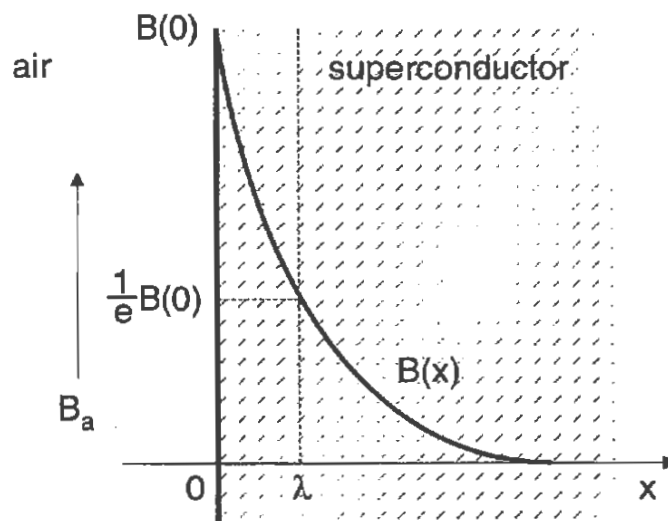


Figure 2.11 Penetration of magnetic field in a superconducting sample [8].

2.5.2 GINZBURG-LANDAU THEORY

The behaviour of superconductors in the presence of strong external magnetic fields is well described by the Ginzburg-Landau theory (1950) developed 15 years after the London theory. Unlike the London Theory that is based on classical electromagnetism, the Ginzburg-Landau theory involves quantum mechanics and non-trivial mathematical equations. The theory states that the behaviour of superconducting electrons may be described by an effective wave function Ψ , which is significant in that $|\Psi|^2$ is the density of superconducting electrons. The two famous equations developed from the theory are given as [1]:

$$\left\{ \frac{1}{4m} [\nabla - 2ie\mathbf{A}]^2 - \beta^{-1} \left[\frac{T_c - T}{T_c} - \frac{1}{n} |\Psi|^2 \right] \right\} \Psi = 0 \quad (2.15)$$

$$\mathbf{J} = \frac{-ie}{2m} [\Psi^* \nabla \Psi - \Psi \nabla \Psi^*] - \frac{2e}{m} \mathbf{A} |\Psi|^2 \quad (2.16)$$

where \mathbf{A} is the magnetic vector potential, \mathbf{J} is supercurrent density; e and m are the charge and mass of a superconducting electron; and $\beta = [7\zeta(3)/6(\pi T_c)^2] E_F$, where E_F is the Fermi energy. The Fermi energy/level is defined as the highest energy level occupied by electrons in a metal at absolute zero temperature.

The Ginzburg-Landau theory is valid for temperatures close to the transition temperature and can be used to study the behaviour of superconductors in strong magnetic fields where the London theory cannot be used. This theory can also be applied to predict magnitudes of critical fields in very thin or very thick films.

2.5.3 TWO FLUID MODEL

This phenomenological theory describes AC resistivity and thermal behaviour of superconductors based on thermodynamic concepts. The theory is based on the concept of two fluids that co-exist in superconducting material, namely a fluid of

normal electrons and a fluid of superconducting electrons. To describe the macroscopic behaviour of electrons in conventional superconductors below the transition temperature, the Two Fluid model suggests that the current in a superconductor is carried by super-electrons and normal electrons. The superconductor electrons flow through the superconductor without any resistance while the normal electrons encounter resistance due to collisions with other electrons or interactions with the crystal lattice. For the special case of a constant DC current flowing in a superconductor in the absence of external fields only, the current is carried entirely by the super-electrons which flow through the superconductor without any resistance (no scattering or collisions with other electrons). This can also be understood by considering that if a DC current is to remain constant then there must be no electric field in the superconductor, otherwise the super-electrons in a zero resistance medium would be accelerated by the field and the current would continue to increase. The absence of an electric field also means that no normal electrons can flow.

Under AC conditions, the density of super-electrons in a superconductor depends on the temperature. At absolute zero temperature, all conduction electrons behave as super-electrons [1,8] except at frequencies close to the critical frequency [8]. When the temperature is raised slightly above 0 K, a small portion of super-electrons become normal electrons due to thermal excitations which overcome the forces of attraction between pairs of super-electrons. As the temperature is raised further, more normal electrons are formed until the transition temperature is reached, when all of the electrons are in the normal state.

An equivalent circuit model for the Two Fluid model consists of two conductor in parallel; one being a normal conductor with finite resistance and inductance, and the other is a perfect conductor with zero resistance but has a inductance as shown in Fig. 2.12. For the DC case, the system is short circuited by the perfect conductor. If a battery was to be connected across the two terminals of the circuit, then the current is limited only by the internal resistance of the battery. For the AC case, the inertia of electrons causes lag between the motion of the electron and the applied field so that the superconductor has an associated inductance L_s .

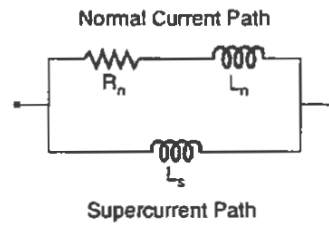


Figure 2.12 Equivalent circuit for a superconductor modelled on the Two Fluid model [9].

The Two Fluid model allows expressions for the intrinsic properties of classical superconductors to be determined. The parameters of importance include the current density, complex conductivity and the surface impedance. The total current density due to the two fluids is given as [17]:

$$\mathbf{J} = \mathbf{J}_n + \mathbf{J}_s = (\sigma_1 - j\sigma_2)\mathbf{E} \quad (2.17)$$

where σ_1 and σ_2 are the real and imaginary parts of the complex conductivity respectively, given by :

$$\sigma_1 = \frac{n_n e^2 \tau}{m(1 + \omega^2 \tau^2)} \quad \text{and} \quad \sigma_2 = \frac{n_s e^2}{m\omega} + \frac{n_n e^2 (\omega \tau)^2}{m\omega(1 + \omega^2 \tau^2)} \quad (2.18)$$

where e is a fundamental unit of charge; n_n and n_s are the densities of normal electrons and superconducting electrons respectively; m is the mass of an electron; ω is the radian frequency, and τ is the momentum relaxation time. From (2.18), it can be seen that the real part σ_1 of the complex conductivity involves only the normal fluid, while the imaginary part involves both (normal electrons and superconducting) fluids. The complex conductivity can be represented by the equivalent circuit of Fig. 2.13.

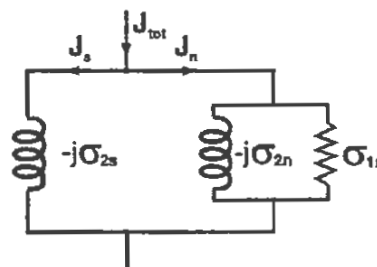


Figure 2.13 Equivalent circuit for the admittance of a unit cube of superconductor in the Two Fluid model [17].

2.5.4 BCS THEORY OF SUPERCONDUCTIVITY

The Bardeen, Cooper, and Schrieffer (BCS) microscopic theory of superconductivity was formulated in 1957 by John Bardeen, Leon Cooper and Robert Schrieffer. For their major achievement in the development of a theory to explain the physical mechanisms to cause superconductivity in conventional superconductors, Bardeen, Cooper, and Schrieffer were awarded the 1972 Nobel Prize in Physics. The BCS theory states that while interactions between electrons with themselves and with the crystal lattice are the cause of electrical resistance in materials, a special condition can exist at sufficiently low temperatures where interactions between the electrons and the crystal lattice form a mechanism to cause the phenomenon of superconductivity. The mechanism involved is generalised to the concept of electron-phonon interactions where a electron in a superconductor material radiates a energy packet (a Phonon) to the crystal lattice, which is then re-radiated and absorbed by a second electron [1]. This exchange of energy between electrons in pairs (called Cooper Pairs) provide the basic mechanism for superconductivity. In the superconducting state, a correlation exists between electrons in pairs, and this is collectively known as a macroscopic coherent quantum state. Such a state provides the means for electrons to flow through a superconducting material with little or no resistance.

2.5.5 PROGRESS IN THE UNDERSTANDING OF HIGH TEMPERATURE SUPERCONDUCTIVITY

While the nature of conventional superconductivity is clearly explained using the existing theories of superconductivity, the underlying mechanisms causing high temperature superconductivity are not yet understood. The classical phenomenological theories, namely the London Equations, Two Fluid model and Ginzburg-Landau theory have been used with some success to predict the behaviour of high temperature superconductors such as the temperature dependence of the surface resistance of the superconductor for certain temperature ranges. However it is clear that the behavioural trends of high temperature superconductors cannot be fully predicted by these existing

phenomenological theories and models which apply so well to the low temperature superconductors. There is a general consensus that most of the building blocks needed to understand high temperature superconductivity are available. There is also a consensus that proper modifications to the BCS theory and incorporation of extra factors may lead to a complete explanation for high temperature superconductivity.

Difficulty in the study of the intrinsic behaviours of high temperature superconductors is compounded by imperfections in the microstructure of HTS materials. However, there are well established differences between the properties of conventional low temperature superconductors and high temperature superconductors. The transition temperatures of HTS are much higher than that of any known conventional superconductor. The supercurrent in some high temperature superconductors is considered to be carried by pairs of holes as compared to pairs of electrons in conventional superconductivity [1], although the process of the pairing of the holes (or electrons) in high temperature superconductors are not fully understood. The coherence lengths (the pairing distance for superconducting electron pairs) are much shorter, in the order of 20\AA [1,8] in high temperature materials, as compared to 10000\AA in LTS types [1,8]. The coherence length determines the design of devices based on the tunnelling property of superconductors especially Josephson junctions, as the junction width needs to be in the order of the coherence length to form a working junction. Hence, HTS Josephson junction devices need to have much more narrow gap widths than LTS Josephson junction devices.

2.6 APPLICATIONS OF SUPERCONDUCTING MATERIALS

When ideas to apply the properties of superconductivity were first conceived, they were followed by many enthusiastic predictions about the major impact of superconductors on electronics. Intensive efforts and major funding were used to develop the new technology. However, progress in the application of the properties of superconductors was not easy due to the lack of control of their properties, lack of techniques to produce materials of desired qualities needed for the design of superconducting products, due to the physical limitations of superconducting

materials for intended applications, as well as due to the high cost of refrigeration systems.

Due to the low transition temperatures of LTS and consequently the large overheads associated with refrigeration requirements, nearly all applications proposed for LTS were considered to be economically infeasible. The need for liquid helium (4.2 K) to refrigerate LTS systems presented an enormous economical barrier except for a few applications like superconducting magnets for medical magnetic resonance imaging (MRI). It was eventually realised that most LTS applications would remain infeasible unless materials with much higher operating temperatures could be found. Operation at sufficiently high temperatures enables reductions in the cost of refrigeration to bring the commercial possibilities into the feasible range. However for more than ten years following 1973, a upper limit for transition temperatures of superconductors appeared to be around 25 K, and operation at this temperature would not provide any substantial improvement in refrigeration savings. This led to major scepticism about the commercial viability of superconductor materials. Consequently, major efforts to pursue the technology diminished due to a loss of incentive in the early 1980's. At that stage, the commercial future of superconductors appeared to be unspectacular. However unexpectedly, high temperature superconductors were eventually discovered in 1986. Having transition temperatures much higher than any conventional superconductor, high temperature materials created tremendous excitement around the world and restored enthusiasm in superconductive electronics. Since the discovery of HTS, revolutionary advances have been made on many technological fronts to bring superconductive electronics within reach of successful commercialisation.

2.7 APPLICATIONS OF HIGH TEMPERATURE SUPERCONDUCTORS

At the moment, applications of superconductivity are focused strongly on the high temperature materials. The ability of HTS to operate at much higher temperatures than conventional LTS provide a number of significant practical advantages. Higher temperatures reduces the amount of stress on device components

during temperature cycling. Operation at higher temperatures is economical because the efficiency of refrigeration increases with temperature, and less power is required to maintain higher cryogenic temperatures. For example, the power needed to cool to 4.2 K (liquid helium) can be about 100 times more than for cooling at 77 K (liquid nitrogen) when using a mechanical cryocooler [9]. For HTS materials with T_c 's greater than 77 K, it even becomes possible to use a liquid nitrogen bath to refrigerate HTS systems instead of using a mechanical cooler. Using liquid nitrogen is economical for short term refrigeration as it is 10 times cheaper than helium and it is also easier to handle. However, immersion cooling using cryogen baths is not considered to be a serious candidate for refrigeration of commercial superconducting systems because of the frequent need to replenish the cryogen [24]. Mechanical cooling systems are favoured as they can keep a superconducting system at a stable temperature within fractions of a Kelvin for over long periods of time. However, mechanical systems are not yet suitable for refrigeration of systems of very large mass and volume. Hence, the first successful commercial HTS products are expected to be one's with sufficiently low mass and volume.

In areas of HTS product development, demonstrations already show that the performance of developed HTS test products can match and even exceed those of normal conductor state-of-the-art equivalents, often with additional benefits of reduced size and weight. The demonstrations have provided clear indication that high temperature superconductor products have realistic market opportunities. HTS filters are already being marketed as subsystem components for terrestrial cellular wireless communications base stations now in commercial service. Field trials of other wireless communications systems using HTS filter subsystems have been going on since early 1998 with excellent results reported on the system performance [25].

In the sections to follow, various applications of high temperature superconductors are reviewed. But unfortunately, there are too many applications to review on an individual basis. Therefore, the potential applications for HTS are given in the list of Fig. 2.14 that indicates the foreseen market opportunities of high temperature superconductor materials.

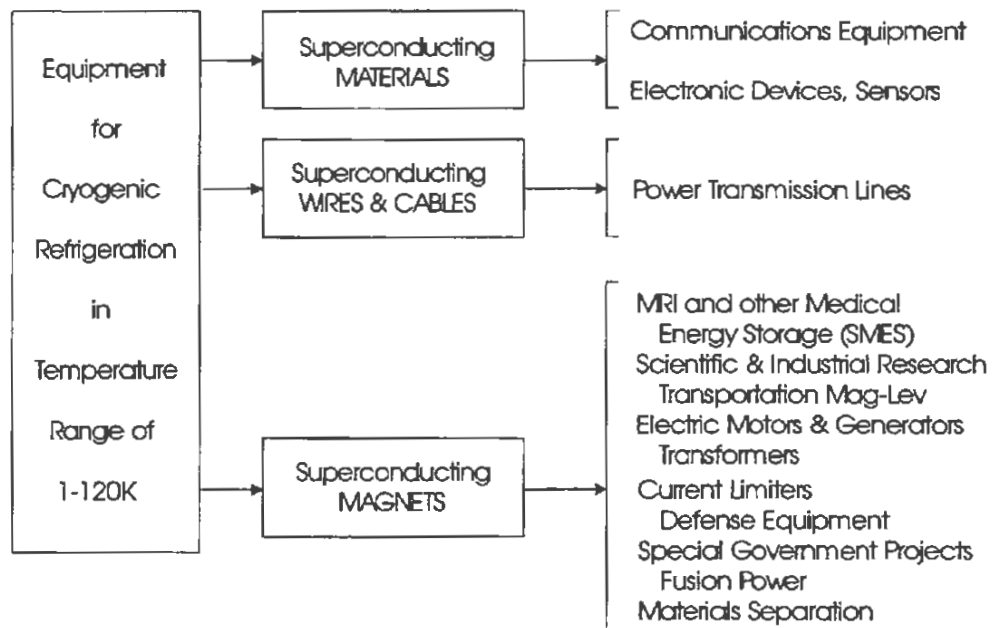


Figure 2.14 Possible applications of high temperature superconductors [16].

2.7.1 FILTERS AND OTHER SYSTEMS FOR WIRELESS COMMUNICATIONS

The low loss property of HTS thin films can provide significant benefits in the performance of wireless communications devices and components, as well as desirable reductions in the size and weight of filter subsystems in cellular and PCS base stations. In cellular phone communications today, there are over 25 million subscribers world-wide, with projected figures exceeding 63 million by the year 2000 [26]. As the number of subscribers continue to rise at a rapid rate, carriers will need to increase their capacity. Unfortunately, the amount of available bandwidth for communications is limited, and it would not be possible to accommodate the projected numbers of subscribers using existing communications systems. Hence it is necessary to improve existing systems or to develop new ones to make more efficient usage of bandwidth.

To improve bandwidth efficiency, the idea of packing communications channels as close together as possible is a logical approach. To succeed in this approach, analog filters with excellent frequency selectivity are needed for precise

selection of communication channels. Imprecise selection of a channel can lead to adjacent channel interference which is detrimental to the performance of a communications system. Normal conducting state-of-the-art waveguide filters are capable of high performance, but the conductor losses limits the maximum number of poles to about nine without exceeding maximum insertion loss requirements related to considerations of signal reception. In comparison, planar superconducting filters made out of coupled high Q-factor HTS transmission line resonators can be realised with performances to match conventional and even exceed conventional state of the art ones, with the added benefits of reduced weight and volume. For example, the higher Q-factors of up to 10^4 of superconducting resonators (as compared to only 10^2 in resonators made of conventional conductors) enable superconducting filters to have much sharper filter skirts, higher out-of-band-rejection, and lower insertion loss than conventional filters. Figure 2.15 shows the generalised insertion loss characteristics of HTS filters and conventional filters.

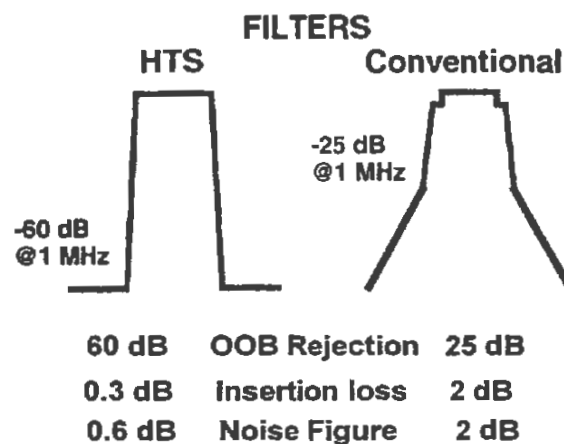


Figure 2.15 Comparison of performance parameters between a high temperature superconducting filter and a conventional normal conducting filter [27].

Figure 2.16 shows a 19 pole bandpass HTS filter and its superior filter characteristics which cannot be achieved in conventional filters.

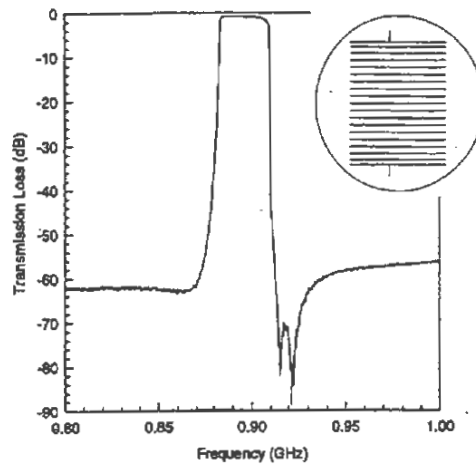


Figure 2.16 A 19 pole HTS bandpass filter developed by Conductus Inc. for cellular wireless communications and the insertion loss characteristics of the filter. Such 'brickwall' characteristics cannot be achieved in conventional filters [28].

Superconducting filters also have inherently better noise performance than conventional normal conducting filters because operation at reduced temperatures means reduced thermal noise. In Fig. 2.17, the system noise figures are compared between a conventional MRC-800 cellular receiver system and the same system using a superconducting filter and low noise amplifier on the front end [26].

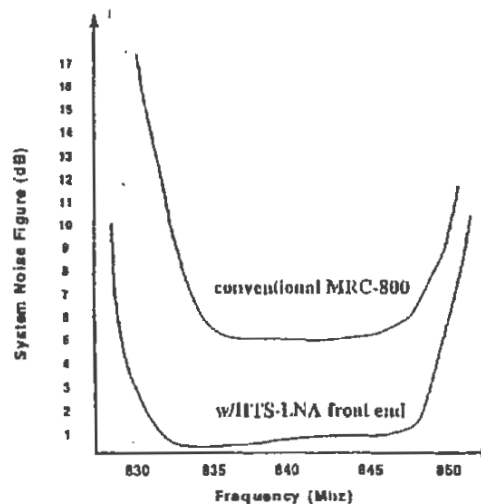


Figure 2.17 Comparison of system noise figure between a conventional MRC-800 cellular receiver system with the same system fitted with a superconducting filter and low noise amplifier on the front end [26].

The low insertion loss of superconducting filters combined with the low noise properties means that the receiver system can detect weak signals from the low power output of mobile phones much better than in conventional system. The resulting benefits include a much wider area of coverage (typically 50 percent improvement), reduced number of dropped calls, and therefore improved quality of service. Because of the superior capabilities of high temperature superconducting filters, over 500 HTS cellular phone base station filters have already been installed.

Apart from HTS resonator based filters being developed, a host of other HTS devices for wireless communications systems have been built. These include multiplexers, ultra stable oscillators, channelisers, power combiners, couplers, patch antennas, and mixers. The excellent performance and compactness of such devices are derived from the unique low loss property of superconductors. Figure 2.18 summarises applications for HTS in wireless communications [16].

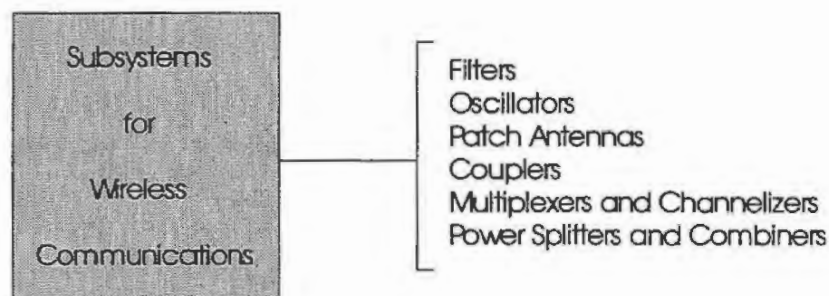


Figure 2.18 Superconductive electronic applications of HTS in wireless communications and digital electronics [16].

2.7.2 DELAY LINES FOR ANALOG SIGNAL PROCESSING

For analog signal processing applications, the low loss and zero dispersion property of HTS combined with stripline technology enable realisations of compact high frequency HTS delay line structures with very high bandwidth. Delay lines are used to provide delay of a pulsed microwave signal typically by many nanoseconds.

Important structures used in analog signal processing are weighted-tapped delay lines, which consist of an array of delay lines with weighted taps. These structures are used to perform real time integral transforms such as Fourier and correlation. The performance of HTS tapped delay lines are superior to ones made of normal conductors, and the size and weight can be significantly smaller.

Copper coaxial cables are used in conventional microwave systems to provide delays of ten to hundreds of nanoseconds. Such cables are heavy and bulky. HTS delay lines, which weigh only a fraction of the coaxial cable, can be made to give the same delay. For example, a HTS delay line which works from DC up to several GHz has been developed by STI to provide a delay of 30 nanoseconds, with a weight and volume of only 1 percent of the equivalent coaxial cable [29]. In another example, a 29 nanosecond delay line using the coplanar waveguide structure in a meander pattern has been achieved with 2.5 metre long centre conductor, and fitted on 3cm by 3cm lanthanum aluminate substrate. To achieve the same delay using a Teflon coaxial cable, a six metre length of cable would be required. A realisation of a compact 11 ns HTS delay line made by Dupont is shown in Fig. 2.19 below.

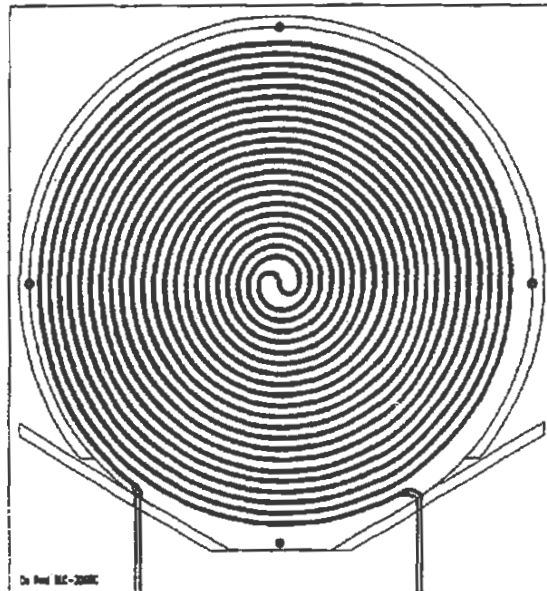


Figure 2.19 A 11 nanosecond delay line made by Dupont. The superconducting line is arranged in a spiral pattern [30].

2.7.3 HTS WIRES AND TAPES FOR ELECTRICAL POWER APPLICATIONS, MAGNETIC LEVITATIONAL TRANSPORT, AND HIGH ENERGY PHYSICS RESEARCH

Many important applications based on the low loss property of high temperature superconductors have been proposed for the power industry. For the transmission of power, significant reduction in overheads can be expected by replacing conventional power lines with superconducting lines. The advantage of superconducting lines over conventional copper ones is increased efficiency, provided that the cost of cooling the line can be made to be cheap enough. While superconductor lines for commercial power transmission have not yet been achieved, work is currently being done to develop lines with the desirable properties needed for practical and economical implementation. As a rule of thumb for competitive transmission and distribution of power, the critical current density of superconductors for high power lines should be at least 10kA/cm^2 [14]. Using powder-in-tube technology, superconducting wires made of BSCCO have been produced with critical currents of up to 18kA/cm^2 at 77 K and zero applied field [31]. In another fabrication process, a successful technique has been developed which uses the ion-beam assisted deposition (IBAD) process to produce centimetre-wide metal tapes coated with YBCO HTS thin film material with high current carrying capacity greater than 1MA/cm^2 [32].

HTS wires have been developed which are capable of operating in high critical fields exceeding 10T. Also, progress has been made in the development of strong magnets based on HTS superconducting coils for applications in magnetic levitation (Maglev) for transportation of the future, high energy particle accelerators for physics research, large HTS solenoids for superconducting energy storage SMES systems, electrical motors and generators, as well as medical magnetic resonance imaging (MRI) which was the first and foremost major commercial application for superconductors [14,16].

2.7.4 JOSEPHSON DEVICES FOR DSP APPLICATIONS, DETECTION OF WEAK MAGNETIC FIELDS, MIXERS FOR WIRELESS COMMUNICATIONS, MEDICAL DIAGNOSTICS, DIGITAL ELECTRONICS AND OTHER APPLICATIONS

The tunnelling phenomenon of superconductivity in Josephson junctions provides many prospective applications for superconducting materials. Several commercial superconductive applications to emerge are expected to be based on this phenomenon. Josephson junctions are formed from two superconducting films separated by a very thin insulating barrier such as silicon or an oxide. If the thickness is suitably chosen - typically in the order of the coherence length, the superconductor current can pass without any resistance between the two superconductors as if no barrier was present [1], and there are important applications for such phenomena.

The useful property of Josephson junctions lies in its very high switching speed and extremely high sensitivity to magnetic fields [1]. Josephson junctions have a semiconductor like behaviour. When the current flowing through the junction is below a maximum critical value, the voltage across the junction is zero due to the supercurrent. When the critical current is exceeded, the voltage 'switches' sharply to a value approximately equal to twice the energy gap of the superconducting films [1]. The intrinsic switching time is extremely fast with typical values of less than a picosecond, and is only limited by the junction capacitance. The critical current of the junction is also influenced by extremely weak magnetic fields. If a sufficiently high field is applied to the junction then it will no longer exhibit the zero-voltage characteristic, but will retain the semiconductor-like behaviour. It is known that the behaviour of the I-V curve for currents increasing and decreasing about the critical current is not the same, and there is in fact a large hysteresis between the two. However there are methods in fabrication of the junctions to remove the hysteresis. The I-V characteristic of the junction is similar to semiconductors. The main difference is that the voltage at the knee of the curve is in the order of millivolts instead of volts. The knee can be very sharp in high quality junctions, and the highly non-linear characteristic have applications in high frequency mixers. A practical Josephson mixer is Fig. 2.20 [24].

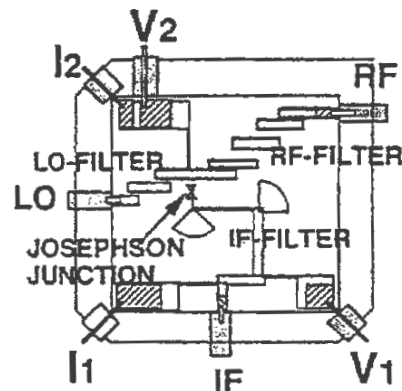


Figure 2.20 Block diagram of a monolithic YBCO Josephson mixer circuit mounted in a microwave package [24].

Based on the switching and hysteretic properties, Josephson Junctions have applications in digital electronics with utilisations in memory and logic elements. In particular, applications include high-speed (Gigabit) logic circuits based on Rapid Single Flux Quantum (RSFQ) logic derived from Josephson junctions. These circuits are expected to outperform best conventional (GaAs type) circuits. In demonstrations, RSFQ circuits have been operated up to exceptionally fast clock speeds of up to 100 GHz. RSFQ may be used in future A/D converters, shift registers, and fast digital processors [29].

The extreme sensitivity of the critical current to magnetic flux in Josephson junctions has been applied in devices called SQUIDS or superconducting quantum interference device, which is used in the most sensitive magnetic field detectors currently available. SQUID detectors can measure changes in magnetic fields a thousand times smaller than with any other non-superconducting detectors [14]. SQUID based magnetometers have already been developed for magnetoencephalography (MEG), used to measure minute magnetic fields caused by electrical activity from neurons in the brain [33]. SQUID magnetometers have also been employed for geological purposes to detect fields from magnetic materials within the earth's crust [14]. Other devices based on SQUIDS include very sensitive voltmeters which can detect down to a billionth of a billionth of a volt, or ammeters which can measure current as small as 10 electrons per second passing through a wire [14].

2.7.5 DEVICE PACKAGING FOR HIGH SPEED DIGITAL ELECTRONICS

HTS also has applications in digital system packaging. As is known already, the speed of a computer processor is limited by the interconnections between chips making up that processor. A CPU in a computer may contain up to 100 chips and each chip may have up to 100 input/output wires connected to it. Multi-chip module (MCM) technology has enabled integrated circuit chips to be placed closely together inside a central processing unit (CPU) to provide significant performance benefits and opportunities for device miniaturisation. These benefits go towards improving computer speed. MCMs have been manufactured by IBM for its mainframe computers, which consist of 64 layers of copper wiring embedded in low dielectric constant glass ceramic [29]. To further improve the MCM technology, it would be desirable to further reduce the cross sectional area of the copper tracks which interconnect the chips, but the associated increase in resistance and associated ohmic losses imposes practical restrictions so that it cannot be done successfully. For example, it is infeasible to use copper tracks of width less than 20 micron. Such practical restrictions could be removed if HTS superconductor tracks are used for the interconnects. While conventional MCM technology is already very complex, the technologies involved to achieve HTS MCMs would be extremely complex. However, the large benefits of such technologies is foreseen and steps are being made to pursue it.

BIBLIOGRAPHY OF CHAPTER 2

- [1] Z. Kresin, S.A. Wolf, "Fundamentals of Superconductivity", Plenum Press, New York, 1990.
- [2] M. Tinkham, "Introduction to Superconductivity", McGraw-Hill, 1975.
- [3] M. Haller, R.L. Snyder, "The structural conditions for high-temperature superconductivity", JOM publication of the Minerals, Metals and Materials Society, pp. 12-17. Oct 1997.
- [4] J.D. Jorgensen et al., "Structural properties of oxygen deficient $\text{YBa}_2\text{Cu}_3\text{O}_{7-\delta}$ ", Phys. Rev. B, Vol. 41, pp. 1863. 1990.
- [5] D.M. Ginsberg, "Physical Properties of High Temperature Superconductors I-III", World Scientific, Singapore.
- [6] Z. Ma, "RF properties of high temperature superconducting materials", PhD thesis, G.L. Report No. 5298, Edward L. Ginzton Laboratory, Stanford University, pp 34-41. May 1995.
- [7] Conductus Inc. [Notes].
- [8] A.C. Rose-Innes, E.H. Rhoderick, "Introduction to Superconductivity", 2nd Edition, Pergamon, 1994.
- [9] W.G. Lyons, R.S. Withers, "Passive microwave device applications of high T_c superconducting thin films", technical feature from Microwave Journal, Nov 1990.
- [10] D.K. Cheng, "Field and Wave Electromagnetics", Addison-Wesley Publishing Company, 1989.
- [11] H.H. Skilling, "Fundamentals of Electric Waves Second Edition", Wiley and Sons Inc., 1964.
- [12] H.A. Atwater, "Introduction to Microwave Theory", M^cGraw Hill Book Company Inc., 1962.
- [13] I.M. Firth, "Superconductivity", Mills & Boon Ltd, 1972.
- [14] A.J. Jones, "Superconductivity", Commonwealth of Australia, 1988.
- [15] Z-Y. Shen, "High Temperature Superconducting Microwave Circuits", Artech House, 1994.
- [16] C. Rosner, "Emerging 21st century markets and outlook for applied superconducting products", presented paper from the The Cryogenic Engineering

- Conference/International Cryogenic Materials Conference, Portland, Oregon, July 29 1997.
- [17] T. Van Duzer, C.W. Turner, "Principles of Superconductive Devices and Circuits", Elsevier North Holland, 1981.
- [18] D. Halliday, R. Resnick, "Physics Parts 1 and 2", Third Edition, Wiley & Sons, Inc., 1978.
- [19] D.M. Pozar, "Microwave Engineering", Addison-Wesley Publishing Company, 1990.
- [20] J. Bybokas, B. Hammond, "High temperature superconductors", Microwave Journal, Feb 1990.
- [21] K. Zhang, D.A. Bonn, S. Kamal, R. Liang, D.J. Baar, W.N. Hardy, D. Basov, T. Timusk, "Measurement of the ab plane anisotropy of microwave surface impedance of untwinned $\text{YBa}_2\text{Cu}_3\text{O}_{6.95}$ single crystals", Phys. Rev. Lett., Vol. 73, No. 18, pp. 2484. 1994.
- [22] R. Fletcher, J. Cook, "Measurement of surface impedance versus temperature using a generalized sapphire resonator technique", Rev. Sci. Instrum. Vol. 65, No. 8, pp. 2685. Aug 1994.
- [23] J. Ceremuga, J. Krupka, J. Modelski, "Influence of superconducting film thickness on resonant frequencies and Q-factor of the sapphire dielectric resonator and on resulting surface impedance of high T_c superconductors", Proceedings of Asia-Pacific Microwave Conference, 6-9 December, 1994, Tokyo, pp. 1069-1072. 1994.
- [24] M.A. Hein, "Microwave properties of high-temperature superconductors: surface impedance, circuits and systems", contribution to Studies of High-Temperature Superconductors Vol. 18 Narlikar Editor, (Nova Science Publishers, New York, 1996), pp. 141-216.
- [25] Superconductor Technologies Inc. SuperFilterTM systems field trial summary [notes].
- [26] G.C. Liang, "Base Station Selectivity and Sensitivity : Attacking Interference- and Noise-Limited Environments with Superconducting Filters and Cryoelectronics",

- seminar presentation at the Wescon/95 Communications Technology Conference, San Francisco, Nov. 8, 1995.
- [27] C.E. Mahle, IEEE MTT-S workshop, San Francisco, June 17-21, 1996.
- [28] D. Zhang et al, IEEE Microwave and Guided Wave Letters, Vol. 5, No. 11, pp. 405, 1998.
- [29] R.B. Hammond, L.C. Bourne, "Survey of Potential Electronic Applications of High Temperature Superconductors", Addison-Wesley Publishing Company, 1991.
- [30] DuPont Superconductivity [Notes].
- [31] IEEE Spectrum Magazine, "Power and Energy", Jan 1997.
- [32] D.B. Chrisey, "Progress in the First Ten Years of HTS Film Growth", JOM publication of the Minerals, Metals and Materials Society, pp. 28-32. Oct 1997.
- [33] A.I. Braginski, "Superconducting electronics coming to market", IEEE Trans. on Applied Superconductivity, Vol. 9, No. 2, pp. 2825-2836. June 1999.

CHAPTER 3

REVIEW OF EXPERIMENTAL TECHNIQUES USED FOR MEASUREMENTS OF THE SURFACE RESISTANCE OF HTS THIN FILMS

Measurements of the microwave surface resistance R_s of superconductor films are based on techniques using microwave resonators. In general, the superconductor sample is made an integral part of a resonator, and measurements are made to determine the unloaded Q_0 -factor of the resonator which is then used in calculations of R_s . Equations used to calculate the surface resistance of the sample are derived from the analysis of the microwave losses in the resonator. Several types of resonators can be used for the characterisation of materials, with the sapphire dielectric resonator being the most popular structures for measurements of surface resistance of HTS thin films. In this chapter, loss analysis techniques for microwave resonators are reviewed, beginning with some important concepts about resonant systems to provide the necessary background in the understanding of the measurement techniques.

3.1 QUALITY FACTOR DEFINITION AND ENERGY TRANSACTIONS IN RESONATORS

The quality factor is used extensively in the analysis of losses in resonant systems. It is a measure of the energy stored within the resonator compared to the energy dissipated in a given region of the resonant system as defined by the following energy ratio [1]:

$$Q = 2\pi \frac{\text{maximum energy stored over a cycle}}{\text{average energy dissipated per cycle}} \quad (3.1)$$
$$= \frac{2\pi W_{\max}}{W_d} = \frac{2\pi W_{\max}}{PT} = \frac{\omega_o W_{\max}}{P}$$

where W_{\max} is the maximum energy stored in the system over a full cycle of microwave excitation, W_d is the energy dissipated in the system over one period, P is the power dissipated in a given region per cycle, T is the period of oscillations, and ω_0 is the radian resonant frequency.

When analysing losses in microwave resonators, the microwave losses associated with various parts of the resonator are often expressed in terms of reciprocals of Q-factor as described later in this chapter. This makes it convenient for the development of a high level loss equation involving geometrical and material constants while strong relationships with the Q-factors are maintained. It is this high level loss equation which is used to calculate the surface resistance of the superconducting thin films.

The understanding the energy transactions in resonators is fundamental in the analysis of microwave resonators. A microwave resonator is a structure that is capable of storing electromagnetic energy. The energy is stored alternately between the electric and magnetic fields, namely as the stored electric energy $W_e(t)$ and the stored magnetic energy $W_m(t)$ [1]. These energies vary in time between zero and their maximum values, and they follow a time-quadrature behaviour such that when the stored electric energy is maximum, the stored magnetic energy is zero (and vice versa), as illustrated in Fig. 3.1. The average values W_e and W_m are equal to half of the corresponding maximum values of $W_e(t)$ and $W_m(t)$.

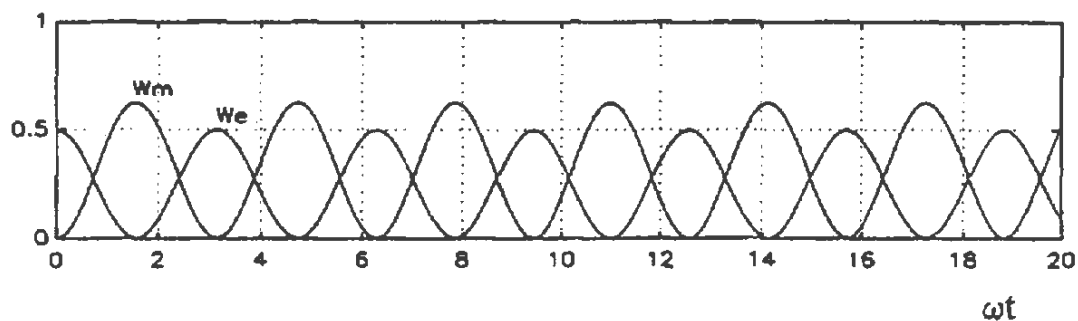


Figure 3.1 Time dependence of stored energies in a resonator [1].

When considering circuit models of resonators, the energies W_e and W_m are related to circuit behaviour. The difference between the stored electric and magnetic energy is proportional to the reactance of the resonator. At a certain frequency, when the peak stored electric energy becomes equal to the peak stored magnetic energy (that is, $W_{e,max} = W_{m,max}$), the reactance vanishes and the input impedance of the resonator is purely real. The frequency at which this condition occurs is known as the resonant frequency f_0 .

3.2 EQUATIONS FOR CALCULATIONS OF THE SURFACE RESISTANCE OF SUPERCONDUCTOR FILMS USING LOSS EQUATIONS AND ACCURACY OF CALCULATIONS

In measurements of the surface resistance of superconductor films using resonance methods, the surface resistance of superconductor sample(s) is typically calculated from the unloaded quality factor, and the geometrical and material constants associated with the resonator. Equations used in such calculations are derived from the analysis of losses in microwave resonators. For any resonator system, the losses may be grouped into three types identified as conductor losses P_c , dielectric losses P_d , and radiation loss P_r as is illustrated in Fig. 3.2 showing a cross sectional view of a Hakki-Coleman [2] dielectric resonator system. The dielectric resonator consists of a cylindrical metallic cavity, a sapphire dielectric puck, and two HTS films on both ends of the puck.

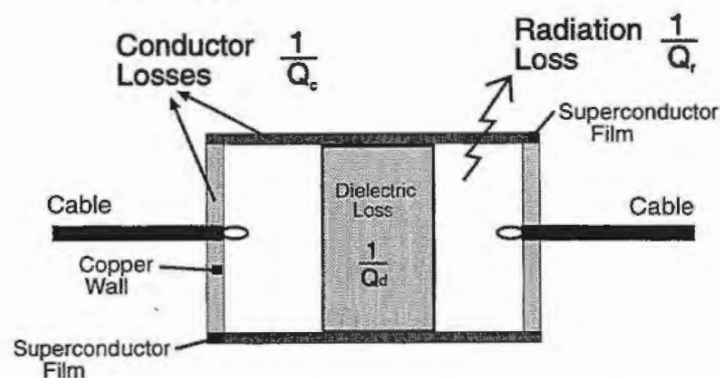


Figure 3.2 Microwave losses of a dielectric resonator.

The total loss P_o of the uncoupled resonator with the loss components taken into consideration is given by [3] :

$$P_o = P_c + P_d + P_r \quad (3.2)$$

Application of the Q-factor definition of (3.1) to the above loss equation provides the relationship between the unloaded Q-factor in terms of partial Q-factors as [3,4]:

$$\frac{1}{Q_o} = \frac{1}{Q_c} + \frac{1}{Q_d} + \frac{1}{Q_r} \quad (3.3)$$

where Q_o^{-1} represents the total loss in the resonator; and the terms Q_c , Q_d , and Q_r are the quality factors associated with the conductor, dielectric and radiation losses respectively. The conductor Q_c -factor is related to the total dissipation in all conductors including superconducting parts by :

$$Q_c = \frac{\omega_o W}{P_c} \quad (3.4)$$

The dielectric loss of the resonator is characterised by the loss tangent of the dielectric part, which is given by [3] :

$$\tan \delta = \sigma / (\omega \epsilon_o \epsilon_r) \quad (3.5)$$

where $\epsilon_o \epsilon_r$ is the permittivity of the dielectric, σ is the conductivity of the dielectric, and ω is the radian frequency. Equation (3.5) indicates that $\tan \delta$ decreases with frequency. But at microwave frequencies, the behaviour is just the opposite. Using the Q-factor definition, the dielectric Q_d -factor can be expressed as [3]:

$$Q_d = \frac{\omega_o W}{P_d} = \frac{\omega_o \epsilon \int |E|^2 dv}{\sigma \int |E|^2 dv} = \frac{\omega_o \epsilon}{\sigma} = \frac{1}{\tan \delta} \quad (3.6)$$

The above relationship between the dielectric quality factor and the loss tangent is valid only for uniformly filled dielectric cavities. For inhomogeneously filled structures, the dielectric Q-factor is given by [5] :

$$Q_d = \frac{1}{p_e \tan \delta} \quad (3.7)$$

where p_e is the electric filling factor defined as the ratio of the stored electric energy W_{ei} in the dielectric part to the total stored electric energy W_e in the cavity as [3]:

$$P_e = \frac{W_{ei}}{W_e} \quad (3.8)$$

The total conductor loss ($1/Q_c$) is equal to the sum of the losses in the superconductor sample and in the normal conducting parts of the cavity as :

$$\frac{1}{Q_c} = \frac{1}{Q_s} + \frac{1}{Q_m} \quad (3.9)$$

where Q_s^{-1} represents the conductor loss in the superconductor sample, and Q_m^{-1} represents the remainder of the conductor losses that is not due to the sample. Using (3.3), the loss in the HTS films can be expressed as :

$$\frac{1}{Q_s} = \frac{1}{Q_o} \left[\frac{1}{Q_m} + \frac{1}{Q_d} + \frac{1}{Q_r} \right] \quad (3.10)$$

The loss Q_s^{-1} in the superconductor sample is related to the surface resistance R_s of the sample and the geometrical factor A_s associated with the geometry of the sample by [5]:

$$\frac{1}{Q_s} = \frac{R_s}{A_s} \quad (3.11)$$

Substitution of (3.11) of equation (3.10) provides the equation to calculate the surface resistance of the superconductor from the unloaded Q_o -factor and predetermined components of loss :

$$R_s = A_s \left\{ \frac{1}{Q_o} \left[\frac{1}{Q_m} + \frac{1}{Q_d} + \frac{1}{Q_r} \right] \right\} \quad (3.12)$$

where the loss Q_m^{-1} due to the metal wall is related to the surface resistance R_m of the metal wall and the geometrical factor A_m associated with the geometry of the wall as [5]:

$$\frac{1}{Q_m} = \frac{R_m}{A_m} \quad (3.13)$$

From equation (3.12), it is clearly seen that the uncertainty in R_s will be due to uncertainties in the various components of loss, which need to be determined. Radiation losses, if they are present can be difficult to determine accurately, but can be minimised or even eliminated by appropriate design and choice of the resonator.

The dielectric losses ($1/Q_d$) have the form of $p_e \tan \delta$. While the energy filling factor p_e is calculated from geometry, the loss tangent needs to be obtained from measurements. Low loss dielectric is typically used such as sapphire with loss tangent less than $5 \cdot 10^{-8}$ at 77K so that the dielectric loss is usually negligibly small compared to other losses in the resonator (which is often the case at low temperatures).

3.3 REVIEW OF Q-FACTOR RELATIONSHIPS IN MICROWAVE RESONATORS

In the analysis of microwave resonator systems, there are four parameters to be considered, namely the resonant frequency, the unloaded Q_0 -factor, the loaded Q_L -factor and the coupling coefficient(s). In terms of microwave power loss at resonance, the unloaded Q_0 -factor describes the total losses of a isolated resonator, while the loaded Q_L -factor describes the losses of the resonator connected to a external circuit such as a measurement system. The coupling coefficient describes the amount of power dissipated in the external circuit compared to the dissipation in the resonator. As the relationship between the unloaded and loaded Q-factors and the coupling coefficients is fundamental to the understanding of resonant systems and is also important in measurements of the unloaded Q_0 -factor of microwave resonators, the mathematical relationships between these quantities are reviewed below. Consider the power dissipation in a single input loaded dielectric resonator cavity system illustrated in Fig 3.3.

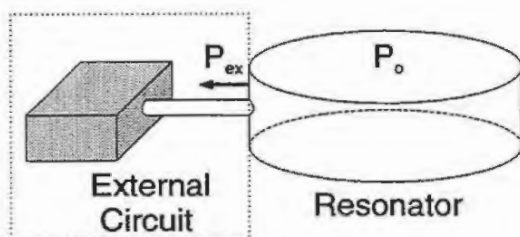


Figure 3.3 Power dissipation in a loaded resonant system consisting of a microwave resonator connected to a external circuit.

Defining Q_{ex} to be the partial quality factor associated with the dissipation P_{ex} in the external circuit, an expression for the unloaded Q_o -factor has been obtained in terms of the loaded quality factor and the external dissipation in the following way [1]. The loss equation for the loaded system is :

$$P_L = P_o + P_{ex} \quad (3.14)$$

where P_L is the power dissipated in the overall circuit. P_o and P_{ex} are the powers dissipated in the resonator and the external circuit respectively. Using the quality factor definition, equation (3.14) is converted to an equivalent partial Q-factor equation by first considering that the energy W_{diss} dissipated in a specified part of the resonator in one period is [1]:

$$W_{diss} = P_{diss} T \quad (3.15)$$

where the period of oscillation T related to the radian frequency ω is :

$$T = \frac{2\pi}{\omega} \quad (3.16)$$

This gives :

$$W_{diss} = P_{diss} \frac{2\pi}{\omega} \quad (3.17)$$

Using the Q factor definition as in (3.1) :

$$Q = 2\pi(W_{max} / W_{diss}) \quad (3.18)$$

Substituting (3.17) into (3.18), the quality factor is expressed as [1]:

$$Q = \frac{\omega W_{max}}{P_{diss}} \quad (3.19)$$

where W_{max} is the maximum energy stored in the resonator per cycle, and P_{diss} describes the dissipation in a specified part of the resonator. Hence, the dissipated power P_{diss} is inversely proportional to the quality factor by a constant equal to ωW_{max} . Now, when both sides of the power equation (3.14) are divided by ωW_{max} , the equation relating the unloaded Q_o -factor, loaded Q_L -factor, and the external quality factor Q_{ex} is obtained as [1]:

$$\frac{1}{Q_L} = \frac{1}{Q_o} + \frac{1}{Q_{ex}} \quad (3.20)$$

As the coupling coefficient β is defined to be the ratio of the power P_{ex} dissipated in the external circuit to the power P_o dissipated within the resonator [6], and

in view of the relationship between the Q factor and power dissipation in (3.19), the following equation relating the unloaded Q_o -factor and the external Q_{ex} -factor to the coupling coefficient has been obtained [1,6] :

$$\beta = \frac{P_{ex}}{P_o} = \frac{Q_o}{Q_{ex}} \quad (3.21)$$

The combination of (3.20) and (3.21) provides the well known equation to relate the unloaded Q_o -factor for the single input resonator to the loaded Q_L -factor and the coupling coefficient [6]:

$$Q_o = Q_L(1 + \beta) \quad (3.22)$$

For resonators working in the transmission mode (Fig. 3.4) where there are two coupling coefficients β_1 and β_2 , the following equation relates the unloaded Q_o -factor with the loaded Q_L -factor and the coupling coefficients [6]:

$$Q_o = Q_L(1 + \beta_1 + \beta_2) \quad (3.23)$$

where β_1 is the coupling coefficient related to the external power dissipation P_{ex1} on the port 1 side, and β_2 is the coupling coefficient related to the external power dissipation P_{ex2} on the port 2 side, according to [6] :

$$\beta_i = \frac{P_{exi}}{P_o} \quad (i = 1 \text{ or } 2) \quad (3.24)$$

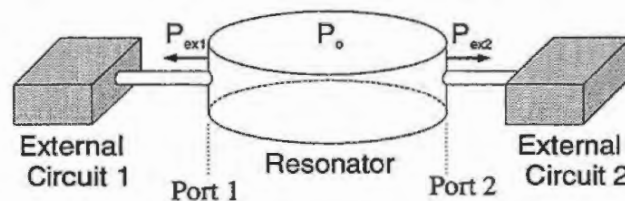


Figure 3.4 Power dissipation in a loaded resonant system consisting of a microwave resonator working in the transmission mode.

There are four cases of coupling in resonators. For the case where the power dissipated P_{ex} in the external circuit is greater than the power dissipated P_o in the cavity, the coupling coefficient is greater than unity ($\beta > 1$), the system is said to be an over-coupled one. If the external dissipation is equal to the dissipation in the cavity (ie. $P_{ex} =$

P_o), then the coupling coefficient is equal to unity ($\beta=1$) and the system is said to be critically coupled. For P_{ex} less than P_o , the coupling coefficient is less than unity ($\beta<1$), and the system is under-coupled. In the case of a uncoupled resonator (which is not connected to any external circuit), there is no external power dissipated so that the coupling coefficient is zero ($\beta=0$). As practical measurements cannot be made when the coupling is zero, the coupling coefficients and the loaded Q_L -factor must be measured in order to determine the unloaded Q_o -factor. However, for cases of a very weak coupling where the coupling coefficients in (3.22) and (3.23) are assumed to be negligibly small with respect to unity, the measured loaded Q_L -factor is sometimes used to approximate the unloaded Q_o -factor.

3.4 RESONATORS USED FOR THE MICROWAVE CHARACTERISATION OF SUPERCONDUCTING FILMS

There are several types of microwave resonators which have been used for the characterisation of superconductor films. These include dielectric resonators [3,7], parallel plate resonator [8], transmission line resonators [9,10,11], confocal resonator [12], and hollow cavity resonators [13]. Differences between each resonator type results in differing accuracy, sensitivity, and ease of measurements.

Dielectric resonators which consist of a very low loss and temperature-stable dielectric puck located central to a shielded cavity have been very popular for measurements of surface resistance of HTS films. Measurements of R_s using these resonators have been performed using a single film placed at one end of the dielectric puck [14], or using two films (one at each end of the dielectric puck [5,15]). Fig. 3.5 shows a dielectric resonator in a single HTS film is used. Fig. 3.6 shows a Hakki-Coleman dielectric resonator in which two superconductor films of similar quality are used. As the permittivity of the dielectric is typically much higher than the permittivity of free space, the dielectric confines most of the microwave energy so that a significant part of the total microwave losses occurs in the HTS samples, which enables very sensitive measurements of R_s to be made (with a reported sensitivity of $1 \mu\Omega$ for a

Hakki-Coleman dielectric resonator [16]). Dielectric resonators are typically much smaller than empty cavity resonators at the same operating frequency, and can accommodate standard small sized wafer samples such as 1cm square, or 1 inch (square or round). The relatively simple geometry of Hakki-Coleman dielectric resonators (Fig. 3.6) allow for very convenient mounting of HTS wafers. The structure is very robust and requires low maintenance. Analytical techniques exist to obtain the electromagnetic field distribution for Hakki-Coleman dielectric resonators so that the geometry factors can be calculated precisely. Accurate knowledge of the geometry factors are needed in accurate calculations of the surface resistance.

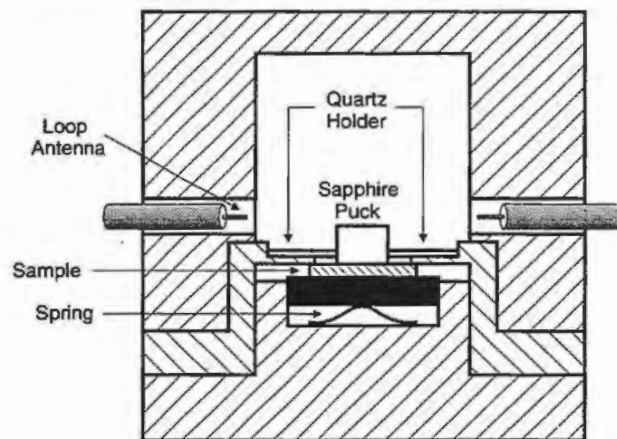


Figure 3.5 Dielectric resonator fitted with single superconductor film sample [14].

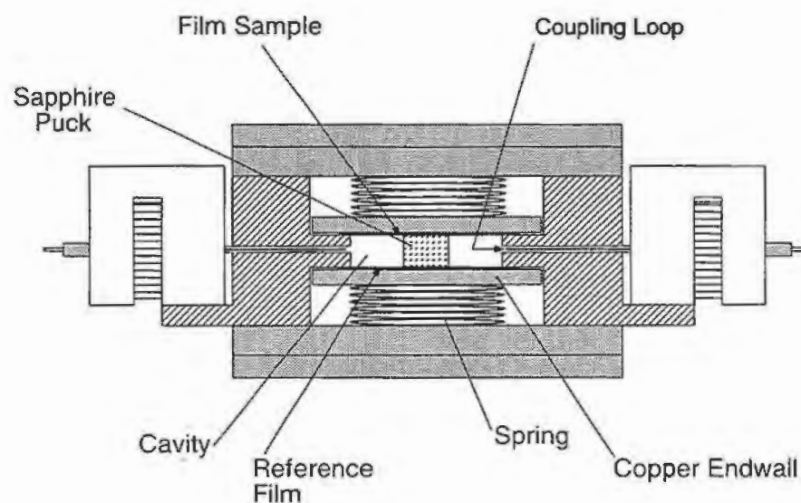


Figure 3.6 Hakki-Coleman type dielectric resonator used in this thesis [16].

Parallel plate resonators of Fig. 3.7 had been used to measure the surface resistance of HTS films before the Hakki Coleman dielectric resonator became the most extensively used structure [8,17]. The parallel plate resonator is made up of two superconductor film samples arranged in a parallel configuration with the film sides facing each other, and having a very thin layer of dielectric material (eg. 10 μm) in between the two superconducting samples. The parallel plate technique is reported to be a sensitive one. However, there are no exact solutions to mathematically describe the field distribution for the resonator in the sense of finding exact solutions to Maxwell's equations applied to the structure. Hence there are no exact equations to calculate the surface resistance from the measured value of unloaded Q_0 -factor, which could lead to uncertainty in the calculation of the surface resistance. In practical measurements of surface resistance using the parallel plate resonator, the plates need to be parallel for reliable measurements. Hence it can take a considerable amount of time and careful effort to prepare the structure for accurate and reliable measurements of surface resistance using the parallel plate resonator. Also, the resonant frequencies of different modes are very close together so that it can be difficult to identify the correct mode to be used for measurements of the unloaded Q_0 -factor [16].

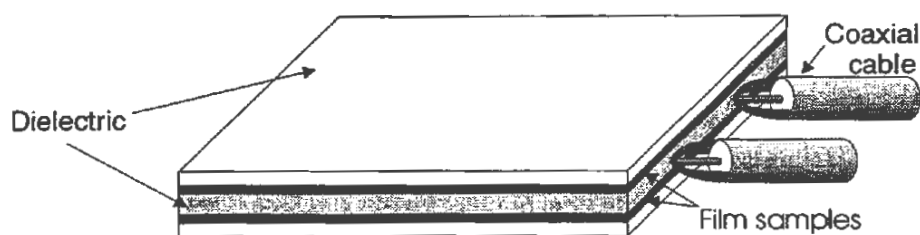


Figure 3.7 Parallel plate resonator [17].

The transmission line resonators used for the microwave characterisation of HTS films, include the microstripline, stripline and the coplanar waveguide configurations. Two types of microstripline line resonators have been used for measurements of the penetration depth. One type consists of a superconductor strip sample and normal conducting ground-plane with a dielectric layer in between them

as shown in Fig. 3.8 [18]. The other type of microstrip resonator which has been used for penetration depth measurements is the flip-chip variety of Fig. 3.9, which also consists of a dielectric sheet in between the superconducting sample and ground plane except that the sample is a patterned meander line [19]. The flip-chip design has been used in measurements of penetration depth of $\text{YBa}_2\text{Cu}_3\text{O}_7$ HTS films as well as low temperature superconducting films including Nb and NbN [9]. Unfortunately, microstrip resonators have not been able to provide very sensitive measurements of R_s because the radiation loss make up a significant part of the total loss and it is difficult to account for the energy that is lost due to radiation. Also, energy losses due to patterning and current crowding are presented.

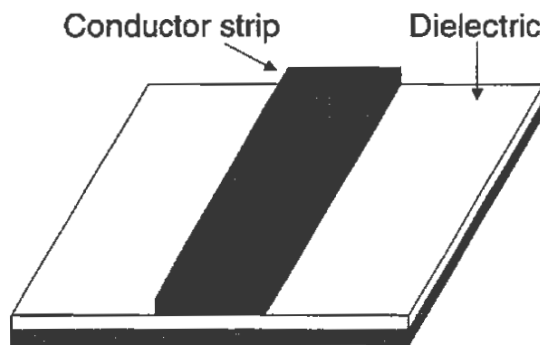


Figure 3.8 Conventional microstrip resonator [18].

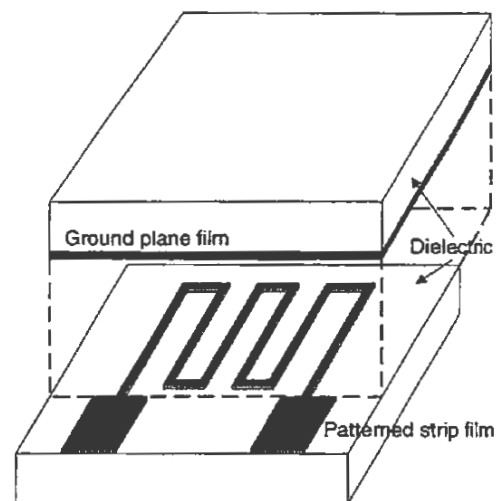


Figure 3.9 Microstrip resonator in the flip-chip configuration [19].

Stripline resonators of Fig. 3.10 are similar to microstrip resonators, except that the stripline structure has two groundplanes instead of one. Having two groundplanes effectively reduces the radiation losses and increases sensitivity of tests. Stripline resonators have been used for surface resistance measurements of low temperature superconducting films such as NbN [11].

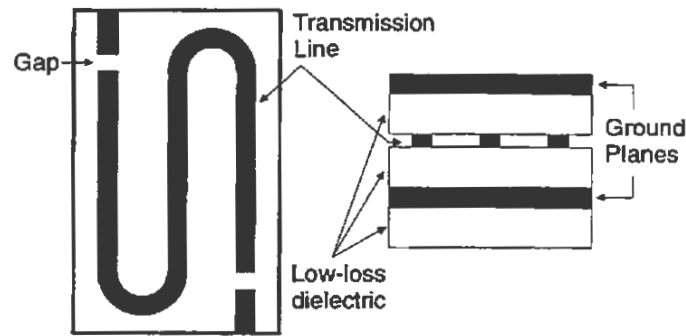


Figure 3.10 Stripline resonator [11].

Coplanar waveguide resonators, as shown in Fig. 3.11 have all the conductors on a single plane [20]. They consist of a superconductor sample strip in between two normal conducting ground planes. The strip is separated from the ground planes by a small gap. By making the gap width to be very small, the electromagnetic field can be confined to the vicinity of the gap, and this helps to minimise the radiation loss. Coplanar waveguides have been used to measure both the penetration depth and the surface resistance of HTS films [10].

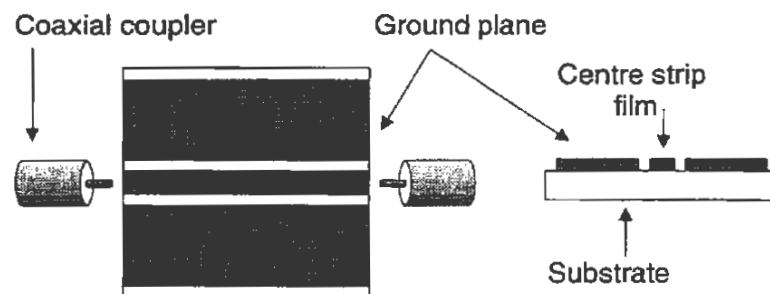


Figure 3.11 Coplanar wave guide resonator [10].

Microwave characterisation of HTS films using transmission line resonators is less accurate than when using dielectric resonators or parallel plate resonators. Current crowding at the edges of the film results in over-assessed values of the surface resistance of the HTS material. Also, the need for patterning significantly increases the costs of the tests.

Confocal resonators (Fig. 3.12) such as of the Fabry Perot type may be sensitive enough for microwave characterisation of HTS films [12]. In techniques using confocal resonators, microwave energy is focused onto a small area of the superconductor sample using a spherical metal mirror. For accurate measurements of R_s , strict calibration procedures are needed to set up the mirror accurately. Inaccurate positioning of the mirror cause significant uncertainty in the distribution of the resonance mode, which ultimately leads to uncertainty in measurements of R_s . The technique is also very sensitive to vibrations in the mirror so that the apparatus needs to be mounted on a very stable foundation. So far, a working measurement system based on the confocal resonator has not been developed.

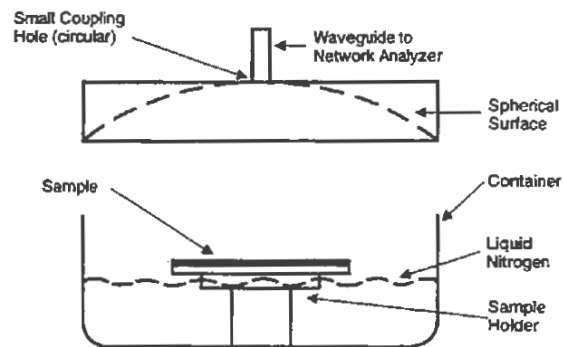


Figure 3.12 Confocal resonator [12].

Hollow cavity resonators which simply consist of a hollow cylindrical cavity with superconducting endwalls and copper (or superconducting niobium) lateral walls have been used in the past for measurements of the surface resistance of superconducting films at frequencies above 30 GHz. However for frequencies considered for applications of HTS thin films such as in the range 1 GHz and even at 10 GHz, the size of the empty cavities are too large to accommodate typical film samples such as 1 cm^2 and 2.5 cm^2 in area. It is also difficult and very expensive to produce large samples with very uniform properties throughout to be used as samples for large cavities. The configuration consists of a cylindrical microwave cavity where the superconducting sample is used as one of the endplates (known as 'end-plate replacement'). In the end-plate replacement structure shown in Fig. 3.13, the losses in

the copper walls limits the sensitivity of the structure so that it can only be used to measure fairly lossy samples (not of a high quality). However, if the copper parts are coated with superconducting material as Nb, then the measurement sensitivity can be greatly increased.

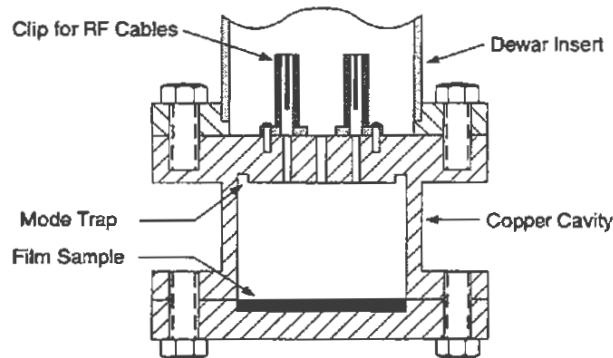


Figure 3.13 Endplate replacement cavity [13].

3.5 GEOMETRICAL FACTORS AND EM FIELD DISTRIBUTION IN DIELECTRIC RESONATORS

Calculations of the surface resistance of HTS films based on dielectric resonator methods requires knowledge of geometrical factors, as mentioned earlier in this thesis (equation (3.12)). The determination of geometrical factors of dielectric resonators require knowledge of the EM fields in the resonator which are obtained from the solution to Maxwell's equations applied to the structure. For simple hollow cavities, the fields can be determined easily. But to obtain the field distribution of structures with even slightly more complicated geometry is not trivial, and requires a high degree of skill in analytical mathematics and electromagnetic theory. Consequently, there is a very limited number of feasible structures for R_s measurements. For the sapphire resonators used in this thesis, the Mode Matching method was used to obtain exact equations for the resonant frequencies and field distributions [3]. In general, the Finite Element, Finite Difference, and Rayleigh-Ritz methods can also be used for this purpose. Once the field equations are known,

they can be used to compute the geometry factors. For example, the geometry factor 'A' (such as A_s or A_m) that corresponds to a defined surface of cavity-type of dielectric resonator can be calculated from the magnetic field using :

$$A = \omega_o \frac{\iiint_{V_t} \mu_o |\vec{H}|^2 dv}{\iint_S |\vec{H}_t|^2 ds} \quad (3.25)$$

where \vec{H} is the magnetic field vector; the numerator is a volume integral around the region V_t contained inside cavity; the denominator is an integration of the tangential component of the magnetic field over the defined surface; and ω_o is the radian resonant frequency.

The energy filling factor which is related to the electromagnetic energy stored in the dielectric is defined to be :

$$P_\epsilon = \frac{\iiint_{V_d} \epsilon |\vec{E}|^2 dv}{\iiint_{V_t} \epsilon(v) |\vec{E}|^2 dv} \quad (3.26)$$

where \vec{E} is the electric field vector; the numerator is a volume integral around the volume contained within the dielectric puck; the denominator is a volume integral around the entire region V_t contained within the cavity; ϵ is the permittivity of the dielectric, and $\epsilon(v)$ is a permittivity defined over the internal volume of the cavity.

Dielectric resonators have many resonant frequencies or modes, and each mode has a unique field distribution. The most popular nomenclature classifies field types into three groups, namely TE, TM or Hybrid Modes [3]. Each classification is associated with three numbers p, m, and n. In the example of the TE_{mnp} family of modes, the first number m is the azimuthal mode number, n is the radial mode number and p is the axial mode number which describe variations of the field in the respective directions. For measurements of surface resistance of superconductor films using dielectric resonators, the TE_{0mp} family of modes is used because due to axial symmetry there is no influence of discontinuities in the resonator geometry on the Q-factor. The TE_{011} mode is typically used as it is the dominant TE mode, and can be identified more conveniently than higher modes. Figure 3.14 and Fig. 3.15 illustrate the magnetic and electric field distribution for the TE_{011} mode for a 10 GHz

sapphire dielectric resonator (of Fig. 3.6) used in this thesis. These three dimensional field plots based on the field equations of [5] are presented as normalised field intensity versus the height of the dielectric resonator and the radius of the cavity. In both figures, the dielectric-air interface lies at the radius equal to 6.16 mm. The intensity of the electric field outside the dielectric region decays rapidly with increasing radial distance from the dielectric-air interface. The decrease in the E-field intensity means that the contribution of microwave losses from the lateral (cylindrical) wall of the metal cavity may be negligibly small, so that the losses in the superconductor samples make up a significant part of the total losses in the resonator. This allows high sensitivity in measurements of R_s .

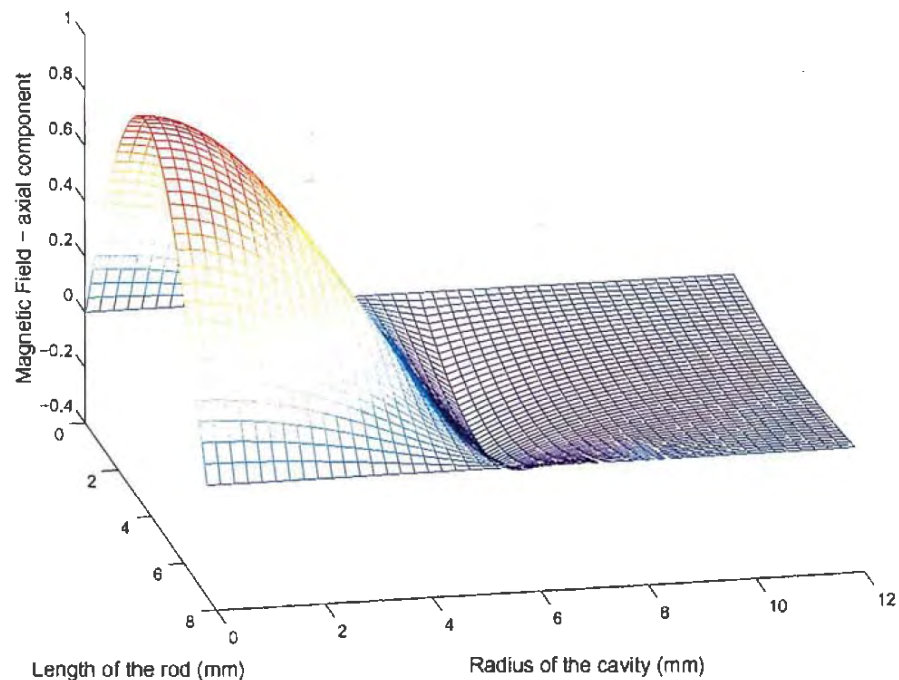


Figure 3.14 Magnetic field distribution (axial Z component) for TE_{011} mode of sapphire resonator with dimensions : Height of the sapphire = 7.41 mm, cavity diameter = 24 mm, sapphire diameter = 12.32 mm, dielectric constant₁ = 9.28, Resonant frequency = 10 GHz [21].

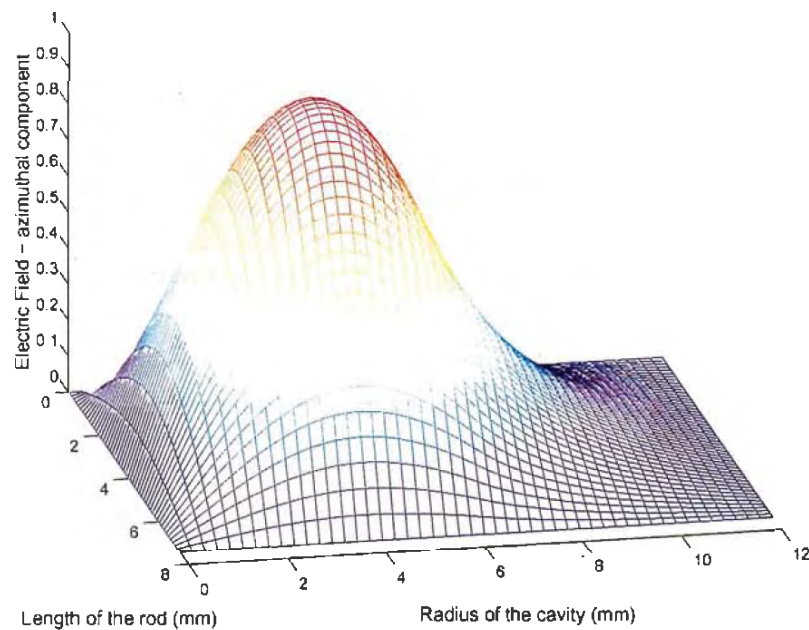


Figure 3.15 Electric field distribution (azimuthal ϕ component) for the TE_{011} mode of sapphire resonator with dimensions : Height of the sapphire = 7.41 mm, cavity diameter = 24 mm, sapphire diameter = 12.32 mm, dielectric constant₁ = 9.28, Resonant frequency = 10 GHz [21].

3.6 DETERMINATION OF THE SURFACE RESISTANCE OF HTS FILMS USING THE SAPPHIRE DIELECTRIC RESONATOR OF THE HAKKI COLEMAN TYPE

As the Hakki-Coleman sapphire dielectric resonator is the resonator of choice for R_s measurements in this thesis, important equations used in the development of the equation used to calculate the R_s of the HTS sample(s) are reviewed based on the general method of loss analysis described earlier in this chapter. The sapphire resonator system of Fig. 3.16 shows a cylindrical cavity with a copper lateral wall, superconducting endwalls (which are the HTS samples), and a sapphire dielectric in the centre of the cavity.

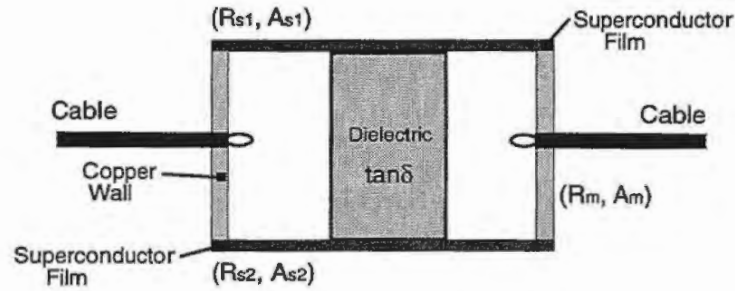


Figure 3.16 Losses in Sapphire DR.

Since the cavity system is closed, there are no radiation losses ($1/Q_r = 0$) [1], so that the total microwave losses P_o in the sapphire resonator are due to conductor and dielectric losses only, which is mathematically described by the loss equation :

$$P_o = P_{s1} + P_{s2} + P_m + P_d \quad (3.27)$$

where P_{s1} and P_{s2} are the losses in the two superconducting endwalls, P_m is the normal conductor loss in the lateral wall which is made out of metal, and P_d is the dielectric loss. Applying the Q-factor definition [1,3] of (3.1) to the above loss equation, the following loss equation in terms of quality factors is obtained as :

$$\frac{1}{Q_o} = \frac{1}{Q_{s1}} + \frac{1}{Q_{s2}} + \frac{1}{Q_m} + \frac{1}{Q_d} \quad (3.28)$$

where Q_o represents the unloaded factor of the resonator; Q_{s1} and Q_{s2} are the quality factors associated with the two superconducting endwalls; Q_m and Q_d are the quality factors associated with the normal conductor losses and the dielectric losses respectively. The loss equation can be developed further to provide an equation for the the total losses in the structure in terms of the parameters related to the geometry and material properties, namely :

$$\frac{1}{Q_o} = \frac{R_{s1}}{A_{s1}} + \frac{R_{s2}}{A_{s2}} + \frac{R_m}{A_m} + p_e \tan\delta \quad (3.29)$$

where R_{s1} and R_{s2} are the surface resistances of the two superconducting endwalls; A_{s1} and A_{s2} are the geometrical factors of each superconducting endwall; A_m is the geometrical factor of the lateral wall made out of copper metal, p_e is the energy

filling factor, and $\tan\delta$ is the dielectric loss tangent. The geometry factors of the two samples are the same, so that :

$$A_{s1} = A_{s2} = A \quad (3.30)$$

Manipulation of the equation (3.29) gives the average surface resistance between the two films as [5] :

$$R_{s(average)} = A_s \left[\frac{I}{Q_o} - \left(\frac{R_m}{A_m} + p_e \tan\delta \right) \right] \quad (3.31)$$

where

$$R_{s(average)} = \frac{(R_{s1} + R_{s2})}{2} \quad (3.32)$$

and A_s is the geometrical factor of the two endwalls combined, defined as :

$$A_s = \frac{A}{2} \quad (3.33)$$

The equation (3.31) is used to calculate the average surface resistance of the two samples provided that the dielectric loss and the surface resistance of the metal (R_m) are known. However, if the surface resistance of one of the films is already known as in the case of one film used as a known reference, then (3.32) can be used to calculate the surface resistance of the other test film. If the surface resistance of both films are unknown, then a third film is required to determine the individual surface resistances. That is, the individual surface resistances of the three films can be determined by knowing the average surface resistances of all paired combinations of films.

For the sapphire resonator, the filling factor p_e is typically close to unity. Using a pure sapphire with loss tangent below $5 \cdot 10^{-8}$ at 77K [5,22], the dielectric loss $p_e \tan\delta$ is negligible compared to the losses in the superconductor sample. For example, for a sapphire resonator operating at 10GHz and 77K with the following parameters : diameter of cavity D_s of 24 mm, diameter of sapphire puck d_s of 12.32 mm, height of the sapphire puck h of 7.41, filling factor p_e of 0.971, and loss tangent of sapphire $\tan\delta$ of 10^{-8} , geometrical factor of the endwalls A_s of 279, geometrical factor of the copper lateral wall A_m of 27616, and surface resistance of

superconducting films $R_s(\text{average})$ of $1 \text{ m}\Omega$, the total loss in the superconductor films is directly related to $Q_s^{-1} = R_{s(\text{average})} / A_s = 1 \text{ m}\Omega / 279$ of $3.58 \cdot 10^{-6}$. Comparison of this value to the losses in the dielectric $p_e \tan \delta$ of $9.71 \cdot 10^{-9}$ demonstrates that the losses in the dielectric are on the order of 400 times smaller than the losses in the superconductor. Hence, in measurements of R_s performed using the above specified parameters, the dielectric losses $p_e \tan \delta$ in the sapphire can be ignored.

According to equation (3.31), the calculation of $R_s(\text{average})$ requires the unloaded Q_o -factor as well as the surface resistance R_m of the metal walls. Hence two separate measurements of Q_o -factor are needed to obtain these values. The first measurement is to find the unloaded Q_o -factor of the resonator with superconductor endwalls. The second measurement is to measure Q_{om} , which represents the unloaded Q -factor of the resonator with metal endwalls so that the surface resistance of the metal wall R_m can be calculated from Q_{om} using a modified form of (3.31), with $R_s(\text{average})$ replaced by R_m , namely as :

$$R_m = \frac{A_s A_m}{A_s + A_m} \left[\frac{1}{Q_{om}} - p_e \tan \delta \right] \quad (3.34)$$

Once the surface resistance R_m is known, it is (in theory) no longer necessary to measure Q_{om} in future measurements of R_s , which is convenient. In practice, the assumption of a R_m being a constant may not always be true because the surface resistance of metals may change with time depending on environmental factors. However, if the resonator is kept in a stable environment, the value R_m should remain constant.

There has been another equation used to calculate the surface resistance R_s of the superconductor sample which does not require the parameter R_m , namely [5] :

$$R_s = A_s Q_o^{-1} - \frac{A_s^2}{A_s + A_m} Q_{om}^{-1} - \frac{P_e \tan \delta}{A_s^{-1} + A_m^{-1}} \quad (3.35)$$

It requires values of the unloaded Q_o -factors of the resonator for the case with superconducting endwalls (Q_o) and copper endwalls (Q_{om}), as well as the

geometrical factors associated with the superconducting walls and the lateral copper wall. However for practical cases, it has been demonstrated [16] that equation (3.35) provides a less accurate value for the surface resistance than (3.31), based on the propagation of errors due to uncertainties in the unloaded Q_0 -factors, geometrical factors, and material constants through the equation.

3.7 ANALYSIS OF ERRORS IN CALCULATIONS OF R_s OF HTS FILMS USING HAKKI COLEMAN RESONATORS DUE TO UNCERTAINTIES IN MEASUREMENT PARAMETERS

Accurate computations of surface resistance R_s of superconducting films rely on accurate knowledge of several parameters of the resonant structure [4,16]. The parameters include the unloaded Q_0 -factor, geometrical factors, microwave losses in the normal conducting parts of the resonator, the dielectric losses and the radiation losses of the resonator. To analyse errors in R_s due to uncertainties in the measured unloaded Q_0 -factor, geometrical factors, loss tangents and other parameters when a sapphire rod resonator is used, the Differential Uncertainty Method has been used. In this method, the most probable relative error in a multivariable function $Z = f(x_1, x_2 \dots x_n)$ is given by :

$$\frac{\Delta z}{z} = \sqrt{\sum_{k=1}^n \left(z'_{x_k} \frac{\Delta x_k}{z} \right)^2} \quad (3.36)$$

where

$$z'_{x_k} = \frac{\partial z}{\partial x_{x_k}} \quad (3.37)$$

For the Hakki-Coleman dielectric resonator, the surface resistance of the HTS films is described in terms of the unloaded Q_0 -factor, geometrical factors, the surface resistance of the lateral copper wall, and dielectric Q_0 -factor as discussed earlier, namely as :

$$R_s = A_s \left(\frac{I}{Q_o} - \frac{R_m}{A_m} - \frac{I}{Q_d} \right) = \frac{A_s}{Q_o} - \frac{A_s R_m}{A_m} - \frac{A_s}{Q_d} \quad (3.38)$$

The Most Probable Relative Error for R_s using the sapphire resonator technique is then obtained as [4,16] :

$$\frac{\Delta R_s}{R_s} = \sqrt{\left(\frac{\Delta A_s}{A_s} \right)^2 + \left(\frac{R_m A_s}{R_s A_m} \left[\left| \frac{\Delta A_m}{A_m} \right| + \left| \frac{\Delta R_m}{R_m} \right| \right] \right)^2 + \left(\frac{\Delta Q_o}{Q_o} \left(1 + \frac{R_m A_s}{R_s A_m} + \frac{A_s}{R_s Q_d} \right) \right)^2 + \left(\frac{\Delta Q_d}{Q_d} \left(\frac{A_s}{R_s Q_d} \right) \right)^2} \quad (3.39)$$

The above equation has been used to investigate the uncertainty in the surface resistance R_s of the sample due to uncertainties in various parameters used in the calculation of R_s . Figure 3.17 shows the most probable relative error in the surface resistance calculated (by the author of this thesis) for the 10 GHz resonator used in the course of this thesis for differing values of R_s and relative error in Q_o -factor. The following parameters and their uncertainties have been assumed in calculations :

Geometrical factor of the lateral copper wall A_m equal to 27616, geometrical factor of superconducting endwalls A_s equal to 279; surface resistance R_m of the lateral wall of the cavity equal to 15 m Ω ; dielectric loss tangent $\tan\delta$ equal to $5 \cdot 10^{-8}$; energy filling factor p_e of 0.971; and the uncertainties $\Delta A_m/A_m$ of 0.5%, $\Delta A_s/A_s$ of 0.5%, $\Delta Q_d/Q_d$ of 1%, $\Delta \tan\delta/\tan\delta$ of 5%. The values given are typical for a 10 GHz sapphire resonator operating at 77K.

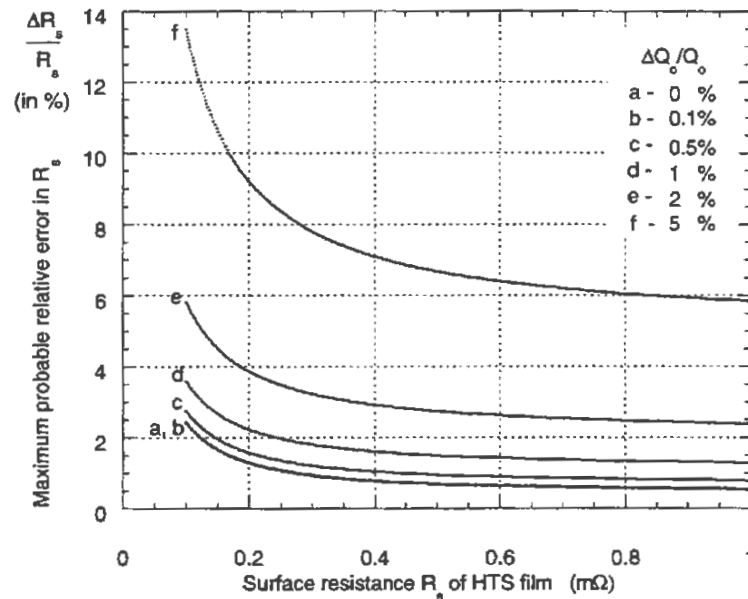


Figure 3.17 The most probable relative error in R_s versus R_s for various values of uncertainty in unloaded Q_0 -factor $\Delta Q_0/Q_0$ for a 10 GHz sapphire resonator with assumed uncertainties $\Delta A/A = 0.5\%$, $\Delta Q_d/Q_d$ of 1%, $\Delta \tan \delta / \tan \delta = 5\%$; and assumed values $A_m = 27616$, $A_s = 279$, $R_m = 15 \text{ m}\Omega$, $\tan \delta = 5 \cdot 10^{-8}$, $p_e = 0.971$.

3.8 UNLOADED Q_0 -FACTOR MEASUREMENT TECHNIQUES

In procedures used to determine the unloaded Q_0 -factor of microwave resonators, the resonator is connected to a microwave source [6]. Appropriate measurements are made according to a chosen type of system response behaviour, which are processed to evaluate the characteristic parameters of the resonance, namely the loaded Q_L -factor, the resonant frequency and the coupling coefficient(s). For resonators working in the reflection mode, there is only one coupling coefficient β , and the unloaded Q_0 -factor is calculated using [6]:

$$Q_0 = Q_L(1 + \beta) \quad (3.40)$$

Transmission resonators have two coupling coefficients, and the unloaded quality factor is calculated using [6]:

$$Q_0 = Q_L(1 + \beta_1 + \beta_2) \quad (3.41)$$

where β_1 and β_2 are the port coupling coefficients.

It is clearly seen from the above two equations that the determination of the unloaded Q_o -factor involves the determination of the coupling coefficient(s) and the loaded Q_L -factor, unless the coupling is very weak where the coupling coefficient(s) are much less than unity. Using a weak coupling also usually means the measurements of signals with low signal to noise ratio which can significantly contribute to uncertainties in measurements. Hence, it is desirable to use sufficiently high levels of coupling to achieve a good signal to noise ratio. In that case, it is necessary to determine the loaded Q_L -factor and the coupling coefficients so that equations (3.40) or (3.41) (depending on the type of resonator used) can be used to calculate the unloaded Q_o -factor.

In the following review of methods used to determine the unloaded Q_o -factor of resonators, it is important to understand that all Q_o -factor techniques are developed from ideal models of resonator systems and inadequacies in the modelling of the real systems and inadequacies in calibration techniques used for real measurement systems results in discrepancies between the ideal behaviour of the system and the observed (measured) behaviour of the real system. These discrepancies lead to uncertainty in the Q_o -factor obtained from Q_o -factor techniques. Hence the accuracy of any Q_o -factor technique relies on its ability to account for discrepancies between the ideal system and the real resonator system. While there are a variety of methods used to determine the unloaded Q_o -factor of microwave resonators, not all of them take into account practical effects introduced by a real measurement system so that some techniques are more accurate than others. Hence in the following review of methods used to obtain Q_o -factor of resonators, some remarks will be made about the deficiencies of particular methods used.

Methods used to obtain the unloaded Q_o -factor of resonators can be based on measurements of various types of system response, and can be divided into two groups, namely the time domain methods and frequency domain methods as shown in Fig. 3.18.

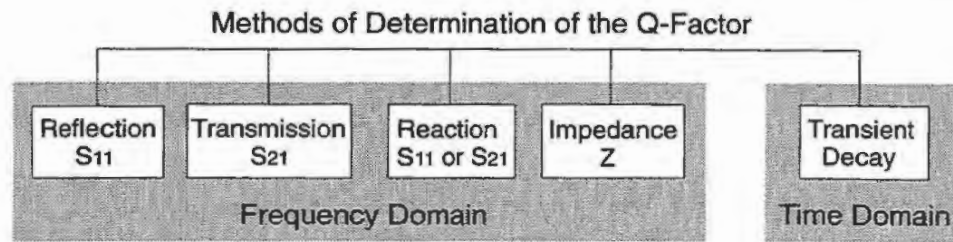


Figure 3.18 Two groups of methods used in determination of the unloaded Q_0 -factor of microwave resonators with typical modes and names of measurements indicated.

3.8.1 TIME DOMAIN TECHNIQUES FOR MEASUREMENTS OF UNLOADED Q_0 -FACTOR

In the time domain techniques, which include the Transient Decay method (or the Decrement method) [6], the unloaded Q_0 -factor is determined from the analysis of the power charge and discharge curves of the resonator (typically a cavity type resonator) after a momentary excitation by a pulse of energy from a microwave source. The loaded Q_L -factor and coupling coefficient(s) (and hence the Q_0 -factor) are determined from special points on the power response curves. A typical time-domain measurement system consists of a synthesised microwave source, couplers and power measurement devices as shown in Figure 3.19 for measurements of the unloaded Q_0 -factor of a transmission mode resonator.

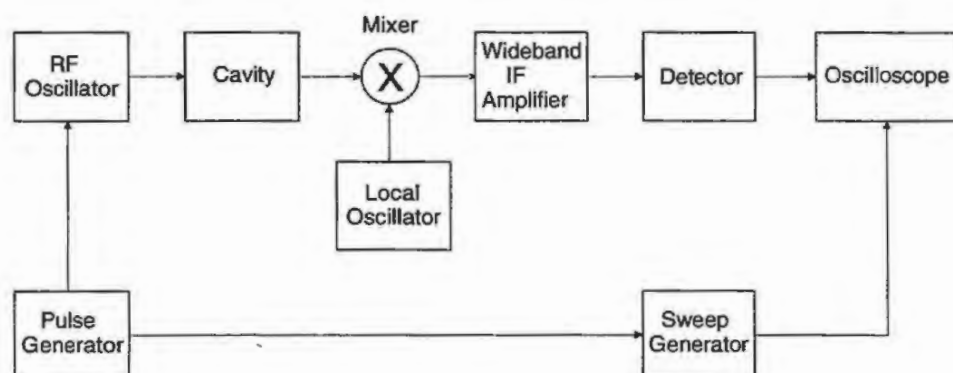


Figure 3.19 Time domain Q-Factor measurement system [6].

The time constant of the decay response typically provides the loaded Q_L -factor as [6]:

$$Q_L = \pi f_o \tau \quad (3.42)$$

where f_o is the frequency of the decaying microwave signal, and τ is the time constant which can be defined as the time taken for the measured relative voltage to decay to a factor of $1/e$ of some initial reference value. To obtain the unloaded Q_o -factor, the simplest approach is to decrease the coupling gradually until the loaded Q_L -factor reaches a maximum value. At that point, the unloaded Q_o -factor can be approximated by the loaded value under the assumption of very weak coupling.

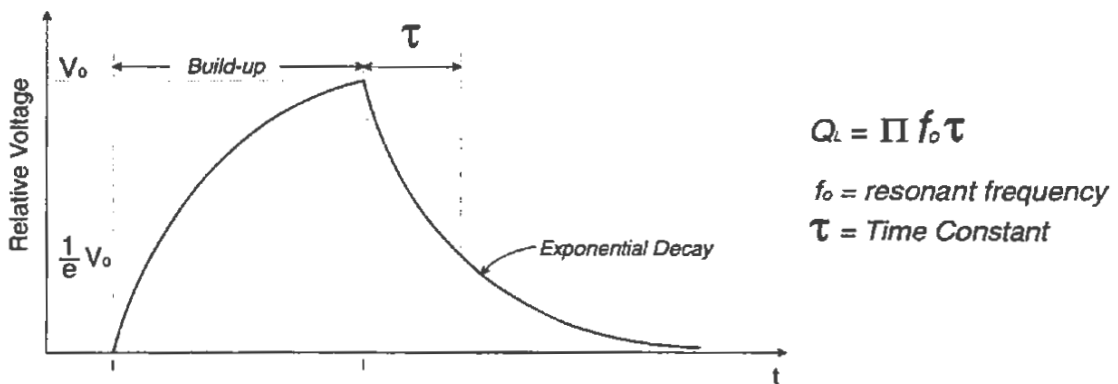


Figure 3.20 Time domain determination of Q factor [6].

If non-negligible couplings are used instead, then the coupling coefficients need to be determined, which requires measurements of the transmitted power as well as the reflected power. A typical approach to obtain the coupling coefficients is to excite the transmission mode cavity (which is initially uncharged) with a pulse of microwave power and then make simultaneous measurements of the reflected power and the transmitted power to obtain the respective power curves illustrated in Fig. 3.21 and Fig. 3.22 [23].

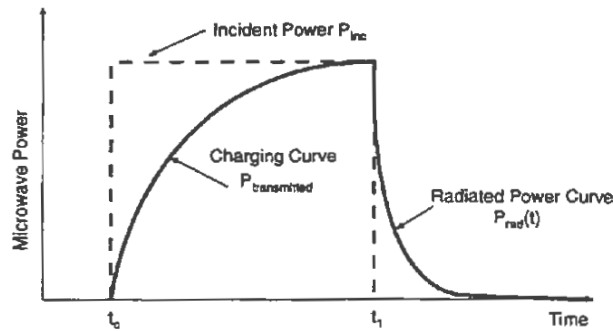


Figure 3.21 Power curves measured at the output side, needed to obtain the radiated power $P_{\text{rad}}(t_1)$ to be used in the calculation of the coupling coefficient on the output side of transmission mode cavity resonator [23].

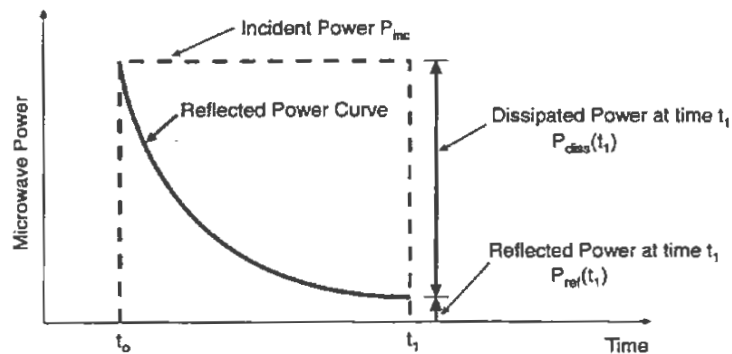


Figure 3.22 Reflected power curve measured from the input side, needed to obtain the reflected power $P_{\text{ref}}(t_1)$ to be used in the calculation of the coupling coefficient on the output side of transmission mode cavity resonator [23].

From the transmitted and reflected power curves of Fig. 3.21 and Fig. 3.22, it is possible to obtain the dissipated power in the cavity and the radiated power at the time t_1 where the incident pulse (observed at the cavity input) ends, which are needed to calculate the coupling coefficient at the output side (port 2 side). For example, at time t_1 , the dissipated power $P_{\text{diss}}(t_1)$ is equal to the difference between the incident power P_{inc} and the reflected power $P_{\text{ref}}(t_1)$. The radiated power $P_{\text{rad}}(t_1)$ is simply equal to the transmitted power. Using the radiated and dissipated powers, the coupling coefficient at port 2 is then calculated according to [23]:

$$\beta_2 = \frac{P_{rad}(t_1)}{P_{diss}(t_1)} \quad (3.43)$$

The procedure to obtain the coupling coefficient β_1 for port 1 is exactly the same as described above, except that the roles of ports 1 and 2 are interchanged so that port 2 becomes the input port.

Time domain techniques can be used when the loaded Q_L -factor is of a sufficiently high value so that the time constant is large enough to measure accurately. Accurate measurements of the time constant can be difficult in the presence of noise. Hence, sufficiently high source power and good power detector sensitivity need to be used. The time domain techniques described above are based on the assumption of lossless coupling between the microwave source and the inputs of the resonator. As far as is known, no specialised methods have been developed to take coupling losses into consideration, which is essential for accurate measurements of the unloaded Q_0 -factor. Coupling losses and their influence on unloaded Q_0 -factor measurements will be discussed later in this chapter.

3.8.2 FREQUENCY DOMAIN TECHNIQUES FOR MEASUREMENTS OF UNLOADED Q_0 -FACTOR

In frequency domain methods, the unloaded Q_0 -factor is determined by analysing frequency response measurements obtained over a narrow range of frequencies about resonance. Frequency domain methods can be based on measurements of impedance [6, 24], power [6,25,26,27], VSWR [6], and S-parameters [1,8,28,29,30,35]. With the benefits of modern microwave measurement technology, microwave measurements can now be done much more conveniently and accurately than earlier systems which required tedious procedures for the calibration. At present, modern vector network analysers are standard instruments in microwave measurement laboratories. They can be used to measure S-parameters of microwave resonators very accurately and conveniently. Hence network analysers are typically used for measurements of Q_0 -factors of microwave resonators. The

definition of S-parameters for a two port network device under test (DUT) of Fig. 3.23 is given below by (3.44).

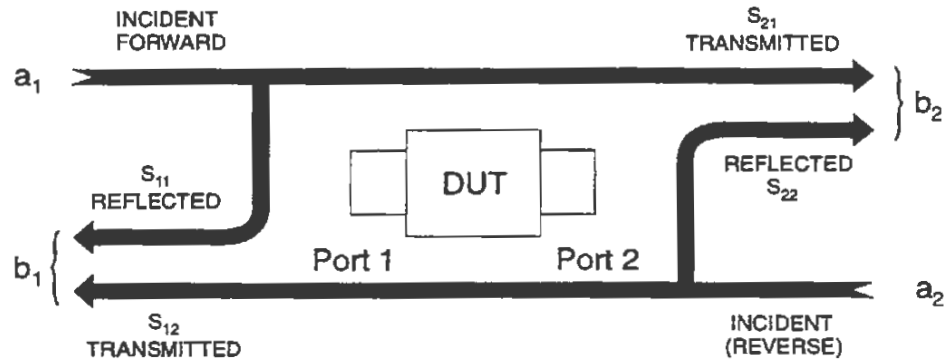


Figure 3.23 Microwave signals entering and leaving ports for 2-Port microwave resonator [31].

For the 2-port device, microwave signals can be fed into the system from either port 1 side or port 2 side. When the microwaves reach the input of the DUT, some of the energy in the signal can be reflected back towards the signal source, and some of it can be transmitted through to the port on the other side. If the microwave signals are considered to be complex quantities with a magnitude and phase, then the S-parameters of the two-port system are defined using the following signal ratio's [32] :

$$\begin{aligned} S_{11} &= \left. \frac{b_1}{a_1} \right|_{a_2=0} & S_{21} &= \left. \frac{b_2}{a_1} \right|_{a_2=0} \\ S_{12} &= \left. \frac{b_1}{a_2} \right|_{a_1=0} & S_{22} &= \left. \frac{b_2}{a_2} \right|_{a_1=0} \end{aligned} \quad (3.44)$$

where the signals a_1 , a_2 , b_1 , and b_2 are complex quantities, which represent the magnitude and phase of microwave signals. Figure 3.24 shows directions of signal power flow for S-parameter measurements performed on a microwave resonator system working in the transmission mode with the ends of the system terminated with non-reflective (matched) loads [32].

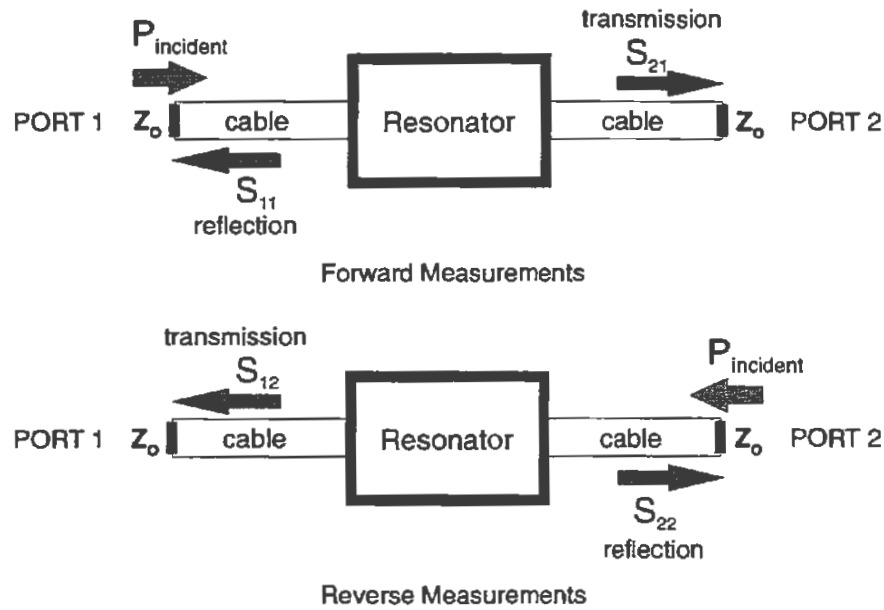


Figure 3.24 Illustration of measurements of S-parameters on a Two Port microwave resonator.

As was mentioned before, the majority of techniques used to determine the unloaded Q_o -factors of microwave resonators are based on S-parameter measurements. The simplest way to obtain the unloaded Q_o -factor using any technique (either time domain or frequency domain) is to obtain the loaded Q_L -factor under a weak coupling condition so that [6] :

$$Q_o \approx Q_L \Big|_{\beta_1 = \beta_2 = 0} \quad (3.45)$$

The simplest way to obtain the loaded Q_L -factor from measurements of S-parameters is to use the well known Three Frequency Method, also known as the Three dB Method. The Three Frequency method involves locating three points which best represent the resonant point and the two half-power points from a data set corresponding to the S_{21} magnitude trace measured around the resonance as illustrated in Fig. 3.25. The loaded Q_L -factor is then calculated according to [3,6] :

$$Q_L = \frac{f_{res}}{f_2 - f_1} \quad (3.46)$$

where f_{res} is the resonant frequency and the f_1 and f_2 are the lower and upper half power frequencies respectively.

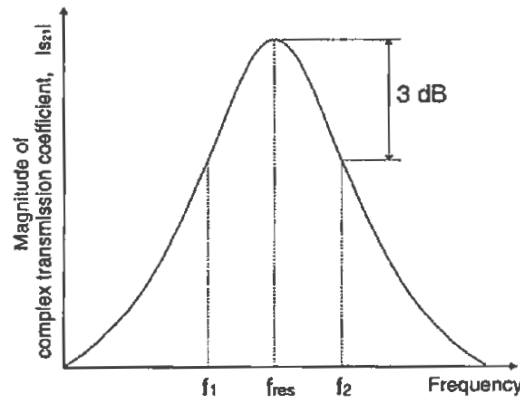


Figure 3.25 Three Frequency Method used to obtain the loaded Q_L -factor from the S_{21} transmission (magnitude) response.

Another simple method used to obtain the unloaded Q_0 -factor of transmission mode resonators applies to the case of equal couplings. For such case, the unloaded Q_0 -factor can be calculated using the following equation [33,34] :

$$Q_0 = \frac{Q_L}{1 - |S_{21}|} \Big|_{\beta_1 = \beta_2} \quad (3.47)$$

Only the loaded Q_L -factor (which may be obtained using the Three Frequency method as described before) and the magnitude of S_{21} at the resonant frequency are required. While equation (3.47) is widely used due the simplicity in its application to S_{21} measurements, there are no detailed procedures described in literature to establish equal couplings in the presence of practical effects introduced by a real measurement environment such as coupling loss and coupling reactance. It is important to have equal couplings on the input and output ports in order to calculate the unloaded Q_0 -factor accurately using (3.47) [34]. The error in the unloaded Q_0 -factor calculated using (3.47) can also be influenced significantly by inaccuracies in the measurement of the magnitude of S_{21} at the resonant frequency [34].

In practical measurements of S-parameter traces, the presence of noise and the finite resolution of a S-parameter measurement device results in a noisy S_{21} trace, which makes it difficult to determine the resonant and half power frequencies accurately as illustrated in Fig. 3.26 and Fig. 3.27. Therefore, the Three Frequency Method can be inaccurate if errors in the measurement of the transmission S-parameters are not taken into account [34].

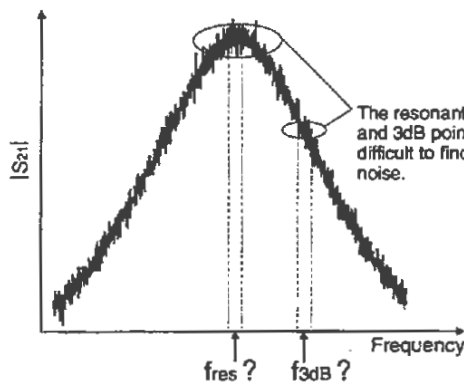


Figure 3.26 A noisy trace introduces uncertainty in the selected resonant frequency and half power frequencies used in the Three Frequency Method to calculate the loaded Q_L -factor.

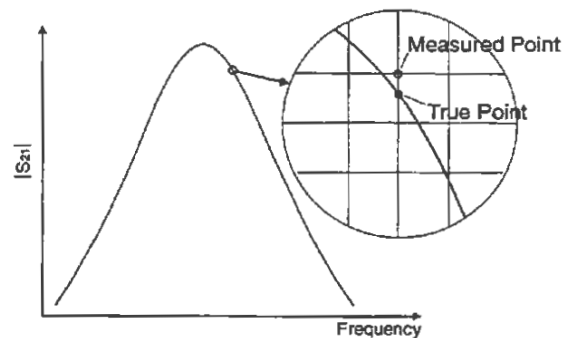


Figure 3.27 The finite resolution of measurement instrument introduces measurement uncertainty, which contributes to uncertainties in the determination of the loaded Q_L -factor using Three Frequency Method.

To eliminate uncertainties in the determination of the resonant frequency and half power frequencies due to a noisy S-parameter trace, multi-frequency measurements need to be used. Multi-frequency measurements require numerical curve fitting procedures to be developed in order to obtain the necessary parameters, namely the loaded Q_L -factor and coupling coefficient(s).

For resonators working in the reflection mode, there are expressions on which multi-frequency techniques to determine the loaded Q_L -factor and the coupling coefficient (hence Q_0) can be based. These expressions describe the frequency dependence of the reflection coefficient S_{11} around the resonance using the following functional forms [26]:

$$|S_{11}(f)|^2 = 1 - \frac{1 - |S_{11res}|^2}{1 + 4Q_L^2((f_o - f)/f_o)^2} \quad |S_{11res}|^2 = 1 - \frac{4\beta}{(1 + \beta)^2} \quad (3.48)$$

$$S_{11} = -1 + \frac{1 + S_{11res}}{1 - j2Q_L(f_o - f)/f_o} \quad S_{11res} = -1 + \frac{2\beta}{1 + \beta} \quad (3.49)$$

There are multi-frequency techniques developed for reflection mode resonators which operate on S_{11} magnitude data sets only [29]; and on complex (magnitude and phase) data sets [1,35]. For reflection mode resonators, both the loaded Q_L -factor and the coupling coefficient (hence the unloaded Q_o -factor) can be obtained from the S_{11} trace (either magnitude or complex form). The most accurate reflection mode technique used for practical Q_o -factor measurements of reflection mode resonators, namely the Kajfez method [1], will be described in Chapter 3.9.

For the resonators working in the transmission mode, there are expressions for the frequency dependencies of S_{11} , S_{22} and S_{21} in the magnitude and complex forms on the basis of which multi-frequency techniques for transmission resonators can be develop, namely [26]:

$$|S_{11}(f)|^2 = 1 - \frac{1 - |S_{11res}|^2}{1 + 4Q_L^2((f_o - f)/f_o)^2} \quad |S_{11res}|^2 = 1 - \frac{4\beta_1(1 + \beta_2)}{(1 + \beta_1 + \beta_2)^2} \quad (3.50)$$

$$|S_{22}(f)|^2 = 1 - \frac{1 - |S_{22res}|^2}{1 + 4Q_L^2((f_o - f)/f_o)^2} \quad |S_{22res}|^2 = 1 - \frac{4\beta_2(1 + \beta_1)}{(1 + \beta_1 + \beta_2)^2} \quad (3.51)$$

$$|S_{21}(f)|^2 = 1 - \frac{|S_{21res}|^2}{1 + 4Q_L^2((f_o - f)/f_o)^2} \quad |S_{21res}|^2 = \frac{4\beta_1(1 + \beta_2)}{(1 + \beta_1 + \beta_2)^2} \quad (3.52)$$

$$S_{11}(f) = -1 + \frac{1 + S_{11res}}{1 - j2Q_L(f_o - f)/f_o} \quad S_{11res} = -1 + \frac{2\beta_1}{1 + \beta_1 + \beta_2} \quad (3.53)$$

$$S_{21}(f) = \frac{S_{21res}}{1 - j2Q_L(f_o - f)/f_o} \quad S_{21res} = \frac{2\sqrt{\beta_1}\sqrt{\beta_2}}{1 + \beta_1 + \beta_2} \quad (3.54)$$

where S_{21res} , S_{11res} and S_{22res} represent the value of the S-parameter at the resonant frequency. The magnitude of the reflection coefficient $|S_{11res}|$ (or $|S_{22res}|$) at the resonant frequency is equal to the minimum value on the resonance curve $|S_{11}(f)|$ (or

$|S_{22}(f)|$), while the magnitude of the transmission coefficient $|S_{21res}|$ at the resonant frequency is equal to the maximum value on the resonance curve $|S_{21}(f)|$.

There are multi-frequency techniques developed for transmission mode resonators which operate on magnitude ($|S_{21}|$ or $|S_{11}|$ or $|S_{22}|$) data sets [27], or on complex (magnitude and phase of S_{21} or S_{11} or S_{22}) data sets [26,35]. For a transmission mode resonator, the loaded Q_L -factor can be obtained from either a transmission (S_{21}) response alone, or from the reflection (S_{11} or S_{22}) response alone. To obtain coupling coefficients for transmission mode resonators, measurements of at least two of the three parameters (such as S_{21} and S_{11} traces; or S_{11} and S_{22} traces) are required. When S_{11} and S_{22} trace data are available, the following equations can be used to calculate the coupling coefficients [36] :

$$\beta_1 = \frac{1 - |S_{11}|}{|S_{11}| + |S_{22}|} \quad \beta_2 = \frac{1 - |S_{22}|}{|S_{11}| + |S_{22}|} \quad (3.55)$$

where $|S_{11}|$ and $|S_{22}|$ represent the magnitudes of the reflection coefficients at the resonant frequency measured at port 1 and port 2 respectively. When S_{21} and S_{11} trace data are available, the coupling coefficients (obtained by mathematical manipulations of (3.50), (3.52), (3.55)) are calculated as :

$$\beta_1 = \frac{(1 - |S_{11}|)^2}{1 - |S_{11}|^2 - |S_{21}|^2} \quad \beta_2 = \frac{|S_{21}|^2}{1 - |S_{11}|^2 - |S_{21}|^2} \quad (3.56)$$

where $|S_{11}|$ and $|S_{22}|$ are as previously described, and $|S_{21}|$ is the magnitude of the transmission coefficient at the resonant frequency.

For dielectric resonators coupled to a microstripline, the Reaction Method [3,30] has been used to obtain the unloaded Q_0 -Factor.

The S-parameter techniques to determine the unloaded Q_0 -factors of microwave resonators so far reviewed are based on the assumption that the coupling network is lossless with the exception of [1], [24], [35] which include the case of a lossy coupling. A lossless coupling means that no power is dissipated in the coupling circuit. However for a practical case, the coupling is always lossy. The response behaviour of a resonator with lossy coupling is not the same as with lossless

coupling. Hence application of S-parameter techniques developed for the case of lossless coupling to measurements involving coupling losses results in inaccuracies in the determination of the unloaded Q_0 -factor. So far, there has been only two multi-frequency practical techniques ([1] and [24]) which take coupling losses into consideration. There are also other practical effects introduced by the real measurement environment apart from noise and coupling losses which need to be accounted for by a Q_0 -factor measurement technique. Such effects include impedance mismatch, frequency dependence of components in the coupling network (which include electrical delay effects) [1,8], and crosstalk effects (associated with transmission mode resonators) [8].

Crosstalk effects in transmission mode resonators manifests itself in the non-symmetrical magnitude response of the S_{21} curve as illustrated in Fig. 3.28 [8]. The distorted transmission curve caused by the presence of crosstalk makes it difficult to locate the resonance and half-power points in the magnitude method based on the Three Frequency method [3,6].

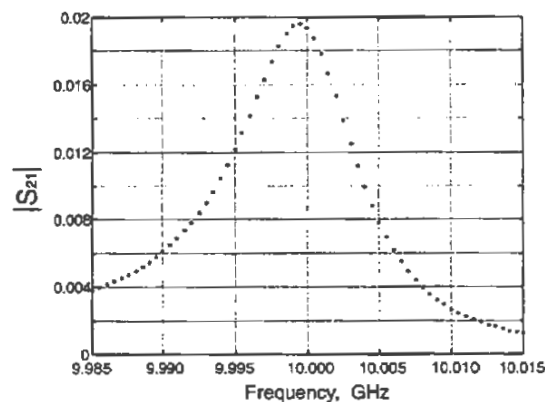


Figure 3.28 Distortion in S_{21} trace due to crosstalk [8].

Unlike the S_{21} magnitude curve which becomes distorted by crosstalk effects, and unlike the S_{11} or S_{22} magnitude curves which become distorted due to the presence of coupling reactance and impedance mismatch, a resonance is well preserved within S-parameter Q-circles [1,6].

3.9 CIRCLE FITTING PROCEDURES USED TO OBTAIN THE UNLOADED Q_0 -FACTORS OF MICROWAVE RESONATORS FROM MEASUREMENTS OF S-PARAMETERS

The most accurate multi-frequency S-parameter techniques to obtain the loaded Q_L -factors and/or coupling coefficients of microwave resonators are based on fitting a curve to measured Q-circles [1,8]. There have been two practical techniques developed so far : the S_{21} (phase) technique for transmission mode resonators [8], and the S_{11} technique for reflection mode resonators developed by Kajfez [1,28] as described below in Chapters 3.91 and 3.92.

3.9.1 S_{21} PHASE TECHNIQUE OF LOADED Q_L -FACTOR MEASUREMENTS

A practical multi-frequency technique based on phase has been developed at Hewlett Packard and Stanford University [8]. The loaded Q_L -factor is determined from the phase of S_{21} around the resonance and is based on a series RLC model of a transmission mode resonator of Fig. 3.29.

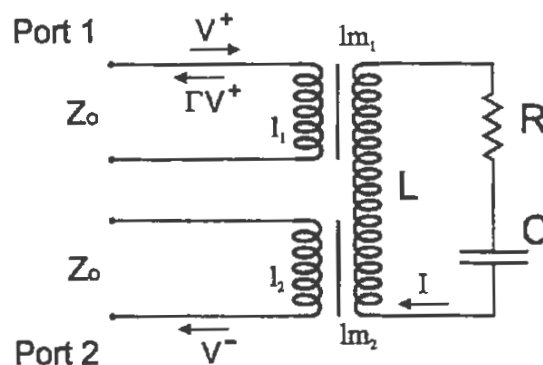


Figure 3.29 A series RLC circuit of a microwave resonator [8].

The equations relating the complex transmission coefficient (S_{21}) and the current (I) of the resonator are given in [8] as :

$$S_{21} = \frac{V^-}{V^+} = \frac{2\omega^2 l_{m1} l_{m2} Z_o / (Z_o + j\omega l_1)(Z_o + j\omega l_2)}{R + j\left(\omega L - \frac{I}{\omega C}\right) + \omega^2 \left(\frac{l_{m1}^2}{Z_o + j\omega l_1} + \frac{l_{m2}^2}{Z_o + j\omega l_2}\right)} \quad (3.57)$$

$$I = \frac{Z_o + j\omega l_2}{\omega l_{m2} Z_o} V^+ S_{21} \quad (3.58)$$

The above equation is simplified when the coupling to the external circuit is weak, in which case the terms in the denominator of (3.57) with mutual inductances are ignored. Also, the terms ωL_1 and ωL_2 are considered small compared to Z_o and can be ignored. The simplified equation for the frequency dependence of S_{21} around the resonance is given as [8] :

$$S_{21}(\omega) = \frac{\omega^2 l_{m1} l_{m2} / Z_o L}{\frac{R}{2L} + j(\omega - \omega_o)} \quad (3.59)$$

$$I = \frac{V^+ S_{21}}{\omega l_{m2}} \quad (3.60)$$

ω_o is the unloaded resonant angular frequency,

$$\omega_o = \frac{1}{\sqrt{LC}} \quad (3.61)$$

and the loaded Q-factor is

$$Q_L = \frac{\omega_o L}{R} \quad (3.62)$$

The peak magnitude of the transmission coefficient occurring at resonance is equal to :

$$|S_{21}| = \frac{2\omega_o^2 l_{m1} l_{m2}}{Z_o R} \quad (3.63)$$

The loaded resonant frequency ω_L occurs when the imaginary part of S_{21} is zero. The loaded resonant frequency mainly depends on the L and C elements but also depends on the frequency dependent term

$$\omega^2 \left(\frac{L_{m1}^2}{Z_o + j\omega L_1} + \frac{L_{m2}^2}{Z_o + j\omega L_2} \right) \quad (3.64)$$

from equation (3.57). The resistive losses in the resonant system are also influenced by (3.64) in that it's real part adds to the resistance R of the system, which is an effect of loading. The effect of (3.64) on the resonant frequency has been assumed to be constant when the coupling is held constant [8].

The equations (3.57) and (3.59) which describe the frequency dependence of S_{21} are ideal ones and do not account for the practical non-idealities which exist a real measurement system such as coupling losses. The technique [8] however accounts for crosstalk between the coupling loops of a microwave resonator and influence of transmission lines connected between the test ports of the network analyser and the resonator. For a case with no crosstalk present in the system, a S_{21} circle is centred on the real axis and passes through the origin as shown in Fig. 3.30 [8].

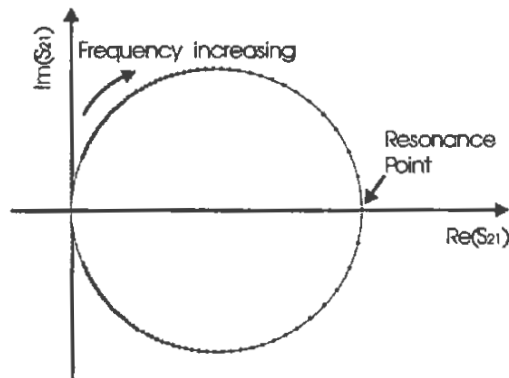


Figure 3.30 Ideal S_{21} Q-circle [8].

The resonance peak lies on the positive real axis with a magnitude given by (3.63). Transmission lines connected between the resonator and the measurement system cause phase change in the microwave signals which is observed as a rotation of all

the points about the origin on the Q-circle (Fig. 3.31). When crosstalk exists between the coupling loops, an extra complex term is added to the transmission coefficient, resulting in a displacement of the circle (Fig. 3.32) [8].

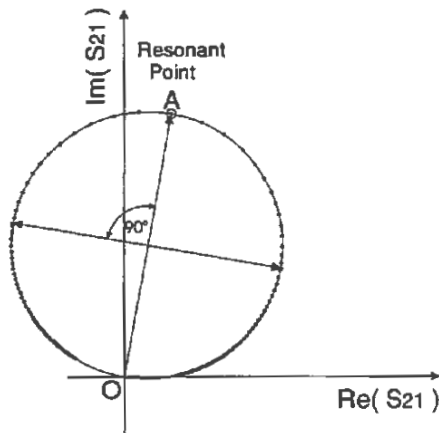


Figure 3.31 Q-circle which has undergone a rotation around the origin due to cable phase shift.

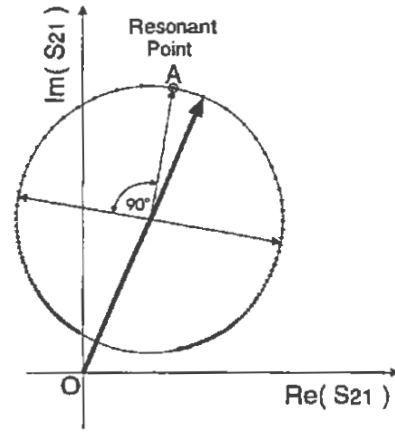


Figure 3.32 Q-circle which has undergone a rotation around the origin due to cable phase shift, followed by a translation due to crosstalk effects [8].

When a translation is performed on the original S_{21} circle so that the centre of the new circle becomes located at the origin of the cartesian coordinate system as shown in Fig. 3.33.

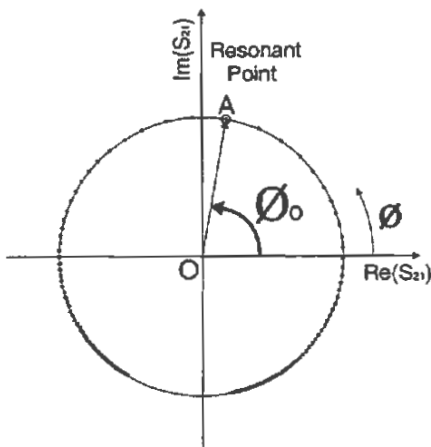


Figure 3.33 S_{21} Q-circle with centre at the origin. The phase-frequency dependence of the S_{21} vector is given by (3.65) to the phase data [8].

The phase of the S_{21} Q-circle of Fig. 3.33 has the functional form described as [8] :

$$\phi = 2 \arctan \left(\frac{f - f_o}{f_o} 2Q_L \right) + \phi_o \quad (3.65)$$

A non-linear curving technique has been used to fit (3.65) to S_{21} Q-circle data to obtain the resonant frequency f_o , loaded quality factor Q_L and the phase ϕ_o at the resonance [8]. Unfortunately, the method of [8] has been developed to process S_{21} measurements only to obtain the loaded Q_L -factor. As far as is known, there has not been any similar method developed to process reflection coefficient data (S_{11} and S_{22}) to obtain the coupling coefficients. Hence the method is useful in measurements of unloaded Q_o -factor for the case of very weak coupling, where the unloaded Q_o -factor is approximated by the loaded Q_L -factor as described by (3.45).

3.9.2 THE S_{11} TECHNIQUE OF LOADED Q_L -FACTOR AND COUPLING COEFFICIENT MEASUREMENTS

The Kajfez technique [1,28] of circle-fitting to obtain the loaded Q_L -factor and coupling coefficient is based on measurements of S_{11} and is applicable to reflection mode resonators. There are two variants of the Kajfez technique. The first one applies to the case of resonators with lossless coupling, and the second applies to resonators with lossy coupling. The methods do not account for the effects of long cables connected to the resonator, or impedance mismatch between test ports of the measurement instrument and connecting cables. However, the influence of line length on S_{11} Q-circles has been investigated [1] and it has been found that significant distortion can exist in the reflection Q-circle when the line length is much greater than the operating wavelength. In measurements systems used to measure the surface resistance of HTS films, the line lengths can be more than 20 times the operating wavelength depending on the system, and the distortion in the Q-circle caused the delay effects of transmission lines can significantly influence the accuracy of a circle fitting technique [1].

The equations used in the development of the Kajfez circle-fitting procedure are based on the parallel RLC equivalent circuit shown in Figure 3.34.

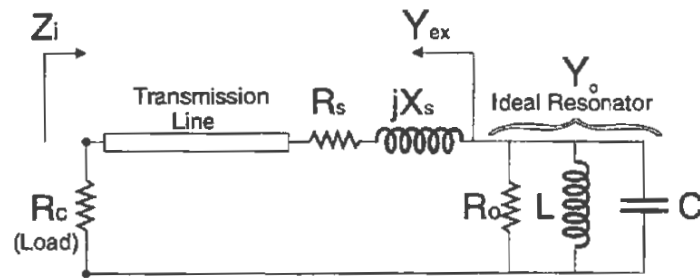


Figure 3.34 Equivalent circuit of the dielectric resonator in the reflection mode [1].

The circuit elements R_s and X_s are used to model the coupling loss and coupling reactance respectively. Y_o is the admittance of the ideal resonator with parallel R_o - L - C circuit elements to model the ideal resonant frequency and microwave losses in the ideal resonator. Y_{ex} is the external admittance looking out from the ideal resonator, Z_i is the input impedance, and R_c is the load or internal resistance of a microwave source typically matched to the characteristic impedance of the transmission line which connects the microwave source to the resonator port. When the coupling losses and the influence of the delay effect of transmission lines are ignored, the reflection coefficient for this circuit is expressed as [1] :

$$\Gamma_i = \Gamma_d \left(1 - \frac{2\beta}{1+\beta} \frac{1}{1 + jQ_L 2 \frac{\omega - \omega_L}{\omega_o}} \right) \quad (3.66)$$

where Γ_d is the detuned value of reflection coefficient (when frequency is far away from the resonant frequency), β is the coupling coefficient, Q_L is the loaded Q-factor. Also, ω_L and ω_o are the loaded and unloaded resonant frequencies respectively. The equation (3.66) also was presented as :

$$\Gamma_i = \frac{j\Gamma_d 2Q_L \frac{\omega - \omega_L}{\omega_o} + \Gamma_d(1-d)}{j2Q_L \frac{\omega - \omega_L}{\omega_o} + 1} \quad (3.67)$$

When the imaginary part of complex reflection coefficient in (3.67) is plotted against real part over frequencies close to the resonant frequency (3.35), the locus traces out a circle which passes through the point ($\Gamma = -1$) and with centre on the real axis. The

detuned value of reflection coefficient Γ_d lies at the point ($\Gamma = -1$) and the point Γ_{res} at the resonant frequency lies on the real axis diametrically opposite the detuned value.

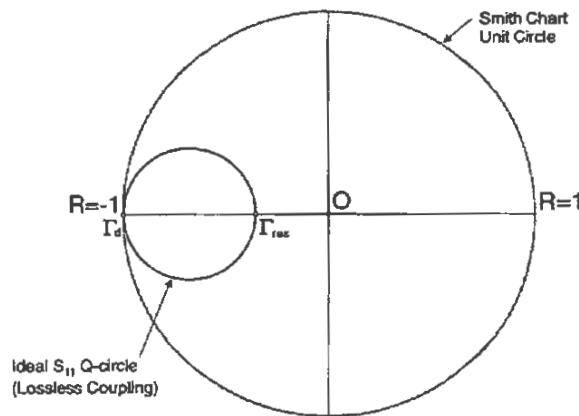


Figure 3.35 Position of a S_{11} Q-circle for a case of lossless coupling, zero coupling reactance, and no delay due to transmission lines.

The equation (3.67) is of a fractional linear form (or bilinear form) given by :

$$\Gamma_i = \frac{a_1 t + a_2}{a_3 t + 1} \quad (3.68)$$

where

$$a_1 = jQ_L \Gamma_d \quad a_2 = \Gamma_d (1-d) \quad a_3 = jQ_L \quad (3.69)$$

and t is a normalised frequency variable defined as [1]:

$$t = 2 \left(\frac{\omega - \omega_L}{\omega_L} \right) \quad (3.70)$$

The coefficients a_1, a_2 , and a_3 may be determined by using a linear fractional curve fitting technique to fit the function of (3.68) to a set of reflection coefficient data measured around the resonance [1]. By observing the function described by (3.68), significant points on the Q-circle can be determined. For frequencies far from the resonance (when $t \gg 1$) the detuned reflection coefficient is :

$$\Gamma_d = \frac{a_1}{a_3} \quad (3.71)$$

and at the loaded resonant frequency when $t=0$, the resonance value is :

$$\Gamma_L = a_2 \quad (3.72)$$

The centre of the Q-circle is :

$$\Gamma_c = \frac{a_3^* a_2 - a_1}{a_3^* - a_3} \quad (3.73)$$

Using the results of the fitting, the loaded Q_L -factor is simply the imaginary part of the complex constant a_3 described as :

$$Q_L = \text{imag}(a_3) \quad (3.74)$$

and the coupling coefficient is determined from the diameter, d of the Q-circle as :

$$\beta = \frac{l}{\frac{2}{d} - l} \quad (3.75)$$

where diameter d is determined from the coefficients as :

$$d = \left| a_2 - \frac{a_1}{a_3} \right| \quad (3.76)$$

The unloaded Q factor is then calculated using (3.40) as :

$$Q_o = Q_L(1 + \beta) \quad (3.77)$$

For the case of a lossy coupling (modelled by the resistance R_o of Fig. 3.34), Kajfez uses the modified circuit of Fig. 3.36 to account for the coupling losses.

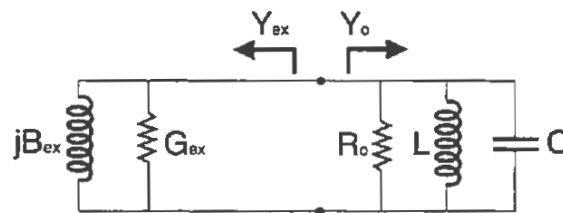


Figure 3.36 Equivalent circuit to model lossy coupling [1].

The external circuit is modelled by the shunt elements G_{ex} and B_{ex} which are the external conductance and external susceptance respectively. Using the circuit model of Fig. 3.36, the frequency dependence of the reflection coefficient for the case of a lossy coupling is [1] :

$$\Gamma_i = \frac{\Gamma_d + de^{j\gamma} + j2Q_L\Gamma_d\left(\frac{\omega - \omega_L}{\omega_o}\right)}{1 + jQ_L2\left(\frac{\omega - \omega_L}{\omega_o}\right)} \quad (3.78)$$

where d is the diameter of the Q-circle :

$$d = \frac{2\beta}{1 + \beta} \quad (3.79)$$

and the constant γ is given as :

$$\gamma = 2 \tan^{-1} \left[\frac{X_s}{R_c + R_s} \right] \quad (3.80)$$

Equation (3.78) for the case of lossy coupling is of a fractional linear form suitable for a curve fitting procedure [1] to be applied to determine Q_L and the coupling coefficient (from which Q_o is calculated) similarly as for equation (3.67). The coupling coefficient requires knowledge of the diameter (d) of the Q-circle and the diameter (d_2) of the coupling loss circle [1] which are both obtained from the results of the circle fitting procedure. The coupling coefficient is then calculated from the diameter of the Q-circle and the diameter of the coupling loss circle as [1]:

$$\beta = \frac{1}{\frac{d_2}{d} - 1} \quad (3.81)$$

where the diameter of the loss circle d_2 is calculated as [1] :

$$d_2 = \frac{1 - |\Gamma_d|^2}{1 - |\Gamma_d| \cos \phi} \quad (3.82)$$

where ϕ is the angle between the vector from the detuned point and the circle centre, and the vector from the detuned point to the origin [1].

The ability of the Kajfez technique to account for coupling losses enables the unloaded Q_o -factor of microwave resonators to be determined with accuracy better than 1 percent. Unfortunately, this elegant technique was developed for reflection mode resonators and does not apply to measurements of S_{11} (or S_{22}) of transmission mode resonators. Based on similar circuit theory and circle fitting procedure used in the Kajfez technique, the author of this thesis has developed a novel technique to

determine the loaded Q_L -factor and the port coupling coefficients (β_1 and β_2) (hence unloaded Q_o -factor) for transmission mode resonators with lossy coupling. The developed Transmission Mode Q_o -Factor Technique is presented in the next chapter.

BIBLIOGRAPHY OF CHAPTER 3

- [1] D. Kajfez, "Q Factor", Vector Fields, 1994.
- [2] B.W. Hakki, P.D. Coleman, "A dielectric resonator method of measuring inductive capacities in the millimetre range", IEEE Trans. Microwave Theory Tech., Vol. MTT-8, pp. 402-410, July 1960.
- [3] D. Kajfez, P. Guillon, "Dielectric Resonators", Vector Fields, 1990.
- [4] J. Ceremuga, J. Krupka, T. Kosciuk, "Resonant measurements of surface resistance of high T_c superconducting films: how good/bad they are?", Journal of Superconductivity, Vol. 8, No. 6, pp 681-689, 1995.
- [5] J. Krupka et al, "Surface resistance measurements of HTS films by means of sapphire dielectric resonators", IEEE Transactions on Applied Superconductivity, Vol. 30, No. 3, pp. 3043-3048. Sept 1993.
- [6] E.L. Ginzton, "Microwave Measurements", McGraw Hill Book Co., pp 403-408, 1957.
- [7] Y. Kobayashi, T. Imai, H. Kayano, "Microwave measurements of surface impedance of high- T_c superconductor", IEEE MTT-S digest, pp. 281-284, 1990.
- [8] Z. Ma, "RF properties of high temperature superconducting materials", PhD thesis, G.L. Report No. 5298, Edward L. Ginzton Laboratory, Stanford University, May 1995.
- [9] S.M. Anlage, B.W. Langley, G. Deutscher, J. Halbritter, M.R. Beasley, "Measurements of the temperature dependence of the magnetic penetration depth in $YBa_2Cu_3O_{7.8}$ superconducting thin films", Phys. Rev. B, Vol. 44, No. 17, pp. 9764, 1991.
- [10] A. Porch, M.J. Lancaster, R.G. Humphreys, N.G. Chew, "Non-linear microwave surface impedance of patterned $YBa_2Cu_3O_7$ thin films", Journal of Alloys and Compounds, Vol. 195, No. 1-2, pp. 563-566, 1993.
- [11] D.E. Oates et al, "Surface impedance measurements of superconducting NbN films", Phys. Rev. B, Vol. 43, No. 10, pp. 7655-7663, April 1991.
- [12] J.S. Martens et al, "Confocal resonators for measuring the surface resistance of high-temperature superconducting films", Appl. Phys. Lett., Vol. 58, No. 22, pp. 2453, 1991.

-
- [13] C.L. Bohn, J.R. Delayen, U. Balachandran, M.T. Lanagan, "Radio frequency surface resistance of large-area bismuth strontium calcium copper oxide thick films on silver plates", *Appl. Phys. Lett.*, Vol. 55, No. 3, pp. 304, 1989.
- [14] N. Klein et al, "Microwave surface resistance of epitaxial $\text{YBa}_2\text{Cu}_3\text{O}_7$ thin films at 18.7 GHz measured by a dielectric resonator technique", *Journal of Superconductivity*, Vol. 5, No. 2, pp. 195, April 1992.
- [15] C. Wilker, Z-Y. Shen, V.X. Nguyen, M.S. Brenner: "A sapphire resonator for microwave characterization of superconducting thin films", *IEEE Transactions on Applied Superconductivity*, Vol. 3, No. 1, pp. 1457-1460. 1993.
- [16] J. Mazierska, "Dielectric resonators as a possible standard for characterisation of high temperature superconducting films for microwave applications", *Journal of Superconductivity*, Vol. 10, No. 2, pp. 73-85, 1997.
- [17] R.C. Taber, "A parallel plate resonator technique for microwave loss measurements on superconductors", *Rev. Sci. Instrum.*, Vol. 61, pp. 2200, Aug 1990.
- [18] P.V. Mason, R.W. Gould, "Slow wave structure utilizing superconducting thin-film transmission lines", *Journal of Applied Physics*, Vol. 40, pp. 2039, 1969.
- [19] B.W. Langley, S.M. Anlage, R.F.W. Pease, M.R. Beasley, "Magnetic penetration depth measurements of superconducting thin films by a microstrip resonator technique", *Rev. Sci. Instrum.*, Vol. 62, No. 6, pp. 1801, June 1991.
- [20] K.C. Gupta, R. Garg, I.J. Bahl, "Microstrip Lines and Slotlines", Artech House, 1979.
- [21] J. Mazierska, R. Grabovickic, "Circulating power, RF magnetic field and RF current density of shielded dielectric resonators for power handling analysis of high temperature superconducting thin films of arbitrary thickness", *IEEE Transactions on Applied Superconductivity*, Vol. 6, No. 4, pp. 178-187, 1998.
- [22] J. Krupka, K. Derzakowski, M. Tobar, J. Hartnett, R. Geyer, "Complex permittivity of some ultralow loss dielectric crystals at cryogenic temperatures", *Meas. Sci. Technol.*, Vol. 10, pp. 387-392, 1999.

-
- [23] J. Wosik et al, "Power handling capabilities of superconducting YBCO thin films: thermally induced nonlinearity effects", *Journal of Superconductivity*, Vol. 10, No. 2, pp. 97, 1997.
- [24] E.J. Vanzura, J.E. Rogers (NIST), "Resonant circuit model evaluation using reflected S-parameter data", *Proceedings of IEEE Instrumentation and Measurement Technology Conference*, May 14-16 Atlanta, 1991.
- [25] T. Miura, T. Takahashi, M. Kobayashi, "Accurate Q-Factor evaluation by resonance curve area method and it's application to the cavity perturbation", *IEICE Trans. Electron.*, Vol. E77-C, No. 6, pp. 900-907, June 1994.
- [26] M.C. Sanchez, E. Martin, J.M. Zamarro, "Unified and simplified treatment of techniques for characterising transmission, reflection, or absorption resonators", *IEE Proceedings*, Vol. 137, Pt. H, No. 4, Aug 1990.
- [27] M.C. Sanchez et al, "New method for the measurement of coupling coefficients of transmission cavities", *IEE Proceedings*, Vol. 134, Pt. H, No. 1, Feb 1987.
- [28] D. Kajfez: "Linear fractional curve fitting for measurement of high Q factors", *IEEE Trans. Microwave Theory Tech.*, Vol. 42, No. 7, pp. 1149-1153, 1994.
- [29] A.L. Luiten, A.G. Mann, D.G. Blair, "High-resolution measurement of the temperature-dependence of the Q, coupling and resonant frequency of a microwave resonator", *Measurement Science and Technology*, Vol. 7, No. 6, pp. 949, 1996.
- [30] A.P.S Khanna, Y. Garault, "Determination of loaded, unloaded, and external quality factors of a dielectric resonator coupled to a microstripline", *IEEE Trans. Microwave Theory Tech.*, Vol. MTT-31, pp. 261-264, March 1983.
- [31] "HP8722C Network Analyser Operating Manual", Hewlett-Packard Company, 1995.
- [32] D.M. Pozar, "Microwave Engineering", Addison-Wesley Publishing Company, 1990.
- [33] G.L. Matthaei, G.L. Hey-Shipton, "Concerning the use of high-temperature superconductivity in planar microwave filters", *IEEE Transactions on Applied Superconductivity*, Vol. 42, No. 7, pp. 1287-1294, 1994.

-
- [34] D. Kajfez et al, "Uncertainty analysis of the transmission-type measurement of Q-factor", IEEE Transactions on Applied Superconductivity, Vol. 47, No. 3, pp. 367-371, March 1999.
- [35] J.E. Aitken, 'Swept-frequency microwave Q-factor measurements with network analyser', IEE Proceedings, Vol. 123, pp. 855-862, 1976.
- [36] M. Sucher, J. Fox, "Handbook of Microwave Measurements, Vol. II, Third Edition", New York, John Wiley & Sons, Inc., pp. 417-493, 1963.

CHAPTER 4

DEVELOPMENT OF A NOVEL METHOD FOR THE ACCURATE DETERMINATION OF UNLOADED Q-FACTORS OF TRANSMISSION MODE DIELECTRIC RESONATORS BASED ON MEASUREMENTS OF SCATTERING PARAMETERS AND CIRCLE-FITTING

4.1 GENERAL ISSUES TO BE CONSIDERED IN THE DEVELOPMENT OF A MODEL OF A HAKKI COLEMAN DIELECTRIC RESONATOR TEST SYSTEM

While various techniques have been developed to obtain the unloaded Q_0 -factors of microwave resonators, they are not always suitable for applications to measurements involving microwave resonators confined to vacuum/cryogenic environments. In these systems, practical constraints prevent measurements being done at the locations relevant to the Q_0 -factor technique. Also the transmission line and other components such as adapters inside the cryocooler cannot be calibrated out using standard device calibration procedures for vector network analysers. Being unable to perform measurements at point(s) or location(s) specific to a measurement technique is a significant problem because each technique has been developed with respect to chosen reference point(s) in circuit models of resonant systems. Figures 4.1 and 4.2 are used to clarify the problem at the input port for a one-port system, but the problem also applies to two-port systems. Figure 4.1 illustrates a ideal measurement system, while Fig. 4.2 illustrates a typical measurement system used for the characterisation of superconducting films.

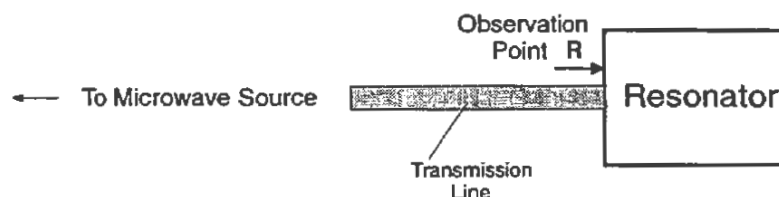


Figure 4.1 A ideal case measurement system used to measure the unloaded Q_0 -factor of microwave resonators. The input ports of the resonator are accessible.

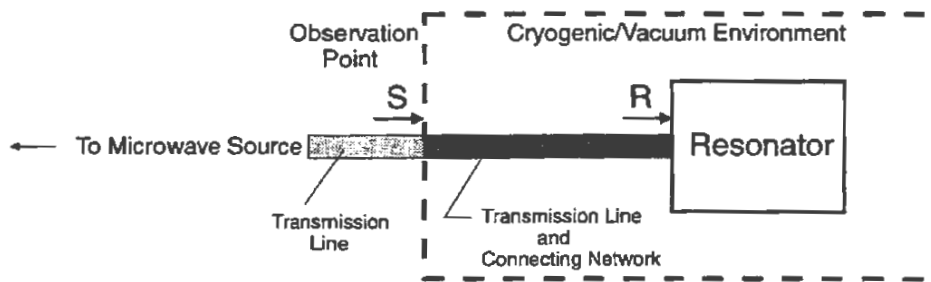


Figure 4.2 A measurement system used to measure the unloaded Q_0 -factor of microwave resonators under low temperature/vacuum conditions. The input ports of the resonator cannot be accessed due to practical constraints.

The difference between the two presented systems shown above is that the resonator of Fig. 4.2 is confined to a cryogenic/vacuum environment so that measurements cannot be done at the true resonator input at the point **R** (resonator). Hence observations need to be made at point **S** (system) which is situated at the input of the cryogenic vessel. Figures 4.3 and 4.4 illustrate circuit models need to be used to model the two measurement systems.

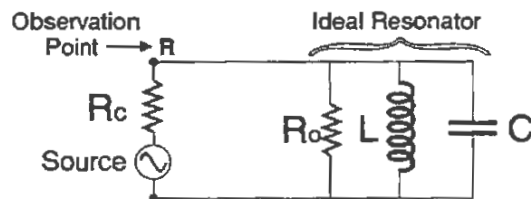


Figure 4.3 A circuit diagram of a perfect one-port measurement system to measure the unloaded Q_0 -factor of microwave resonators.

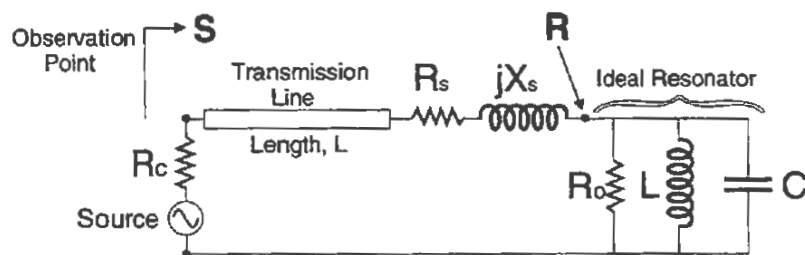


Figure 4.4 A circuit diagram showing the input port of a practical resonant system to measure the unloaded Q_0 -factor of microwave resonators.

In Fig. 4.4, the coupling loss and coupling reactance are modelled by R_s and X_s respectively, and R_c is the internal resistance of the microwave source (which is equal to the characteristic impedance of the transmission line). Using the simple circuit model of a resonant system of Fig. 4.3, feasible response functions can be easily derived and used to fit to a response curve measured with respect to the input (point R) shown in Fig. 4.1.

Unfortunately for the circuit model of Fig. 4.4 which is a better representation of a real measurement system, it is difficult to derive feasible response functions with respect to the observation point S.

Attempts to incorporate effects of transmission lines and all other component effects within the circuit model can prevent the derivation of feasible functions with respect to the observation point S. A possible method to overcome this problem is to assume that various component effects in the connecting network of Fig. 4.2 can be modelled as a cascade of sections as illustrated in Fig. 4.5, and feasible functions can be derived with respect to a 'virtual point' B. Suppose that the effect of section T_1 can somehow be quantified. Under these circumstances, it would be possible to remove the influence of the effect due to T_1 from the response curve measured at the point A to provide a secondary (processed) response curve related to the virtual point B. This means that the feasible response function developed for point B can be applied to the processed response curve (in a curve fitting technique) because the processed curve is relevant to the point B.

Hence a possible solution to overcome the problem of not being able to derive a feasible response function for the observation point (point S) is to shift the observation plane (if possible) to another one where a feasible response function can be derived. To successfully do this, it will be necessary to somehow quantify the influence of components in the network between the observation point and the resonator device. Unfortunately, the transmission line inside the cryocooler cannot be calibrated out for varying temperatures using standard network analyser device calibration procedures. Hence other techniques need to be introduced to eliminate influences of $T_1..T_n$ from the measurement response. Some pre-processing of the raw measurement data may be necessary before a curve fitting process is applied.

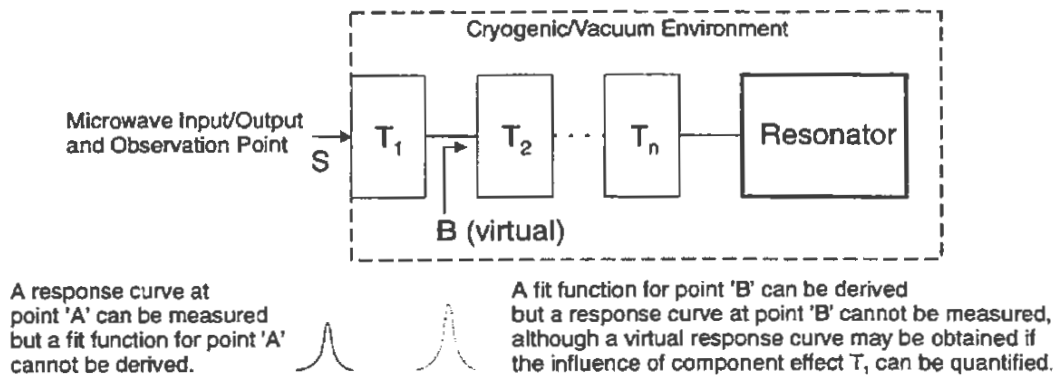


Figure 4.5 Component effects of a network connected between the measurement point and the microwave resonator modelled as a cascade of sections.

Having discussed the importance matching points on a circuit model to corresponding points in a real measurement system, some comments need to be made about circuit models which are needed to derive feasible response functions. Simplest circuit models of resonant systems, as described in fundamental microwave engineering text books, are generally inadequate for the development of accurate curve fitting procedures because they do not adequately represent the behaviour of real systems. Simple response functions derived from simple circuit models of resonator systems do not account for parasitic and practical effects associated with real test systems like coupling losses, coupling reactance, crosstalk effects in transmission mode resonators, impedance mismatch, and delay effects introduced by transmission lines connected between the observation point and the true resonator input. Due to the deficiencies of simplest response functions in describing practical response characteristics of resonant systems, attempts to fit derived simple functions to measured response curves usually lead to inaccurate results. Therefore more accurate circuit models of the resonator test system need to be used.

The development of accurate techniques to determine the unloaded Q_0 -factors of microwave resonators requires skilful approaches to be used in areas of circuit analysis, measurement methods, as well as mathematical methods. Furthermore, a good understanding of practical effects introduced by the measurement environment is necessary. In the next section of this chapter, various effects introduced by the practical measurement system are identified and illustrated.

These effects need to be considered in the development of precise curve fitting techniques based on measurements of S-parameters.

4.2 PRACTICAL EFFECTS INTRODUCED BY THE HTS MICROWAVE CHARACTERISATION SYSTEM

The development of any technique used to obtain unloaded Q_0 -factor of microwave resonators requires knowledge of the sources of discrepancies between the practical measurement system and the model system used in the development of the Q-factor technique. A typical HTS characterisation system shown in Fig. 4.6 consists of a test resonator connected to a measurement device via long cables, connectors and coupling structures such as coupling loops. The resonator device is contained within a dewar and it operates in a cryogenic environment of varying temperature inside the cryocooler.

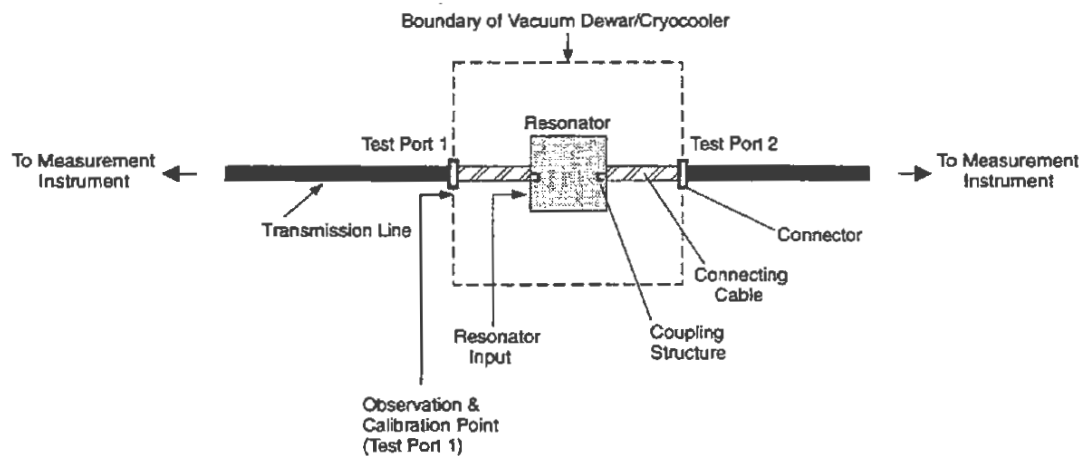


Figure 4.6 The R_s measurement system.

As mentioned in the previous section, the development of accurate curve fitting techniques used to obtain the unloaded Q_0 -factor of microwave resonators requires a good understanding of the practical effects introduced by a real system. Hence investigations were done in the course of this thesis to document various

practical effects which alter measurement results. Measured functions of S-parameters versus frequency around the resonance should form a circle in the complex plane. Due to effects associated with external measurement circuitry, the measured functions are distorted from their circular shape. The identified effects include :

- 1) Electrical delay introduced by transmission lines (cables).
- 2) Coupling losses due to lossy transmission lines (cables), connectors, and coupling structures.
- 3) Impedance mismatch.
- 4) Noise.
- 5) Crosstalk between the coupling loops of transmission mode resonators.

The results of the investigation are presented below with reference to the illustrations of Fig. 4.7 to Fig. 4.14. First, transmission lines introduce a frequency dependent electrical delay, which is equivalent to a frequency dependent phase shift [1]. The introduced phase shift expressed as a linear function of frequency as :

$$\phi(f) = \phi_{ref} \frac{f}{f_{ref}} \quad (4.1)$$

where ϕ_{ref} is the phase introduced by the transmission line at the arbitrary reference frequency f_{ref} [1]. In the complex plane, the frequency dependence of the phase-shift introduced by transmission lines causes a S_{11} resonance trace to be distorted away from a circular shape to a 'balloon' shape (Fig. 4.7).

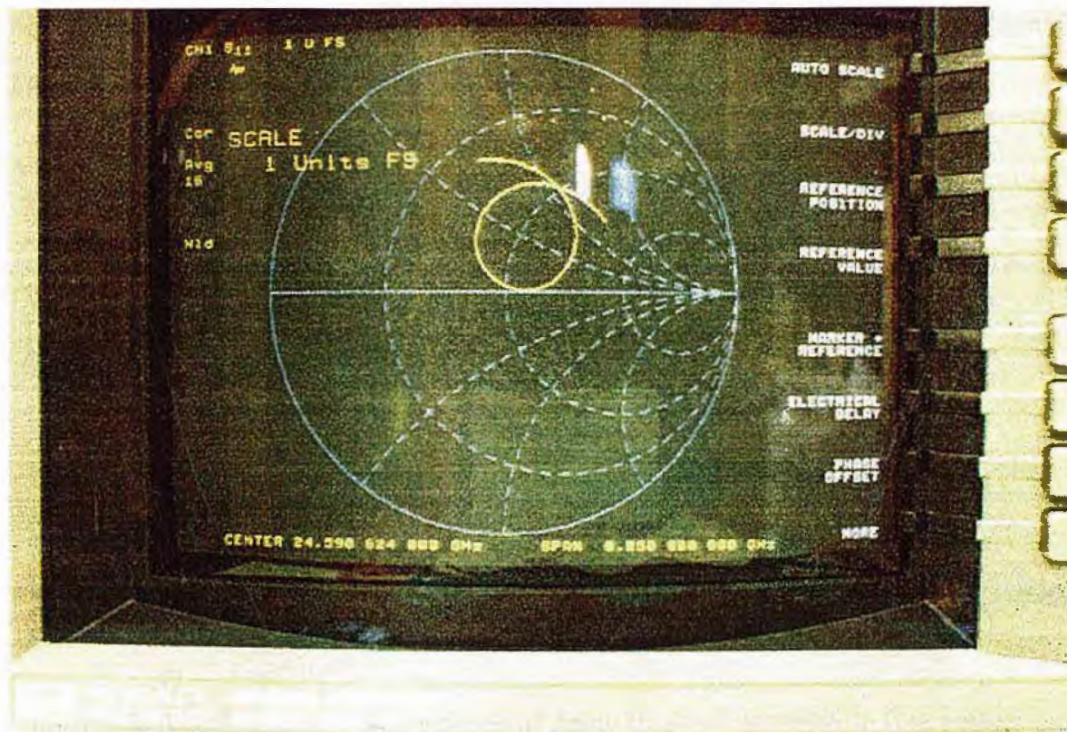


Figure 4.7 Distortion of reflection (S_{11} in this case) Q-circle caused by frequency dependence of transmission line delay.

Figure 4.8 shows the phase characteristics of a reflection trace measured over a wide frequency span of 50 MHz around the resonance. In the regions outside the resonance, the phase angle of S_{11} decreases with frequency due to the frequency dependence of the introduced phase caused by transmission lines (since a ideal resonator does not introduce any phase shift outside the resonance). The irregularity in the phase-frequency response at mid-span is the result of the combined effects of the phase of the resonator at resonance and the introduced (frequency dependent) phase shift due to the transmission lines. The frequency dependence of the introduced phase $\phi(f)$ causes the points on a ideal Q-circle to be rotated in a clockwise direction about the origin of the complex plane. The rotation for points at higher frequencies is bigger than the rotation at lower frequencies, which results in the distortion of the Q-circle (Fig. 4.7). The author of this thesis has noticed that transmission S_{21} Q-circles are significantly less distorted than reflection (S_{11} or S_{22})

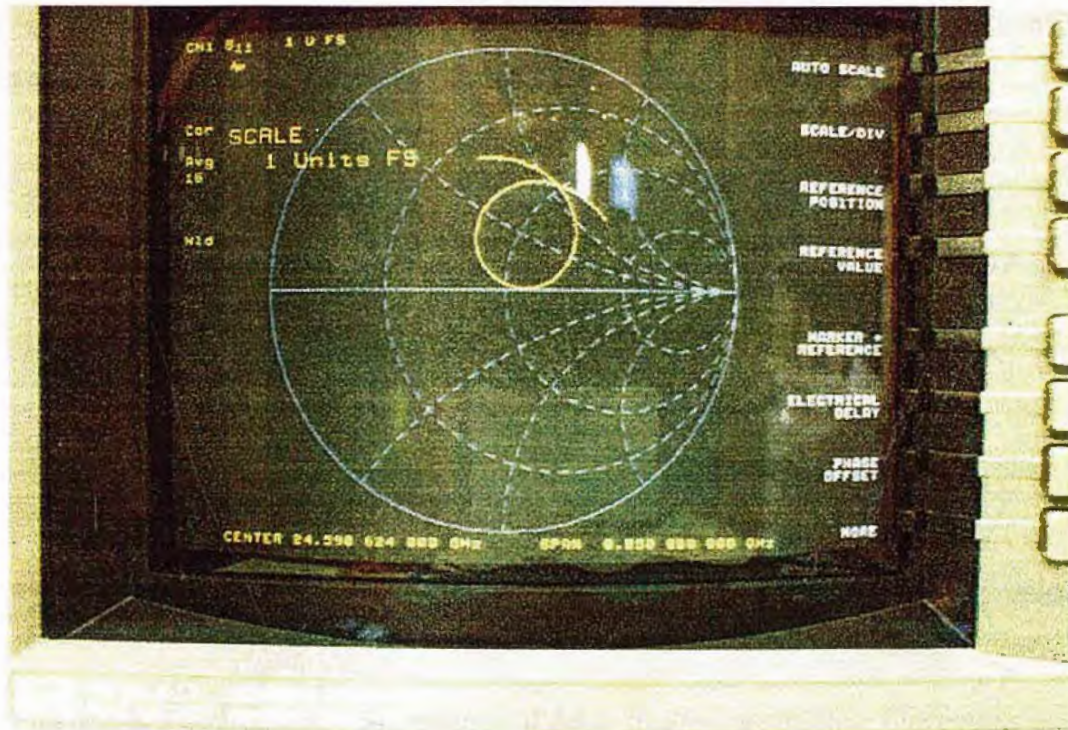


Figure 4.7 Distortion of reflection (S_{11} in this case) Q-circle caused by frequency dependence of transmission line delay.

Figure 4.8 shows the phase characteristics of a reflection trace measured over a wide frequency span of 50 MHz around the resonance. In the regions outside the resonance, the phase angle of S_{11} decreases with frequency due to the frequency dependence of the introduced phase caused by transmission lines (since an ideal resonator does not introduce any phase shift outside the resonance). The irregularity in the phase-frequency response at mid-span is the result of the combined effects of the phase of the resonator at resonance and the introduced (frequency dependent) phase shift due to the transmission lines. The frequency dependence of the introduced phase $\phi(f)$ causes the points on an ideal Q-circle to be rotated in a clockwise direction about the origin of the complex plane. The rotation for points at higher frequencies is bigger than the rotation at lower frequencies, which results in the distortion of the Q-circle (Fig. 4.7). The author of this thesis has noticed that transmission S_{21} Q-circles are significantly less distorted than reflection (S_{11} or S_{22})

Q-circles as illustrated in Fig 4.9 of the S_{21} Q-circle measured using the same lengths of transmission lines as for the reflection S_{11} Q-circle of Fig. 4.7.

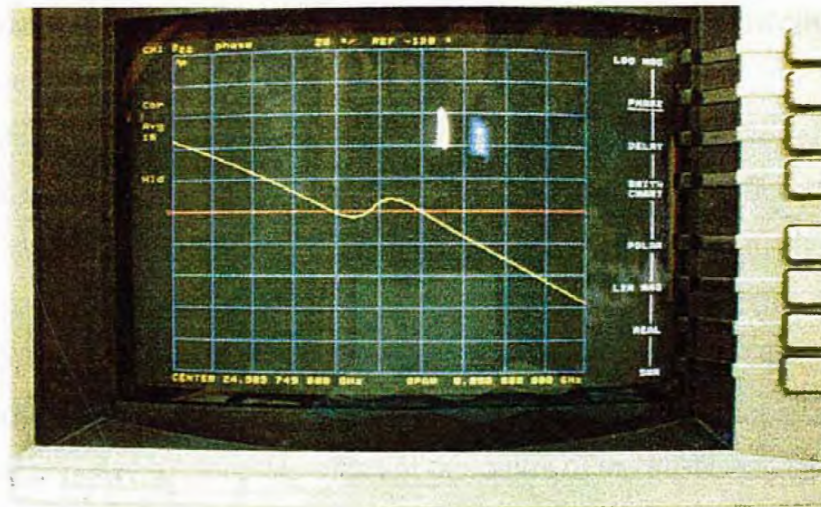


Figure 4.8 The frequency dependence of delay due to transmission line causes the insertion phase to change linearly with frequency. The irregularity at mid-span is due to the phase characteristics of the microwave resonator at resonance, and is influenced by the delay effect of transmission lines.



Figure 4.9 The transmission S_{21} Q-circle is much less effected by the frequency dependence of delay in transmission lines than for reflection (S_{11} or S_{22}) circles.

Connecting cables also cause attenuation of microwave signals. The effect of attenuation on a reflection (S_{11} or S_{22}) Q-circle is a reduction in the diameter as well as a movement away from the unit circle on the Smith Chart. Connectors (adapters) are also lossy components which cause attenuation in microwave signals, with typical losses of around 0.5 dB per connector.

Impedance mismatch between sections of the system cause reflections of microwave signals at mismatched points. Impedance mismatch effects have been observed in measurements of S_{11} and S_{22} . For a matched system, the centre of circular S_{11} or S_{22} trace observed in the *off-resonance* regions (for frequencies outside the resonance) is expected to lie at the origin of Smith Chart. However, observations (by the author of this thesis) of practical reflection traces measured over a wide band revealed a noticeable offset of the centre of the off-resonance trace from the origin as shown in Fig. 4.10. Such an effect is considered to be an important one because it significantly alters both the magnitude and the phase of the reflection (S_{11} or S_{22}) response around the resonance.



Figure 4.10 Mismatch effect observed in the off-resonance part of the reflection S_{22} trace. The S_{22} Q-circle (which is evidently distorted due to transmission line phase effects) is attached to the relatively larger off-resonance circle. The centre of the off-resonance circle clearly does not coincide with the centre of the Smith Circle, indicating the presence of impedance mismatch.

The effect of impedance mismatch can be clearly observed in the magnitude trace of reflection response. If mismatch is not present, then the magnitude of the response in the off-resonance region should be at a constant level. However, due to the presence of mismatch, there is a ripple in the magnitude at frequencies away from the resonance, where the magnitude changes periodically with the frequency as shown in Fig. 4.11.

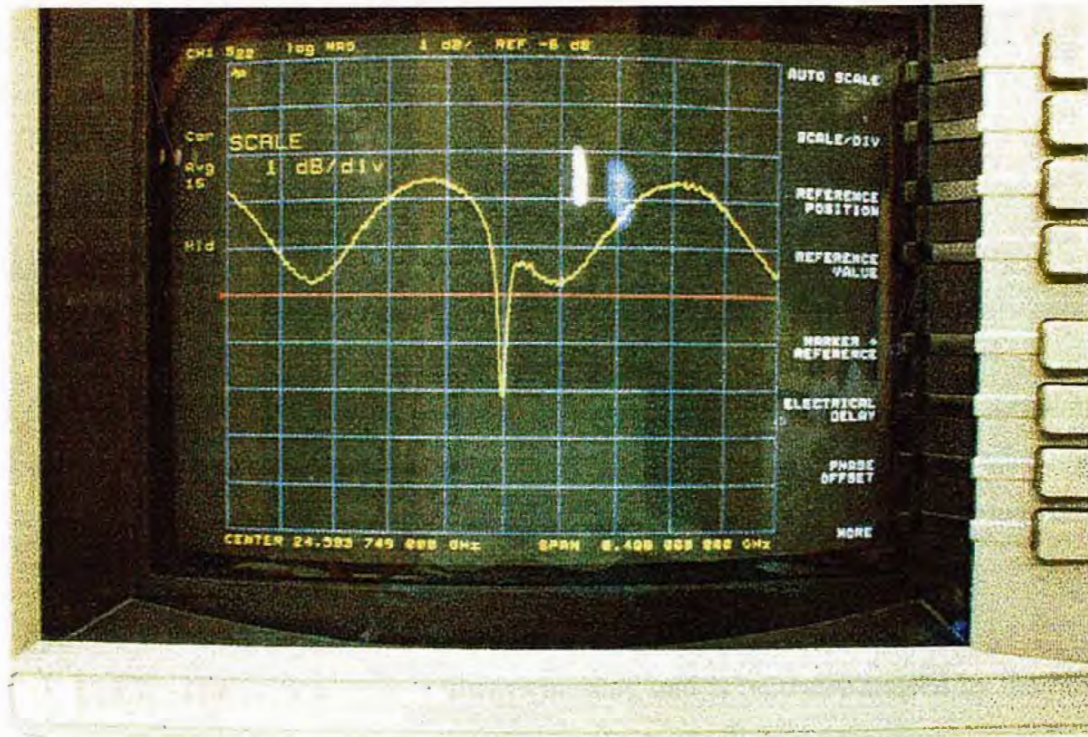


Figure 4.11 Mismatch effect observed in the S_{22} magnitude trace. The sharp 'dip' in the reflection S_{22} trace at mid-span is associated with the resonance. Notice how the resonance dip 'rides' on the off-resonance trace, and that the magnitude of the off-resonance part changes periodically with frequency.

The offset of the centre of the off-resonance trace from the origin due to mismatch also causes non-linearity in the phase of reflection response as shown in Fig. 4.12. If there were no mismatch, and therefore no offset of the centre of the off-resonance circle from the origin, then a periodic linear phase response is expected, with the phase of each linear section going from $+\pi$ to $-\pi$ radians (or $+180$ to -180 degrees).

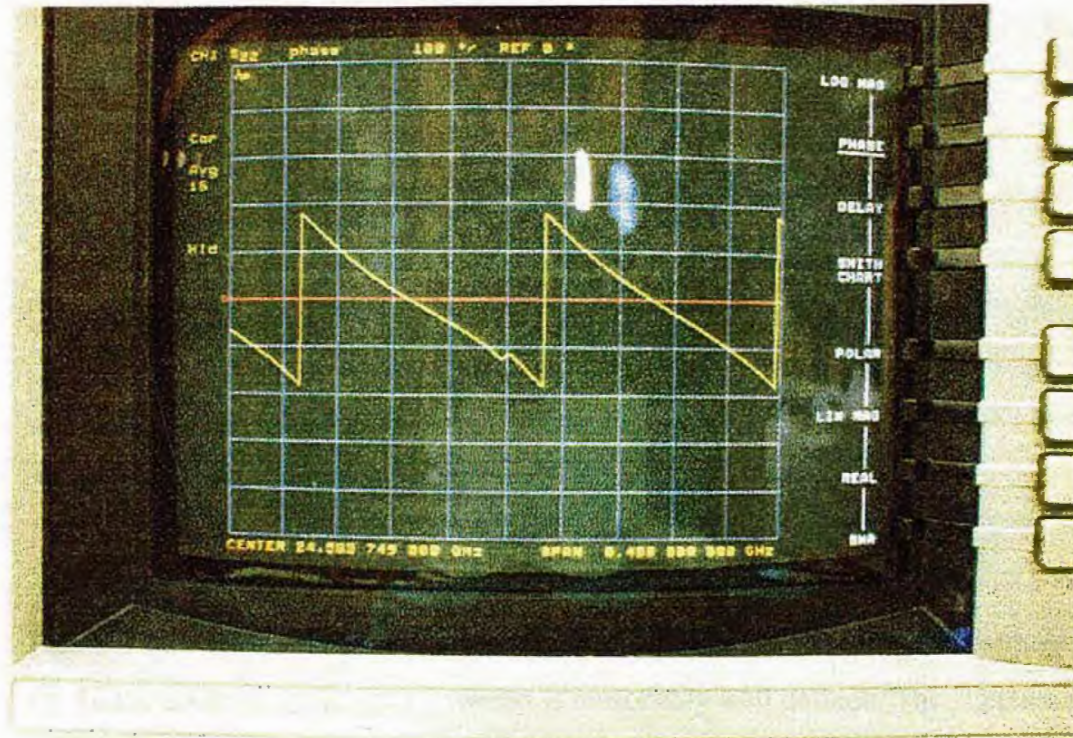


Figure 4.12 Mismatch effects can cause non-linearities in the phase of the reflection response (S_{11} or S_{22}). Notice that the small irregularity in the phase at mid-span is associated with the resonance.

Noise in measurements is always present, and is typically caused by thermal effects, instabilities in microwave sources, and vibrations in the resonator caused by a cooling system. Under conditions of a weak coupling, the noise in a reflection trace is usually significantly higher than in the transmission trace. For example, the signal to noise ratio in the magnitude S_{21} trace of Fig. 4.13 measured under weak coupling conditions is clearly higher than the signal to noise ratio for the reflection trace of Fig. 4.14 measured under the same coupling condition. While curve fitting techniques are used to remove the influence of noise, noise in measurements can influence the accuracy of the fitting technique especially when the amount of noise exceeds a certain limit [1].

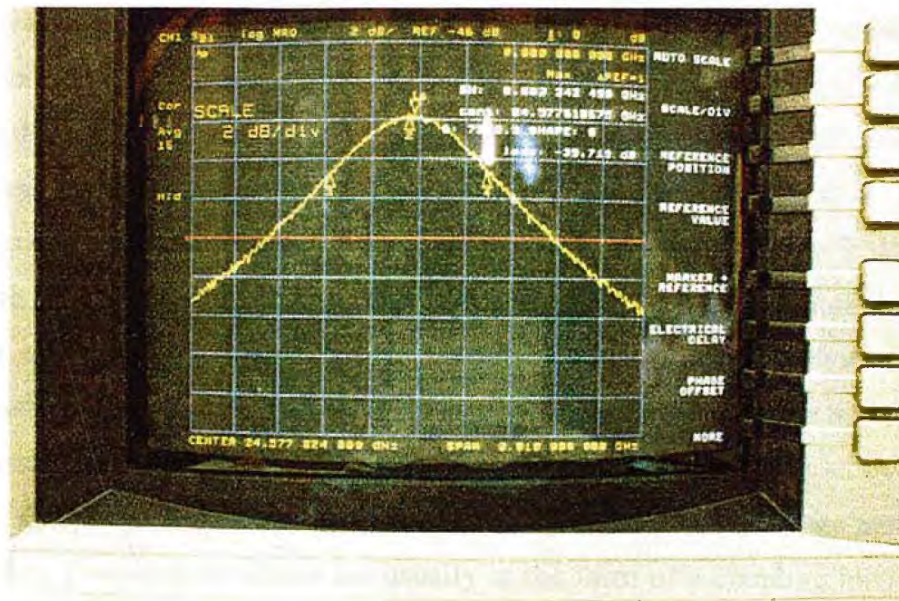


Figure 4.13 The S_{21} magnitude trace measured under a relatively weak coupling condition and averaged over 16 sweeps is reasonably well defined. The signal to noise ratio is high enough for curve fitting techniques to be applied accurately to the measured S_{21} curve.

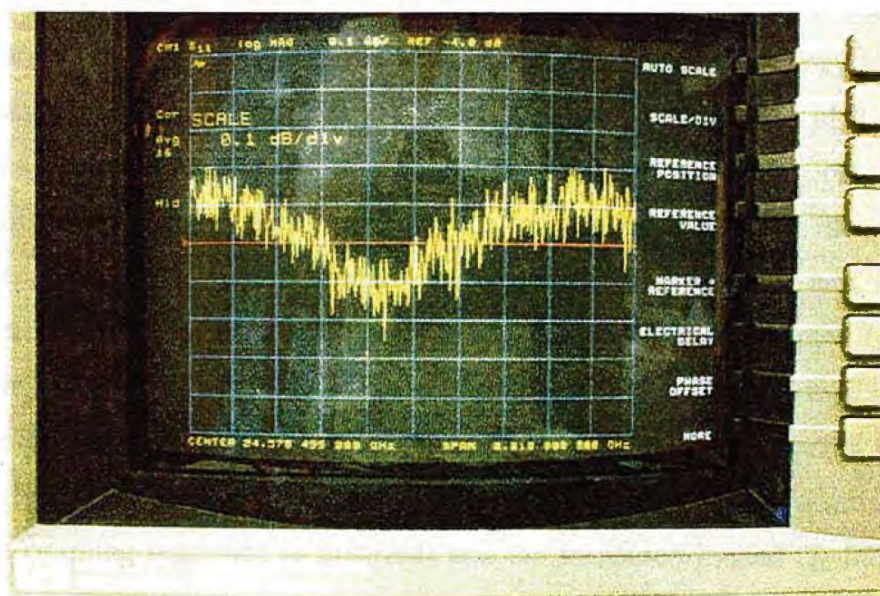


Figure 4.14 The magnitude-of- S_{11} reflection trace is clearly much more noisy than the S_{21} trace of Fig. 4.13 under the same coupling conditions even after averaging over 16 sweeps.

Crosstalk effects can be easily recognised in the offset of the detuned point of S_{21} Q-circles from the origin of the complex plane. If no crosstalk is present, then the detuned point would lie at the origin. When crosstalk is present, the detuned point lies away from the origin. An easy way to recognise crosstalk effects is to fit a full circle over the measured circular S_{21} trace (ie. S_{21} Q-circle). If the circle doesn't pass through the centre of the Smith Circle (which represents the origin of the complex plane), then crosstalk is present. In Fig. 4.9 which was previously shown, the effect of crosstalk effect is clearly evident because a full circle fitted to the S_{21} trace would not pass through the origin.

Coupling of the resonator to external circuitry can also alter measurement responses. Coupling structures are usually in the form of a coupling loop or probe, and have finite resistances which contribute to the microwave losses in the system. Also, microwave energy is stored in the coupling structure, and this phenomenon is usually modelled by a reactance which is frequency dependent (eg. the coupling reactance X_c in Fig. 4.4). However for high Q-factor systems where the bandwidth of measurements is very small (such as when the loaded Q_L -factor is greater than 100), it may be justifiable to assume that the reactance is constant in the frequency band around the vicinity of the resonance [1]. In general, for low Q_L -factor systems it may be necessary to consider the influence of the frequency dependence of the coupling reactance for accurate measurements of the unloaded Q_0 -factor of microwave resonators. From observations done in the course of this work, the frequency dependence of the coupling reactance does not seem to have any significant influence on the magnitude of the off-resonance reflection S_{22} trace (previously shown in Fig. 4.10). If the frequency dependence of the reactance was significant, then the S_{22} vector would not be expected to follow the path of a perfect circle. But the S_{22} trace of Fig. 4.10 is clearly circular, (indicating that the assumption of a constant coupling reactance is justified) and the measured loaded Q_L -factor of the system was about 7000, measured at room temperature using a 25 GHz Hakki Coleman sapphire resonator terminated with copper endwalls. This measurement was done to demonstrate the viability of the 'no dependence of coupling reactance on frequency' assumption for a worst case condition. The Q_L -factor of 7000 is

relatively low compared to the Q_L -factors measured using HTS endwalls, and the assumption of a constant coupling reactance becomes more accurate with increasing Q_L -factor.

4.2.1 ASSESSMENT OF PRACTICAL EFFECTS INTRODUCED BY A REAL MEASUREMENT SYSTEM TO THE TRANSMISSION AND REFLECTION RESPONSES OF THE DIELECTRIC RESONATOR

In this section, the influences of practical effects introduced by the real transmission mode dielectric resonator test system documented in Chapter 4.2 are assessed. As mentioned before in Chapter 3.9, the S_{21} vector observed as a function of frequency obtained using the ideal circuit model of the transmission mode resonator with lossless transmission line (as in Fig. 4.15) traces the path of a circle [2]. Reflection S-parameter vectors also form “Q-circles” [1,3] in the complex plane.

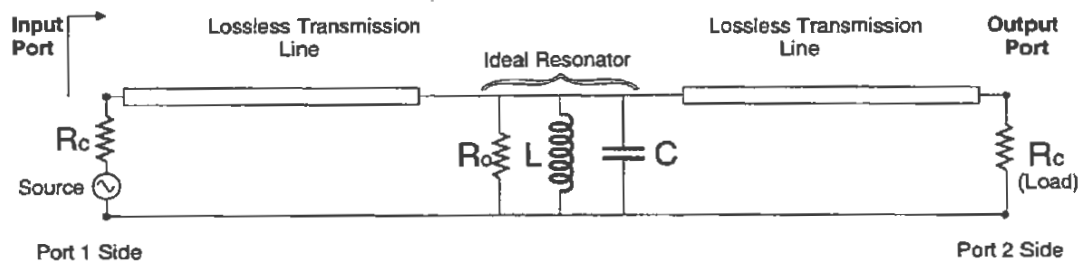


Figure 4.15 A circuit model of ideal transmission mode resonator system modelled by parallel RLC elements with lossless transmission line connecting to the microwave source and load.

If the length of transmission line is zero, the S_{21} Q-circle passes through the origin and has centre on the real axis as shown in Fig. 4.16a. The detuned point, which represents a point at a frequency far away from the resonance lies at the origin. Practical effects introduced by a real measurement environment cause the behaviour of S_{21} Q-circles to deviate from the ideal case. If the connecting transmission lines have a finite length, then the introduced electrical delay causes all

the points on the ideal Q-circle to be rotated about the origin in the clockwise direction (due to the introduced phase lag), and the amount of rotation depends on the length of transmission line (Fig. 4.16b). The rotation of each point is also frequency dependent which results in distorted circles [1].

In the presence of crosstalk between the two ports of the resonator, the detuned point of the S_{21} Q-circle becomes displaced from the origin as shown in Fig. 4.16c. That is, crosstalk effects causes an offset in the detuned point of S_{21} Q-circles from the origin. Crosstalk effects do not distort the shape of Q-circles, but it does causes the magnitude response to deviate from the perfect Lorentzian 'bell shape' as illustrated in Fig. 4.16d [2]. If coupling losses and coupling reactance are present, they effectively reduce the coupling to the resonator and decrease the diameter of S_{21} Q-circles.

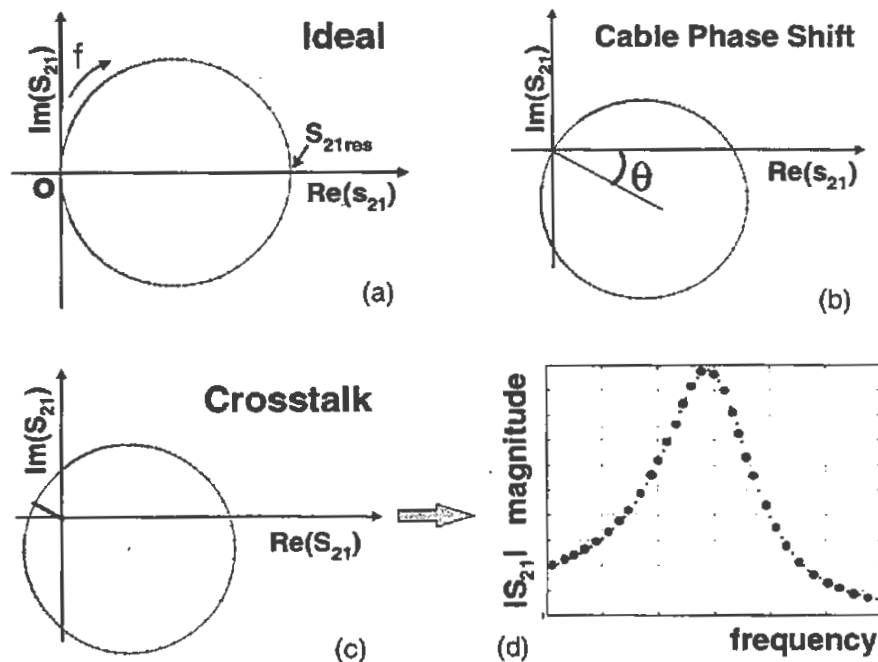


Figure 4.16 Illustrative summary of influences of practical effects on S_{21} Q-circles and S_{21} magnitude trace.

The effect of coupling loss can be detected by examining the location of the reflection mode (S_{11} or S_{22}) Q-circles in the Smith Chart complex plane as illustrated in Fig. 4.17. For a system with no coupling losses, but assuming transmission line

delay, the reflection circle has the centre on the real axis and the detuned point touches the Smith Circle at $\Gamma = -1$. When coupling losses are present, the reflection Q-circle no longer touches the circumference of the Smith Circle and is located some distance away from the perimeter. Figure 4.17 show simulated Q-circle variations in size and position due to changes in coupling loss. When the coupling reactance is held constant and the coupling losses are increased from zero loss, the Q-circle moves away from the perimeter of the Smith Circle with decreasing diameter while all points on the circle maintain the same reactance. When the coupling losses are held constant and the coupling reactance is increased, the Q-circle moves with decreasing diameter in the direction of the change in reactance while the points move along lines of constant resistance as shown in Fig. 4.17.

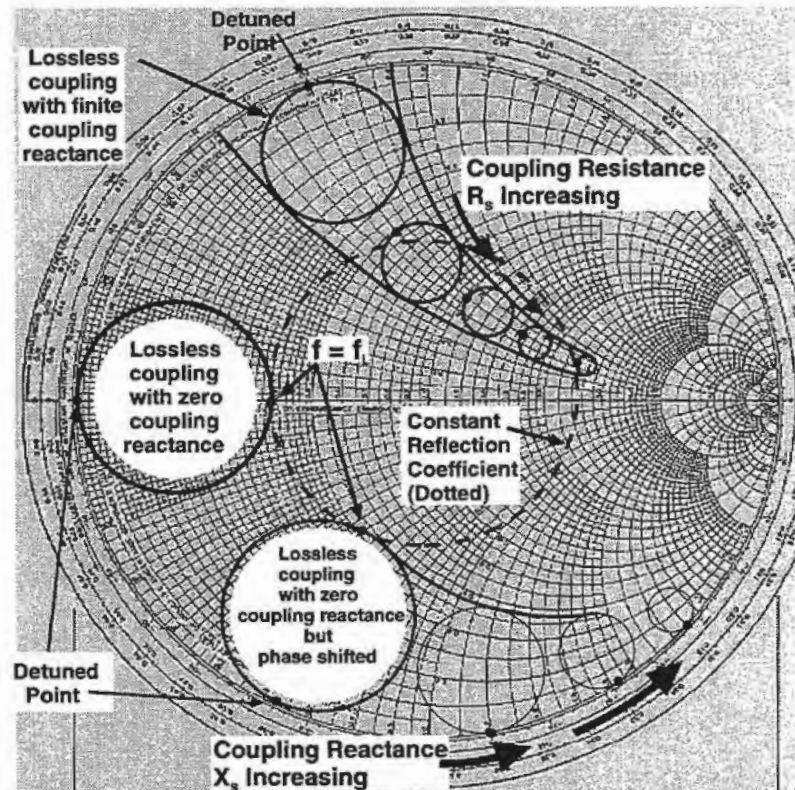


Figure 4.17 Reflection Q-circles for various cases of coupling loss and coupling reactance.

The effects of coupling loss and coupling reactance cannot be removed through calibration procedures. Hence they will need to be incorporated into the

circuit model. Noise is clearly present as random variations of amplitude (and phase) of measured experimental response curves, but curve fitting processes may be used to suppress its influence.

Crosstalk effects in the transmission mode system were observed as a simple offset of the detuned point of the S_{21} circle from the origin of the complex plane. While the effects of crosstalk can be modelled using a circuit model, the incorporation of the effect within the circuit model makes it difficult to derive feasible response functions required for the development of curve fitting techniques. However, crosstalk is an additive effect which can be easily removed by finding the offset, and then subtracting it from the raw response curve if necessary [2]. Furthermore, it is known that resonance information is always preserved in the transmission Q-circle even in the presence of crosstalk effects, so that there is no need to remove the effects of crosstalk when a circle fitting technique is used.

Mismatch effects observed in wide bandwidth reflection S_{11} or S_{22} measurements (greater than 100 MHz for the measurements performed in this thesis) has been identified as an offset in the centre of the circular off-resonance (S_{11} or S_{22}) trace (observed over a enough wide span) from the origin of the complex plane. The effect has been observed at room temperature as well as at cryogenic temperatures. The same result has been observed in measurements of the reflection S_{11} response of a semi-rigid cable 60 centimetres in length and terminated with coupling loops. In this thesis, the effect of impedance mismatch is considered as a simple offset of the circular off-resonance trace from the origin of the complex plane. The nature of such mismatch effect is considered peculiar because it is not believed that the offsets should be not be as significant as the ones observed. While such effect has not yet been investigated thoroughly, the frequency dependence of mismatches can be observed experimentally using a time domain reflectometer.

The last effect which is considered to be an important issue in the development of accurate techniques used to obtain the unloaded Q_0 -factor of microwave resonators is the frequency dependence of the delay in transmission cables. Attempts to incorporate the effects of transmission line delay within a circuit

model can prevent the derivation of feasible response functions for the development of curve fitting techniques. Hence, it is necessary to either remove the influence (if possible) of the phase effects using dedicated calibration methods, or to assume that the influence of the effect is negligible at high enough Q-factors where the change in frequency over the band of measurement is small. If such a assumption is made, then it would be justifiable to ignore the effect of transmission line delay. However, observations of reflection Q-circles at the frequencies of interest show that the effects of delay due to long cables (eg. greater than 20 times the operating wavelength) can be clearly noticed as distortion in the measured Q-circles and can lead to inaccurate results in a curve fitting procedure. Hence it may be necessary to remove the effects of the transmission line as described in Chapter 5.2 and demonstrated for a practical case in Chapter 6.2.

4.3 DEVELOPMENT OF A TRANSMISSION MODE METHOD FOR THE ACCURATE DETERMINATION OF THE UNLOADED Q_o -FACTOR OF MICROWAVE RESONATORS BASED ON MEASUREMENTS OF S-PARAMETERS.

The following fundamental assumptions have been made in the course of this work to develop a feasible, accurate and useful method to determine the Q_o -factor of dielectric resonators for calculations of the surface resistance of superconducting films.

1. The method is to be applicable to resonators working in the transmission mode.
2. The full equation to calculate the unloaded Q_o -factor is to be used, namely :

$$Q_o = Q_L (1 + \beta_1 + \beta_2) \quad (4.2)$$

implying that :

- (a) New equations needed to be derived to relate the loaded Q_L -factor and the coupling coefficients (β_1 and β_2) through a circuit model of the HTS measurement system with the S_{21} , S_{11} and S_{22} transmission parameters.

- (b) A new equation to calculate coupling coefficients β_1 and β_2 with S_{11} and S_{22} reflection parameters for transmission mode resonators needed to be developed.
3. Derivation of equations of loaded Q_L -factor, coupling coefficient and frequency versus S_{21} relationship is to be based on as accurate model of a real measurement system as feasible.
 4. Important parasitic effects of the test system described in Chapter 4.2 not included in the circuit model of the HTS measurement system are to be accounted during the circle fitting to the measured S-parameter response of the system.
 5. Circle fitting techniques to be applied on multi-frequency measurements of scattering parameters S_{21} , S_{11} and S_{22} are to be developed to obtain the loaded Q_L -factor, the coupling coefficients β_1 and β_2 , and the resonant frequency, f_o .
 6. Software to implement the circle fitting technique is developed.

The method presented below enables the determination of the unloaded Q -factor of transmission mode dielectric resonators using measurements on all three S-parameter modes S_{21} , S_{11} and S_{22} . To derive equations relating the S-parameters with the loaded Q_L -factor, coupling coefficients, and the resonant frequency, the circuit model of a transmission mode resonator has been used as illustrated in Fig. 4.18.

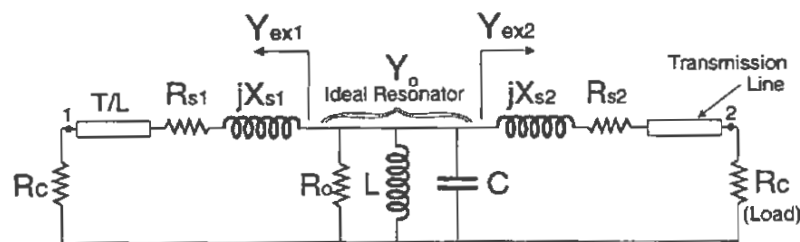


Figure 4.18 Circuit model of a practical transmission resonator measurement system.

The three components R_o , L and C determine the unloaded Q_o -factor as well as the resonant frequency ω_o of the ideal resonator. Y_o represents the admittance of the ideal resonator. The coupling losses are modelled using resistances R_{s1} and R_{s2} and

the coupling reactances are modelled using X_{s1} and X_{s2} . The resistance R_c represents the internal resistance of the microwave source which is matched to the characteristic impedance of the transmission line, typically 50Ω . Y_{ex1} and Y_{ex2} represents the external admittances looking out of the ideal resonator on each side. The electrical delay introduced by the transmission lines shown in the circuit model are not considered in the analysis. However, the microwave losses of the transmission line as well as the losses in connectors and coupling structures are accounted for by the resistances R_{s1} and R_{s2} .

The narrow band approximation for the admittance Y_o of the ideal resonator can have the form of [1]:

$$Y_o = \frac{1}{R_o} \left\{ 1 + j2Q_o \frac{(\omega - \omega_o)}{\omega_o} \right\} \quad (4.3)$$

where Q_o is the unloaded quality factor of the resonator, and ω_o is the radian resonant frequency of the ideal resonator given by :

$$\omega_o = \frac{1}{\sqrt{LC}} \quad (4.4)$$

The external admittances Y_{ex1} and Y_{ex2} looking out from the ports of the resonator as in Fig. 4.18 are given by :

$$Y_{exp} = \frac{1}{R_{sp} + R_c + jX_{sp}} \quad (4.5)$$

where $p = 1$ or 2 denotes the input and the output port of the resonator respectively.

The real and imaginary components of the external admittances described by (4.5) are :

$$Y_{exp} = G_{exp} + jB_{exp} = \frac{R_c + R_p}{(R_c + R_p)^2 + X_{sp}^2} + j \frac{(-X_{sp})}{(R_c + R_p)^2 + X_{sp}^2} \quad (p = 1,2) \quad (4.6)$$

The total admittance Y_L of the resonant system can be described as :

$$Y_L = Y_o + Y_{ex1} + Y_{ex2} \quad (4.7)$$

Substitution of (4.3) and (4.6) into (4.7) gives :

$$Y_L = G_o + G_{ex1} + G_{ex2} + jQ_o G_o 2 \frac{(\omega - \omega_o)}{\omega_o} + j(B_{ex1} + B_{ex2}) \quad (4.8)$$

where

$$G_o = \frac{1}{R_o} \quad (4.9)$$

is simply the conductance associated with the shunt resistance R_o . At the resonance (when $\omega = \omega_L$), the imaginary part of the total admittance Y_L vanishes. Hence, when the imaginary part of (4.8) is equated to zero, the loaded resonant frequency ω_L can be obtained as :

$$\omega_L = \omega_o \left[1 - \frac{B_{ex1} + B_{ex2}}{2Q_o G_o} \right] \quad (4.10)$$

Combining (4.8) and (4.10), the total admittance Y_L of the resonant system also be expressed as :

$$Y_L = (G_o + G_{ex1} + G_{ex2}) \left[1 + j2Q_L \frac{\omega - \omega_L}{\omega_o} \right] \quad (4.11)$$

where the loaded Q_L -factor of the resonant system is :

$$Q_L = Q_o \left[\frac{G_o}{G_o + G_{ex1} + G_{ex2}} \right] \quad (4.12)$$

Using the typical definition of the total coupling coefficient β as the ratio of the total power dissipated in the external circuit to the power dissipated in the resonator, the total coupling coefficient β for the resonator test system is :

$$\beta = \frac{P_{ex}}{P_o} = \frac{\frac{1}{2}|V|^2 G_{ex1} + \frac{1}{2}|V|^2 G_{ex2}}{\frac{1}{2}|V|^2 G_o} = \frac{G_{ex1} + G_{ex2}}{G_o} = \beta_1 + \beta_2 \quad (4.13)$$

where the port coupling coefficients β_1 and β_2 can be expressed as :

$$\beta_1 = \frac{P_{ex1}}{P_o} = \frac{G_{ex1}}{G_o} \quad \text{and} \quad \beta_2 = \frac{P_{ex2}}{P_o} = \frac{G_{ex2}}{G_o} \quad (4.14)$$

and P_{ex1} and P_{ex2} are the external power dissipations on port 1 and port 2 sides respectively, and P_{ex} ($=P_{ex1}+P_{ex2}$) is the total power dissipated in the external circuit.

Having introduced the basic dependencies of the circuit model of the resonant system, equations relating the S_{21} , S_{11} and S_{22} parameters to the loaded Q_L -factor, resonant frequency, and coupling coefficients need to be derived. The derivation of

the feasible response functions for the transmission mode dielectric resonator developed in the course of this thesis is described as follows. The circuit diagram of Fig. 4.18 can be considered as a series of cascaded ABCD sections as :

$$\begin{bmatrix} A & B \\ C & D \end{bmatrix} = \begin{bmatrix} 1 & R_{s1} + jX_{s1} \\ 0 & 1 \end{bmatrix} \begin{bmatrix} 1 & 0 \\ Y_o & 1 \end{bmatrix} \begin{bmatrix} 1 & R_{s2} + jX_{s2} \\ 0 & 1 \end{bmatrix} \quad (4.15)$$

which may be simplified to give the ABCD matrix as :

$$\begin{bmatrix} A & B \\ C & D \end{bmatrix} = \begin{bmatrix} 1 + (R_{s1} + jX_{s1})Y_o & (R_{s2} + jX_{s2})[1 + (R_{s1} + jX_{s1})Y_o] + (R_{s1} + jX_{s1}) \\ Y_o & R_{s2} + jX_{s2} \end{bmatrix} \quad (4.16)$$

Having found the ABCD parameters, the S-parameters of the transmission mode system may be obtained following equations after [4], namely :

$$S_{21} = \frac{2R_c}{AR_c + B + CR_c^2 + DR_c} \quad (4.17)$$

$$S_{11} = \frac{(A - D)R_c + B - CR_c^2}{(A + D)R_c + B + CR_c^2} \quad (4.18)$$

$$S_{22} = \frac{(D - A)R_c + B - CR_c^2}{(A + D)R_c + B + CR_c^2} \quad (4.19)$$

By substituting the ABCD parameters from (4.16) into (4.17), the S_{21} response has been obtained as:

$$S_{21} = \frac{2R_c Y_{ex1} Y_{ex2}}{Y_{ex1} + Y_{ex2} + Y_o} \quad (4.20)$$

The denominator of the S_{21} equation (4.20) can be recognised to be the total admittance Y_L as described by (4.7) and (4.8). Hence the frequency dependence of S_{21} for the resonant system around the resonance can have the form :

$$S_{21}(\omega) = \frac{2R_c Y_{ex1} Y_{ex2}}{G_o(I + \beta_1 + \beta_2) \left[1 + j2Q_L \frac{(\omega - \omega_L)}{\omega_o} \right]} \quad (4.21)$$

The novel equation (4.21) relates S_{21} with the loaded Q_L -factor, the coupling coefficients, and the frequency. This novel equation (4.21) derived for the complex transmission coefficient S_{21} of transmission mode resonators is of a fractional linear form,

$$S_{21} = \frac{a_1 t + a_2}{a_3 t + 1} \quad (4.22)$$

where the complex constants a_1 , a_2 and a_3 for the S_{21} response (Q-circle) around the resonance are :

$$a_1 = 0; \quad a_2 = \frac{2R_c Y_{ex1} Y_{ex2}}{G_o (1 + \beta_1 + \beta_2)}; \quad a_3 = jQ_L \quad (4.23)$$

and 't' is a normalised frequency variable defined by :

$$t = 2 \left(\frac{\omega - \omega_L}{\omega_L} \right) \quad (4.24)$$

A fractional linear curve fitting procedure can be applied to (4.21) to determine the parameters a_1 , a_2 and a_3 . The parameter a_3 is of particular importance because its imaginary part is equal to the loaded Q_L -factor as :

$$Q_L = \text{Im}[a_3] \quad (4.25)$$

To obtain the coupling coefficients (β_1 and β_2) so that the unloaded Q_o -factor can be calculated, the S_{11} and S_{22} parameters need to be analysed. Using the equations (4.16), (4.18) and (4.19), the novel equation that relates the reflection S-parameters S_{11} and S_{22} with the loaded Q_L -factor and the coupling coefficients has been derived as :

$$S_{pp}(\omega) = \frac{jQ_L S_{ppd} 2 \frac{(\omega - \omega_L)}{\omega_o} + \left\{ S_{ppd} + \frac{2R_c Y_{exp}^2}{G_o (1 + \beta_1 + \beta_2)} \right\}}{jQ_L 2 \frac{(\omega - \omega_L)}{\omega_o} + 1} \quad (4.26)$$

where $p=1,2$ denotes the port number, and S_{ppd} represents the detuned value of the reflection coefficient.

Just like the transmission response of (4.21), the reflection responses S_{11} and S_{22} around the resonance described by (4.27) are also of the fractional linear form

$$S_{pp} = \frac{a_1 t + a_2}{a_3 t + 1} \quad (4.28)$$

where t is a normalised frequency described by 4.24. The complex constant a_1 is :

$$a_1 = jQ_L S_{ppd} \quad (4.29)$$

The complex constant a_2 (depending on the port number) is :

$$a_2 = S_{ppd} + \frac{2R_c Y_{exp}^2}{G_o (1 + \beta_1 + \beta_2)} \quad (4.30)$$

where $p = 1$ or 2 denoting the port number. The complex constant a_3 is the same as for the transmission case, and is equal to :

$$a_3 = jQ_L \quad (4.31)$$

The novel equation (4.26), which is of the form of (4.28) is suitable for a fractional linear curve fitting technique to be applied [1]. The complex constants a_1 , a_2 and a_3 are the fit parameters to be obtained from the curve fitting process are used to determine the coupling coefficients, and the imaginary part of a_3 provides the loaded Q-factor, Q_L . Hence the value of a_3 evaluated from a curve-fitting to either a reflection (S_{11} or S_{22}) Q-circle or a transmission (S_{21}) Q-circle will provide the loaded Q_L -factor.

The complex constants a_1 , a_2 and a_3 can be related to important points on the Q-circles. For example, the ratio a_1/a_3 represents the detuned value S_{ppd} of the complex reflection coefficient when the frequency is far from the resonance frequency, and a_2 is the reflection coefficient at the resonant frequency (for the case $t=0$). The diameter of the reflection circle can be obtained from the detuned point and the resonance point, which lie diametrically opposite to each other on the Q-circle.

To model the coupling losses in order to obtain the port coupling coefficients β_1 and β_2 , the equivalent circuit model of the transmission mode measurement system (of Fig. 4.18) is shown below in Fig. 4.19.

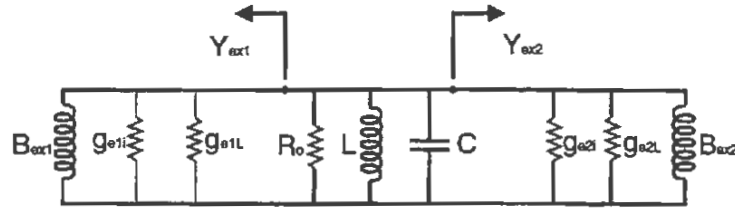


Figure 4.19 Equivalent circuit to model coupling losses.

The circuit model of Fig. 4.19 is similar to the one used to model a reflection mode (1-port) resonator in the Kajfez S_{11} technique [1], but this circuit has two ports. The total coupling coefficient on one of the resonator ports can be expressed following (4.14) as :

$$\beta_p = \frac{G_{\text{exp}}}{G_o} = \left(\frac{g_{epi}}{G_o} \right) + \left(\frac{g_{epL}}{G_o} \right) \quad (4.32)$$

where the real part of the external admittance (the conductance) can be considered as the sum of the ideal lossless part and an additional lossy part as :

$$G_{\text{exp}} = g_{epi} + g_{epL} \quad (4.33)$$

and $p = 1, 2$ denotes the port number. The ratios g_{epi}/G_o and g_{epL}/G_o are the lossless and lossy parts of the total coupling coefficients respectively so that the total coupling coefficients can be considered to be the sum of lossless, β_i , and lossy, β_L , terms, namely as :

$$\beta_p = \beta_{pi} + \beta_{pL} \quad \text{and} \quad \beta_q = \beta_{qi} + \beta_{qL} \quad (4.34)$$

where the lossless and lossy coupling coefficients are :

$$\beta_{pi} = \frac{g_{epi}}{G_o} = \frac{R_o R_c}{(R_c + R_{sp})^2 + X_{sp}^2} \quad (4.35)$$

$$\beta_{pL} = \frac{g_{epL}}{G_o} = \frac{R_o R_{sp}}{(R_c + R_{sp})^2 + X_{sp}^2} \quad (4.36)$$

where again, $p=1, 2$ denotes the port number, and the subscripts 'i' and 'L' denote the lossless and lossy parts of coupling loss respectively.

The coupling coefficients are initially unknown, and they need to be evaluated in order to calculate the unloaded Q_0 -factor. For the case of lossy coupling, Kajfez [1] demonstrated that the lossless and lossy parts of the coupling coefficients can be calculated from the diameter of reflection Q -circle and the diameter of the *coupling-loss* circle. The author of this thesis demonstrates that the same approach can be used to obtain the lossless and lossy parts of the coupling coefficients for resonators working in the transmission mode. The main difference is that transmission resonators have two coupling coefficients instead of one, so that there are four components of coupling coefficients to be solved, which are namely β_{1i} , β_{1L} , β_{2i} , β_{2L} (instead of 2 unknowns β_i , β_L for reflection mode resonators).

To solve for the four coupling coefficients, equations for the diameters of Q -circles and coupling-loss circles need to be derived. First of all, the diameters of Q -circles can be determined according to the fundamental knowledge that the detuned point lies diametrically opposite the resonant point for any Q -circle. That is :

$$\text{diameter of } Q \text{ circle} = \left| a_2 - \frac{a_1}{a_3} \right| \quad (4.37)$$

For the transmission (S_{21}) Q -circle, the diameter can thus be described by :

$$\text{diameter of } S_{21} \text{ } Q \text{ circle} = \frac{2R_o R_c |Y_{ex1}| |Y_{ex2}|}{(1 + \beta_1 + \beta_2)} \quad (4.38)$$

For the reflection (S_{11} or S_{22}) Q -circles, the diameters of the circles may be described as :

$$\text{diameter of } S_{pp} \text{ } Q \text{ circle} = \left| \frac{2R_o R_c Y_{exp}^2}{(1 + \beta_1 + \beta_2)} \right| = \frac{2R_o R_c |Y_{exp}|^2}{(1 + \beta_1 + \beta_2)} \quad (4.39)$$

where the magnitude of the external admittance Y_{ex} at either port 1 or port 2 is :

$$|Y_{exp}| = \left| \frac{I}{R_{sp} + R_c + jX_{sp}} \right| = \frac{I}{\sqrt{(R_{sp} + R_c)^2 + X_{sp}^2}} \quad (4.40)$$

By substituting (4.40) into the equations describing the diameters of the transmission S_{21} circle (4.38) and reflection (S_{11} or S_{22}) Q -circles (4.39), and by knowing the form of the lossless part of the coupling coefficient described by (4.35),

For the ideal case described above, the diameter of the coupling loss circle is calculated using :

$$\text{Diameter of Loss Circle)}|_{\text{port } p} = \frac{1 - |S_{ppd}|^2}{1 - |S_{ppd}| \cos \phi} \quad (4.44)$$

where $p = 1$ or 2 denotes the port number. Equation (4.44) requires only the detuned point (S_{ppd}) and the angle ϕ to be known, which are determined from the results of the curve fitting procedure referred to the functional form of the Q-circle described by (4.28). For example, the detuned point S_{ppd} is found as the ratio the ratio a_1/a_3 as described earlier in this chapter, and the centre of the circle S_{11c} is simply a point that is halfway between S_{11d} and the resonance point S_L . The resonance point S_L is equal to the fit parameter a_2 evaluated from the curve-fitting process. The angle ϕ is simply the absolute value of the angle between the vector from S_{11d} to the origin O of the complex plane, and the vector from S_{11d} to the centre S_{11c} of the reflection Q-circle, as shown in Fig. 4.20. Also, the angle ϕ that is associated with the port 1 reflection Q-circle can be different to the one that is associated with the port 2 reflection Q-circle.

For a practical case, a transmission line is connected between the observation point and the resonator input so that reflection measurements need to be made at point S as shown in Fig. 4.2. The phase shift introduced by the transmission line causes all the points on the reflection Q-circle of Fig. 4.20 to be rotated about the origin in a clockwise direction by a certain amount depending on the length of the transmission line. For such a case, it is still feasible to use (4.44) to calculate the diameter of the coupling loss circle, where the definitions for S_{ppd} , and the angle ϕ are the same as the ones described before.

Having obtained methods to determine the diameters of coupling loss circles from the results of the circle fitting process, equations to relate the diameters of the coupling loss circles to the lossless and lossy parts of the coupling coefficients need to be found. The steps involved to find such equations are described below.

The diameter of a coupling loss circle is related to the coupling resistance (R_{s1} or R_{s2} depending on the port number 1 or 2 considered) and the characteristic

source resistance R_c and can be described following an equation for the one-port resonator as [1] :

$$d_p = \text{diam}(\text{coupling loss circle})\Big|_{\text{of port } p} = \frac{2}{1 + \frac{R_{sp}}{R_c}} \quad (4.45)$$

The ratio between the coupling resistance and the characteristic impedance of the system have equivalent ratios described by [1] :

$$\frac{R_{sp}}{R_c} = \frac{g_{epL}}{g_{epi}} = \frac{\beta_{pL}}{\beta_{pi}} \quad (4.46)$$

Hence, the diameters of the coupling loss circles (d_1 and d_2) for ports 1 and 2 respectively can be obtained in terms of the lossy parts of the port coupling coefficients as [1]:

$$d_p = \frac{2}{1 + \frac{\beta_{pL}}{\beta_{pi}}} \quad (4.47)$$

where $p=1,2$ denotes the port number.

To evaluate the four unknown coupling coefficients (β_{1i} , β_{1L} , β_{2i} , β_{2L}), the equations describing the diameters of the reflection circles and the diameters of the coupling loss circles, namely (4.42), (4.43) and (4.47) need to be solved. Once those equations are solved, the following expressions for the coupling coefficients are obtained as :

$$\beta_{1i} = \frac{x}{2 \left[1 - \left(\frac{x}{d_1} + \frac{y}{d_2} \right) \right]} \quad (4.48)$$

$$\beta_{1L} = \left(\frac{2}{d_1} - 1 \right) \beta_{1i} \quad (4.49)$$

$$\beta_{2i} = \frac{y}{2 \left[1 - \left(\frac{x}{d_1} + \frac{y}{d_2} \right) \right]} \quad (4.50)$$

$$\beta_{2L} = \left(\frac{2}{d_2} - 1 \right) \beta_{2i} \quad (4.51)$$

where d_1 is a diameter of port 1 coupling loss circle,
 d_2 is a diameter of port 2 coupling loss circle,
 x is a diameter of port 1 (S_{11}) Q-circle,
 y is a diameter of port 2 (S_{22}) Q-circle.

Once the lossless and lossy components of the port coupling coefficients are evaluated, they can then be used to calculate the the port coupling coefficients β_1 and β_2 using (4.34). The port coupling coefficients and the loaded Q_L -factor evaluated from the curve fitting can then be used to calculate the unloaded Q_o -factor using the full equation :

$$Q_o = Q_L (1 + \beta_1 + \beta_2) \quad (4.52)$$

4.4 EQUATIONS FOR THE FRACTIONAL LINEAR CURVE FITTING PROCEDURE TO THE TRANSMISSION MODE RESONATOR RESPONSES

Once equations relating the Q_L , β_1 and β_2 with S_{21} , S_{11} and S_{22} S-parameters for the transmission mode dielectric resonator have been derived, multi-frequency measurements of S_{21} , S_{11} and S_{22} need to be performed. The ideal test data should form Q-circles on the Smith Chart complex plane. Also, equations to fit a circle to S_{21} resonance data based on equation (4.21) and (4.22) needed to be derived. These equations were later used to develop software to enable calculations of the loaded Q_L -factor and resonant frequency from measurements data. As derived in Chapter 4.3, the expression (4.21) for the S_{21} Q-circle in the developed Transmission Mode Q_o -Factor Technique is of the following form :

$$S_{21} = \frac{a_1 t + a_2}{a_3 t + 1} \quad (4.53)$$

This can be rearranged to the following form :

$$S_{21} = a_1 t + a_2 - a_3 s_{21} t \quad (4.54)$$

where t is a normalised frequency variable described previously as (4.24) :

$$t = 2 \left(\frac{\omega - \omega_L}{\omega_L} \right) \quad (4.55)$$

As the form for S_{21} for the transmission mode resonator is the same as for S_{11} for the reflection mode resonator [1], the equations presented in this thesis for S_{21} are of similar mathematical formulas. Derivation of the equations is given in the Appendix A of this thesis, and implementation procedure in the Appendix B.

The novel curve Transmission Mode Q_o -Factor Technique developed in this thesis to obtain the Q_o -factor of transmission mode resonators taking into account lossy coupling has been implemented in the computer software **Q_Fit**. A MATLAB V5.3 [6] script has also been developed to synthesise sets of S_{21} , S_{11} and S_{22} data based on the derived functions describing the S-parameter responses of transmission resonators to be used in simulations and verification of the developed Q_o -factor technique to be presented in the following chapters.

BIBLIOGRAPHY OF CHAPTER 4

- [1] D. Kajfez, "Q factor" , Vector Fields, 1994.
- [2] Z. Ma, "RF properties of high temperature superconducting materials", PhD thesis, G.L. Report No. 5298, Edward L. Ginzton Laboratory, Stanford University, May 1995.
- [3] E.L. Ginzton, "Microwave Measurements", McGraw Hill Book Co., pp 403-408, 1957.
- [4] K.C. Gupta, R. Garg, R. Chadha, "Computer Aided Design of Microwave Circuits", Artech House Inc., 1981.
- [5] L.G. Parrat, "Probability And Experimental Errors In Science", New York: Wiley, 1961.
- [6] MATLAB Users Guide, Maths Works (1989).

CHAPTER 5

ASSESSMENT OF THE ACCURACY OF THE NOVEL TRANSMISSION MODE Q_0 -FACTOR TECHNIQUE USING COMPUTER SIMULATIONS

Software developed in the course of this thesis has been used to assess the accuracy of the developed Transmission Mode Q_0 -Factor Technique. The names of the software and their functions are listed as follows :

Q_Fit, Implements the Fractional Linear Curve Fitting procedure [1] of the Transmission Mode Q_0 -Factor Technique to obtain the unloaded Q_0 -factor of transmission mode resonators (from loaded Q_L -factor of the S_{21} fit and the port coupling coefficients from S_{11} and S_{22} fits).

Q_Gen, Q-circle generator/simulator used to simulate S_{21} , S_{11} and S_{22} Q-circles according to the circuit model of the transmission mode dielectric resonator of Fig. 5.1 used in the development of the Transmission Mode Q_0 -Factor Technique.

PlotQ, Utility for plotting S_{21} , S_{11} and S_{22} trace data contained in data files; data point selection and deletion; and implementation of the wide-span phase correction procedure [2].

All the software is provided on a **CDROM** instead of listing as an Appendix.

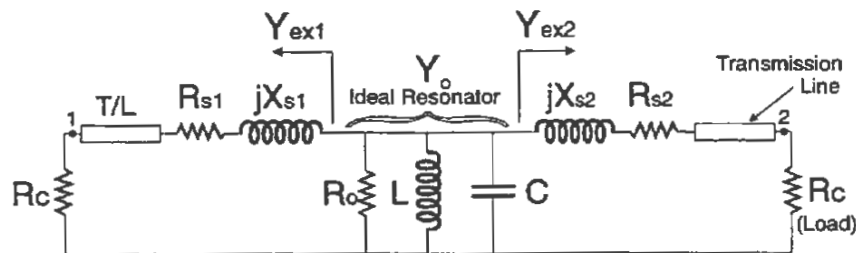


Figure 5.1 Circuit model of the transmission mode dielectric resonator used in the development of the Transmission Mode Q_0 -factor Technique.

The software **Q_Gen** (Q-circle Generator written in MATLAB V5.3 script) has been used to generate S-parameter data test sets for simulations of Q-circles in

the Smith Chart complex plane (based on the equations describing the frequency dependencies of S_{21} , S_{11} and S_{22} around the resonance for transmission mode dielectric resonators of Chapter 4.3). By choice of the circuit parameters (such as the length of transmission lines L_1 and L_2 , coupling reactances X_{s1} and X_{s2} , coupling resistances R_{s1} and R_{s2} unloaded Q_0 -factor, resonant frequency, and the amount of introduced noise), the number of data points, and the frequency span of the data sets, it was possible to simulate Q-circles influenced by the various practical component effects introduced by the practical measurement system and environment such as noise, coupling loss, frequency dependence of the coupling reactance, and electrical delay of transmission lines. **Q_Gen** also displays the generated S_{21} , S_{11} and S_{22} Q-circles on a Smith Chart, and stores the Q-circle data sets in data files.

Simulated Q-circles generated from **Q_Gen** were used in the testing, verification and assessment of the accuracy of the Transmission Mode Q-Factor Technique implemented within the software **Q_Fit**. Based on the Fractional Linear Curve Fitting routine implemented within the program, the **Q_Fit** program processes multi-frequency measurements of S_{21} , S_{11} and S_{22} Q-circles and returns various results which include :

- 1) The loaded Q_L -factor and resonant frequency f_0 obtained from fits to all three S-parameter Q-circle data sets (ie. Q_L and f_0 of S_{21} -fit, S_{11} -fit, and S_{22} -fit).
- 2) The coupling coefficients β_1 and β_2 (as well as their lossy and lossless components computed from S_{11} and S_{22} Q-circle data.
- 3) The unloaded Q_0 -factor calculated from the loaded Q_L -factor of S_{21} -fit and the coupling coefficients using the full equation $Q_0 = Q_L(1 + \beta_1 + \beta_2)$.
- 4) The fit parameters a_1 , a_2 and a_3 ; diameters of the fitted Q-circles; and the diameters of the loss circles associated with the S_{11} and S_{22} Q-circles.
- 5) The data scatter D_s parameter which indicates the reliability of results obtained from the curve fitting process.
- 6) The signal to noise ratio in the S_{21} , S_{11} , and S_{22} Q-circles.

The software **PlotQ** implements the phase correction procedure [2], namely the enhanced phase correction procedure described in Appendix C to remove distortion in the reflection (S_{11} or S_{22}) Q-circles caused by electrical delay of uncalibrated transmission lines. **PlotQ** first computes the rate of change of (S_{11} (or S_{22})) phase with frequency (ie. $\Delta\phi/\Delta F$) from measured wide-span S_{11} (or S_{22}) data. The program then uses $\Delta\phi/\Delta F$ to correct the phase of the measured S_{11} (or S_{22}) Q-circle data.

Assessment of the accuracy of the Transmission Mode Q_o -Factor Technique using computer simulations has done in two stages. The first stage was a verification stage where the technique was applied to ideal Q-circle data sets which excluded effects of noise, frequency dependence of the coupling reactances, and electrical delay introduced by transmission lines. Applying the **Q_Fit** software implementation of the Transmission Mode Q_o -Factor Technique to the ideal S-parameter data sets yielded perfect recovery of the unloaded quality factor as expected.

The second stage of the assessment involved studies of the accuracy of the Transmission Mode Q_o -factor Technique applied to Q-circles influenced by practical effects introduced by the connecting network and real measurement environment such as noise, electrical delay of transmission lines, coupling losses, and coupling reactances. By varying the value of a circuit parameter (usually a detrimental parameter) and keeping all other detrimental parameters at minimum (or constant) values, Q-circle test sets were generated using the **Q_Gen**. Each test set consisted of three data sets, namely the multi-frequency transmission (S_{21}) mode and reflection mode (S_{11} and S_{22}) S-parameter Q-circle data sets associated with the circuit parameters used in that test. By applying the Transmission Mode Q_o -Factor Technique to each Q-circle test set, the obtained values of unloaded Q_o -factor, loaded Q_L -factor and coupling coefficients results were compared to the nominal values for the test. The tests enabled assessment of the accuracy of the Transmission Mode Q_o -Factor Technique (applied to S-parameter Q-circles influenced by practical

effects introduced by a connecting network and real measurement environment) to be assessed. The details of the tests are presented in Chapter 5.1 to 5.5.

In all tests presented in this chapter, the coupling coefficients have been assigned to the symbol \mathbf{K} which can be interchanged with the symbol β . The symbol \mathbf{K} has been used because the conventional symbol β used to represent coupling coefficients is not supported by the software developed in this thesis, which operate in a MSDOS operating environment.

5.1. INFLUENCE OF NOISE ON THE ERROR IN THE UNLOADED Q_0 -FACTOR OBTAINED FROM THE TRANSMISSION MODE Q_0 -FACTOR TECHNIQUE

The effect of noise on the Transmission Mode Q_0 -Factor Technique was investigated over a wide range of noise levels (ie. noise radius level of 0.0005 to 0.02) [1]. The tests were performed for the worst case condition where the same noise data set was added to all three modes S_{21} , S_{11} and S_{22} for each noise level tested. To set the location of the Q-circles on the complex plane in positions typical for a practical case, the following parameters of the circuit model of the resonator system of Fig. 5.1 were used :

Coupling loss resistances $R_{s1}=R_{s2}=5 \Omega$, coupling reactances $X_{s1}=X_{s2}=20 \Omega$, shunt resistance of the ideal resonator $R_o=5 \Omega$, source resistance $R_c=50 \Omega$, transmission line to wavelength ratio $L/\lambda = 0$, unloaded Q_0 -factor = 9000, loaded Q_L -factor = 7754.7, $f_o = 10$ GHz, coupling coefficients $K_1 = K_2 = 0.080$, $N=401$ points, noise radius [1] ranging from 0.0005 to 0.02.

In the simulation, equal couplings were used and the frequency span of all Q-circles were chosen to be six times the loaded bandwidth centred about the resonant frequency.

The investigation required the generation of noise [1] to be added to synthesised S-parameter responses used to study the influence of noise on the results of the curve fitting technique. Simulated noise data sets were generated using

MATLAB V5.3 [3] to follow a Gaussian distribution - that is, having a zero mean and a standard deviation σ specified by the noise radius (R_N) [1] according to :

$$\sigma = R_N / \sqrt{2} \quad (5.1)$$

Noisy S-parameter data sets were obtained by superimposing the random noise on to a noise-free S-parameter data set using the following procedure. To add noise to the N point S-parameter data set **S** (containing elements S_i where $i = 1$ to N), two N point random number data sets **A** and **B** (containing elements A_i and B_i) need to be generated to represent the noise. Each random number has a standard deviation $R_N / \sqrt{2}$. By superposition, the noisy S-parameter data set can be obtained by adding the noise elements to the S-parameter elements according to :

$$S_i^{noisy} = Re[S_i] + A_i + j[Im[S_i] + B_i] \quad (i = 1..N) \quad (5.2)$$

The above procedure was used to synthesise noisy S_{21} , S_{11} and S_{22} traces (Q-circles) to be used for the tests to be presented on investigations of the influence of noise on the results (namely unloaded Q_o -factor, loaded Q_L -factor and coupling coefficients) obtained from the application of the Transmission Mode Q_o -Factor Technique. To take into account the statistical nature of the tests, ten independent simulations were performed for each noise level investigated. The **Q_Fit** program was applied to each of the Q-circle test sets (S_{21} , S_{11} and S_{22}) to provide the results (unloaded Q_o -factor, loaded Q_L -factor and coupling coefficients and their errors) of the study to be presented.

Table 5.1 shows the maximum calculated error in the unloaded and loaded Q-factors obtained from Q_L of S_{21} and S_{11} fits over 10 simulations for each noise level ranging from noise radius of 0.0005 to 0.02. For each noise radius, the table also shows the associated coupling coefficients and signal to noise ratio calculated according to the following formula [4] :

$$SNR_{dB} = 20 \log_{10} \left(\frac{1}{N} \sum_{i=1}^N \frac{R}{R - r_i} \right) \quad (5.3)$$

where R is the radius of the Q-circle, r_i is the distance from the centre of the Q-circle to the i_{th} point in the data set, and N is the total number of points in the data set.

Table 5.1 Errors in unloaded and loaded values of Q-factor, and coupling coefficients under equal couplings in the presence of noise. The computed signal to noise ratio for each noise condition is also given. The noise radius is varied between 0.0005 and 0.02.

Noise Radius	ΔQ_0 (max)% S_{21} fit	ΔQ_L % S_{21} fit	ΔK % S_{21} fit	ΔQ_0 (max)% S_{11} fit	ΔQ_L % S_{11} fit	ΔK % S_{11} fit	SNR For S_{21} (dB)
0.0005	-0.2	-0.21	0.04	-0.44	-0.42	-0.19	45
0.0010	-0.56	-0.57	0.09	-0.7	-0.65	-0.42	39
0.0015	-0.79	-0.7	-0.65	1.65	1.58	0.48	36
0.0020	-1.52	-1.37	-1.09	1.62	1.6	0.19	33
0.0030	-2.77	-2.74	-0.23	-1.71	-1.71	-0.01	29
0.0040	-5.19	-5.02	-1.29	-2.87	-2.81	-0.46	26
0.0050	-7.11	-7.04	-0.56	5.14	4.91	1.57	23
0.0100	-22.49	-22.72	2.23	-6.78	-7.28	3.93	15
0.0200	-56.02	-50.24	-83.96	-22.22	-12	-83.96	6

The results of Table 5.1 above show that the Transmission Mode Q_0 -Factor Technique can be used to obtain the unloaded Q_0 -factor from relatively noisy synthesised S-parameter trace data (up to noise radius of 0.004) with error not exceeding 5 %. For the test with noise radius of 0.004, the signal to noise ratio in the S_{21} trace is equal to 26 dB. For a noise radius value of 0.002 (and computed signal-to-noise ratio in the S_{21} trace equal to 33 dB), the error in the unloaded Q_0 -factor calculated from the loaded Q_L -factor of the S_{21} -fit and the coupling coefficients obtained from the technique is only about 1.52 %. Figures 5.2, 5.3, 5.4 and 5.5 provide a visual comparison of the noise in the S_{21} Q-circle trace for noise radii of 0.001, and 0.002 respectively under the equal coupling condition.

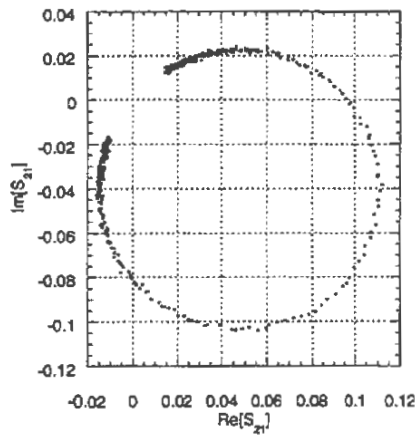


Figure 5.2 S_{21} , $NR=0.001$ equal couplings.

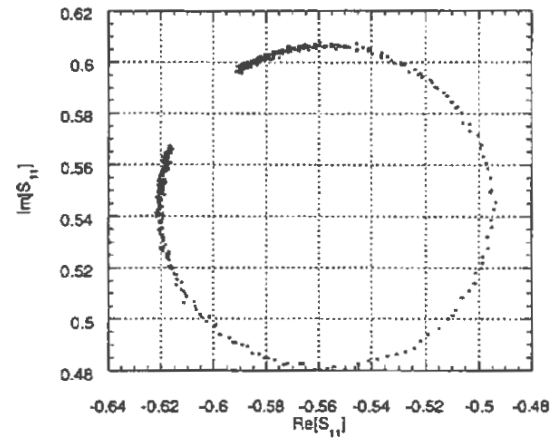


Figure 5.3 S_{11} , $NR=0.001$ equal couplings.

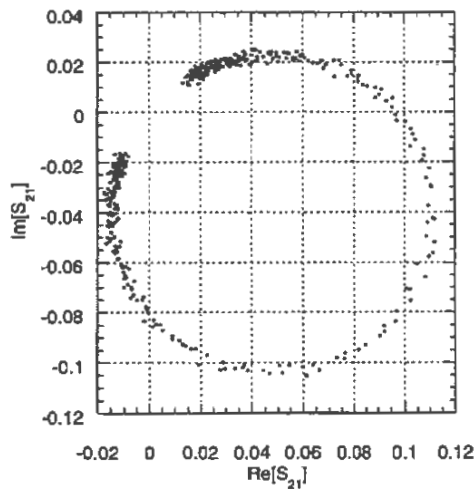


Figure 5.4 S_{21} , $NR=0.002$ equal couplings.

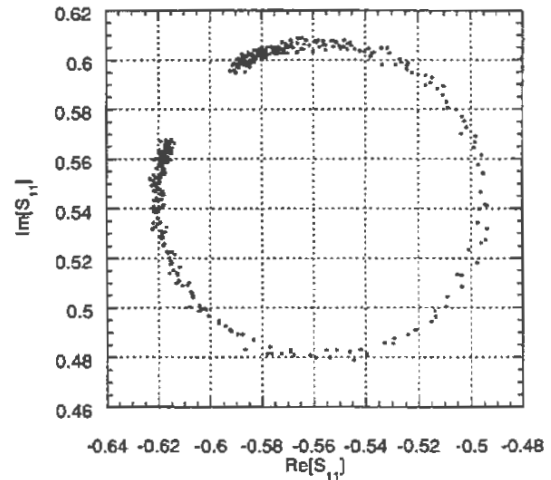


Figure 5.5 S_{11} , $NR=0.002$ equal couplings.

The results of the Table 5.1 also indicate that for large noise radius greater than about 0.003, the errors in the unloaded Q_0 -factor calculated from the Q_L -factor of S_{21} -fit are larger than from the unloaded Q_0 -factor calculated from the Q_L -factor

of S_{11} -fit. In practice, S_{21} Q-circles are typically less noisy than the case of Fig. 5.2 corresponding to noise radius of 0.001 (with calculated signal to noise ratio equal to 39 dB; and coupling coefficients $K_1 = K_2 = 0.080$).

To investigate the influence of noise on the error in Q_o of transmission and reflection fit with different couplings, the following parameters were used :

$R_{s1}=R_{s2}=5 \Omega$, $X_{s1}=20 \Omega$, $X_{s2}=60 \Omega$, $R_o=5 \Omega$, $R_c=50 \Omega$, $L/\lambda = 0$, unloaded Q_o -factor = 9000, unloaded Q_L -factor = 8112, $f_o = 10$ GHz, coupling coefficients $K_1 = 0.080$, $K_2 = 0.029$, $N=401$ points, noise radius ranging from 0.0005 to 0.004.

Table 5.2 below gives the maximum error in the unloaded Q-factor from S_{21} fit and S_{11} fit together with the corresponding errors in the fitted loaded Q-factor and coupling coefficients obtained for the simulations for noise radius from 0.0005 to 0.004.

Table 5.2 Errors in unloaded and loaded values of Q-factor, and coupling coefficients under different couplings in the presence of noise. The computed signal to noise ratio for each noise condition is also given. The noise radius is varied between 0.0005 and 0.004.

Noise Radius	$\Delta Q_o(\text{max})\%$	$\Delta Q_L \%$	$\Delta K \%$	$\Delta Q_o(\text{max})\%$	$\Delta Q_L \%$	SNR dB	SNR dB	SNR dB
	S_{21} fit	S_{21} fit		S_{11} fit	S_{11} fit	S_{21}	S_{11}	S_{22}
0.0005	-0.30	-0.30	-0.04	-0.20	-0.19	40.7	44.8	35.1
0.0010	-0.83	-0.93	0.94	1.04	0.97	34.6	38.4	29.9
0.0015	-1.75	-1.67	-0.83	-0.63	-0.68	30.8	35.6	25.8
0.0020	-3.05	-2.93	-1.20	-1.61	-1.65	27.8	32.5	22.7
0.0030	-6.71	-6.71	-0.06	-2.23	-2.17	23.3	29.6	19.5
0.0040	-10.94	-10.9	-0.49	-2.32	-2.60	19.8	26.7	17.0

The above results shows that the Transmission Mode Q_o -Factor Technique works well for relatively high levels of noise in the S_{21} trace, such as for the case of noise radius equal to 0.002 (and computed SNR equal to 27.8 dB) where the error in the unloaded Q_o -factor obtained from Q_L of S_{21} -fit is about 3 %. The results show

that the error in the loaded Q_L -factor and the coupling coefficients (and hence the unloaded Q_o -factor) obtained from the developed technique increases with the noise level as expected. The error in the unloaded quality factor exceeds 10% only when the noise radius exceeds 0.004 (and computed SNR equal to 19.8 dB). For large noise radius, the error in the unloaded Q_o -factor calculated from Q_L -factor of S_{21} -fit is bigger than the error in the unloaded Q_o -factor calculated from the Q_L -factor of S_{11} -fit.

Figures 5.6, 5.7, and 5.8 shows simulated noisy S_{21} , S_{11} and S_{22} Q-circles respectively for a case of unequal coupling and simulated noise radius of 0.001. The coupling coefficient for port 1 is about 2.75 times greater than the coupling on port 2. Using the fitted results of 10 runs for a noise radius NR of 0.001, the maximum calculated error in fitted Q_o is 0.83% using the Q_L of S_{21} -fit and 1.04% using the Q_L of S_{11} -fit. As the coupling for port 2 is weaker than for port 1, the S_{22} trace is expected to have a higher SNR, and the error in Q_o fitted using Q_L of S_{22} -fit is expected to be higher than for Q_o using the Q_L of S_{11} -fit. While it is not shown in the results of Table 5.2, a maximum error in Q_o using the fitted value of Q_L of the S_{22} -fit was found to be 4.27%, which is higher than the fitted value using Q_L of S_{11} -fit as expected.

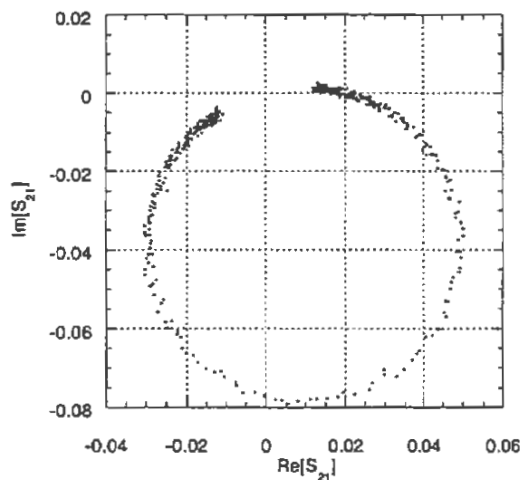


Figure 5.6 S_{21} , NR=0.001 unequal couplings.

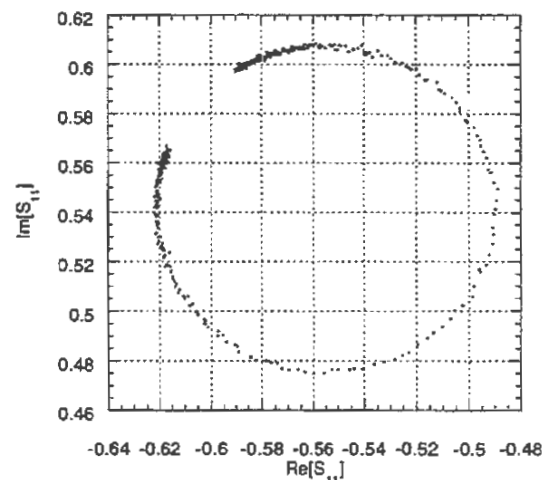


Figure 5.7 S_{11} , NR=0.001 unequal couplings.

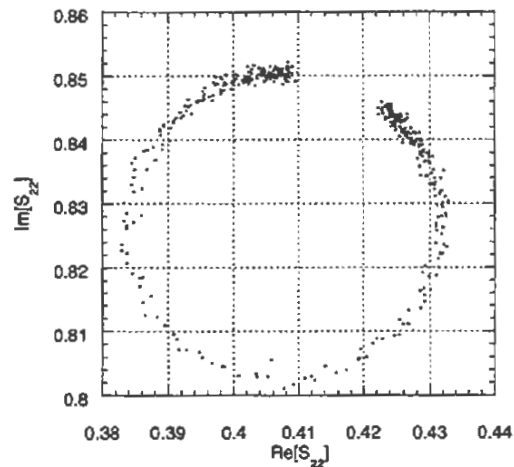


Figure 5.8 S_{22} , $NR=0.001$ unequal couplings.

The investigation of the influence of noise on the error in the Q_0 -factor obtained from the Transmission Mode Q_0 -Factor Technique indicates that the technique can effectively eliminate the influence of noise to provide accurate values of the Q_0 -factor for noise levels typically encountered in practical test conditions. The noise level in the simulated S_{21} trace for the case of noise radius equal to 0.001 is slightly higher than the levels encountered in practical measurements of S_{21} Q -circles performed by author of this thesis. For noise radius equal to 0.001 (and calculated signal to noise ratio in the S_{21} trace equal to 34.6 dB; coupling coefficients K_1 and K_2 equal to 0.080 and 0.029 respectively), the accuracy in the obtained Q_0 -factor is better less than 1 percent (when phase effects due to transmission lines are not included in the simulation).

5.2. INFLUENCE OF FREQUENCY DEPENDENCE OF DELAY DUE TO TRANSMISSION LINES ON ERRORS IN Q_0 AND A METHOD TO REMOVE THIS EFFECT FROM REFLECTION (S_{11} OR S_{22}) Q -CIRCLES

Errors in the unloaded Q_0 -factor due to delay introduced by transmission lines were investigated for short transmission lines ($L/\lambda < 0.6$) and long transmission

lines ($L/\lambda = 30$). For investigations of the effect of delay, the following parameters were selected to simulate a equal coupling condition ($K_1=K_2=0.08$), and to place the Q-circles in positions typical for practical measurements on the complex plane : $R_{s1}=R_{s2}=5 \Omega$, $X_{s1}=X_{s2}=20 \Omega$, $R_o=5 \Omega$, $R_c=50 \Omega$, $N=401$ points. The fitting procedure was applied to the synthesised traces for L/λ ratios ranging from 0 to 0.55λ . Tables 5.3 and 5.4 show the errors in the unloaded and loaded values of the Q-factors and coupling coefficient (obtained using the Transmission Mode Q_o -Factor Technique) for each L/λ tested for two Q-factor values, a relatively low Q_o of 1000, and a higher value of 10000.

Table 5.3 : Maximum error in Q_o obtained from Q_L of S_{21} and S_{11} fit, and corresponding values of Q_L and coupling coefficient for $Q_o = 1000$ for varying transmission line length.

L/λ	$\Delta Q_o(\text{max})\%$ using Q_L of S_{21}	$\Delta Q_o(\text{max})\%$ using Q_L of S_{11}	$\Delta Q_L\%$ (S_{21} fit)	$\Delta Q_L\%$ (S_{11} fit)	$\Delta K\%$
0	0.00	0.00	0.00	0.00	0.00
0.05	-0.06	0.94	0.00	0.99	-0.43
0.1	-0.11	1.83	0.00	1.94	-0.84
0.15	-0.17	2.67	0.00	2.85	-1.23
0.2	-0.22	3.47	0.00	3.69	-1.60
0.25	-0.26	4.21	0.00	4.49	-1.95
0.3	-0.31	4.89	0.00	5.21	-2.28
0.35	-0.35	5.50	0.00	5.88	-2.60
0.4	-0.39	6.04	0.01	6.47	-2.89
0.45	-0.43	6.51	0.01	6.98	-3.16
0.5	-0.46	6.91	0.01	7.41	-3.42
0.55	-0.49	7.22	0.01	7.76	-3.65

Table 5.4 : Maximum error in Q_o obtained from Q_L of S_{21} and S_{11} fit, and corresponding values of Q_L and coupling coefficient for $Q_o = 10000$ for varying transmission line length.

L/λ	$\Delta Q_o(\text{max})\%$ using Q_L of S_{21}	$\Delta Q_o(\text{max})\%$ using Q_L of S_{11}	$\Delta Q_L\%$ (S_{21} fit)	$\Delta Q_L\%$ (S_{11} fit)	$\Delta K\%$
0	0.00	0.00	0.00	0.00	0.00
0.05	-0.01	0.10	0.00	0.10	-0.04
0.1	-0.01	0.19	0.00	0.20	-0.09
0.15	-0.02	0.28	0.00	0.30	-0.13
0.2	-0.02	0.38	0.00	0.40	-0.17
0.25	-0.03	0.47	0.00	0.50	-0.22
0.3	-0.04	0.57	0.00	0.60	-0.26
0.35	-0.04	0.66	0.00	0.70	-0.30
0.4	-0.05	0.75	0.00	0.80	-0.34
0.45	-0.05	0.84	0.00	0.90	-0.39
0.5	-0.07	0.93	0.00	0.99	-0.47
0.55	-0.07	1.02	0.00	1.09	-0.51

Figures 5.9-5.14 below show errors in the unloaded Q_o and Q_L factors obtained after applying the Transmission Mode Q_o -Factor Technique to the simulated S_{21} , S_{11} and S_{22} data sets for nominal Q_o factor of 1000, 10000, and 100000.

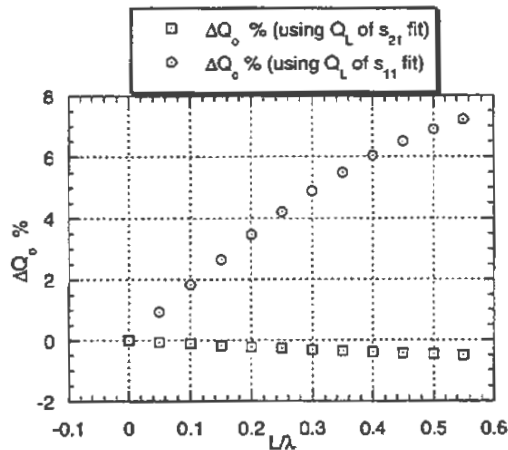


Figure 5.9 : Error in Q_o using Q_L of S_{21} and S_{11} fits for Q_o of 1000.

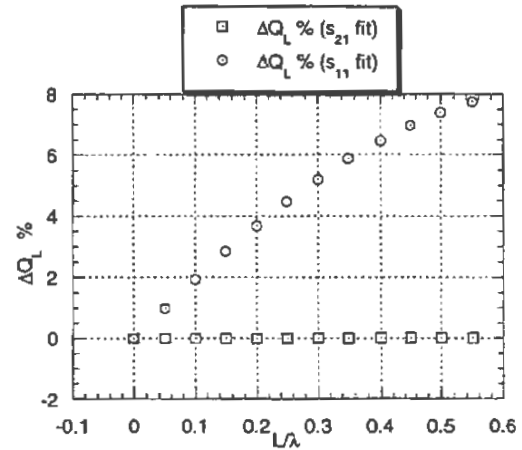


Figure 5.10 Error in Q_L obtained from S_{21} and S_{11} fits for Q_o of 1000.

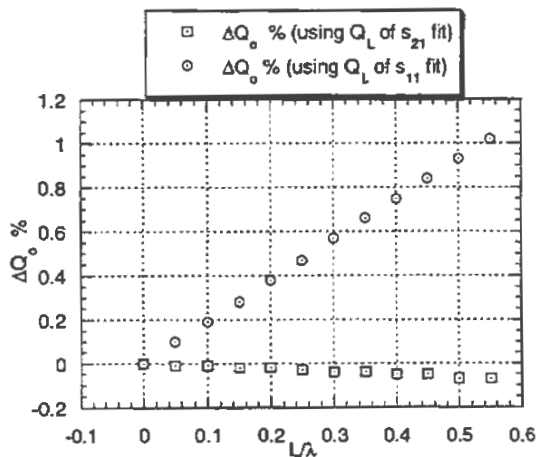


Figure 5.11 : Error in Q_o using Q_L of S_{21} and S_{11} fits for Q_o of 10000.

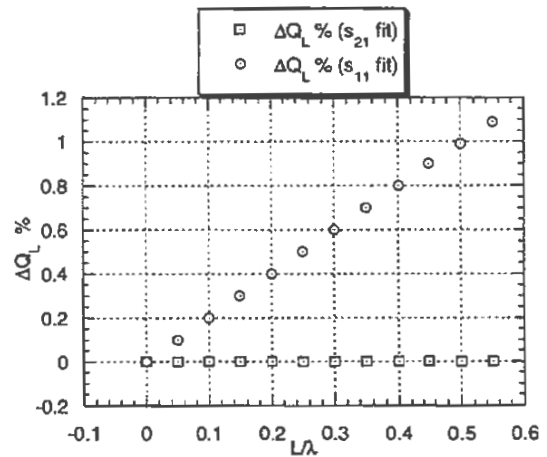


Figure 5.12 : Error in Q_L obtained from S_{21} and S_{11} fits for Q_o of 10000.

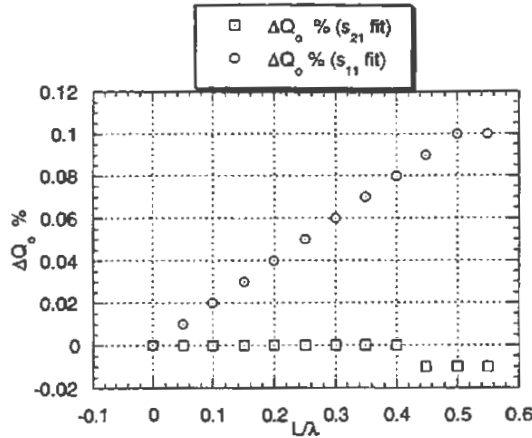


Figure 5.13 : Error in Q_0 using Q_L of S_{21} and S_{11} fits for Q_0 of 100000.

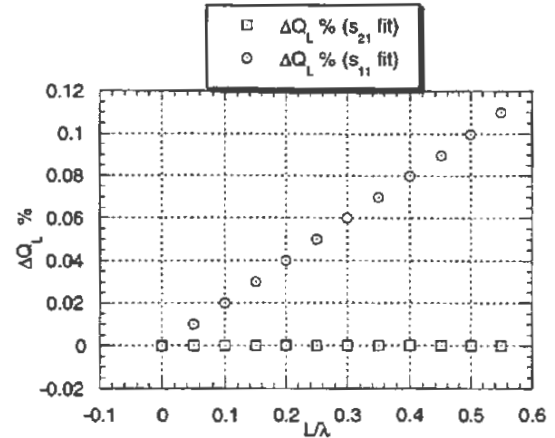


Figure 5.14 : Error in Q_L obtained from S_{21} and S_{11} fits for Q_0 of 100000.

It is clearly seen from the above results that for any finite cable length, the error in the unloaded Q_0 -factor obtained from the S_{21} -fit is always less than unloaded Q_0 -factor of the S_{11} -fit, indicating that the reflection (S_{11} or S_{22}) Q-circles are distorted more than transmission S_{21} Q-circles in the presence of transmission line delay. Also, simulations show that for any length of cable present in the system, the error in the fitted Q_0 becomes reduced as the Q_0 of the resonator increases. The results indicate that the error in the fitted Q_0 for a system with Q_0 of 10000 is about 10 times lower than the case for a system with Q_0 of 1000. In fact, errors in the unloaded Q_0 -factor and the loaded Q_L -factor reduce by a factor of about ten for each relative increase in the Q_0 -factor by a factor of ten for any resonator system. It can also be seen that for the cases where lines have a length greater than 0.2λ , the error in the Q_L -factor obtained from S_{11} or S_{22} fits can be much higher than the error in Q_L of S_{21} fit. The error is clearly due to the distortion in the reflection circle due to the frequency dependence of the cable phase shift. The results show that the distortion in reflection circles due to long uncalibrated lengths of cable is typically much greater than in transmission circles.

The influence of the uncalibrated cable on the simulated S_{21} and S_{11} Q-circles for $L = 30\lambda$ (nominal $Q_0 = 1000$, nominal $Q_L = 861$) can be observed in Fig. 5.15 and Fig. 5.16. For such large line length, severe distortions can be seen in the reflection

Q-circle while the S_{21} Q-circle is much better preserved. The Q_L of S_{21} -fit on the 401 point S_{21} Q-circle of Fig. 5.15 was equal to 990 (15% error compared to the nominal value of Q_L). When the most distorted part of the S_{21} Q-circle is removed (the points with index below 160 and the above 260) from the original 401 point S_{21} Q-circle of Fig. 5.15 to give a 101 point reduced data set S_{21} Q-circle (Fig. 5.17), a loaded Q_L of 893 was obtained with only 3.7 % difference from the nominal value of 861. Such low errors in the Q_L obtained from the S_{21} -fit were typical once the distorted off-resonance regions are removed.

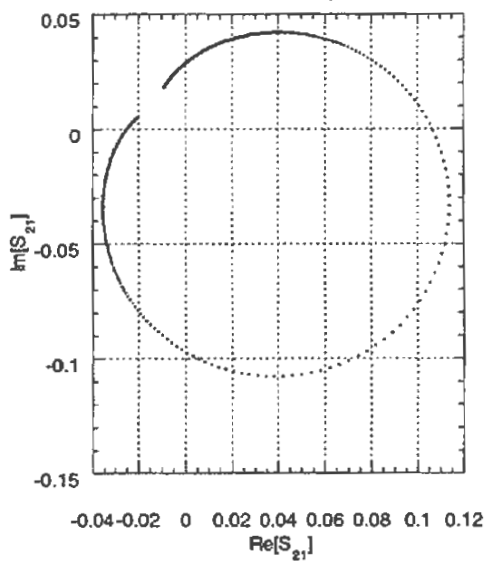


Figure 5.15 S_{21} Q-circle for line length
 $= 30\lambda$, span = 6.96 MHz.

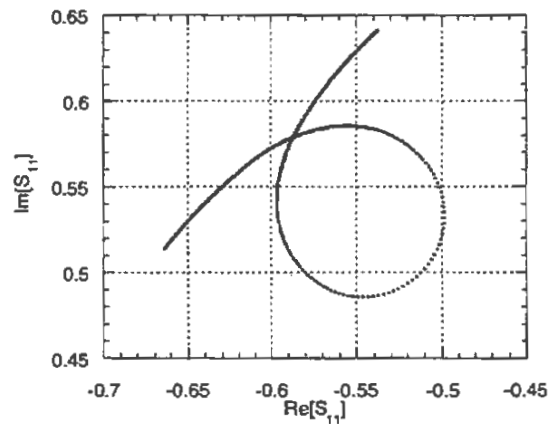


Figure 5.16 S_{11} Q-circle for line length
 $= 30\lambda$, span = 6.96 MHz.

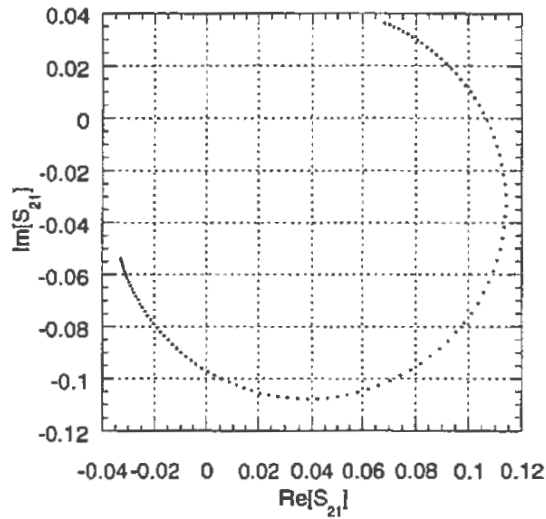


Figure 5.17 A 101 point S_{21} Q-circle subset of the 401 point S_{21} Q-circle of Fig. 5.15.

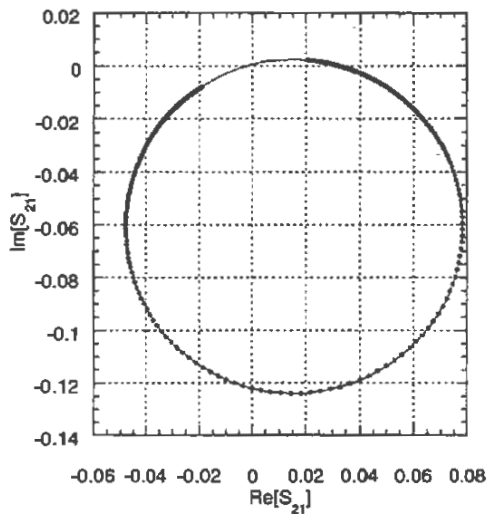


Figure 5.18 S_{21} circle fitted over 401 points of simulated data, with parameters $R_{s1}=R_{s2}=5\Omega$, $X_{s1}=X_{s2}=20\Omega$, $Q_o = 1000$, $L/\lambda=0.55$, $f_o = 10$ GHz.

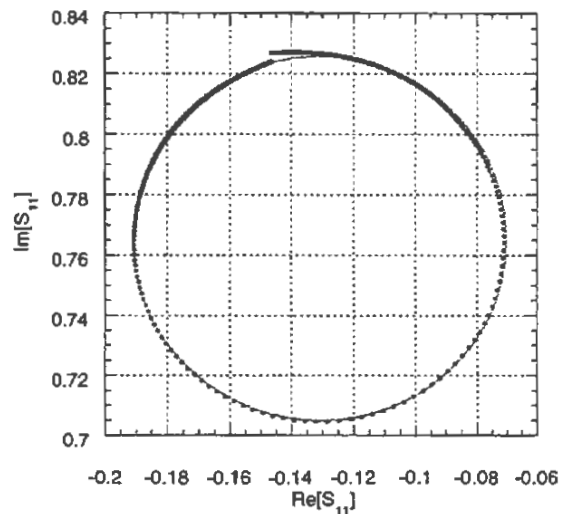


Figure 5.19 S_{11} circle fitted over 401 points of simulated data, with parameters $R_{s1}=R_{s2}=5\Omega$, $X_{s1}=X_{s2}=20\Omega$, $Q_o = 1000$, $L/\lambda=0.55$, $f_o = 10$ GHz.

The presented simulation results show that the reflection curves are heavily influenced by cable effects such as in the S_{11} Q-circle shown in Fig. 5.16 (which

corresponds to transmission line length on each port of 30 wavelengths long). Under such circumstance the influence of the delay due to the cables needs to be removed in order to obtain accurate coupling coefficients and hence the Q_o -factor using the Transmission Mode Q_o -Factor Technique. If the rate of change of phase with frequency is known, then it is possible to remove the phase effects of the cable through an enhanced procedure involving measurements of wide-span reflection coefficient (S_{11} and S_{22}) data. Such enhanced procedure to remove phase effects is described in Appendix C.

5.3. INFLUENCE OF THE FREQUENCY DEPENDENCE OF THE COUPLING REACTANCE X_s ON ERRORS IN Q_o IN THE ABSENCE OF TRANSMISSION LINE DELAY

In circuit model of Fig. 5.1 used in the development the Transmission Mode Q_o -Factor Technique, it has been assumed that the coupling reactances X_{s1} and X_{s2} which represent reactances due to coupling structures are independent of frequency. In practice, coupling reactances are frequency dependent. However the assumption of constant reactance has been proven justifiable in resonant systems with Q -factors greater than 100 as mentioned earlier in Chapter 4 [1], where the percentage bandwidth relative to the resonance frequency is less than 1 percent. Simulations have been performed to investigate the influence of the frequency dependence of the coupling reactance on the accuracy of the Transmission Mode Q_o -Factor Technique using the following circuit parameters :

$X_{s1}=X_{s2}=X_s$ ranging from 0 to 250 Ω , $R_1=R_2=1\Omega$, $R_o=5\Omega$, $f_o=10\text{GHz}$, $L_1=L_2=0$ (ie. no introduced phase effects from transmission lines), $N=401$ points.

In simulations, the coupling reactance is assumed to be inductive with the frequency dependence :

$$X_s(f) = X(f_o) \frac{f}{f_o} \quad (5.4)$$

where $X_s(f_o)$ is the value of the coupling reactance at the resonant frequency f_o . As shown below, Table 5.5 and Table 5.6 gives errors in unloaded Q_o -factors calculated

from the loaded Q_L -factor of S_{21} -fit and S_{11} -fit respectively over various values of X_s/R_c (ranging from 0 to 5) for two nominal system unloaded Q -factors - 1000 and 10000.

Table 5.5 Error in Q_o calculated from Q_L of S_{21} -fit for variations in X_s/R_c .

X_s (Ω)	X_s/R_c	ΔQ_o from S_{21} fit (%)		X_s (Ω)	X_s/R_c	ΔQ_o from S_{21} fit (%)	
		$Q_o = 1000$	$Q_o = 10000$			$Q_o = 1000$	$Q_o = 10000$
0	0	0.00	0.00	60	1.2	-0.09	-0.01
1	0.02	0.00	0.00	80	1.6	-0.08	-0.01
5	0.1	-0.02	0.00	100	2.0	-0.07	-0.01
10	0.2	-0.04	0.00	150	3.0	-0.05	-0.01
20	0.4	-0.08	-0.01	200	4.0	-0.03	0.00
50	1	-0.10	-0.01	250	5.0	-0.02	0.00

Table 5.6 Error in Q_L calculated from Q_L of S_{11} -fit for variations in X_s/R_c .

X_s (Ω)	X_s/R_c	ΔQ_o from S_{11} fit (%)		X_s (Ω)	X_s/R_c	ΔQ_o from S_{11} fit (%)	
		$Q_o = 1000$	$Q_o = 10000$			$Q_o = 1000$	$Q_o = 10000$
0	0	0.00	0.00	60	1.2	2.70	0.28
1	0.02	0.05	0.01	80	1.6	3.41	0.37
5	0.1	0.27	0.03	100	2.0	4.07	0.45
10	0.2	0.54	0.05	150	3.0	5.67	0.66
20	0.4	1.04	0.11	200	4.0	6.87	0.86
50	1	2.32	0.24	250	5.0	7.88	1.06

The results of simulations shown in Table 5.5 and Table 5.6 indicate that the influence of the frequency dependence of the coupling reactance X_s on the accuracy of the fitted results reduces for higher Q_o factor systems, and that the coupling reactance can be assumed constant for high Q_o -factor resonators. Figures 5.20 and 5.21 show graphs based on the results of Table 5.5 and Table 5.6 to show errors in the Q_o -factor calculated from the loaded Q_L -factor obtained from S_{21} and S_{11} -fits for

nominal Q_0 of 1000 as X_s/R_c is varied over the range 0 to 5. For the same range of X_s/R_c , Fig. 5.22 shows errors in the coupling coefficients.

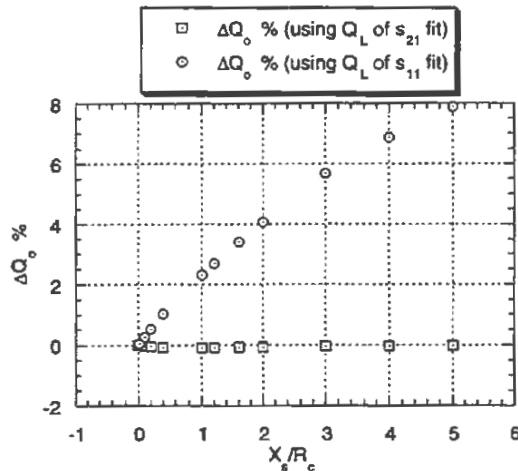


Figure 5.20 Error in Q_0 using Q_L of S_{21} and S_{11} fits for Q_0 of 1000 over various values of X_s with dependence on frequency.

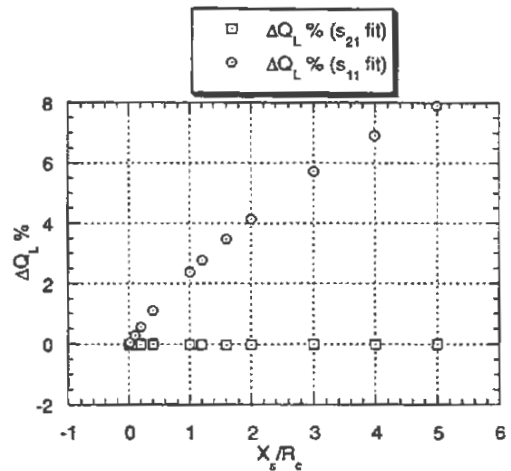


Figure 5.21 Error in Q_L obtained from S_{21} and S_{11} fits for Q_0 of 1000 over various values of X_s with dependence on frequency.

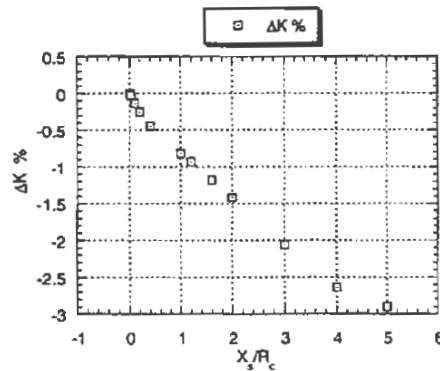


Figure 5.22 Error in fitted coupling coefficient obtained for Q_0 of 1000 over various values of X_s with dependence on frequency. Equal couplings are used.

Figures 5.23 and 5.24 show errors in the Q_0 -factor calculated from the loaded Q_L -factor obtained from S_{21} and S_{11} -fits based on the results of Table 5.5 and Table 5.6

for nominal Q_o of 10000 as X_s/R_c is varied over the range 0 to 5. For the same range of X_s/R_c , Fig. 5.25 shows the error in the coupling coefficients.

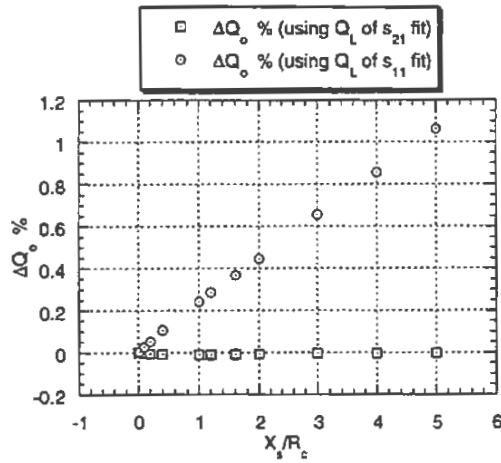


Figure 5.23 Error in Q_o using Q_L of S_{21} and S_{11} fits for Q_o of 10000 over various values of X_s with dependence on frequency.

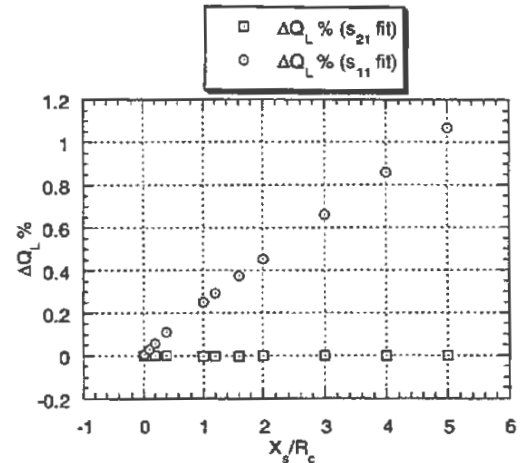


Figure 5.24 Error in Q_o using Q_L of S_{21} and S_{11} fits for Q_o of 10000 over various values of X_s with dependence on frequency.

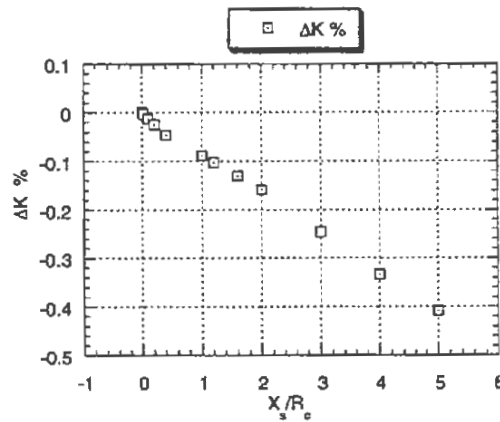


Figure 5.25 Error in fitted coupling coefficient for a case of $Q_o = 10000$ over various values of X_s with dependence on frequency.

In general, the results of the investigation shows that the error in the unloaded Q_o -factor obtained from Q_o of S_{21} -fit and S_{11} -fit increases with the coupling

reactance X_s . For all tests, the loaded Q_L -factor (and hence Q_o) obtained from S_{21} -fit is always much more accurate than the loaded Q_L -factor (and hence Q_o) of S_{11} -fit, indicating that a S_{21} Q-circle is distorted much less than the reflection circle for each value of X_s/R_c investigated. From the results of the test done with a relatively low Q_o -factor of 1000, the error unloaded Q_o -factor calculated from Q_L of S_{21} fit is found to be 0.1 % or less over the tested range of X_s/R_c , while the error in the unloaded Q_o -factor calculated from Q_L of S_{11} fit is less than 8 % over the same range of X_s/R_c .

5.4. INFLUENCE OF VARIATION IN COUPLING LOSSES (MODELLED USING R_s) ON ERRORS IN Q_o IN THE PRESENCE OF CABLE DELAY

This study investigates the accuracy of the developed Transmission Mode Q_o -Factor Technique when it is applied to synthesised S-parameter data sets influenced by coupling losses and in the presence of electrical delay introduced by transmission lines. If no electrical delay were to be introduced, the Transmission Mode Q_o -Factor Technique would find the unloaded Q_o -factor with perfect accuracy. Hence, short lengths transmission line (each of $L=0.2\lambda$) were introduced in the simulations. For the simulations, the following circuit parameters as referred to the circuit model the transmission system of Fig. 5.1 were used :

$X_{s1}=X_{s2}=0.2\Omega$, $L_1=L_2=L=0.2\lambda$, $f_o = 10\text{GHz}$, $R_{s1}=R_{s2}=R_s$ (resistances used to model the coupling losses, ranging from from 0 to 250Ω ie. R_s/R_c ranging from 0 to 5 where R_c is the characteristic impedance of 50Ω). Equal couplings have been assumed.

Simulations using the above circuit parameters were performed for cases of a low Q_o of 1000 and a higher Q_o factor 10000, using 401 data points spanning 6 times the loaded bandwidth around the resonant frequency. Table 5.7 and Table 5.8 show obtained errors in the unloaded Q_o -factor calculated from the Q_L -factors of S_{21} -fit and S_{11} -fit respectively tested for R_s/R_c ranging from 0 to 5 and for nominal unloaded Q_o -factor values of 1000 and 10000.

Table 5.7 Errors in the unloaded Q_0 -factor calculated from the Q_L -factors of S_{21} -fit for variations of R_s/R_c .

R_s (Ω)	R_s/R_c	$\Delta Q_0/Q_0$ from S_{21} fit (%)		R_s (Ω)	R_s/R_c	$\Delta Q_0/Q_0$ from S_{21} fit (%)	
		$Q_0 = 1000$	$Q_0 = 10000$			$Q_0 = 1000$	$Q_0 = 10000$
0	0	-0.28	-0.03	60	1.2	0.07	0.01
1	0.02	-0.28	-0.03	80	1.6	0.19	0.02
5	0.1	-0.25	-0.03	100	2.0	0.31	0.03
10	0.2	-0.22	-0.02	150	3.0	-0.44	0.06
20	0.4	-0.16	-0.02	200	4.0	-2.41	0.09
50	1	0.01	0.00	250	5.0	-1.79	0.12

Table 5.8 Errors in the unloaded Q_0 -factor calculated from the Q_L -factors of S_{11} -fit for variations of R_s/R_c .

R_s (Ω)	R_s/R_c	$\Delta Q_0/Q_0$ from S_{11} fit (%)		R_s (Ω)	R_s/R_c	$\Delta Q_0/Q_0$ from S_{11} fit (%)	
		$Q_0 = 1000$	$Q_0 = 10000$			$Q_0 = 1000$	$Q_0 = 10000$
0	0	3.17	0.34	60	1.2	-1.67	-0.16
1	0.02	3.15	0.34	80	1.6	-5.30	-0.50
5	0.1	3.08	0.33	100	2.0	-10.56	-0.93
10	0.2	2.94	0.32	150	3.0	> 10	-2.44
20	0.4	2.53	0.27	200	4.0	> 10	-4.58
50	1	0.02	0.00	250	5.0	> 10	-7.55

Figures 5.26 and 5.27 show errors in the unloaded Q_0 -factor calculated using the loaded Q_L -factor of S_{21} and S_{11} fits (Table 5.7 and Table 5.8) for varying values of R_s/R_c and for a nominal Q_0 -factor of 1000. Figure 5.28 shows errors in the coupling coefficient over the same range of R_s/R_c and Q_0 -factor.

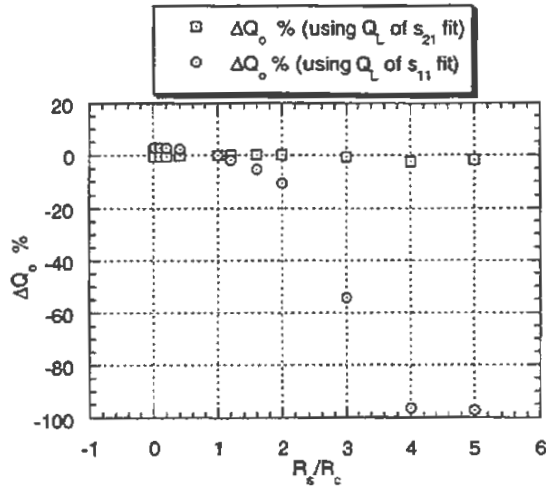


Figure 5.26 Error in Q_o using Q_L of S_{21} and S_{11} fits for various R_s and nominal Q_o of 1000. $L=0.2\lambda$.

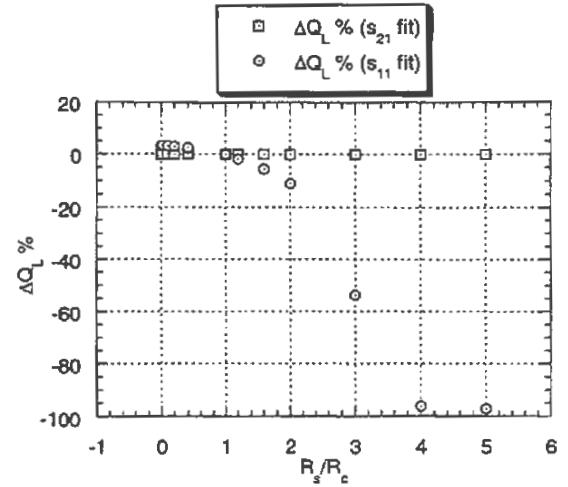


Figure 5.27 Error in Q_L obtained from Q_L of S_{21} and S_{11} fits for various R_s and nominal Q_o of 1000. $L=0.2\lambda$.

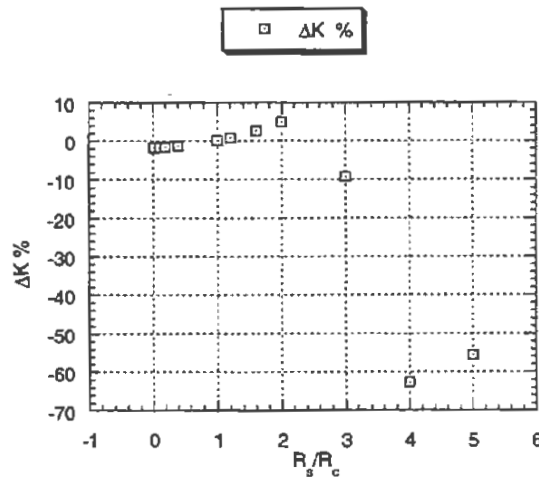


Figure 5.28 Error in coupling coefficient for various R_s and nominal Q_o of 1000. $L=0.2\lambda$.

Figures 5.29 and 5.30 show errors in the unloaded Q_o -factor calculated using the loaded Q_L -factor of S_{21} and S_{11} fits (based on the results of Table 5.7 and Table 5.8) for varying values of R_s/R_c and for a nominal Q_o -factor of 10000. Figure 5.31 shows errors in the coupling coefficient over the same range of R_s/R_c and Q_o -factor.

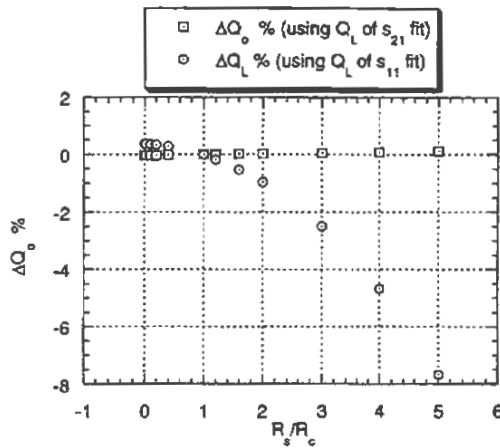


Figure 5.29 Error in Q_o using Q_L of S_{21} and S_{11} fits for various R_s and nominal Q_o of 10000. $L=0.2\lambda$.

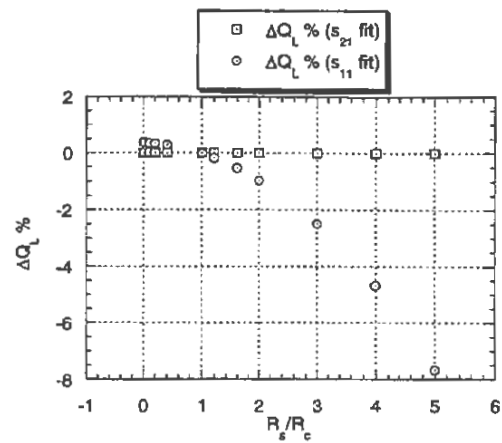


Figure 5.30 Error in Q_L obtained from S_{21} and S_{11} fits for various R_s and nominal Q_o of 10000. $L=0.2\lambda$.

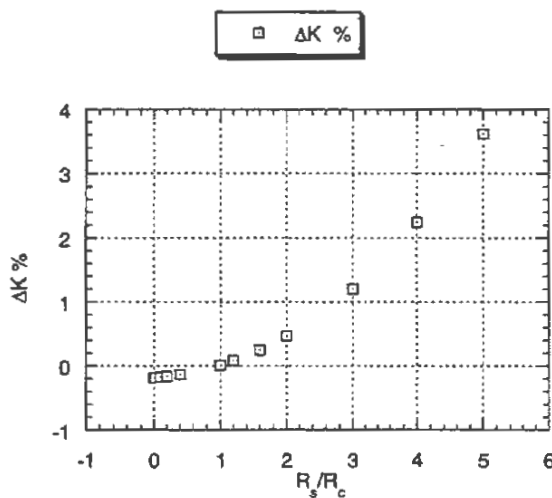


Figure 5.31 Error in coupling coefficient for various R_s and nominal Q_o of 10000. $L=0.2\lambda$.

From Table 5.7 and Table 5.8, and illustrated in Fig. 5.26-5.31, it is clear that the error in the fitted Q_o -factor increases as the coupling losses are increased. However, the error in Q_o is primarily due to the error in the fitted coupling coefficients resulting from the distortion of the reflection Q -circles caused by the delay of transmission lines in the system. The distortion increases with the coupling loss. For the case of $Q_o = 1000$ and R_s/R_c greater than 3, significant distortion is observed in the reflection Q -circles. For the same range of R_s/R_c values but for a system with a

Q_0 -factor 10 times larger ($Q_0 = 10000$), the distortion in the reflection Q-circle is significantly reduced, and the error in Q_0 obtained from S_{11} (or S_{22}) fit is also significantly reduced (as compared to the case of $Q_0 = 1000$). The error in the Q_0 -factor for the case of Q_0 of 10000 is approximately ten smaller than for the case of Q_0 of 1000. The error is reduced because the variation of delay around the resonance is smaller for higher Q_L -factors as a result of the reduced bandwidth. The same trend in the error reduction for higher Q_L -factors also applies for S_{21} fits. It is found that S_{21} Q-circles are not greatly affected by cable delay even for very long lengths of cable up to 60λ , whereas reflection circles can be influenced significantly by the phase effect, especially when the coupling losses are high (and coupling is weak).

5.5. INFLUENCE OF VARIATION IN THE COUPLING REACTANCE X_s ON ERRORS IN Q_0 IN THE PRESENCE OF CABLE DELAY

Based on the circuit model of Fig. 5.1, the effect of variations in the coupling reactance X_s on the error in the Q_0 -factor (obtained from the Transmission Mode Q_0 -Factor Technique) in the presence of a small amount of delay due to transmission lines in the system was investigated using the following parameters :

Coupling resistance $R_s=R_{s1}=R_{s2}=1\Omega$, $f_0 = 10$ GHz, $R_c = 50\Omega$, $R_o = 5\Omega$, line lengths $L_1=L_2=0.2\lambda$, and the coupling reactance $X_s (= X_{s1}= X_{s2})$ was varied from 0 to 250Ω (ie. X_s/R_c from 0 to 5). The reactance X_s depends on the frequency as described by [1] :

$$X_s(f) = X_s(f_0) \frac{f}{f_0} \quad (5.5)$$

Tables 5.9 and Table 5.10 gives errors in the unloaded Q_0 -factors calculated from Q_L of S_{21} -fit and S_{11} -fit respectively versus X_s/R_c for transmission resonators of nominal Q_0 of 1000 and 10000.

Table 5.9 Errors in the unloaded Q_0 -factors calculated from Q_L of S_{21} -fit for variations in X_s/R_c and $L_1=L_2=0.2\lambda$.

X_s (Ω)	X_s/R_c	$\Delta Q_0/Q_0$ from S_{21} fit (%)		X_s (Ω)	X_s/R_c	$\Delta Q_0/Q_0$ from S_{21} fit (%)	
		$Q_0 = 1000$	$Q_0 = 10000$			$Q_0 = 1000$	$Q_0 = 10000$
		0	0			-0.27	-0.03
1	0.02	-0.28	-0.03	80	1.6	-0.19	-0.03
5	0.1	-0.29	-0.03	100	2.0	-0.12	-0.03
10	0.2	-0.31	-0.03	150	3.0	0.06	-0.02
20	0.4	-0.32	-0.04	200	4.0	0.32	-0.02
50	1	-0.27	-0.03	250	5.0	6.20	-0.02

Table 5.10 Errors in the unloaded Q_0 -factors calculated from Q_L of S_{11} -fit for variations in X_s/R_c and $L_1=L_2=0.2\lambda$.

X_s (Ω)	X_s/R_c	$\Delta Q_0/Q_0$ from S_{11} fit (%)		X_s (Ω)	X_s/R_c	$\Delta Q_0/Q_0$ from S_{11} fit (%)	
		$Q_0 = 1000$	$Q_0 = 10000$			$Q_0 = 1000$	$Q_0 = 10000$
		0	0			3.15	0.34
1	0.02	3.20	0.35	80	1.6	8.21	1.37
5	0.1	3.40	0.37	100	2.0	7.31	1.80
10	0.2	3.68	0.41	150	3.0	> 10	3.21
20	0.4	4.33	0.49	200	4.0	> 10	4.86
50	1	6.68	0.84	250	5.0	> 10	6.64

Figures 5.32 and 5.33 show the trend in the errors in the fitted Q_0 and Q_L factors respectively calculated from Q_L of S_{21} fit and of S_{11} fits for increasing X_s for nominal Q_0 of 1000. For the same range of X_s and Q_0 -factor value, the error in the coupling coefficient obtained also from the Transmission Mode Q_0 -factor Technique is shown in Fig. 5.34.

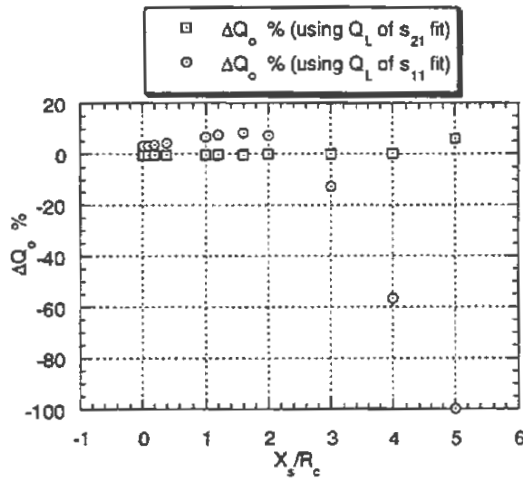


Figure 5.32 Error in Q_0 using Q_L of S_{21} and S_{11} fits for various X_s , nominal Q_0 of 1000 and $L=0.2\lambda$.

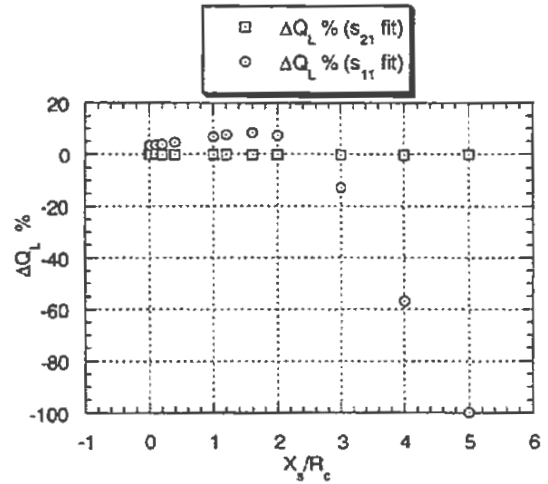


Figure 5.33 Error in Q_L obtained from S_{21} and S_{11} fits for various X_s , nominal Q_0 of 1000 and $L=0.2\lambda$.

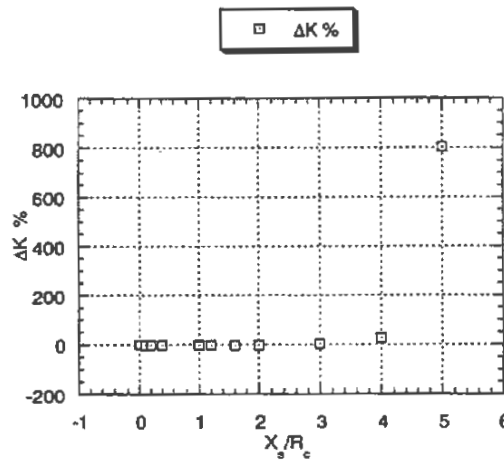


Figure 5.34 Error in coupling coefficient for various X_s , nominal Q_0 of 1000 and $L=0.2\lambda$.

Figures 5.35 and 5.36 show the errors in the fitted Q_0 and Q_L factors respectively calculated from Q_L of S_{21} fit and Q_L of S_{11} fits over the same range of X_s for nominal Q_0 of 10000. For the same range of X_s and Q_0 -factor value, the error in the coupling coefficient obtained from the Transmission Mode Q_0 -factor Technique is shown in Fig.5.37

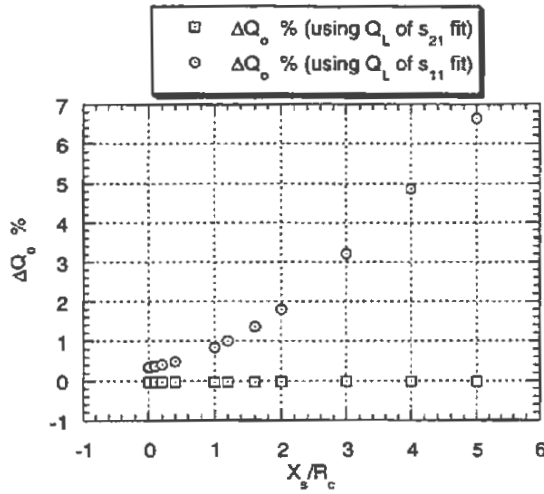


Figure 5.35 Error in Q_0 using Q_L of S_{21} and S_{11} fits for various X_s , nominal Q_0 of 10000 and $L=0.2\lambda$.

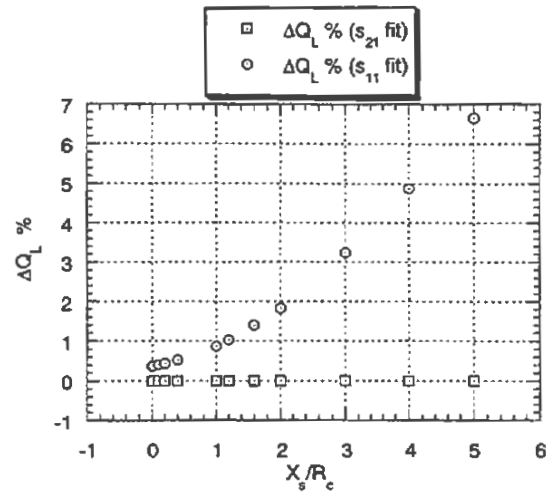


Figure 5.36 Error in Q_L obtained from S_{21} and S_{11} fits for various X_s , nominal Q_0 of 10000. $L=0.2\lambda$.

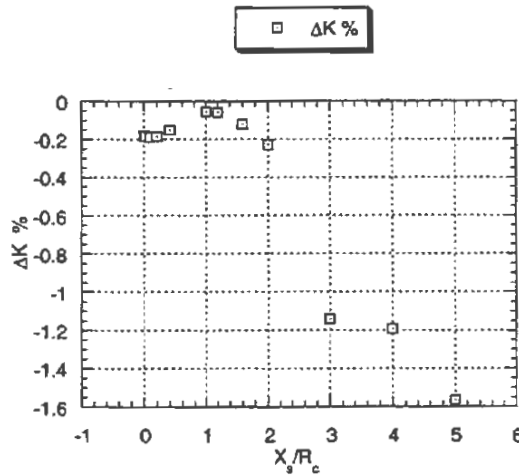


Figure 5.37 Error in coupling coefficient for various X_s , nominal Q_0 of 10000 and $L=0.2\lambda$.

For the simulations done on the transmission resonator system with transmission line of 0.2λ length and nominal Q_0 factor values of 1000 using the Transmission Mode Q_0 -Factor Technique, the errors in Q_0 calculated from Q_L of S_{21} fit were found to be small, uniform with a negative sign; with absolute error less than

0.31% over the range of X_s/R_c from zero to 1.2. For higher values of X_s/R_c , the error in the unloaded Q_0 -factor tends toward zero and then changes to positive values. For the same range of X_s/R_c but with a nominal Q_0 factor 10 times higher, the effect of the cable delay is reduced significantly, with error in Q_0 of S_{21} fit less than 0.04 % over the range of X_s/R_c tested. In general, at low values of X_s ($<0.4R_c$), the distortion of the Q-circle which causes the error in the fitted Q_0 -factor - is mainly due to the frequency dependence of the phase of connecting cables. For higher values of X_s , the frequency dependence of X_s also contributes to the distortion and the error in the fitted Q_0 is increased accordingly.

The testing of the Transmission Mode Q_0 -Factor Technique using computer simulations described in this chapter showed that the technique is capable of extracting unloaded Q_0 -factor from S_{21} , S_{11} and S_{22} Q-circle data sets with errors less than 1 % under relatively noisy conditions, in the presence of delay effects due to transmission lines and frequency dependence of coupling reactances.

BIBLIOGRAPHY OF CHAPTER 5

- [1] D. Kajfez, "Q Factor" , Vector Fields, 1994.
- [2] Private communication, L.M. Xie, Texas Center for Superconductivity, University of Houston.
- [3] MATLAB Users Guide, Maths Works (1989).
- [4] P.J. Petersan, S.M. Anlage, "Measurement of resonant frequency and quality factor of microwave resonators : comparison of methods", Journal of Applied Physics, Vol. 84, No. 6, pp. 3398, 1998.

CHAPTER 6

MEASUREMENTS OF SURFACE RESISTANCE OF $\text{YBa}_2\text{Cu}_3\text{O}_7$ THIN FILMS USING THE SAPPHIRE RESONATOR AND THE TRANSMISSION MODE Q_0 -FACTOR TECHNIQUE BASED ON S-PARAMETERS

In this chapter, microwave measurements of HTS films using the Transmission Mode Q_0 -Factor Technique developed in the course of this thesis are presented. Measurements were performed on $\text{YBa}_2\text{Cu}_3\text{O}_7$ thin films of good and poor quality at frequency of 10 and 25 GHz, temperature of 77K, and medium and very low coupling to the sapphire resonator, to verify applicability of the Transmission Mode Q_0 -Factor Technique under differing conditions. Measurements of the surface resistance of superconducting films required the unloaded Q_0 -factor of the resonator to be determined. The Transmission Mode Q_0 -Factor Technique was applied to multi-frequency measurements of transmission S_{21} parameters (measured around the resonance) to calculate the loaded Q_L -factor, and to measurements of reflection (S_{11} and S_{22}) parameters to obtain the coupling coefficients β_1 and β_2 . The surface resistance of the $\text{YBa}_2\text{Cu}_3\text{O}_7$ was then found according to the loss equation described in Chapter 3.6, namely :

$$R_{s(\text{average})} = A_s \left[\frac{1}{Q_0} - \left(\frac{R_m}{A_m} + p_e \tan \delta \right) \right] \quad (6.1)$$

where

$$Q_0 = Q_L (1 + \beta_1 + \beta_2) \quad (6.2)$$

6.1. MEASUREMENT SYSTEMS FOR R_s TESTING OF HTS FILMS

Measurements of the surface resistance R_s of HTS films have been performed using a liquid nitrogen bath for tests at 77K and a closed cycle cryocooler system. A advantage of the nitrogen bath system (Fig. 6.1) is that it has a minimal cool-down time of about ten minutes to enable relatively fast measurements of Q -factor. The

APD cryocooler system (Fig. 6.2) is capable of measurements over a wide range of temperatures but has a much longer cool-down time typically ranging from two to three hours. The system used in this thesis consists of the following equipment :

- HP 8722C vector network analyser fitted with 1 Hz frequency resolution.
- Sapphire resonators (Hakki-Coleman type) for frequency of 10 GHz and 25 GHz with two 60 centimetre low-loss semi-rigid cables - each with one end terminated with a coupling loop and the other end with SMA connector.
- Neocera LTC-10 temperature controller fitted with resistive heating element (50 watt maximum power), and two silicon temperature diode sensors.
- Vacuum dewar and APD DE204SL closed cycle cryogenic laboratory system suitable for measurements in the temperature range from 10K up to room temperature.
- IBM-PC type computer fitted with GPIB card used for the computer control of temperature controller and the network analyser, and for downloading S-parameter measurement data from the network analyser.

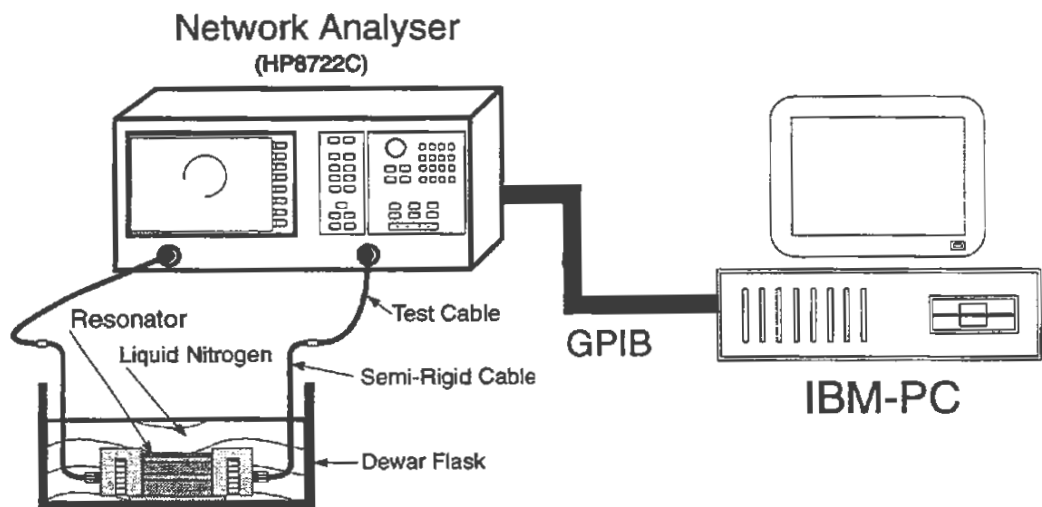


Figure 6.1 R_s measurement system using the liquid nitrogen bath for refrigeration of the resonator containing the superconductor samples.

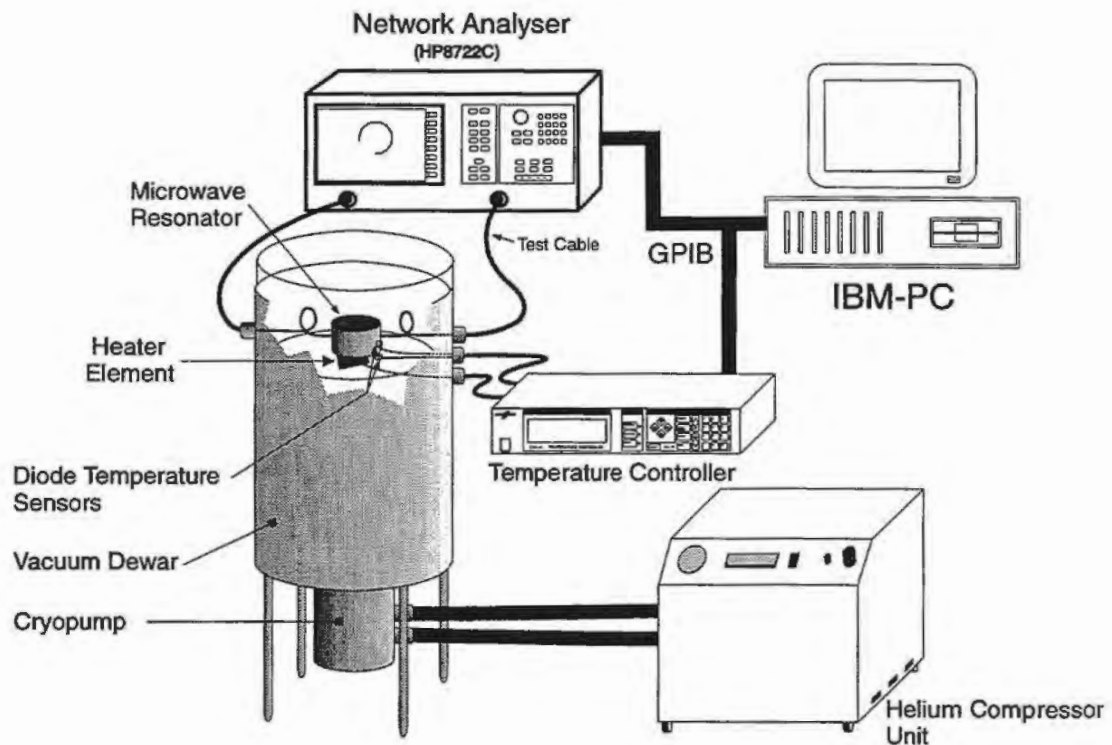


Figure 6.2 R_s measurement system using the closed cycle cryocooler for refrigeration of the resonator containing the superconductor samples.

The 10 GHz Hakki-Coleman sapphire resonator used for measurements of one inch diameter, $\text{YBa}_2\text{Cu}_3\text{O}_{7-x}$ superconducting thin films of thickness 500 nm on LaAlO_3 substrate of 0.5 mm thickness is shown below in Fig. 6.3. Since the thickness of the substrate is about 3 to 4 times the penetration depth, the losses of the substrate do not affect the Q_0 -factor. On each side of the resonator is a knurled knob which is used to adjust the position of coupling loops. The same resonator with the top endplate removed is shown in Fig. 6.4, in which the sapphire puck and the superconductor film directly below the sapphire can be seen.

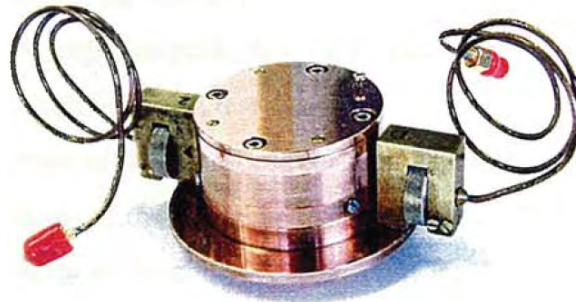


Figure 6.3 The 10 GHz Hakki Coleman resonator used in this thesis for measurements of the surface resistance of one inch round wafers of $\text{YBa}_2\text{Cu}_3\text{O}_{7-x}$ HTS thin films.

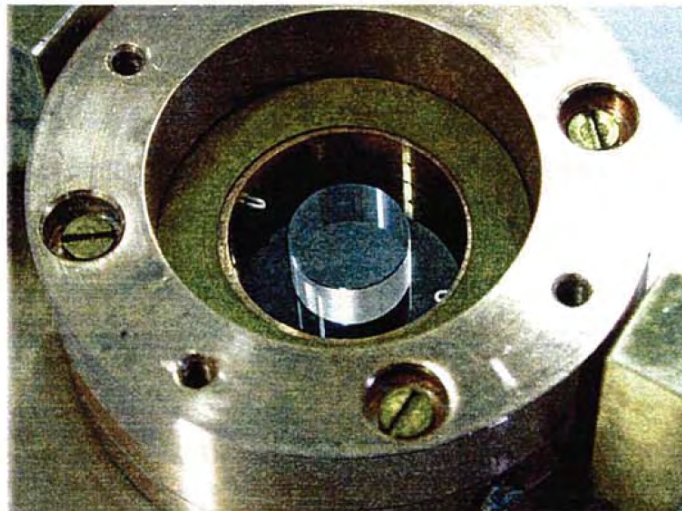


Figure 6.4 10 GHz Hakki Coleman sapphire resonator with one of the endplates removed, showing the sapphire dielectric puck sitting on top of a superconductor film. The coupling loops are inside the cavity for display purposes only.

The parameters for the 10 GHz and 25 GHz sapphire resonators (and computed geometrical factors using the software **SUPER** [1]) are given below :

Parameters of the 10 GHz resonator at 77K

Diameter of cavity, $D_c = 24$ mm,

Diameter of the sapphire puck, $d_s = 12.32$ mm,

Height of the sapphire puck, $h = 7.41$ mm,

Surface resistance of the lateral copper wall, $R_m = 16$ m Ω

Geometrical factor of the lateral copper wall, $A_m = 27617$

Geometrical factor of the endwalls combined, $A_s = 279$

Energy filling factor, $p_e = 0.971$,

Permittivity of the the sapphire, $\epsilon_{r,l} = 9.38$,

Dielectric loss tangent of the sapphire, $\tan\delta = 5 \cdot 10^{-8}$

Parameters of the 25 GHz resonator at 77K

Diameter of cavity, $D_c = 9.25$ mm,

Diameter of the sapphire puck, $d_s = 3.98$ mm,

Height of the sapphire puck, $h = 3.975$ mm,

Surface resistance of the lateral copper wall, $R_m = 25$ m Ω

Geometrical factor of the lateral copper wall, $A_m = 12179$

Geometrical factor of the endwalls combined, $A_s = 559$

Energy filling factor, $p_e = 0.947$

Permittivity of the the sapphire, $\epsilon_{r,l} = 9.38$,

Dielectric loss tangent of the sapphire, $\tan\delta = 5 \cdot 10^{-8}$

Figure 6.5 shows how the sapphire resonator is mounted inside the vacuum dewar. The resonator is firmly fixed to the brass platform using a rigid brass strip and fastening screw bolts. To achieve good thermal contact between the resonator and brass platform, a sheet of indium foil is placed in between the base of the resonator and the platform. A good vacuum seal is made using a single rubber O-ring between the clear perspex plate and the top of the stainless steel dewar block.

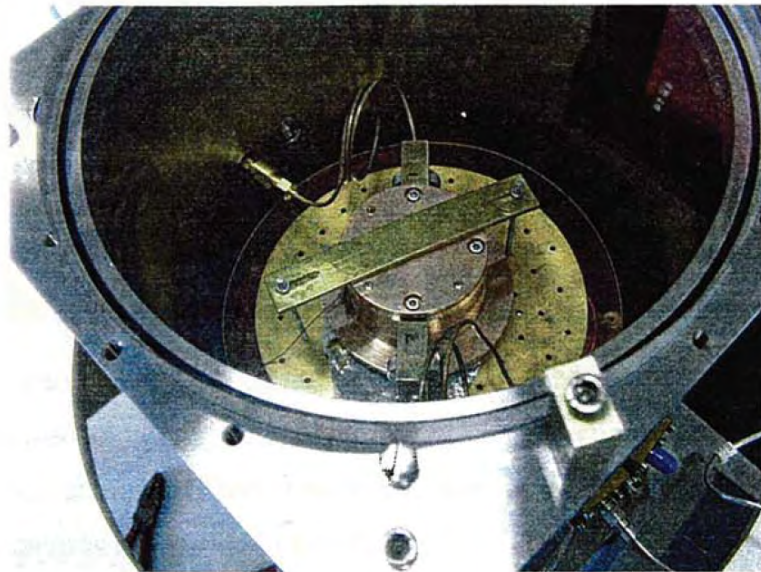


Figure 6.5 Sapphire resonator inside the vacuum dewar can be seen through the round perspex plate. The cold head which is not visible is below the brass platform.

Figure 6.6 presents the measurement system in the microwave laboratory at the James Cook University. The HP8722C network analyser mounted on a rack with the temperature controller above it, and the stainless steel vacuum dewar is mounted on the trolley. Before each test, the measurement system was calibrated using the THRU calibration procedure for S_{21} ; and the 1-Port reflection calibration procedures for S_{11} and S_{22} at the SMA connectors at the walls of the dewar.



Figure 6.6 Photo of the main measurement system used in this thesis, showing the HP8722C network analyser, temperature controller, vacuum dewar with the cold head, IBM-PC computer, and rotary vacuum pump. The compressor of the cryocooler system is not visible in the photo.

6.2. MEASUREMENTS OF GOOD QUALITY $\text{YBa}_2\text{Cu}_3\text{O}_7$ THIN FILMS USING A 10 GIGAHERTZ HAKKI COLEMAN SAPPHIRE RESONATOR

For testing of good quality $\text{YBa}_2\text{Cu}_3\text{O}_7$ films of thickness 500 nm deposited on LaAlO_3 substrate 0.5 mm thick deposited with the thermal co-evaporation technique [2]. The measurements for the first test were performed at 77K, with microwave source power of -15dBm, 1601 measurement points, and with the tips of the coupling loops positioned at a distance of 1 millimetre outside the cavity (relative to the cavity wall). Figure 6.7 shows the 1601 point S_{21} Q-circle measured with the vector network analyser as well as the fitted circle obtained using the Transmission Mode Q_0 -Factor Technique described in Chapter 4 of this thesis. Calculations

provided a value of 403130 for the loaded Q_L -factor and a resonant frequency of 9.997 GHz from the curve fit implemented in the **Q_Fit** software.

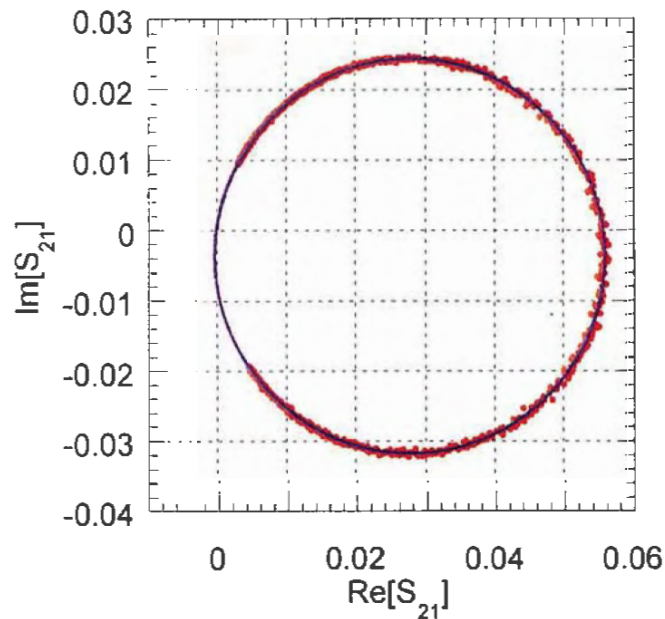


Figure 6.7 Measured S_{21} Q-circle with 1601 points spanning 100 kHz and the fitted circle. The fitted Q_L -factor is 403130, and the fitted resonant frequency f_0 is 9.997 GHz.

Figure 6.8 and Figure 6.9 show the narrow-span reflection S_{11} and S_{22} traces measured around the resonance, containing 1601 measurement points on the 2 MHz span. The spans of 2 MHz were chosen so that small portions of the off-resonance regions could be seen in the trace data. To apply the curve fitting procedure of the Transmission Mode Q_0 -Factor Technique to the narrow-span S_{11} and S_{22} traces, the wide-span traces had to be measured to remove the phase distortion from the narrow-span data.

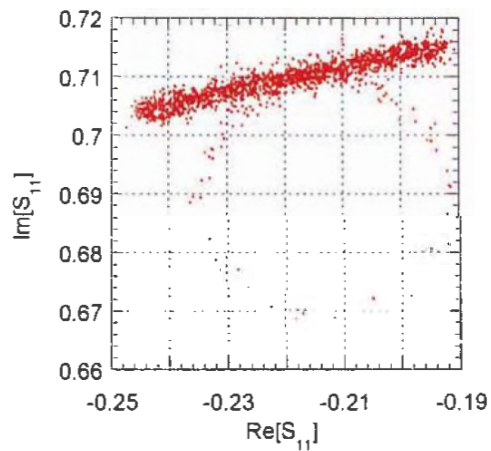


Figure 6.8 Measured S_{11} Q-circle with some of the off-resonance trace visible.

The span is 2 MHz.

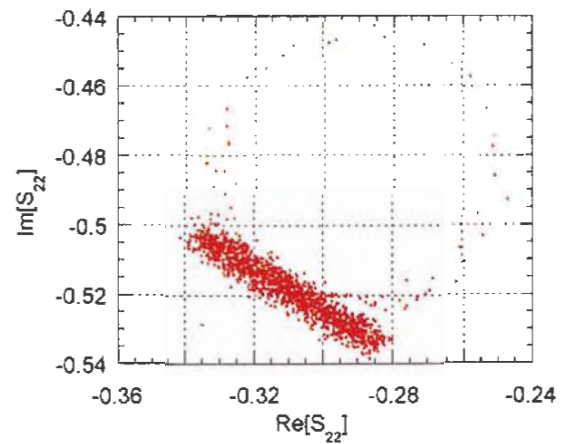


Figure 6.9 Measured S_{22} Q-circle with some of the off-resonance trace visible.

The span is 2 MHz.

Figure 6.10 and Figure 6.11 show the measured wide-span S_{11} and S_{22} traces respectively, each spanning 120 MHz centred at 9.997 GHz together with fitted S_{11} and S_{22} circles obtained by applying a linear circle-fitting procedure described in Appendix D. The wide span of 120 MHz was chosen to capture a significant portion of the circular off-resonance reflection trace needed for the enhanced phase correction procedure to correct the phase of the reflection (S_{11} and S_{22}) Q-circles of Fig. 6.8 and Fig. 6.9.

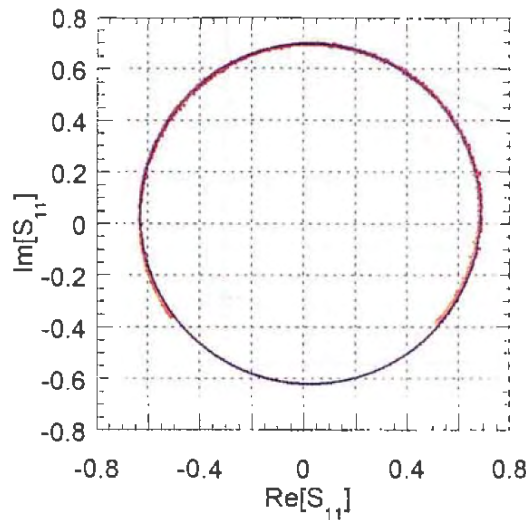


Figure 6.10 Measured S_{11} wide-span off-resonance trace (red) shown with the fitted circle (blue). The central coordinates of the circle are (0.026963,0.038702).

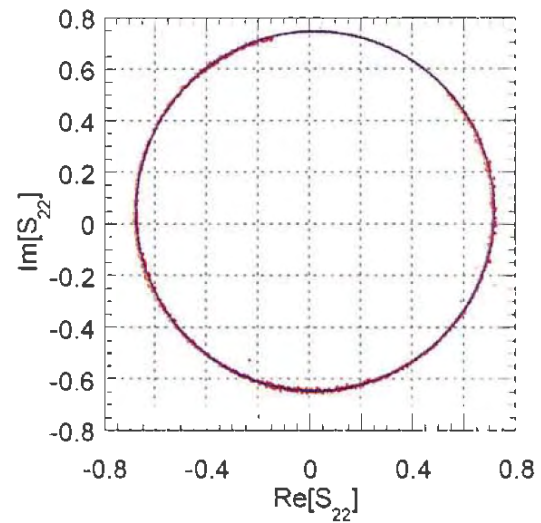


Figure 6.11 Measured S_{22} wide-span off-resonance trace (red) shown with the fitted circle (blue). The central coordinates of the circle are (0.020116,0.050223).

After applying the circle fitting technique to the wide-span circular off-resonance reflection S_{11} and S_{22} traces, the central coordinates were found to be (0.026963,0.038702) for the S_{11} and (0.020116,0.050223) for S_{22} . The fitted circles (Fig. 6.10 and Fig. 6.11) showed that centre of the circular wide-span S_{11} and S_{22} off-resonance traces were displaced from the origin, which indicated signs of impedance mismatch. Hence the phase versus frequency characteristics of the reflection traces were non-linear in the off-resonance regions and required the non-linearity to be subsequently removed by using the enhanced phase correction procedure described in Appendix C. Figure 6.12 and Figure 6.13 shows the phase of each point on the S_{11} and S_{22} reflection traces with respect to the central coordinates as functions of frequency.

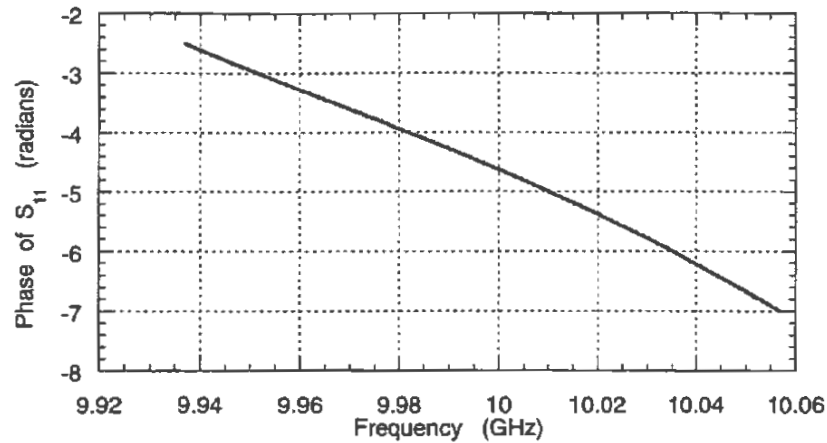


Figure 6.12 Phase of S_{11} plotted with respect to the centre of the off-resonance circle (of Fig. 6.10) versus frequency. A linear fit gives of rate of change in phase of about $-3.668 \cdot 10^{-8}$ rad/Hz.

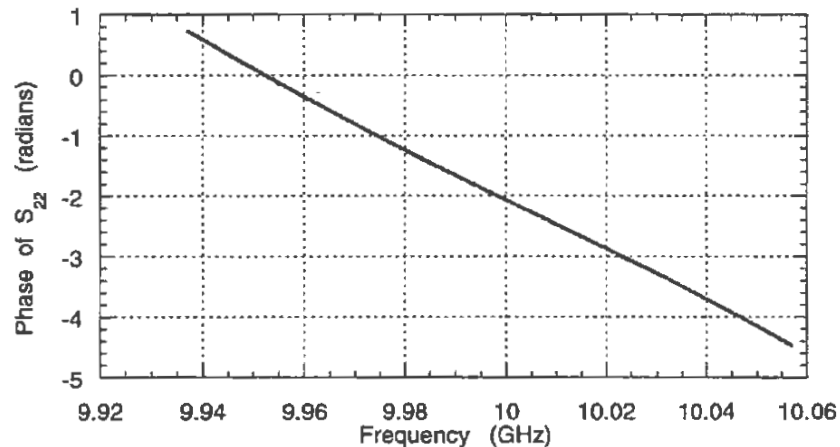


Figure 6.13 Phase of S_{22} plotted with respect to the centre of the off-resonance circle (of Fig. 6.11) versus frequency. A linear fit gives a rate of change in phase of about $-4.224 \cdot 10^{-8}$ rad/Hz.

From the slopes of the functions (Fig. 6.12 and Fig. 6.13), rates of change of phase with frequency $d\phi/dF$ of $-3.668 \cdot 10^{-8}$ rad/Hz and $-4.224 \cdot 10^{-8}$ rad/Hz for S_{11} and S_{22} were obtained respectively and these values were used to correct the phase distortion

in the S_{11} and S_{22} reflection Q-circles of 6.8 and Figure 6.9. Figure 6.14 and Figure 6.15 show the reflection Q-circles after correction of the phase distortion.

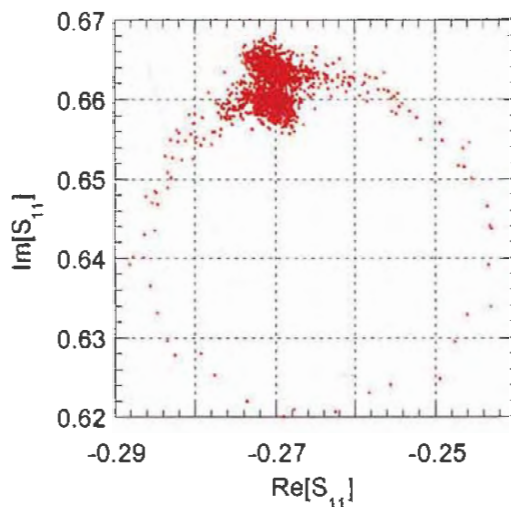


Figure 6.14 Corrected S_{11} Q-circle after phase correction has been applied to the Q-circle of Fig. 6.8.

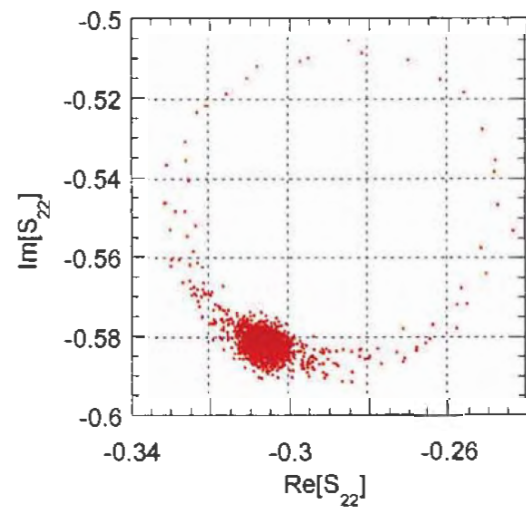


Figure 6.15 Corrected S_{22} Q-circle after phase correction has been applied to the Q-circle of Fig. 6.9.

The corrected reflection Q-circles (Fig. 6.14 and Fig. 6.15) contained a large concentration of points around the detuned regions. Due to the weights used in the linear fractional curve fitting procedure of the Transmission Mode Q_0 -Factor Technique, such large concentration of points would cause heavy bias in the fit. Hence the end sections of the Q-circles were deleted before the curve fitting was applied in order to remove bias in a curve-fitting. Figure 6.16 and Fig. 6.17 represent reduced data sets of the corrected S_{11} and S_{22} Q-circles (of Fig. 6.14 and Fig. 6.15) and the resulting fitted circles.

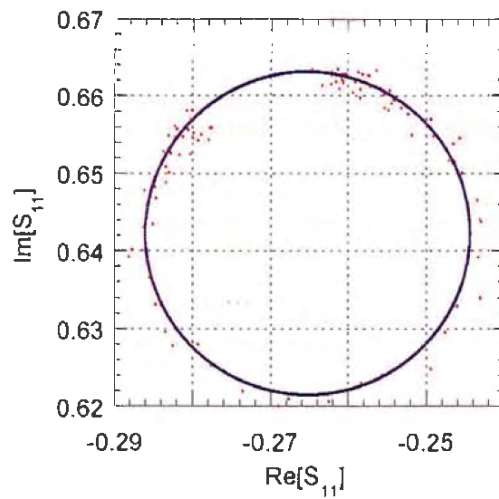


Figure 6.16 Reduced data set of the corrected S_{11} Q-circle of Fig. 6.14, together with the fitted circle.

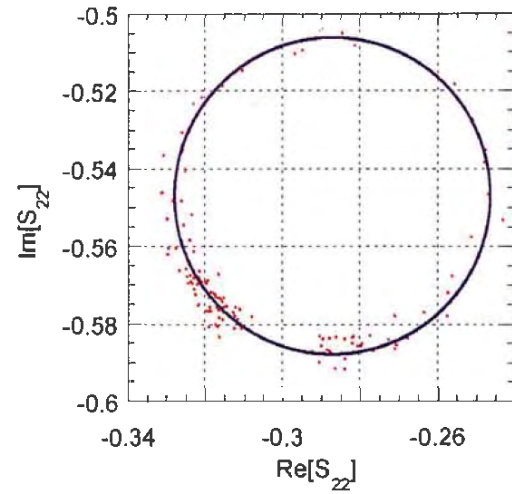


Figure 6.17 Reduced data set of the corrected S_{22} Q-circle of Fig. 6.15, together with the fitted circle.

Results of the Transmission Mode Q_o -Factor Technique applied to the measured S_{21} , S_{11} and S_{22} Q-circle data for the $\text{YBa}_2\text{Cu}_3\text{O}_7$ films (Appendix E) are summarised below in Table 6.1. The unloaded Q_o -factor calculated using the loaded Q_L -factor obtained from the S_{21} fit and the fitted coupling coefficients was calculated to be 435393. The port one and port two coupling coefficient K_1 and K_2 were obtained to be 0.027 and 0.053 respectively.

Table 6.1 Results obtained from the Transmission Mode Q_o -Factor Technique showing the loaded Q_L -factor of S_{21} fit, coupling coefficients, and the unloaded Q_o -factor calculated from Q_L of S_{21} -fit and the coupling coefficients.

Unloaded Q_o -factor	$Q_o = 435393$
Loaded Q_L -factor from S_{21} -fit	$Q_L = 403130$
Port 1 and Port 2 coupling coefficient	$\beta_1 = 0.027, \beta_2 = 0.053$
Resonant frequency	$f_o = 9.997 \text{ GHz}$
Signal to noise ratio	$\text{SNR } S_{21} = 43.1 \text{ dB}$

	SNR S_{11} = 24.4 dB SNR S_{22} = 24.6 dB
Lossless (β_{1i}) and lossy (β_{1L}) parts of the coupling coefficients on Port 1	β_{1i} = 0.0226 β_{1L} = 0.0044
Lossless (β_{2i}) and lossy (β_{2L}) parts of the coupling coefficients on Port 2	β_{2i} = 0.0440 β_{2L} = 0.0091

6.2.1. MEASUREMENTS OF THE UNLOADED Q_0 -FACTOR USING THE TRANSMISSION MODE Q_0 -FACTOR TECHNIQUE WITHOUT PHASE CORRECTION OF S_{11} AND S_{22} TRACES

For comparison purposes, a test was done to study the Q_0 -factor result for the case when no phase correction procedure was applied to measured reflection Q -circles. For the test, the fitting procedure was applied directly to the uncorrected S_{11} and S_{22} Q -circles with a span of 120 kHz for each trace (Fig. 6.18 and Fig. 6.19). The port coupling coefficients β_1 and β_2 were obtained to be 0.026 and 0.053 respectively (Appendix E).

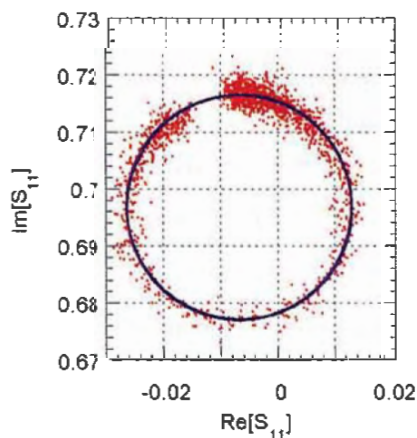


Figure 6.18 A 1601 point S_{11} Q -circle spanning 120 kHz shown with the fitted circle.

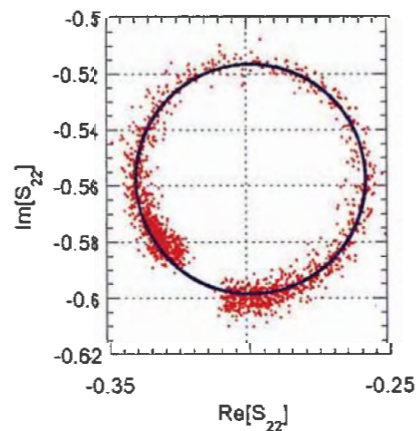


Figure 6.19 A 1601 point S_{22} Q -circle spanning 120 kHz shown with the fitted circle.

Using the loaded Q_L -factor of 403130 of the S_{21} -fit (obtained from the test in the previous section) and the coupling coefficients obtained from the Transmission Mode Q_0 -Factor Technique applied to the uncorrected S_{11} and S_{22} Q-circles of Fig. 6.18 and Fig. 6.19, the unloaded Q_0 -factor result was calculated to be 434765, giving 0.14 % error as compared to the result of the TMQFT with the phase correction procedure.

6.2.2. MEASUREMENTS OF THE UNLOADED Q_0 -FACTOR UNDER VERY WEAK COUPLING

It was appropriate to compare the Q_0 -factor results obtained using the equation (6.2) from the previous tests with the value of loaded Q_L -factor obtained under conditions of a very weak coupling where the unloaded Q_0 -factor can be approximated by the loaded Q_L -factor ($Q_0 \approx Q_L|_{\beta_1=\beta_2=0}$). For the test, a weak coupling condition was achieved by reducing the coupling until the observed S_{21} magnitude curve became relatively noisy (due to a weak transmitted signal) but not too noisy for a fitting procedure to be applied to the S_{21} Q-circle in the complex plane. Under such condition, the coupling was so weak that the reflection Q-circles were too small to be seen even when the highest resolution scale of the network analyser was used. Hence, only the S_{21} trace was measured as shown Fig. 6.20. Applying the fractional curve fitting to the S_{21} Q-circle, the approximated value of Q_0 using the fitted Q_L -factor was obtained to be 421426, with a 24.6 dB signal to noise ratio in the S_{21} trace. Unfortunately, the data scatter D_s , described in Appendix A (referred to Chapter 4.4) for the S_{21} fit was calculated to be 0.195, which exceeded the recommended limit of 0.1 for reliable results [3].

It can be seen in Fig. 6.20 that the large concentration of data points around the extremities of the transmission S_{21} Q-circle trace has caused a bias in the fit, so that the fitted trace doesn't pass evenly through the data points around the resonance regions. Hence the obtained Q_L -factor result for this fit is not considered to be

reliable. To obtain a reliable value of Q_o -factor, the problematic points causing the bias were removed to give the 628 point S_{21} Q-circle of Fig. 6.21.

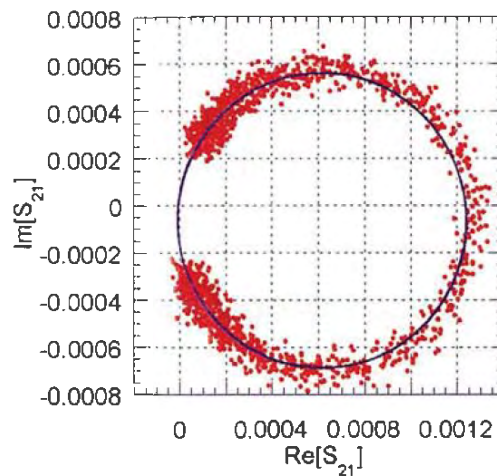


Figure 6.20 A 1601 point S_{21} Q-circle measured under very weak coupling condition, spanning 100 kHz. The insertion loss at the resonance is about 58 dB. The fitted trace is shown and the fitted Q_L -factor is 421426. The data scatter D_s is 0.195.

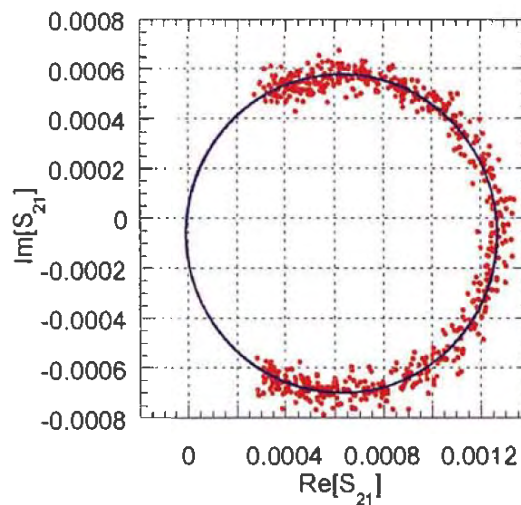


Figure 6.21 A 628 point subset from the S_{21} Q-circle of Fig. 6.20 and showing the fitted circle. The span is 39.187 kHz and the fitted loaded Q_L -factor is 431634. The data scatter D_s is 0.075.

A fit to the measured reduced S_{21} data set of Fig. 6.21 provided a reliable Q_L -factor value of 431634 which was then assigned to be the approximated unloaded Q_0 -factor under the assumption of a very weak coupling used. The approximated value of Q_0 -factor is only 0.8 % less than the value of Q_0 obtained in the previous section using the Transmission Mode Q_0 -Factor Technique for coupling coefficients β_1 and β_2 of 0.027 and 0.053 respectively. This good agreement shows high accuracy of the developed technique for unloaded Q_0 -factor measurements.

6.2.3. CALCULATIONS OF THE SURFACE RESISTANCE OF $YBa_2Cu_3O_7$ HTS FILMS ON $LaAlO_3$ SUBSTRATE

The surface resistance of the $YBa_2Cu_3O_7$ superconducting thin films on $LaAlO_3$ substrate under test was computed using the software **SUPER** [1] based on equation (6.1), namely :

$$R_{s(average)} = A_s \left[\frac{l}{Q_0} - \left(\frac{R_m}{A_m} + p_\epsilon \tan \delta \right) \right] \quad (6.3)$$

and parameters as listed earlier in this chapter. The values of the unloaded Q_0 -factors obtained from the three performed tests, namely

- 1) The Transmission Mode Q_0 -Factor Technique with phase correction done on the reflection Q-circles, with coupling coefficients $\beta_1 = 0.027$ and $\beta_2 = 0.053$.
- 2) The Transmission Mode Q_0 -Factor Technique involving no phase correction procedure on the reflection Q-circles, with the same coupling as in test 1 (Chapter 6.2.1).
- 3) Q_L -to- Q_0 approximation method under a very weak coupling condition. The weak coupling condition was achieved by moving the coupling loops outwards until the reflection (S_{11} and S_{22}) Q-circles were too small to be measured (Chapter 6.2.2).

The tests 2 and 3 were for the verification of measurements using the Transmission Mode Q_o -Factor Technique. Table 6.2 below gives the values of Surface Resistance calculated according to the three different values of unloaded Q_o -factor obtained from the Q_o -factor tests.

Table 6.2 Surface resistances of $YBa_2Cu_3O_7$ on $LaAlO_3$ substrate at 9.997 GHz and 77 K calculated from the unloaded Q_o -factors obtained using three different methods.

Measurement condition	Q_o	Surface resistance, R_s
TMQFT (phase correction done on reflection Q-circles)	435393	453.8 $\mu\Omega$
TMQFT (no phase correction)	434765	454.7 $\mu\Omega$
$Q_L \approx Q_o$ approximation	431634	459.4 $\mu\Omega$

From the results of Table 6.2, it can be seen that the 0.8 percent difference between the Q_o -factor results obtained from the full procedure involving phase correction on reflection circles and the results of the weak-coupling case translates to a 1.2 percent difference in the calculated surface resistance. The close agreement in the surface resistance values obtained for the three tests confirms the usefulness of the Transmission Mode Q_o -Factor Technique in measurements of the surface resistance of high quality HTS films.

6.2.4. MEASUREMENTS OF POOR QUALITY $YBa_2Cu_3O_7$ THIN FILMS USING A 25 GIGAHERTZ HAKKI COLEMAN SAPPHIRE RESONATOR

This test involved measurements of the surface resistance of 1 cm square wafers of silver doped $YBa_2Cu_3O_7$ HTS films on MgO substrates. The thickness of the films and the substrate were 450 nm and 0.5 mm respectively. The purpose of the study apart from testing the developed Transmission Mode Q_o -Factor Technique was

to investigate the influence of low levels of silver doping on the surface resistance of $\text{YBa}_2\text{Cu}_3\text{O}_7$ HTS films, as had been reported that for certain levels of silver doping, the surface resistance of $\text{YBa}_2\text{Cu}_3\text{O}_7$ HTS films could be decreased [4]. However for the films under test, although the quality of the films were improved significantly by the silver doping, the surface resistance was still high due to the influence of the MgO substrate.

The measurement procedure using the 25 GHz sapphire dielectric resonator was similar to the one described for the 10 GHz resonator. The tips of the coupling loops were positioned about 1 millimetre outside the walls of the resonator cavity. The source power used was -15 dBm and the number of data points used was 401. Unlike the 10 GHz test as described earlier in this chapter, the 25 GHz tests were done without the narrow-span reflection measurements to show that the number of steps required to apply the Transmission Mode Q_0 -Factor Technique can be reduced if the reflection Q -circles can be resolved in wide-span measurements. The results of the test are described below.

Figure 6.22 shows the measured 401 point S_{21} Q -circle spanning 5 MHz and the fitted trace. The circle-fit to the S_{21} trace of Fig. 6.22 provided a loaded Q_L -factor of 22718 and a resonant frequency of 24.75 GHz.

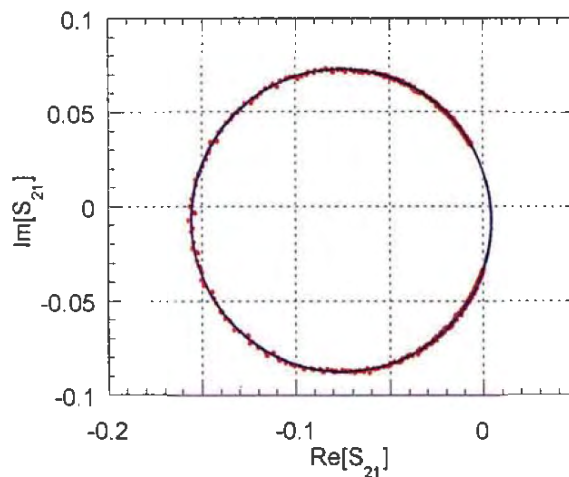


Figure 6.22 Measured 401 point S_{21} Q -circle (red) spanning 5 MHz and fitted circle (blue). The fitted loaded Q_L -factor is 22718 and resonant frequency is 24.75 GHz.

Figures 6.23, and 6.24 show the S_{11} and S_{22} traces measured over a wide span of 120 MHz around the resonance. From these figures, it can be seen that the centres of the circular off-resonance traces are not centred at the origin, and the zero crossings on the real axis are not at equal distances from the origin. These observations clearly indicated that the traces were influenced by the effects of impedance mismatch. The effects of Q-circle distortion due to the electrical delay of uncalibrated transmission cables were not so noticeable in either of the reflection (S_{11} and S_{22}) Q-circles, which are seen as the smaller circles within the larger off-resonance circles of Fig. 6.23, and Fig. 6.24. Nevertheless, the phase correction procedures were still applied to the reflection traces.

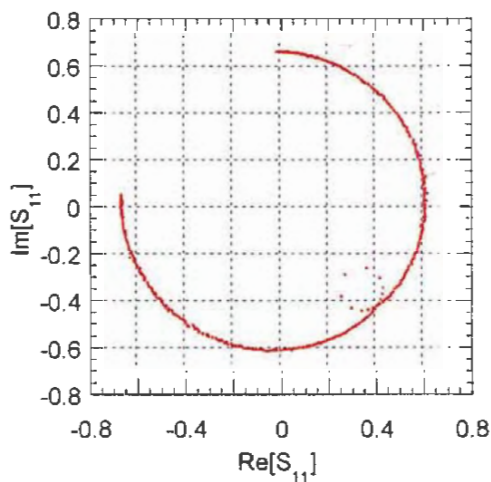


Figure 6.23 Measured S_{11} trace over a wide span of 120 MHz centred about the resonance. The S_{11} Q-circle is lies within the circular off-resonance trace.

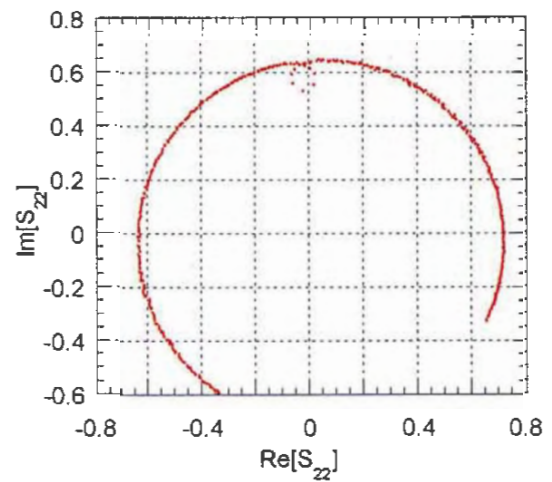


Figure 6.24 Measured S_{22} trace over a wide span of 120 MHz centred about the resonance. The S_{22} Q-circle is lies within the circular off-resonance trace..

After applying the enhanced phase correction procedure to the wide-span reflection S_{11} and S_{22} traces of Fig. 6.23, and Fig. 6.24, the corrected reflection Q-circles with phase distortion removed were then obtained. For each of the corrected reflection Q-

circles, the data points which lay at the extremities (where points are heavily concentrated) were removed to prevent bias in the circle fitting procedures to follow. The reduced data subsets of the corrected reflection Q-circle are shown Fig. 6.25 and Fig. 6.26.

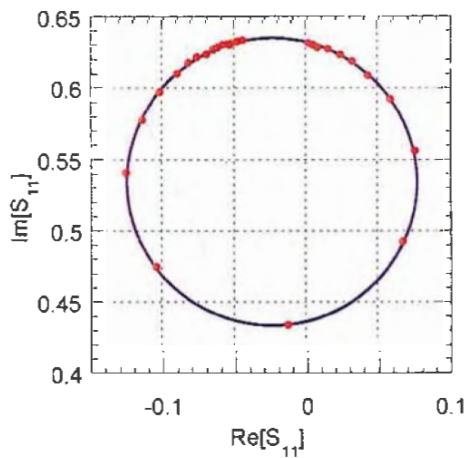


Figure 6.25 Corrected S_{11} circle containing 28 points spanning 8.1 MHz with the fitted trace.

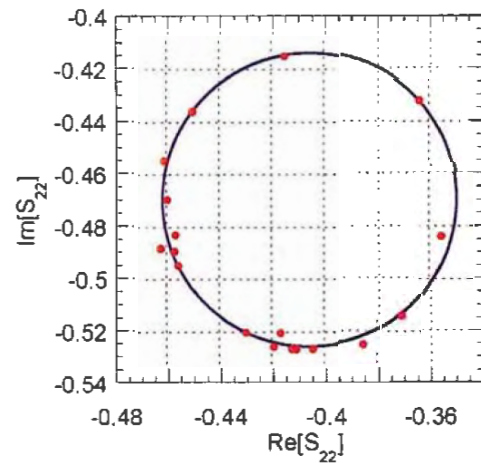


Figure 6.26 Corrected S_{22} circle containing 18 points spanning 5.1 MHz with the fitted trace.

The results of the Transmission Mode Q_0 -Factor Technique (Appendix F) are summarised in Table 6.3 below.

Table 6.3 Results obtained from the Transmission Mode Q_0 -Factor Technique showing the loaded Q_L -factor of S_{21} fit, coupling coefficients and the calculated unloaded Q_0 -factor calculated from Q_L of S_{21} -fit and the coupling coefficients.

Unloaded Q_0 -factor	$Q_0 = 28063$
Loaded Q_L -factor from S_{21} -fit	$Q_L = 22718$
Port 1 and Port 2 coupling coefficient	$\beta_1 = 0.153, \beta_2 = 0.083$
Resonant frequency	$f_0 = 24.75 \text{ GHz}$

Signal to noise ratio	SNR S_{21} = 45.0 dB SNR S_{11} = 43.8 dB SNR S_{22} = 28.4 dB
Lossless (β_{1i}) and lossy (β_{1L}) parts of the coupling coefficients on Port 1	β_{1i} = 0.1248 β_{1L} = 0.0278
Lossless (β_{2i}) and lossy (β_{2L}) parts of the coupling coefficients on Port 2	β_{2i} = 0.0693 β_{2L} = 0.0134

The unloaded Q_0 -factor value of 28063 was obtained and the port coupling coefficients were $\beta_1 = 0.153$ and $\beta_2 = 0.083$. The coupling coefficients were significantly different, which was also evident by the difference in diameters of the reflection Q-circles for port 1 and 2, with diameters of 0.2 and 0.11 respectively. It shows that there can be significant differences in the coupling even when the coupling loops are approximately at equal distances from the cavity wall. The observed asymmetry in the coupling between port 1 and port 2 reflection circles indicate that the properties on each side of the resonator are not necessarily the same due to the differences in coupling loop sizes and physical differences in cables and connectors.

Using the parameters of the 25 GHz sapphire dielectric resonator given earlier in this section, the equation (6.1), and the unloaded Q_0 -factor of 28063 obtained from the Transmission Mode Q_0 -Factor Technique, the computed surface resistance of the silver-doped $YBa_2Cu_3O_7$ superconducting film at 24.75 GHz and 77K was calculated to be 18.9 m Ω . This high value of surface resistance indicates that the quality of the superconductor film sample is very poor because the value is about the same as that of copper at same frequency and temperature.

6.3. ASSESSMENT OF THE FEASIBLE RANGE OF Q_o -FACTOR MEASUREMENTS USING THE TRANSMISSION Q_o -FACTOR TECHNIQUE

The Transmission Mode Q_o Factor Technique (TMQFT) developed in this thesis has been applied to measurements of unloaded Q_o -factors of the sapphire resonator ranging from 7000 up to one million. A upper range for feasible Q_L and Q_o -factor measurements for the TMQFT has not yet been established. However, Q_L -factors as high as 800000 have been measured easily using the Transmission Mode Q_o -Factor Technique using the 10 GHz Hakki-Coleman resonant system with good quality $YBa_2Cu_3O_7$ films at 13 K. It is expected that Q_L and Q_o -factors as high as 10 million can be measured accurately. The lowest values of unloaded Q_o -factors measured using the Transmission Mode Q_o -Factor Technique have been about 7000 using the 25 GHz Hakki-Coleman sapphire resonator with copper end-walls at room temperature. The unloaded Q_o -factor value of 1 million was measured using good quality $YBa_2Cu_3O_7$ HTS films in the 10 GHz resonator at 13 K. Tests were not performed for Q_o -factors less than 7000 because Q_o -factors much less than this value are not expected in measurements of the surface resistance of high temperature superconductor films using the sapphire resonator. Also, it was not feasible to do it using the sapphire resonator. However, a lower limit of Q_o -factor which can be measured reliably is about 100 [3].

It is more relevant to base assessment of the allowed measurement range on the loaded Q_L -factor instead of the range of unloaded Q_o -factor because the bandwidth increases with the amount of loading. For loaded Q_L -factors below 100, the fitting method can be inaccurate because the bandwidth becomes too large where the assumption of frequency independent coupling reactance components in circuit model is no longer valid.

The developed Transmission Mode Q_o -Factor Technique is especially valid for surface resistance measurements using dielectric resonators for frequencies in the microwave range where resonators of suitable size may be constructed to

accommodate the superconductor sample. It is expected that the Transmission Mode Q_0 -Factor Technique cannot be used in the highest microwave frequency ranges where the noise is no longer considered to be Gaussian since the technique assumes that the noise is Gaussian.

The coupling of the resonator to the external circuitry needs to be adequately strong for reflection Q-circles to be measured. As was mentioned already previously in this thesis, the coupling loops should not be allowed to protrude into the cavity otherwise the nominal EM fields inside the resonator can be disturbed. In that case, the imposed constraints for the coupling loop positions places a maximum value on the coupling coefficients for the dielectric resonator used. For the 10 and 25 GHz resonators used in this thesis, the coupling coefficients were always greater than 0.02 and less than about 0.25, (depending on how far the coupling loops were placed outside of the resonator cavity) for measurements of the unloaded Q_0 -factor to be feasible.

BIBLIOGRAPHY OF CHAPTER 6

- [1] "SUPER", Software developed by J. Krupka, Institute of Microelectronics and Optoelectronics, Warsaw University of Technology.
- [2] B. Utz, R. Semerad, M. Bauer, W. Prusseit, P. Berberich, H. Kinder, "Deposition of YBCO and NBCO films on areas 9 inches in diameter", IEEE Transactions on Applied Superconductivity, Vol. 7, No. 2, pp. 1272-1277, June 1997.
- [3] D. Kajfez, "Q factor" , Vector Fields, 1994.
- [4] M. Jacob, J. Mazierska, J. Kim, K-Y. Kang, G.P. Srivastava, "Microwave and microstructural studies of silver doped $\text{YBa}_2\text{Cu}_3\text{O}_7$ thin films", Superconducting Science and Technology, Vol. 11, No. 11, pp. 1217-1221, 1998.

CHAPTER 7

CONCLUSIONS

As mentioned at the beginning of this thesis, precise measurements of the unloaded Q_o -factor are needed for accurate measurements of the surface resistance of high temperature superconducting (HTS) thin films for applications in microwave wireless communications. In the course of this thesis, a novel and accurate procedure to obtain the unloaded Q_o -factor of transmission mode dielectric resonators, namely the Transmission Mode Q_o -Factor Technique has been developed. The developed technique is based on a multi-frequency circle-fitting technique applied to S_{21} , S_{11} and S_{22} scattering parameters measured around the resonance and takes into account important parasitic effects introduced by a real measurement environment, namely noise, cross talk, coupling loss, coupling reactance and electrical delay due to uncalibrated transmission lines. The Transmission Mode Q_o -Factor Technique is not only applicable to the characterisation of HTS films, but can be used in any tests involving transmission mode dielectric resonators such as measurements of loss tangents of dielectrics for high frequency applications [1,2].

In the process of measurements of the surface resistance of HTS films using the Hakki-Coleman sapphire dielectric resonator, the Transmission Mode Q_o -Factor Technique is applied to the measured S_{21} Q-circle data to obtain the loaded factor Q_L , and to the measured S_{11} and S_{22} Q-circle data to find the port coupling coefficients β_1 and β_2 . The surface resistance of the HTS films is then found using :

$$R_{s(average)} = A_s \left[\frac{I}{Q_o} - \left(\frac{R_m}{A_m} + p_e \tan \delta \right) \right]$$

where

$$Q_o = Q_L (1 + \beta_1 + \beta_2)$$

In the course of this work, several new equations were derived in Chapter 4 as listed below.

1. Novel equations relating the S_{21} , S_{11} and S_{22} scattering parameters to the loaded Q_L -factor and coupling coefficients β_1 and β_2 , namely :

$$S_{21}(\omega) = \frac{2R_c Y_{ex1} Y_{ex2}}{G_o(I + \beta_1 + \beta_2) \left[1 + j2Q_L \frac{(\omega - \omega_L)}{\omega_o} \right]} \quad \text{eqn(4.21)}$$

$$S_{pp}(\omega) = \frac{jQ_L S_{ppd} 2 \frac{(\omega - \omega_L)}{\omega_o} + \left\{ S_{ppd} + \frac{2R_c Y_{exp}^2}{G_o(I + \beta_1 + \beta_2)} \right\}}{jQ_L 2 \frac{(\omega - \omega_L)}{\omega_o} + 1} \quad \text{eqn(4.22)}$$

2. Novel equations relating diameters of S_{21} , S_{11} and S_{22} Q-circles to the lossless and lossy components of the port coupling coefficients namely as :

$$\text{Diameter of } S_{21} \text{ Q circle} = \frac{2\sqrt{\beta_{1i}} \sqrt{\beta_{2i}}}{I + \beta_1 + \beta_2} \quad \text{eqn(4.41)}$$

$$\text{Diameter of } S_{11} \text{ Q circle} = \frac{2\beta_{1i}}{I + \beta_1 + \beta_2} \quad \text{eqn(4.42)}$$

$$\text{Diameter of } S_{22} \text{ Q circle} = \frac{2\beta_{2i}}{I + \beta_1 + \beta_2} \quad \text{eqn(4.43)}$$

Novel equations have also been developed to calculate the port coupling coefficients for transmission mode resonators with lossy couplings:

$$\beta_1 = \beta_{1i} + \beta_{1L} \quad \text{and} \quad \beta_2 = \beta_{2i} + \beta_{2L}$$

where

$$\beta_{1i} = \frac{x}{2 \left[1 - \left(\frac{x}{d_1} + \frac{y}{d_2} \right) \right]} \quad \beta_{1L} = \left(\frac{2}{d_1} - 1 \right) \beta_{1i} \quad \text{eqn(4.48-49)}$$

$$\beta_{2i} = \frac{y}{2 \left[1 - \left(\frac{x}{d_1} + \frac{y}{d_2} \right) \right]} \quad \beta_{2L} = \left(\frac{2}{d_2} - 1 \right) \beta_{2i} \quad \text{eqn(4.50-51)}$$

where x and y are the diameters of the S_{11} and S_{22} Q-circles respectively; d_1 and d_2 are the diameters of the coupling loss circles for port 1 and port 2 respectively.

Using computer simulations, the accuracy of the developed Transmission Mode Q_o -Factor Technique applied to synthesised S_{21} , S_{11} , and S_{22} Q-circle test sets influenced by noise, electrical delay due to transmission lines, and the frequency dependence of coupling reactance have been assessed and proved that the technique performs well under practical measurement conditions.

Assuming no delay effects of transmission lines and equal noise radii in S_{21} , S_{11} and S_{22} , errors in the obtained Q_o -factors were less than 1 % for a transmission mode resonator system with a unloaded Q_o -factor of 9000, loaded Q_L -factor of 7754, resonant frequency of 10 GHz, coupling coefficients β_1 and β_2 both equal to 0.08, number of points N of 401 for noise radii ranging from 0.0005 to 0.0015. For the same range of noise radii and using unequal couplings (with β_1 and β_2 equal to 0.08 and 0.029 respectively), the errors in the obtained unloaded Q_o -factors were less than 2 %.

In the presence of transmission line delay (with the length of transmission lines less than 30λ) and assuming nominal Q_o and Q_L -factors of 1000 and 861 respectively; equal couplings $\beta_1=\beta_2=0.08$; noise-free condition, the errors in the loaded Q_L -factors obtained from the Transmission Mode Technique were less than 4 %. Computer simulations showed that the errors in the unloaded Q_o -factors and the loaded Q_L -factors due to the influence of transmission line delay typically decrease by a factor of 10 when the nominal unloaded Q_o -factor increases by the same factor.

Also, computer simulations showed that the frequency dependence of coupling reactances has negligible contribution to errors in unloaded Q_o -factors obtained from the Transmission Mode Q_o -Factor Technique when the Q_L -factor (and hence Q_o -factor) of the system is greater than 1000. For a system tested with Q_o of 1000, errors in the unloaded Q_o -factor obtained from the S_{21} -fit were smaller than 0.1 %. For a system with a Q_o -factor which is ten times higher, the errors were smaller than 0.01 %.

The applicability of the Transmission Mode Q_o -Factor Technique has been verified in measurements of the unloaded Q_o -factor under non-negligible couplings and in measurements of the loaded Q_L -factor under very weak couplings. Practical measurements performed at 10 and 25 GHz on $\text{YBa}_2\text{Cu}_3\text{O}_7$ HTS thin films using sapphire resonators were described in Chapter 6 for SNR in the S_{21} Q-circles from about 43 dB to 45 dB, and the port coupling coefficients from about 0.01 up to 0.07. For the 10 GHz resonator with good quality YBCO films on LaAlO_3 substrates, R_s of $454 \mu\Omega$ was obtained at a temperature of 77 K. The parameters of the measurement system (unloaded Q_o -factor 435393, coupling coefficients $\beta_1=0.027$ and $\beta_2=0.053$; signal to noise ratio in S_{21} of about 43 dB) lay within the ranges investigated in the computer simulations for which errors obtained from the TMQFT is less than 1 %. For the 25 GHz measurements on poor quality YBCO films on MgO substrates, R_s of $18.9 \text{ m}\Omega$ was obtained using the TMQFT. The parameters of the system also lay within the 1 % error in unloaded Q_o -factor when the delay effects of transmission lines were removed.

The unloaded Q_o -factor measured under non-negligible couplings ($\beta_1 = 0.027$, $\beta_2 = 0.053$) closely matched the unloaded Q_o -factor obtained from the loaded Q_L -factor approximation under very weak couplings, with only 0.8 % difference. The Transmission Mode Q_o -Factor Technique provides a reliable way to measure the unloaded Q_o -factor of microwave resonators working in the transmission mode without the need to use the trial and error approach required for the $Q_L \approx Q_o$ approximation method under very weak couplings and can be used for investigation of HTS films under high RF power levels.

Range of unloaded Q_o -Factor values that can be measured with the TMQFT is assessed to be from 100 to 10 million. In practical tests done in the course of this work, unloaded Q_o -factors from 7000 up to $1 \cdot 10^6$ have been measured using the TMQFT.

In the course of this thesis, the author has developed a range of software for the implementation and testing of the Transmission Mode Q_0 -Factor Technique. The developed software includes :

- 1) **Q_Fit** : Implementation of the Transmission Mode Q_0 -Factor Technique.
- 2) **Q_Gen** : MATLAB V5.3 scripts used to generate and simulate S_{21} , S_{11} and S_{22} Q-circles used in the verification and assessment the accuracy of the developed Transmission Mode Q_0 -Factor Technique.
- 3) **PlotQ** : Processes S_{11} and S_{22} resonance data sets to remove phase distortion caused by the electrical delay of uncalibrated transmission lines.
- 4) **Logger** : Software for the GPIB control of the HP8722C vector network analyser to acquire measured S-parameter resonance data sets.

7.1. FUTURE WORK AND RECOMMENDATIONS

The implementation and testing of software developed in this thesis for the Transmission Mode Q_0 -Factor Technique can be enhanced. Also, the impedance mismatch effect can be included in the TMQF technique. The software **PlotQ** (which implements the enhanced phase correction procedure used to remove the distortion in reflection mode S_{11} and S_{22} Q-circles caused by electrical delay introduced by transmission lines) requires some degree of user interaction, namely to select the feasible range of points in the S_{11} or S_{22} data set to be processed by the phase correction algorithm. There are plans to develop the **PlotQ** software to automate the selection process. The functions of **PlotQ** will be integrated into the **Q_Fit** software implementation of the Transmission Mode Q_0 -Factor Technique. So far, the **Q_Fit** software has been developed for a IBM-PC DOS operating environment. Future versions of **Q_Fit** will be developed for Windows 95/98/2000 environments.

So far, the Transmission Mode Q_0 -Factor Technique does not take into account the impedance mismatch effect described in Chapter 4.2. A full investigation

is to be done to assess the influence of the effect on the accuracy of the Transmission Mode Q_0 -Factor Technique (and other Q_0 -Factor techniques which require processing of reflection S-parameters).

7.2. PUBLICATIONS RELATED TO WORK PRESENTED IN THIS THESIS

During the course of the thesis, the author has collaborated with other researchers in the field to produce the publications listed below.

- [1] K. Leong, J. Mazierska, "Accounting for lossy coupling in measurements of Q-factors of transmission mode dielectric resonators", Proceedings of the Asia Pacific Microwave Conference, APMC'98, Tokyo, pp. 209-212, 1998.
- [2] K. Leong, J. Mazierska, J. Krupka, "Measurements of unloaded Q-factor of transmission mode dielectric resonators", Proceedings of the IEEE MTT-S Int. Microwave Symposium, Denver, OF-38, June 8-13, pp. 1639-1642, 1997. - 3rd Prize for the best paper in the Student Paper Competition at the IEEE MTT-S Int. Microwave Symposium 1997.
- [3] J. Ceremuga, J. Wosik, R. Grabovickic, K. Leong, H. Kinder, M. Konczykowski, "Power effects in co-evaporated YBCO thin films", Proceedings of the Fourth Symposium on High Temperature Superconductors in High Frequency Fields, Monterey, 29 September - 2 October 1996.
- [4] J. Ceremuga, K. Leong, R. Grabovickic, "Characterisation of high temperature superconducting films using a sapphire resonator and fitting procedures for calculations of the Q-Factor", Proceedings of the 6th International Microwave Conference, MIKON'96, Warsaw, vol. 1, pp. 305-309, 1996.
- [5] K. Leong, R. Grabovickic, J. Ceremuga, "Review of methods for determining the loaded Q-factor of microwave resonators", Book of Abstracts of the 20th ANZIP

Condensed Matter Physics Meeting , Wagga Wagga, 30 January - 2 February 1996, pp. TP 30, 1996.

[6] N. Savvides, A. Katsaros, D. Reilly, K. Foley, J. Ceremuga, K. Leong, "Microwave properties and microstructure of $Y_1Ba_2Cu_3O_7$ thin films", Book of Abstracts of the 20th ANZIP Condensed Matter Physics Meeting , Wagga Wagga, 30 January - 2 February 1996, pp. WP 71, 1996.

BIBLIOGRAPHY OF CHAPTER 7

- [1] J. Krupka, R. G. Geyer, M. Kuhn, J. H. Hinken, "Dielectric properties of single crystals of Al_2O_3 , LaAlO_3 , NdGaO_3 , SrTiO_3 , and MgO at cryogenic temperatures", *IEEE Trans. Microwave Theory Tech.*, Vol. 42, No. 10, pp. 1886-1890, Oct 1994.
- [2] Y. Kobayashi, M. Katoh, "Microwave measurements of dielectric properties of low-loss materials by the dielectric rod resonator method", *IEEE Trans. Microwave Theory Tech.*, Vol MTT-33, No. 7, pp. 586-592, July 1985.

APPENDIX A

EQUATIONS FOR THE FRACTIONAL LINEAR CURVE FITTING PROCEDURE TO THE TRANSMISSION MODE RESONATOR RESPONSES

The S_{21} Q-circle in the developed Transmission Mode Q_0 -Factor Technique is of the following form :

$$S_{21} = \frac{a_1 t + a_2}{a_3 t + 1} \quad (A1)$$

This can be rearranged to the following form :

$$S_{21} = a_1 t + a_2 - a_3 S_{21} t \quad (A2)$$

where t is a normalised frequency variable described as [A1] :

$$t = 2 \left(\frac{\omega - \omega_L}{\omega_L} \right) \quad (A3)$$

For N measured data points ($S_{21,i}$ and corresponding frequency $\omega_i = 2\pi f_i$, where the index 'i' denotes the i^{th} element in the data set) following (A2) there are N equations:

$$\begin{aligned} S_{21,1} &= a_1 t_1 + a_2 - a_3 S_{21} t_1 \\ S_{21,2} &= a_1 t_2 + a_2 - a_3 S_{21} t_2 \\ &\vdots \\ S_{21,N} &= a_1 t_N + a_2 - a_3 S_{21} t_N \end{aligned} \quad (A4)$$

This set of equations may be written in vector form as :

$$a_1 \mathbf{e}_1 + a_2 \mathbf{e}_2 + a_3 \mathbf{e}_3 = \mathbf{f}$$

where $\mathbf{e}_1 = \begin{bmatrix} t_1 \\ t_2 \\ \vdots \\ t_N \end{bmatrix}$; $\mathbf{e}_2 = \begin{bmatrix} 1 \\ 1 \\ \vdots \\ 1 \end{bmatrix}$; $\mathbf{e}_3 = - \begin{bmatrix} a_3 S_{21,1} \\ a_3 S_{21,2} \\ \vdots \\ a_3 S_{21,N} \end{bmatrix}$; $\mathbf{f} = \begin{bmatrix} S_{21,1} \\ S_{21,2} \\ \vdots \\ S_{21,N} \end{bmatrix}$

(A5)

Projection of the vector \mathbf{f} in the direction of vectors $\bar{\mathbf{e}}_1^T$, $\bar{\mathbf{e}}_2^T$, and $\bar{\mathbf{e}}_3^T$ respectively (which are the transpose conjugates of \mathbf{e}_1 , \mathbf{e}_2 , and \mathbf{e}_3 respectively.) gives :

$$\begin{bmatrix} \bar{\mathbf{e}}_1^T \mathbf{e}_1 a_1 & \bar{\mathbf{e}}_1^T \mathbf{e}_2 a_2 & \bar{\mathbf{e}}_1^T \mathbf{e}_3 a_3 \\ \bar{\mathbf{e}}_2^T \mathbf{e}_1 a_1 & \bar{\mathbf{e}}_2^T \mathbf{e}_2 a_2 & \bar{\mathbf{e}}_2^T \mathbf{e}_3 a_3 \\ \bar{\mathbf{e}}_3^T \mathbf{e}_1 a_1 & \bar{\mathbf{e}}_3^T \mathbf{e}_2 a_2 & \bar{\mathbf{e}}_3^T \mathbf{e}_3 a_3 \end{bmatrix} = \begin{bmatrix} \bar{\mathbf{e}}_1^T \mathbf{f} \\ \bar{\mathbf{e}}_2^T \mathbf{f} \\ \bar{\mathbf{e}}_3^T \mathbf{f} \end{bmatrix} \quad (\text{A6})$$

Instead of using ordinary scalar products, weighted scalar products are used for the procedure, which has no effect on the solution to the system of equations but will however give a more accurate result in the fitting process such that no point in the measured S_{21} data set can receive too much undeserved influence [A1]. To allow for weights to be used, equation (A5) is operated on by a N by N weight matrix P to give :

$$\mathbf{P}\mathbf{e}_1 a_1 + \mathbf{P}\mathbf{e}_2 a_2 + \mathbf{P}\mathbf{e}_3 a_3 = \mathbf{P}\mathbf{f} \quad (\text{A7})$$

When the vector $\mathbf{P}\mathbf{f}$ is projected in the directions of $\bar{\mathbf{e}}_1^T$, $\bar{\mathbf{e}}_2^T$, and $\bar{\mathbf{e}}_3^T$, the system of vector equations becomes :

$$\begin{bmatrix} \bar{\mathbf{e}}_1^T \mathbf{P} \mathbf{e}_1 & \bar{\mathbf{e}}_1^T \mathbf{P} \mathbf{e}_2 & \bar{\mathbf{e}}_1^T \mathbf{P} \mathbf{e}_3 \\ \bar{\mathbf{e}}_2^T \mathbf{P} \mathbf{e}_1 & \bar{\mathbf{e}}_2^T \mathbf{P} \mathbf{e}_2 & \bar{\mathbf{e}}_2^T \mathbf{P} \mathbf{e}_3 \\ \bar{\mathbf{e}}_3^T \mathbf{P} \mathbf{e}_1 & \bar{\mathbf{e}}_3^T \mathbf{P} \mathbf{e}_2 & \bar{\mathbf{e}}_3^T \mathbf{P} \mathbf{e}_3 \end{bmatrix} \begin{bmatrix} a_1 \\ a_2 \\ a_3 \end{bmatrix} = \begin{bmatrix} \bar{\mathbf{e}}_1^T \mathbf{P} \mathbf{f} \\ \bar{\mathbf{e}}_2^T \mathbf{P} \mathbf{f} \\ \bar{\mathbf{e}}_3^T \mathbf{P} \mathbf{f} \end{bmatrix} \quad (\text{A8})$$

where

$$\mathbf{P} = \begin{bmatrix} p_1 & 0 & 0 & 0 \\ 0 & p_2 & 0 & 0 \\ \vdots & \vdots & \vdots & \vdots \\ 0 & 0 & 0 & p_N \end{bmatrix} \quad (\text{A9})$$

The matrix of equation of (A8) can be expressed in the form of :

$$\mathbf{C}\mathbf{a} = \mathbf{q} \quad (\text{A10})$$

where

$$\mathbf{C} = \begin{bmatrix} \bar{\mathbf{e}}_1^T \mathbf{P} \mathbf{e}_1 & \bar{\mathbf{e}}_1^T \mathbf{P} \mathbf{e}_2 & \bar{\mathbf{e}}_1^T \mathbf{P} \mathbf{e}_3 \\ \bar{\mathbf{e}}_2^T \mathbf{P} \mathbf{e}_1 & \bar{\mathbf{e}}_2^T \mathbf{P} \mathbf{e}_2 & \bar{\mathbf{e}}_2^T \mathbf{P} \mathbf{e}_3 \\ \bar{\mathbf{e}}_3^T \mathbf{P} \mathbf{e}_1 & \bar{\mathbf{e}}_3^T \mathbf{P} \mathbf{e}_2 & \bar{\mathbf{e}}_3^T \mathbf{P} \mathbf{e}_3 \end{bmatrix} \quad (\text{A11})$$

and

$$\mathbf{q} = \begin{bmatrix} \bar{\mathbf{e}}_1^T \mathbf{P} \mathbf{f} \\ \bar{\mathbf{e}}_2^T \mathbf{P} \mathbf{f} \\ \bar{\mathbf{e}}_3^T \mathbf{P} \mathbf{f} \end{bmatrix} \quad (\text{A12})$$

and the vector \mathbf{a} is given as

$$\mathbf{a} = \begin{bmatrix} a_1 \\ a_2 \\ a_3 \end{bmatrix} \quad (\text{A13})$$

contains the 3 unknowns a_1 , a_2 and a_3 to be solved.

The elements of matrix \mathbf{C} and the column vector \mathbf{q} are weighted scalar products. Ordinary scalar products have the form $\bar{\mathbf{x}}^T \mathbf{y}$, where $\bar{\mathbf{x}}^T$ is the transpose conjugate of a column vector \mathbf{x} , and \mathbf{y} is a column vector. Both \mathbf{x} and \mathbf{y} have equal dimensions. For the N dimensional vectors \mathbf{x} and \mathbf{y} , namely :

$$\mathbf{x} = \begin{bmatrix} x_1 \\ x_2 \\ \vdots \\ x_N \end{bmatrix}; \quad \mathbf{y} = \begin{bmatrix} y_1 \\ y_2 \\ \vdots \\ y_N \end{bmatrix} \quad (\text{A14})$$

The scalar product $\bar{\mathbf{x}}^T \mathbf{y}$ is then :

$$\bar{\mathbf{x}}^T \mathbf{y} = \begin{bmatrix} x_1^* & x_2^* & \cdots & x_N^* \end{bmatrix} \begin{bmatrix} y_1 \\ y_2 \\ \vdots \\ y_N \end{bmatrix} = \sum_{i=1}^N x_i^* y_i \quad (\text{A15})$$

For the case of scalar product of a vector with itself we have :

$$\bar{\mathbf{x}}^T \mathbf{x} = \sum_{i=1}^N x_i^* x_i = \sum_{i=1}^N |x_i|^2 \quad (\text{A16})$$

Important algebraic properties which may become useful include :

$$\bar{\mathbf{x}}^T \mathbf{y} = \overline{(\bar{\mathbf{y}}^T \mathbf{x})} \quad (\text{A17})$$

$$(\overline{\alpha \mathbf{x}})^T \mathbf{y} = \overline{\alpha} (\overline{\mathbf{x}}^T \mathbf{y}) \quad (\text{A18})$$

where α is a complex number (a scalar).

When weights are used, the weighted scalar product $\overline{\mathbf{x}}^T \mathbf{P} \mathbf{y}$ can be defined as :

$$\overline{\mathbf{x}}^T \mathbf{P} \mathbf{y} = \begin{bmatrix} x_1^* & x_2^* & \cdots & x_N^* \end{bmatrix} \begin{bmatrix} p_1 & 0 & \cdots & 0 \\ 0 & p_2 & \cdots & 0 \\ \vdots & \vdots & \vdots & \vdots \\ 0 & 0 & 0 & p_N \end{bmatrix} \begin{bmatrix} y_1 \\ y_2 \\ \vdots \\ y_N \end{bmatrix} = \sum_{i=1}^N p_i x_i^* y_i \quad (\text{A19})$$

The solution to the system (A10) is simply :

$$\mathbf{a} = \mathbf{C}^{-1} \mathbf{q} \quad (\text{A20})$$

For convenience, let \mathbf{D} be the inverse of \mathbf{C} as :

$$\mathbf{D} = \mathbf{C}^{-1} \quad (\text{A21})$$

Therefore the solution \mathbf{a} is given as :

$$\mathbf{a} = \mathbf{D} \mathbf{q} \quad (\text{A22})$$

Finally a system of weights \mathbf{P} of (A9) needs to be determined so that the matrix \mathbf{C} of (A11) and vector \mathbf{q} of (A12) can be evaluated. The derivation of equations to calculate a set of weights based on the Propagation of Errors method described by [A1,A2] is described below. The amount of weighting for each measurement point may be based on the error of that measurement. The error for the i^{th} measurement can be described as :

$$\epsilon_i = (a_1 t_i + a_2 - a_3 t_i S_{21,i}) - S_{21,i} \quad (\text{A23})$$

The change in the error ϵ_i ($\Delta \epsilon_i$) due to each independent variable a_1 , a_2 and a_3 is [A1,A2]:

$$\Delta \epsilon_i = \frac{\partial \epsilon_i}{\partial a_1} \Delta a_1 + \frac{\partial \epsilon_i}{\partial a_2} \Delta a_2 + \frac{\partial \epsilon_i}{\partial a_3} \Delta a_3 \quad (\text{A24})$$

If the errors are random, the total squared error (variance) of the i^{th} measurement is found by adding the squares of the individual error terms to give [A1,A2] :

$$\sigma^2(\varepsilon_i) = \left| \frac{\partial \varepsilon_i}{\partial a_1} \right|^2 \sigma^2(a_1) + \left| \frac{\partial \varepsilon_i}{\partial a_2} \right|^2 \sigma^2(a_2) + \left| \frac{\partial \varepsilon_i}{\partial a_3} \right|^2 \sigma^2(a_3) \quad (\text{A25})$$

where $\sigma^2(a_1)$, $\sigma^2(a_2)$ and $\sigma^2(a_3)$ are the variances of the coefficients a_1 , a_2 and a_3 . Now, the weight of the i^{th} measurement should be inversely proportional to the squared error (variance of the i^{th} measurement) as [A2] :

$$p_i = \frac{\mu^2}{\sigma^2(\varepsilon_i)} \quad (\text{A26})$$

where μ^2 is simply an arbitrary constant and may be set to unity. When (A23) is substituted into (A25) the weight equation (A26) becomes :

$$p_i = \frac{1}{|t_i|^2 \sigma^2(a_1) + \sigma^2(a_2) + |t_i S_{2,i}|^2 \sigma^2(a_3)} \quad (\text{A27})$$

For the first iteration of each curve fitting procedure the variances of the coefficients are unknown. In such case, they can be arbitrarily set equal to each other (for example equal to unity) so that the initial weights become :

$$p_i = \frac{1}{1 + |t_i|^2 (1 + |S_{2,i}|^2)} \quad (\text{A28})$$

Once the weights p_i are allocated, the elements of \mathbf{C} and \mathbf{q} can be evaluated and the vector \mathbf{a} may be solved, which completes the first iteration of the curve fitting process. In order to proceed to the next iteration, the variances of the coefficients a_1 , a_2 , and a_3 , namely $\sigma^2(a_1)$, $\sigma^2(a_2)$ and $\sigma^2(a_3)$ needs to be calculated to produce a new set of weights using (A27). To find the variances, the error vector equation (A23) is modified with the weight P to give the two equivalent equations below :

$$\sum_{m=1}^3 \mathbf{P} \mathbf{e}_m a_m - \mathbf{P} \mathbf{f} = \mathbf{P} \boldsymbol{\varepsilon}$$

or equivalently expressed as:

$$\sum_{m=1}^3 \mathbf{e}_{p,m} a_m - \mathbf{f}_p = \boldsymbol{\varepsilon}_p \quad (\text{A29})$$

where the subscript p used in (A29) simply denotes the incorporation of weights within the vector; vectors \mathbf{e}_m and \mathbf{f} have been previously defined in (A5); and :

$$\mathbf{e}_{p,m} = \mathbf{P} \mathbf{e}_m; \quad \mathbf{f}_p = \mathbf{P} \mathbf{f}; \quad \boldsymbol{\varepsilon}_p = \mathbf{P} \boldsymbol{\varepsilon} \quad (\text{A30})$$

where the error vector $\boldsymbol{\varepsilon}$ which appears in (A29) is defined as :

$$\boldsymbol{\varepsilon} = \begin{bmatrix} \varepsilon_1 \\ \varepsilon_2 \\ \vdots \\ \varepsilon_N \end{bmatrix} \quad (\text{A31})$$

The data scatter D_s defined as [A1] :

$$D_s = \frac{|\boldsymbol{\varepsilon}_p|}{|\mathbf{f}_p|} \quad (\text{A32})$$

The data scatter provides an indication of the reliability of results of a curve-fit. The results of a fitting can be unreliable for $D_s \leq 0.1$ [A1].

By applying the propagation-of-errors formula to (A29), the change in the error with weights used can be obtained as [A1,A2]:

$$\begin{aligned} \Delta \boldsymbol{\varepsilon}_p &= \frac{\partial \boldsymbol{\varepsilon}_p}{\partial a_1} \Delta a_1 + \frac{\partial \boldsymbol{\varepsilon}_p}{\partial a_2} \Delta a_2 + \frac{\partial \boldsymbol{\varepsilon}_p}{\partial a_3} \Delta a_3 \\ &= \mathbf{e}_{p,1} \Delta a_1 + \mathbf{e}_{p,2} \Delta a_2 + \mathbf{e}_{p,3} \Delta a_3 \end{aligned} \quad (\text{A33})$$

Now the variance of the weighted measurement with weighting (ie the total sum of squares error of the measurement with weights used) is :

$$\begin{aligned} \sigma^2(\boldsymbol{\varepsilon}_p) &= |\mathbf{e}_{p,1}|^2 \sigma^2(a_1) + |\mathbf{e}_{p,2}|^2 \sigma^2(a_2) + |\mathbf{e}_{p,3}|^2 \sigma^2(a_3) \\ &= \sum_{m=1}^3 |\mathbf{e}_{p,m}|^2 \sigma^2(a_m) \\ &= |\boldsymbol{\varepsilon}_p|^2 \end{aligned} \quad (\text{A34})$$

where $|\boldsymbol{\varepsilon}_p|$ represents the norm of the weighted error vector. The convention used in this thesis to represent the norm of a vector is described by the following example. The norms of N dimensional vectors \mathbf{x} and \mathbf{x}_p (weights used) are given by :

$$\begin{aligned} |\mathbf{x}| &= \sqrt{\bar{\mathbf{x}}^T \mathbf{x}} \\ |\mathbf{x}_p| &= \sqrt{\bar{\mathbf{x}}^T \mathbf{P} \mathbf{x}} \end{aligned} \quad (\text{A35})$$

Hence, the application of definition of the norm described by (A35) to (A34) provides the following relationship which relates $|\epsilon_p|^2$ to the total squared sum of errors S^2 as :

$$\begin{aligned} |\epsilon_p|^2 &= \bar{\epsilon}^T \mathbf{P} \epsilon \\ &= \sum_{i=1}^N p_i |\epsilon_i|^2 = S^2 \end{aligned} \quad (\text{A36})$$

The equation (A36) simply enables $|\epsilon_p|$ to be evaluated, which is needed later to calculate the variances of the coefficients a_1 , a_2 and a_3 . It is also important to see that

$$|e_{p,m}| = \sqrt{e_m^T \mathbf{P} e_m} = \sqrt{C_{mm}} \quad (\text{A37})$$

Combining (A36) and (A37) with (A34) gives :

$$S^2 = \sum_{m=1}^3 C_{mm} \sigma^2(a_m) \quad (\text{A38})$$

For the least squares solution to an overdetermined system of linear equations, the variance (squared error) of each estimation coefficient is proportional to the corresponding diagonal element of matrix \mathbf{D} ($= \mathbf{C}^{-1}$) and to the total squared sum of errors S^2 [A1], hence :

$$\sigma^2(a_n) = D_{nn} S^2 \alpha \quad (\text{A39})$$

$$\sum_{m=1}^3 C_{mm} D_{mm} S^2 \alpha = S^2 \quad (\text{A40})$$

hence :

$$\alpha = \frac{1}{\sum_{m=1}^3 C_{mm} D_{mm}} \quad (\text{A41})$$

$$\sigma(a_n) = \sqrt{\frac{D_{nn} S^2}{\sum_{m=1}^3 C_{mm} D_{mm}}} \quad n = 1..3 \quad (\text{A42})$$

where $\sigma(a_n)$ is the standard deviation (or error) associated with the fit parameter a_n where n is a integer 1, 2 or 3. While above derivations of equations required for the implementation of the fractional linear curve fitting technique has been presented using complex transmission coefficient (S_{21}) values, the equations are feasible to be applied to complex reflection coefficient data (S_{11} or S_{22}). The curve fitting procedure is described in the following section.

BIBLIOGRAPHY OF APPENDIX A

[A1]D. Kajfez, "Q factor" , Vector Fields, 1994.

[A2]L.G. Parrat, "Probability And Experimental Errors In Science", New York:
Wiley, 1961.

APPENDIX B

IMPLEMENTATION OF THE FRACTIONAL LINEAR CURVE FITTING TECHNIQUE FOR FITTING TO S_{21} -PARAMETER Q-CIRCLE DATA SETS

The fractional linear curve fitting method begins with a set of measurement data consisting of real and imaginary values of S-parameter $S_{21,i}$ with corresponding frequency $\omega_i = 2\pi f_i$, where the index 'i' denotes the i^{th} element in the data set. For the first iteration of the fitting procedure, it is necessary to obtain an estimate value for the loaded resonant frequency ω_L which is simply done by taking the frequency at which the magnitude of S_{21} is largest in the S_{21} data set. The next step is to form the vectors \mathbf{e}_1 , \mathbf{e}_2 , and \mathbf{e}_3 and \mathbf{f} according to :

$$\mathbf{e}_1 = \begin{bmatrix} t_1 \\ t_2 \\ \vdots \\ t_N \end{bmatrix}; \mathbf{e}_2 = \begin{bmatrix} 1 \\ 1 \\ \vdots \\ 1 \end{bmatrix}; \mathbf{e}_3 = - \begin{bmatrix} a_3 S_{21,1} \\ a_3 S_{21,2} \\ \vdots \\ a_3 S_{21,N} \end{bmatrix}; \mathbf{f} = \begin{bmatrix} S_{21,1} \\ S_{21,2} \\ \vdots \\ S_{21,N} \end{bmatrix} \quad (\text{B1})$$

Then we use these vectors to form the matrix equation :

$$\begin{bmatrix} \bar{\mathbf{e}}_1^T \mathbf{P} \mathbf{e}_1 & \bar{\mathbf{e}}_1^T \mathbf{P} \mathbf{e}_2 & \bar{\mathbf{e}}_1^T \mathbf{P} \mathbf{e}_3 \\ \bar{\mathbf{e}}_2^T \mathbf{P} \mathbf{e}_1 & \bar{\mathbf{e}}_2^T \mathbf{P} \mathbf{e}_2 & \bar{\mathbf{e}}_2^T \mathbf{P} \mathbf{e}_3 \\ \bar{\mathbf{e}}_3^T \mathbf{P} \mathbf{e}_1 & \bar{\mathbf{e}}_3^T \mathbf{P} \mathbf{e}_2 & \bar{\mathbf{e}}_3^T \mathbf{P} \mathbf{e}_3 \end{bmatrix} \begin{bmatrix} a_1 \\ a_2 \\ a_3 \end{bmatrix} = \begin{bmatrix} \bar{\mathbf{e}}_1^T \mathbf{P} \mathbf{f} \\ \bar{\mathbf{e}}_2^T \mathbf{P} \mathbf{f} \\ \bar{\mathbf{e}}_3^T \mathbf{P} \mathbf{f} \end{bmatrix} \quad (\text{B2})$$

$$\text{where } \mathbf{P} = \begin{bmatrix} p_1 & 0 & 0 & 0 \\ 0 & p_2 & 0 & 0 \\ \vdots & \vdots & \vdots & \vdots \\ 0 & 0 & 0 & p_N \end{bmatrix} \quad (\text{B3})$$

Usually, the set of weights p_i is calculated using :

$$p_i = \frac{1}{|t_i|^2 \sigma^2(a_1) + \sigma^2(a_2) + |t_i S_{21,i}|^2 \sigma^2(a_3)} \quad (\text{B4})$$

In the first iteration of each curve fitting process, the variances are unknown. Hence in the first iteration only, the variances can be set to unity, and the weights are calculated using :

$$p_i = \frac{1}{1 + |t_i|^2 (1 + |S_{21,i}|^2)} \quad (\text{B5})$$

where t_i is a normalised frequency given by :

$$t_i \approx 2 \frac{\omega_i - \omega_L}{\omega_L} \quad (\text{B6})$$

The matrix equation (B2) is of the form : $\mathbf{C}\mathbf{a} = \mathbf{q}$

where

$$\mathbf{q} = \begin{bmatrix} \bar{\mathbf{e}}_1^T \mathbf{P} \mathbf{f} \\ \bar{\mathbf{e}}_2^T \mathbf{P} \mathbf{f} \\ \bar{\mathbf{e}}_3^T \mathbf{P} \mathbf{f} \end{bmatrix} \quad (\text{B7})$$

\mathbf{C} is a 3x3 matrix :

$$\mathbf{C} = \begin{bmatrix} \bar{\mathbf{e}}_1^T \mathbf{P} \mathbf{e}_1 & \bar{\mathbf{e}}_1^T \mathbf{P} \mathbf{e}_2 & \bar{\mathbf{e}}_1^T \mathbf{P} \mathbf{e}_3 \\ \bar{\mathbf{e}}_2^T \mathbf{P} \mathbf{e}_1 & \bar{\mathbf{e}}_2^T \mathbf{P} \mathbf{e}_2 & \bar{\mathbf{e}}_2^T \mathbf{P} \mathbf{e}_3 \\ \bar{\mathbf{e}}_3^T \mathbf{P} \mathbf{e}_1 & \bar{\mathbf{e}}_3^T \mathbf{P} \mathbf{e}_2 & \bar{\mathbf{e}}_3^T \mathbf{P} \mathbf{e}_3 \end{bmatrix} \quad (\text{B8})$$

Once the matrix \mathbf{C} and the vector \mathbf{q} have been evaluated, the vector \mathbf{a} can then be solved to obtain values for the coefficients (ie. fit parameters) a_1 , a_2 and a_3 . The next step is to obtain better values for the weights in order to find more accurate values for the coefficients contained in vector \mathbf{a} . This requires the errors ε_i to be calculated using :

$$\varepsilon_i = (a_1 t_i + a_2 - a_3 t_i S_{21,i}) - S_{21,i} \quad (\text{B9})$$

Using the errors ε_i calculated above , the weighted sum of squared errors value S^2 is calculated using :

$$S^2 = \sum_{i=1}^N p_i |\varepsilon_i|^2 \quad (\text{B10})$$

The variances are calculated from the elements of matrix \mathbf{C} and it's inverse matrix (namely $\mathbf{D}=\mathbf{C}^{-1}$) as :

$$\sigma(a_n) = \sqrt{\frac{D_{nn} S^2}{\sum_{m=1}^3 C_{mm} D_{mm}}} \quad n = 1..3 \quad (\text{B11})$$

Once the variances $\sigma^2(a_1)$, $\sigma^2(a_2)$ and $\sigma^2(a_3)$ are obtained, they can be used to calculate a new weight matrix using (B4) to be used for another iteration of the curve fitting procedure. Usually only three iterations is needed to achieve optimum results for the fit parameters. Hence after three iterations, the first curve fitting procedure is

considered to be completed. At this stage, the loaded resonant frequency chosen for the first curve fitting procedure may not be accurate so that the location of the resonant point S_{L1} may not be at the correct location even though the detuned point S_d is usually accurate as shown in Fig. B1.

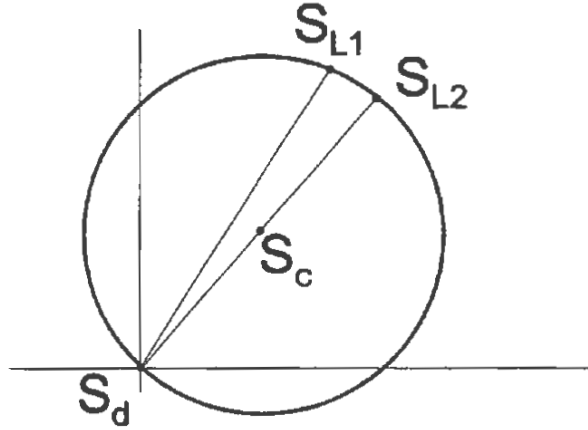


Figure B1 The value of S_{L1} at the resonant frequency may not be so accurate for the first curve fitting procedure.

It is possible to improve upon the value of loaded resonant frequency by first calculating a more accurate value of the loaded value of S-parameter given by :

$$S_{L2} = 2S_c - S_d \quad (\text{B12})$$

where S_c is the centre of the circle calculated as :

$$S_c = \frac{a_3^* a_2 - a_1}{a_3^* - a_3} \quad (\text{B13})$$

and S_d is the detuned value given by $S_d = a_1/a_3$. The improved value of frequency is given calculated as :

$$f_{L2} = f_{L1} \left(1 + \frac{\Delta t}{2} \right) \quad (\text{B14})$$

where Δt is the required normalised frequency shift needed to make the the new loaded resonant point lie on the same line joining the centre of the circle (S_c) to the detuned point S_d .

$$\Delta t = \frac{a_2 - S_{L2}}{S_{L2} a_3 - a_1} \quad (\text{B15})$$

Using the improved value for the resonance frequency, $\omega_{1,2} = 2\pi f_{L,2}$, it is then possible to repeat the whole curve fitting procedure to obtain more accurate values for the fit parameters a_1 , a_2 and a_3 . Hence, this method of finding more accurate values for the resonant frequency enables the curve fitting procedure to be continually repeated until best values for the fit parameters are obtained. Usually, there will be no significant changes to the fit parameter values after about three repeated curve fitting procedures.

The fractional linear curve fitting procedure described above can also be applied to fit a circle to reflection (S_{11} and S_{22}) Q-circles measured around the resonance, except that the first estimate for the resonant frequency required at the beginning of the fitting technique is chosen differently. For an ideal case where the coupling is lossless coupling and the coupling reactances are zero and absence of impedance mismatch effects, the resonant frequency should coincide with the minimum value of S_{11} (or S_{22}) around the resonance. However for a practical case, the resonance does not necessarily coincide with the minimum value of S_{11} around the resonance in the presence of finite coupling reactance and impedance mismatch effects. Nevertheless, it is still feasible to use the frequency which corresponds to the minimum value of the reflection coefficient in the data set as a first estimate for the loaded resonant frequency. While the first estimate of the resonant frequency may not be so accurate, the fractional linear curve fitting procedure will find an accurate value with repeated curve fittings.

APPENDIX C

ENHANCED PHASE CORRECTION PROCEDURE

The following method (to be demonstrated as an example) enables phase effects introduced by transmission lines, namely electrical delay effects to be systematically removed using data processing methods. The enhanced phase correction method provides a option over the trial and error method using the electrical delay removal feature of the HP8722C network analyser.

Consider the synthesised noise-free S_{11} trace observed over a very wide span of about 40 times the loaded bandwidth about the resonance frequency as shown in Fig. C1, which is obtained using the following circuit parameters for the circuit model of a transmission mode dielectric resonator described in Chapter 4.3 (Fig. 4.18) :

$$X_{s1}=X_{s2}=20\Omega, \quad R_1=R_2=5\Omega, \quad R_o=5\Omega, \quad Q_o=9000, \quad Q_L=7754, \quad f_o=10\text{GHz}, \\ L_1=L_2=70\lambda, \quad N=401 \text{ points.}$$

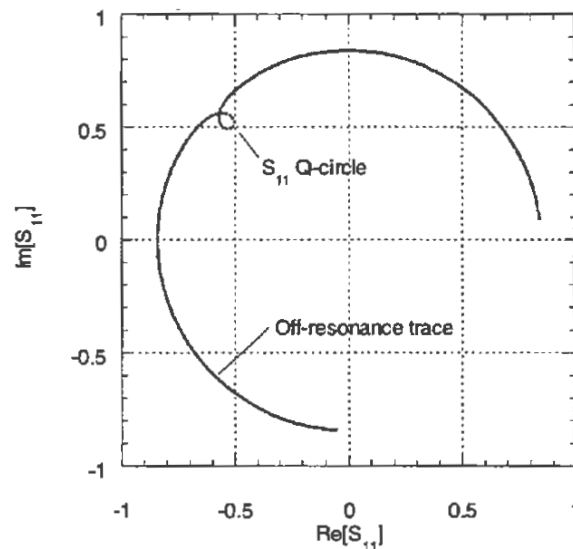


Figure C1 Synthesised S_{11} trace spanning 40 times the loaded bandwidth, showing the distorted S_{11} Q-circle and off-resonance curve. The circuit parameters used to generate the trace are : $X_{s1}=X_{s2}=20\Omega$, $R_1=R_2=5\Omega$, $R_o=5\Omega$, $Q_o=9000$, $Q_L=7754$, $f_o=10\text{GHz}$, $L_1=L_2=70\lambda$, $N=401$ points.

The S_{11} trace of Fig. C1 consists of two parts, namely the off-resonance curve and the Q-circle. The phase of S_{11} in the off-resonance parts decreases linearly with the frequency, and the rate of change of the phase with frequency depends on the length of the uncalibrated cable connected between the measurement point and the resonator. It is the frequency dependence of the phase which is responsible for the circular path of the S_{11} vector for frequencies outside the resonance. The frequency dependence of the introduced phase shift is also responsible for the distortion in the reflection Q-circle. The small Q-circle which 'rides' within the much larger circular off-resonance trace in Fig. C1 is clearly distorted, as recognised by its ovular shape. Correction of the phase of distorted Q-circles is possible if the rate of change of phase with frequency ($d\phi/dF$) is known. Correction of reflection (S_{11}) resonance data can be done by first selecting a point in the data set outside the resonance part [C1] and using this point as reference. Knowing $d\phi/dF$, the phase for any other point is corrected using :

$$\phi_{corr,i} = \phi_i - (f_i - f_1) \frac{\Delta\phi}{\Delta f} \text{ for all elements } i \quad (C1)$$

where ϕ_i and f_i represent the phase and the corresponding frequency of the i^{th} point in the S_{11} data set. The constants ϕ_1 and f_1 represent the phase and frequency of the reference point. Using the corrected phase $\phi_{corr,i}$, the corrected value of the i^{th} point in the S_{11} data set is simply :

$$S_{11cor,i} = |S_{11i}| e^{j\phi_{corr,i}} \text{ for all elements } i \quad (C2)$$

When transmission line phase effects removed, the corrected reflection circle should be circular and suitable for a curve fitting procedure to be applied. To demonstrate the phase correction method, the phase-frequency relationship for frequencies outside the resonance (with points outside the 180th and 220th point removed from the 401 point S_{11} data set corresponding to the S_{11} trace of Fig. C1) is shown in Fig. C2.

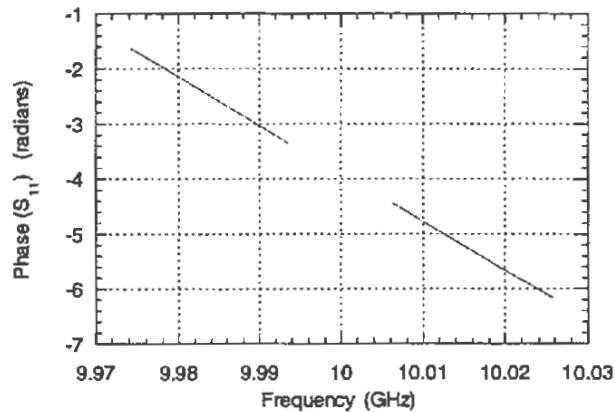


Figure C2 Phase of S_{11} versus frequency in off-resonance region.

When a linear fitting technique [C2,C3] is applied to the off-resonance phase response, the rate of change of phase with frequency is obtained to be about $-8.76 \cdot 10^{-8}$ radians/Hz. After applying the phase correction method to the full data set, the phase-corrected S_{11} Q-circle of Fig. C3 is obtained and the circular off-resonance trace which appears in Fig. C1 is completely removed. Applying the Q-Fit program to the corrected Q-circle of Fig. C3, the loaded Q-factor is recovered precisely (with no error).

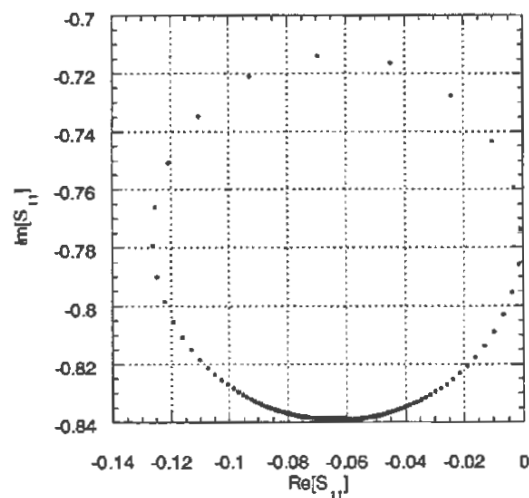


Figure C3 S_{11} Q-circle after the removal of phase distortion from the S_{11} Q-circle of Fig. C1.

When using the described enhanced ‘wide-span’ method to correct the phase of reflection coefficients in the Q-circle, it is assumed that the off-resonance circle is centred about the origin, as expected for a matched system. However, observations of experimental reflection Q-circles reveal that the off-resonance trace is not always centred about the origin due to impedance mismatch. For such cases the phase-frequency response in the off-resonance region is non-linear, and $d\phi/dF$ cannot be obtained from the non-linear response. Correction of this second order effect can be done by finding the centre of the circular off-resonance trace using a circle-fitting technique, which then determines the amount of offset. After the offset is removed from the measured reflection S-parameter data, the resulting trace will provide a linear phase-frequency relationship as is needed to determine the rate of change of phase $d\phi/dF$. It is important to point out that the offset in the wide band off-resonance circle is removed only to obtain the value of $d\phi/dF$. That is, the author of this thesis does not assume that the effect of impedance mismatch (recognised by the offset of the centre of the circular wideband off-resonance reflection trace) can be removed simply by removing the offset from reflection measurements of S_{11} or S_{22} .

BIBLIOGRAPHY OF APPENDIX C

- [C1]Private information obtained from L.M. Xie, Texas Center for Superconductivity, University of Houston.
- [C2]C.F. Gerald, P.O. Wheatley, "Applied Numerical Analysis Third Edition", Addison-Wesley Publishing Company, 1984.
- [C3]W.H. Press, S. Teukolsky, W. T. Vetterling, B. P. Flannery, "Numerical Recipes in C Second Edition", Cambridge University Press, 1994.

APPENDIX D

METHOD TO FIND THE CENTRE AND RADIUS OF THE CIRCLE PASSING THROUGH DATA POINTS DISTRIBUTED AROUND A CIRCULAR PATH USING LINEAR LEAST SQUARES CURVE FITTING TECHNIQUE

The method to find the centre (h,k) and the radius R of a circle fitted to data points distributed around a circular path (Fig. D1) was kindly demonstrated by Dr. Graeme Sneddon of the Department of Mathematics and Physics at the James Cook University.

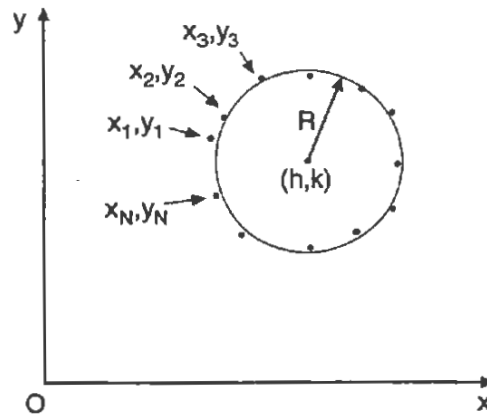


Figure D1 N data points distributed about a circular path with the first point (x_1, y_1) and last point (x_N, y_N) . The circle has centre (h, k) and radius R which need to be determined.

The technique involves the conversion of the standard mathematical equation describing a circle into a linear form. The standard equation representing a circle with centre coordinates (h, k) and radius R is :

$$(x-h)^2 + (y-k)^2 = R^2 \quad (\text{D1})$$

which is rearranged to give :

$$h^2 + k^2 - R^2 - 2hx - 2ky = -(x^2 + y^2) \quad (\text{D2})$$

Using the letter i to denote the index of a point in the data set, the indexed form of (D2) is

$$h^2 + k^2 - R^2 - 2hx_i - 2ky_i = -(x_i^2 + y_i^2) \quad (D3)$$

which is then simplified to the form of :

$$-2x_i h - 2y_i k + v = -(x_i^2 + y_i^2) \quad (D4)$$

where

$$v = h^2 + k^2 - R^2 \quad (D5)$$

For a N point data set, equations (D4) gives the following system of equations :

$$\begin{aligned} -2x_1 h - 2y_1 k + v &= -(x_1^2 + y_1^2) \\ -2x_2 h - 2y_2 k + v &= -(x_2^2 + y_2^2) \\ &\vdots \\ -2x_N h - 2y_N k + v &= -(x_N^2 + y_N^2) \end{aligned} \quad (D6)$$

The matrix equation for the system based on (D6) is :

$$\begin{bmatrix} -2x_1 & -2y_1 & 1 \\ -2x_2 & -2y_2 & 1 \\ \vdots & \vdots & \vdots \\ -2x_N & -2y_N & 1 \end{bmatrix} \begin{bmatrix} h \\ k \\ v \end{bmatrix} = \begin{bmatrix} -(x_1^2 + y_1^2) \\ -(x_2^2 + y_2^2) \\ \vdots \\ -(x_N^2 + y_N^2) \end{bmatrix} \quad (D7)$$

The matrix equation (D7) has the form :

$$\mathbf{A} \mathbf{x} = \mathbf{B} \quad (D8)$$

where :

$$\mathbf{A} = \begin{bmatrix} -2x_1 & -2y_1 & 1 \\ -2x_2 & -2y_2 & 1 \\ \vdots & \vdots & \vdots \\ -2x_N & -2y_N & 1 \end{bmatrix}; \quad \mathbf{x} = \begin{bmatrix} h \\ k \\ v \end{bmatrix}; \quad \mathbf{B} = \begin{bmatrix} -(x_1^2 + y_1^2) \\ -(x_2^2 + y_2^2) \\ \vdots \\ -(x_N^2 + y_N^2) \end{bmatrix} \quad (D9)$$

The vector \mathbf{x} containing the constants h , k , and v can be obtained from (D8) in the linear least squares solution :

$$\mathbf{x} = \mathbf{A}^{-1} \mathbf{B} \quad (D10)$$

The values of h and k obtained from the solution give the x and y coordinates of the circle respectively. And the radius R of the circle from (D5) is :

$$R = \sqrt{h^2 + k^2 - v} \quad (D11)$$

APPENDIX E

FIT RESULTS FOR THE 10 GHz MEASUREMENTS ON $\text{YBa}_2\text{Cu}_3\text{O}_7$ HTS THIN FILMS

```
Enter name of data file ->s21_77t.dat
data scatter = 1.522925e-002

RESULTS
Number of points = 1601
QL fitted = 403130.083042
Qerr = 3.513756e+003

EL fitted = 9996964155.499790 (Hz)
a1 = 1.562193 -25.277970
a2 = 0.055673 -0.007270
a3 = 0.034553 403130.083042

Detuned value = a1/a3 = -0.000063 -0.000004
angle of S21 resonance pt wrt origin = -7.439488 degrees
angle of S21 resonance pt wrt detuned point = -7.427295 degrees
diam of S21 circle = 0.056207
snr_db = 43.110925

Paused - press any key to continue
```

Figure E1 Printout results of the linear fractional curve fitting procedure applied to the S_{21} Q-circle with fitted Q_L of 403130.

```

Enter name of data file ->s11_7t.red
data scatter = 6.870885e-003

RESULTS
Number of points = 99
QL fitted = 399955.216004
Qerr = 5.418710e+003

FL fitted = 9997016098.232176 (Hz)
a1 = -263520.653738 -111714.589596
a2 = -0.259843 0.622048
a3 = -5230.893844 399955.216004

Detuned value = a1/a3 = -0.270654 0.662415

angle of S11 resonance pt wrt origin = 112.671370 degrees
angle of S11 resonance pt wrt detuned point = -75.006976 degrees
snr_db = 24.366260
diameter of s11 circle = 0.041790
diamloss = 1.674768
phi = -1.322197 psi = 1.958683 theta = 0.139287

Paused - press any key to continue

```

Figure E2 Printout results of the linear fractional curve fitting procedure applied to the corrected S_{11} Q-circle showing the real and imaginary parts of the fitted coefficients a_1 , a_2 and a_3 .

```

Enter name of data file ->s22_7t.red
data scatter = 2.177263e-002

RESULTS
Number of points = 130
QL fitted = 423096.575627
Qerr = 2.329077e+003

FL fitted = 9997013364.143942 (Hz)
a1 = 246522.542607 -129666.552872
a2 = -0.267209 -0.511284
a3 = -162.164645 423096.575627

Detuned value = a1/a3 = -0.306694 -0.582545

angle of S22 resonance pt wrt origin = -117.592608 degrees
angle of S22 resonance pt wrt detuned point = 61.009737 degrees
snr_db = 24.621914
diameter of s11 circle = 0.081469
diamloss = 1.657590
phi = 1.064438 psi = -2.055397 theta = 0.021759

Paused - press any key to continue

```

Figure E3 Printout of the linear fractional curve fitting to the corrected S_{22} Q-circle showing the real and imaginary parts of the fitted coefficients a_1 , a_2 and a_3 .

```

** Current status **

Ql_s21 = 403130.083042  fres_s21 = 9.996964155 GHz  s21diam = 0.056207
snr21 = 43.110925 db

s11 fit DONE
Ql_s11 = 399955.216004  fres_s11 = 9.997016098 GHz  s11diam = 0.041790
snr11 = 24.366260 db

s22 fit DONE
Ql_s22 = 423096.575627  fres_s22 = 9.997013364 GHz  s22diam = 0.081469
snr22 = 24.621914 db

Paused - press any key to continue

```

Figure E4 Comparison of the loaded Q_L -factors, resonant frequencies and Q-circle diameters, and signal-to-noise ratios obtained from S_{21} , S_{11} and S_{22} fits.

```

** Calculation of coupling coefficients **

s11diam = 0.041790  s11lossdiam = 1.674768
s22diam = 0.081469  s22lossdiam = 1.657590
k1_1 = 0.022567  k2_1 = 0.004382
k1_2 = 0.043994  k2_2 = 0.009088

K1 = port 1 coupling coefficient = 0.026950
K2 = port 2 coupling coefficient = 0.053082

fitted Qo = QL_s21*(1+K1+K2) = 435393.428420

Paused - press any key to continue

```

Figure E5 Results obtained from the Transmission Mode Q_o -factor Technique showing the computed port coupling coefficients K_1 and K_2 of 0.027 and 0.053 respectively, and the unloaded Q_o -factor of 435393 (calculated from Q_L of S_{21} -fit and the port coupling coefficients).

```
** Calculation of coupling coefficients **  
s11diam = 0.039618 s11lossdiam = 1.665478  
s22diam = 0.081951 s22lossdiam = 1.673318  
k1_1 = 0.021364 k2_1 = 0.004291  
k1_2 = 0.044191 k2_2 = 0.008627  
  
K1 = port 1 coupling coefficient = 0.025655  
K2 = port 2 coupling coefficient = 0.052819  
  
fitted Qo = QL_s21*(1+K1+K2) = 434764.960532  
  
Paused - press any key to continue
```

Figure E6 Unloaded Q_o -factor and port coupling coefficients obtained for the case with no phase correction of reflection Q -circles applied. The computed unloaded Q_o -factor is 434765.

APPENDIX F

FIT RESULTS FOR THE 25 GHz MEASUREMENTS ON $\text{YBa}_2\text{Cu}_3\text{O}_7$ HTS THIN FILMS

```
** Current status **  
  
QL_s21 = 22717.806858  fres_s21 = 24.750245930 GHz  s21diam = 0.159828  
snr21 = 45.040505 db  
  
s11 fit DONE  
QL_s11 = 23906.732919  fres_s11 = 24.750252091 GHz  s11diam = 0.202090  
snr11 = 43.843799 db  
  
s22 fit DONE  
QL_s22 = 23226.305367  fres_s22 = 24.750201069 GHz  s22diam = 0.112192  
snr22 = 28.425804 db  
  
Paused - press any key to continue
```

Figure F1 The loaded Q_L -factors, resonant frequencies, and signal to noise ratios obtained from the curve fitting procedure applied to the S_{21} trace, and the corrected S_{11} and S_{22} traces.

```
** Calculation of coupling coefficients **  
  
s11diam = 0.202090  s11lossdiam = 1.635969  
s22diam = 0.112192  s22lossdiam = 1.676310  
k1_1 = 0.124817  k2_1 = 0.027774  
k1_2 = 0.069294  k2_2 = 0.013380  
  
K1 = port 1 coupling coefficient = 0.152591  
K2 = port 2 coupling coefficient = 0.082674  
  
fitted  $Q_o = Q_L\_s21 * (1 + K1 + K2) = 28062.507478$   
  
Paused - press any key to continue
```

Figure F2 Fitted unloaded Q_o -factor and coupling coefficient results obtained from the full unloaded Q_o -factor circle fitting procedure.